

**HYDROLOGICAL AND HYDROGEOCHEMICAL CHARACTERISTICS OF NEUTRAL
DRAINAGE FROM A WASTE ROCK TEST PILE**

by

DANIEL S. BAY

B.Sc. Queen's University, 2004

A THESIS SUBMITTED IN PARTIAL FULFILLMENT OF
THE REQUIREMENTS FOR THE DEGREE OF

MASTER OF SCIENCE

in

THE FACULTY OF GRADUATE STUDIES

(Geological Science)

THE UNIVERSITY OF BRITISH COLUMBIA

(Vancouver)

August 2009

© Daniel S. Bay, 2009

ABSTRACT

In 2005 the University of British Columbia, Teck's Applied Research & Technology (ART) group and Compañía Minera Antamina S.A. initiated a collaborative study to improve the hydrological, geochemical, mineralogical and biological understanding of mine waste rock. The site of the investigation is the Antamina mine, Peru, which consists of a polymetallic Cu-Zn-skarn deposit that produces high carbonate-content waste rock and typically leads to pH-neutral effluent waters. One component of this study is the construction of five 36 m x 36 m x 10 m (high) waste rock piles upon an impermeable HDPE liner placed to capture and monitor the quality and quantity of all infiltrating water. The first test pile was constructed in 2006 and consists of relatively coarse, heterogeneous marble and hornfels waste rock material that may produce moderately- to poor-quality drainage according to the classification scheme used at the mine. A comprehensive network of instrumentation measures the in-situ temperature and moisture content, and allows the extraction of fluid samples from within the pile. The objective of this thesis is to analyze the hydrological and geochemical data collected from test pile 1 during the initial 21 months of pile operation between January-2007 and October-2008. Results indicate that flow and chemistry exhibit strong spatial and seasonal patterns. Seasonal patterns are driven by the wet season rains that deposit a majority of the annual rainfall over 7 months, and spatial patterns are likely controlled by rock-type heterogeneity and variability in flow path length and residence time that result from the end-dump construction process. Test pile 1 took 3 – 4 months to wet up, and the maximum pile outflow measured during the wet season is nearly 15 m³/day. Water balance calculations indicate that 41 % of precipitation reports as outflow while 59 % evaporates over the course of one water year. Effluent water is pH-neutral (pH = 7 - 8.5), with seasonally varying SO₄ (500 – 2000 mg/L) and Zn (0.5 – 2.5 mg/L) concentrations. Based on the maximum calculated SO₄ and Zn loading rates of 4 – 6 and 0.003 – 0.005 mg/kg/week, respectively, nearly 0.4 % of the total initial solid phase sulphur has been depleted, whereas only 0.01 % of the total initial solid phase Zn has been depleted. Waste rock reactivity appears to be declining with time.

TABLE OF CONTENTS

ABSTRACT.....	ii
TABLE OF CONTENTS.....	iii
LIST OF TABLES.....	viii
LIST OF FIGURES.....	ix
ACKNOWLEDGEMENTS.....	xi
DEDICATION.....	xii
1 INTRODUCTION.....	1
1.1 BACKGROUND AND SIGNIFICANCE.....	1
1.2 THE ANTAMINA MINE.....	2
1.3 PROJECT OVERVIEW	2
1.4 RELEVANCE TO THE ANTAMINA MINE.....	3
1.5 THESIS OBJECTIVES	4
1.6 LITERATURE REVIEW	5
1.6.1 What is Waste Rock?.....	5
1.6.2 End-Dumping and Internal Structure.....	6
1.6.3 Waste Rock: Physical Properties	7
1.6.4 Waste Rock: Flow Processes	8
1.6.4.1 Soil Water Characteristic Curve.....	8
1.6.4.2 Hydraulic Conductivity.....	9
1.6.4.3 Matrix and Preferential Flow	10
1.6.4.3.1 Preferential Flow	11
1.6.4.3.2 Capillary Barrier.....	12
1.6.4.3.3 Macropore Flow	12
1.6.5 Waste Rock: Chemistry	12
1.6.5.1 Residence Time: Impact of Flow on Chemistry.....	13
1.6.6 Challenges in Predicting Weathering from Particle Size and Flow Indices	14
1.6.7 Waste Rock: Neutral Drainage	14
1.6.8 Challenges in Waste Rock Investigations: Scaling Issues.....	15
1.6.9 Waste Rock Test Piles	16
1.7 ORGANIZATION OF THESIS	17
2 SITE DESCRIPTION, INSTRUMENTATION, SAMPLING AND MATERIAL CHARACTERIZATION	21
2.1 LOCATION.....	21
2.2 CLIMATE.....	21
2.3 REGIONAL GEOLOGY.....	21
2.4 DEPOSIT GEOLOGY.....	22
2.5 HYDROGEOLOGY	23
2.6 DEPOSIT DEVELOPMENT.....	24
2.7 WASTE ROCK GENERATION AT ANTAMINA.....	25
2.8 WASTE ROCK CLASSIFICATION	26
2.9 TEST-PILE DESIGN.....	26
2.9.1 Site	27

2.9.2	Base Construction Methods	27
2.9.3	Pile Construction Methods.....	28
2.10	INSTRUMENTATION	29
2.10.1	Pile Instrumentation	29
2.10.1.1	Time Domain Reflectometry Probes.....	30
2.10.1.2	Thermistors.....	30
2.10.1.3	Soil Water Solution Samplers	31
2.10.1.4	Gas Ports	31
2.10.1.5	Tipping Buckets	32
2.10.1.6	Electrical Conductivity Probes.....	32
2.10.1.7	Composite Tank and Flow Splitter	33
2.10.2	Meteorological Instrumentation.....	34
2.10.2.1	Precipitation	34
2.10.2.2	Evaporation	34
2.10.2.3	Air Temperature, Relative Humidity, Wind Speed and Direction.....	34
2.11	WATER SAMPLING.....	35
2.11.1	Water Quality Parameters.....	35
2.11.1.1	Field Parameters	35
2.11.1.2	Lab Parameters.....	35
2.11.1.2.1	Dissolved Metals	36
2.11.1.2.2	Total Metals	36
2.11.1.2.3	Other parameters.....	36
2.12	GAS SAMPLING	37
2.13	WASTE ROCK PROPERTIES	37
2.13.1	Solid Phase Mineralogical Composition.....	37
2.13.2	Solid Phase Elemental Composition.....	38
2.13.3	Acid Base Accounting	38
2.13.4	Particle Size Distribution	39
2.13.5	Hydraulic Properties	40
2.13.6	Dry Bulk Density	40
2.13.7	Porosity	41
2.14	SUMMARY.....	42
3	RESULTS: TEST PILE HYDROLOGY	56
3.1	PRECIPITATION.....	57
3.1.1	Estimation of Missing Precipitation Data.....	57
3.1.1.1	Local Gauges and Linear Least Square Regression Analysis.....	57
3.1.2	Estimation Validity.....	58
3.1.3	Uncertainty in Precipitation Measurements.....	60
3.1.4	Final Site Precipitation and Reported Trends	61
3.2	EVAPORATION	62
3.2.1	Evaporation: Study Period	63
3.2.2	Evaporation: 2007-2008 Water Year	63
3.2.2.1	Pan Evaporation and Penman-Monteith Estimates	64
3.2.2.2	Modeled Evaporative Fluxes: SoilCover	65
3.2.2.3	Lysimetry Water Balance Estimate.....	66
3.3	OUTFLOW	66

3.3.1	Correcting Tipping Bucket Data: RANSAC.....	67
3.3.2	Total Pile Discharge.....	68
3.3.3	Outflow Hydrographs	69
3.3.4	Hydrograph Variability.....	70
3.3.5	Lysimeter Net Infiltration	72
3.3.6	Effect of Antecedent Moisture Content	72
3.3.7	Wet Season Responses.....	74
3.3.7.1	Preferential and Macropore Flow.....	74
3.3.7.2	Pressure-Wave Displacement of Water through the Pile	77
3.3.7.3	Non-Vertical Flow.....	77
3.3.8	Difficulty Identifying Different Flow Pathways and Multiple Arrivals	78
3.3.9	Uncertainty.....	79
3.4	MOISTURE CONTENT	81
3.4.1	Time Domain Reflectometry Data.....	81
3.4.2	TDR Probe Response.....	82
3.4.2.1	Protective Layer	82
3.4.2.2	Compacted Surface	83
3.4.2.3	Batter	85
3.4.2.4	TDR Variability.....	86
3.4.3	Wetting Front Propagation and Evidence of Preferential or Non-Vertical Flow ...	87
3.4.4	Change in Storage.....	88
3.5	DISCUSSION	89
3.5.1	Water Balance.....	89
3.5.2	Pore Water Displacement and Macropore Flow Velocity	90
3.5.3	Effects of the Batter on Pile Hydrology.....	93
3.6	SUMMARY	93
4	RESULTS: TEST PILE GEOCHEMISTRY	108
4.1	ELECTRICAL CONDUCTIVITY	109
4.1.1	Lysimeters.....	109
4.1.2	Composite Tank.....	111
4.1.3	Pile Interior	111
4.1.3.1	Changes at Depth	112
4.2	TEMPERATURE	113
4.2.1	Lysimeters.....	113
4.2.2	Pile Interior	114
4.2.2.1	Internal vs. External Temperatures	115
4.2.2.2	Spatial Variability in Temperatures	116
4.2.2.3	Evidence of Advection and/or Evaporation from Front Batter	116
4.3	PH	117
4.3.1	Lysimeters.....	117
4.3.2	Composite Tank	118
4.3.3	Sump	118
4.3.4	Pile Interior	119
4.4	SOLUTES	119
4.4.1	Metals.....	120
4.4.1.1	Zinc.....	120

4.4.1.1.1	Lysimeters, Composite Tank and Sump.....	120
4.4.1.1.2	Pile Interior.....	121
4.4.2	Cations.....	122
4.4.2.1	Lysimeters, Composite Tank and Sump.....	122
4.4.2.2	Pile Interior.....	123
4.4.3	Trace Metals.....	123
4.4.4	Major Ions.....	124
4.4.4.1	Dissolved Sulphate.....	124
4.4.4.2	Alkalinity.....	125
4.4.4.3	Nitrate.....	125
4.5	PORE GASES.....	126
4.6	GEOCHEMICAL MODELING.....	127
4.7	DISCUSSION.....	128
4.7.1	Gypsum Precipitation and the $\text{SO}_4^{2-}/\text{Ca}^{2+}$ Ratio.....	128
4.7.2	Zinc: Source and Attenuation Mechanisms.....	129
4.7.3	Spatial Variability.....	130
4.7.4	Comparison to Field Cell Chemistry.....	131
4.8	SUMMARY.....	133
5	RESULTS: TEST PILE MASS LOADINGS.....	154
5.1	INITIAL PILE COMPOSITION.....	154
5.2	SOLUTE MASS LOADINGS.....	155
5.2.1	Low-Resolution Mass Loadings.....	156
5.2.1.1	Cumulative Loadings.....	156
5.2.1.2	Time-Averaged Loading Rates.....	156
5.2.1.3	Flow vs. Chemistry.....	157
5.2.1.4	Specific Conductance-Solute Correlations.....	158
5.2.2	High-Resolution Mass Loadings.....	159
5.2.2.1	Basal Lysimeter SO_4 Loading.....	159
5.2.2.2	Lysimeter SO_4 , Ca and Zn Loadings.....	160
5.2.3	Comparison Between Low- and High-Resolution Loadings.....	160
5.2.4	Comparison to Field Cells.....	161
5.3	ELEMENT DEPLETION ESTIMATES.....	162
5.3.1	Mineral Depletion Uncertainties.....	163
5.4	SUMMARY.....	164
6	DATA INTEGRATION.....	174
6.1	EVIDENCE OF DIFFERENT FLOW MECHANISMS.....	174
6.2	PYRITE OXIDATION: ESTIMATING SO_4	175
6.3	OXYGEN DEPLETION ESTIMATE.....	176
6.4	SPATIAL VARIABILITY IN PILE BEHAVIOUR.....	177
6.4.1	Protective Layer.....	178
6.4.2	Tipping Phase I - Sub-lysimeter B.....	179
6.4.3	Tipping Phase II - Sub-lysimeter A.....	180
6.4.4	Tipping Phase III - Sub-lysimeter C.....	181
6.4.5	Entire Pile / Basal Lysimeter D.....	183
6.5	SUMMARY.....	183

7	CONCLUSIONS	187
7.1	PROJECT OVERVIEW AND SIGNIFICANCE	187
7.2	SUMMARY OF RESULTS	187
7.2.1	Material Properties	187
7.2.2	Hydrology	188
7.2.3	Chemistry	188
7.2.4	Solute Loadings	189
7.2.5	Data Integration	190
7.3	RELEVANCE TO THE ANTAMINA MINE.....	191
7.3.1	Tucush Dump.....	191
7.3.2	Re-Classification of Class B Waste Rock.....	192
7.3.3	Possibility to Reduce Solute Concentrations Based on Dump Modifications	192
7.4	RECOMMENDATIONS FOR CURRENT PILE MAINTENANCE AND FUTURE PILE CONSTRUCTION	193
7.4.1	Instrumentation	193
7.4.2	Modeling	193
7.4.3	Data Management	193
7.4.4	Further Tests	194
7.4.5	Personnel.....	195
7.5	CONCLUDING REMARKS.....	195
8	REFERENCES.....	196
APPENDIX A:	PILE DESIGN AND CONSTRUCTION.....	206
APPENDIX B:	PILE 2 & 3 CONSTRUCTION MODIFICATIONS FROM PILE 1.....	217
APPENDIX C:	PRECIPITATION.....	225
APPENDIX D:	EVAPORATION	243
APPENDIX E:	OUTFLOW	262
APPENDIX F:	TIME DOMAIN REFLECTOMETRY PROBES.....	287
APPENDIX G:	COMPOSITE TANK, FLOW SPLITTER AND SUMP.....	296
APPENDIX H:	DATALOGGER PROGRAM.....	300
APPENDIX I:	MATLAB M.FILES	306

LIST OF TABLES

Table 1.1. Comparison of recent waste rock test piles.....	18
Table 2.1. General classification of waste rock types from the Antamina mine.....	44
Table 2.2. Test pile 1 construction timeline.....	45
Table 2.3. Solid phase mineral composition of waste rock.....	46
Table 2.4. Solid phase elemental composition of waste rock.	46
Table 2.5. Summary of instrumentation.....	47
Table 2.6. Final mass calculation.....	47
Table 3.1. Total estimated volume, weekly rate, and daily flux of precipitation and lysimeter outflow....	95
Table 3.2. Summary of evaporation estimates throughout the study period and water year.	96
Table 3.3. Cumulative interpreted flow for each lysimeter.	97
Table 4.1. Parameter comparison between basal-lysimeter and composite tank.	135
Table 4.2. Temperature comparison between top and bottom of pile.....	135
Table 4.3. Solute discharging and receiving limits.....	136
Table 4.4. Minerals modeled to be near saturation in basal lysimeter effluent.....	136
Table 5.1. Cumulative and average wet and dry season loading rates.....	165
Table 5.2. Specific conductance-solute lysimeters and composite tank regression correlations.	165
Table 5.3. High- and low-resolution basal lysimeter loading comparison; 2007.	165
Table 5.4. High- and low-resolution lysimeter loading comparison; 11- to 19-April-2007.	166
Table 5.5. Average field cell and lysimeter loading rates.....	167
Table 6.1. Integration of waste rock material and lysimeter effluent properties.	185

LIST OF FIGURES

Figure 1.1. Neutral drainage waste rock project. Components relevant to this thesis are shaded in blue. .	19
Figure 1.2. Waste rock pile schematic.	19
Figure 1.3. Flow processes in waste rock.	20
Figure 2.1. Map of mine location.....	48
Figure 2.2. Plan view of schematic lithology of the Antamina deposit.	49
Figure 2.3. Schematic lithology and metal zonation of Antamina.....	49
Figure 2.4. Map of the Antamina mine.	50
Figure 2.5. South view of completed test pile 1 and platforms.....	51
Figure 2.6. Test pile 1 base design and instrumentation schematic.	52
Figure 2.7. Test pile 1 side profile and instrumentation schematic.....	52
Figure 2.8. Plan view location of instrumentation points in relation to pile exterior.....	53
Figure 2.9. Inside the instrumentation hut.	54
Figure 2.10. Particle size distribution of waste rock material placed in the pile.	55
Figure 3.1. Antamina rain gauge locations with respect to the study site.....	98
Figure 3.2. Reported and estimated cumulative rainfall compared to the Antamina precipitation.....	98
Figure 3.3. Rainfall comparison between the two site rain gauges.....	99
Figure 3.4. Daily and cumulative estimated precipitation.	99
Figure 3.5. Variability of rain as measured by site rain gauge during Jan-2008	100
Figure 3.6. Class A Pan evaporation schematic and Yanacancha station, Antamina.	100
Figure 3.7. Daily precipitation and evaporation	101
Figure 3.8. Comparison between top and batter of pile.	101
Figure 3.9. Outflow hydrograph for the sub-lysimeters and basal lysimeter.....	102
Figure 3.10. Precipitation and lysimeter fluxes.	104
Figure 3.11. Upper, lower and expected flow for basal lysimeter D and sub-lysimeter C.	105
Figure 3.12. Shallow TDR moisture content and precipitation in mm/day.	106
Figure 3.13. Line 4 TDR moisture content response.	106
Figure 3.14. Line 1 TDR moisture content and precipitation.	107
Figure 3.15. Line 2 TDR moisture content and precipitation.	107
Figure 4.1. Continual and weekly-obtained specific conductivity vs. and pile discharge.	137
Figure 4.2. Parameter comparison between basal lysimeter and composite tank.	138
Figure 4.3. Temporal and spatial distribution of specific conductance.	139
Figure 4.4. Cross-sectional diagram of four construction stages and four lysimeters	140
Figure 4.5. Internal and external pile temperature variation.....	141
Figure 4.6. Average temperatures in lines 1, 2 and 4 over the water year.....	142
Figure 4.7. Temporal and spatial distribution of pH.....	143
Figure 4.8. Temporal and spatial distribution of Zn.	144
Figure 4.9. Sump comparison to basal lysimeter and composite tank.	145
Figure 4.10. Temporal and spatial distribution of Ca.	146
Figure 4.11. Temporal and spatial distribution of Na.	147
Figure 4.12. Temporal and spatial distribution of Mg	148
Figure 4.13. Temporal and spatial distribution of K.....	149
Figure 4.14. Temporal and spatial distribution of SO ₄	150
Figure 4.15. Temporal and spatial distribution of alkalinity.....	150
Figure 4.16. Percent charge balance error of PHREEQC model of basal lysimeter data.	151
Figure 4.17. Gypsum SI for the basal lysimeter D and composite tank E.	151
Figure 4.18. Calcite SI for the basal lysimeter D and composite tank E.	151
Figure 4.19. A trilinear Piper Plot of basal lysimeter D effluent	152
Figure 4.20. Regression analysis of Ca and SO ₄ at basal lysimeter D.	152
Figure 4.21. Correlation between SO ₄ and Zn at lysimeters and composite tank.....	153

Figure 5.1. Best estimated cumulative pile loadings..... 168
Figure 5.2. Best estimated weekly SO₄, Ca and Zn mass loadings for all four lysimeters. 169
Figure 5.3. Weekly SO₄, Ca and Zn solute concentration and mass loading..... 170
Figure 5.4. Specific conductance correlation to SO₄, Ca and Zn as measured at D. 171
Figure 5.5. Basal lysimeter loading comparison to concentration and flow rate; 2007. 172
Figure 5.6. Lysimeter loading variation, 11- to 19-Apr-2007..... 173
Figure 6.1. Integration of physical properties and observations throughout the pile..... 186

ACKNOWLEDGEMENTS

It was a privilege to work with, and learn from, my supervisors Roger Beckie, Leslie Smith and Uli Mayer. Thank you for your guidance and support, and for keeping the atmosphere light and humorous. Many thanks go to Bern Klein, Ward Wilson and Stephane Brienne for their support on the Antamina project.

This thesis could not have been accomplished without the financial support of the Natural Science and Engineering Research Council of Canada, Teck's Advanced Research and Training group, and Compañía Minera Antamina.

I owe a great deal to all of my UBC colleagues, especially Juan Carlos Corazao Gallegos, Matt Neuner, and Craig Nichol. I exceptionally enjoyed sharing an office with several great people and benefitting from the combined wealth of knowledge within it. Specifically, this includes: Sharon Blackmore, Mike Conlan, John Dockrey, Katie Jones, Cassandra Koenig, Holly Peterson and Cindy Starzyk. Special thanks also goes to Celedonio Aranda, Charlene Haupt and Joe Marcoline, and to Andre Wild, David Jones, Karim Damani, Sukhi Hundal and Joern Unger for other logistical and technical help. I would also like to express deep gratitude to Bae Yong Joon for his spiritual support along the way.

At Antamina, I owe a great deal to Humberto Valdivia, Bartolome Vargas and Raul Jamanca. Several others in the environmental area, and people from the contractors Hijos de Ayash were also integral in the process. A very special thanks goes to Fabiola Sifuentes.

To my loving parents Eli and Masza,

Without your endless love and support I could have never accomplished this endeavor. This thesis, my proudest achievement, is dedicated to you both.

Press on.

Nothing in the world can take the place of perseverance.

Talent will not;
Nothing is more common than unsuccessful men with talent.

Genius will not;
Unrewarded genius is almost a proverb.

Education will not;
The world is full of educated derelicts.

Persistence and determination are omnipotent.

- Calvin Coolidge

The important thing is not to stop questioning.

- Albert Einstein

1 INTRODUCTION

1.1 BACKGROUND AND SIGNIFICANCE

The mining of base metals and other resources removes and transports more material than any other industry (ICOLD, 1996; Blowes et al., 2007). Every year, millions of tonnes of earth is exhumed, transported and processed, which consequently impacts the local environment. As a result of the increasing prevalence of mining operations, these local impacts have received global attention. In recent decades, mining practices have departed from the former doctrine of profit generation without concern for socio-environmental issues. Today, efficient and more sustainable practices are being used in the mining industry, and mine waste management continues to draw more attention.

Mining activities focus on the extraction of metals and other resources from geological deposits, which may release contaminants to the environment during extraction and processing operations. Since most metal mines contain sulphide minerals, the exposure of mine wastes such as tailings and waste rock to the atmosphere often generates acidic effluent water that typically contains high dissolved solute concentrations. When this occurs, the effluent is referred to as Acid Rock Drainage (ARD). While mine wastes are typically stationary and remain in a given location indefinitely, their effluent can potentially traverse very large distances. On United States Forest Service Lands alone, there are an estimated 20,000 – 50,000 small mines releasing acidic drainage and an estimated 6,400 km of rivers and streams in the eastern United States that have been affected by this process (USDA, 1993; Blowes et al., 2007; Kleinmann et al., 1991). In Canada an estimated \$ 2 – 5 billion are required to address all of the costs of poor-quality water effluent from mine environments (Feasby and Tremblay, 1995; Price, 2003). Based on these figures, the magnitude of current and future environmental impacts from the mining industry is substantial.

When a significant acid-buffering capacity is found in the host rock of an ore deposit, it is possible for the mine waste effluent to have a neutral pH. This is referred to as Neutral Rock Drainage (NRD). While metals such as aluminum, lead, iron and copper are relatively immobile under neutral conditions, other metals such as zinc, molybdenum, arsenic, antimony, selenium,

cadmium and chromium may be more mobile than under lower pH conditions (the term metal is broadened to include metalloid elements such as arsenic; Price, 2003). The pH-neutral effluent water may still contain a high dissolved load and lead to environmental impacts. There is relatively little literature concerning neutral mine drainage, particularly originating from waste rock. It is for this reason that a comprehensive investigation examining the physical, hydrological, chemical, and biological mechanisms involved in metal release, transport and attenuation in neutral-pH mine effluent is underway at the Antamina mine, Peru.

1.2 THE ANTAMINA MINE

The Antamina mining facilities are operated by Compañía Minera Antamina S.A. (CMA), which is a privately held company owned by BHP Billiton (33.75 %), Xtrata (33.75 %), Teck (22.5 %) and Mitsubishi (10 %). CMA is a multi-billion dollar copper and zinc mining project located in the Peruvian Andes, approximately 270 km north of Lima. Project facilities extend from 4,700 m a.s.l where the conventional open pit mine, milling, and concentrator flotation operations are located down to the sea-level port facilities. The mine is connected to the port via a 302-km concentrate pipeline. Official mining operations began in 2001 and are expected to continue until at least 2020. Processing of the low-/marginal-grade stockpile is expected to occur between 2021 and 2024, and mine closure is scheduled to be completed by at least 2029 (Golder, 2007a). Throughout the life of the mine, an estimated 600 million tonnes of ore will be unearthed, resulting in an additional 1,500 million tonnes of waste rock. The ‘waste rock-to-ore’ ratio is approximately 2.5 (Golder, 2007a).

With several neighbouring village communities relying on the seeps, springs and rivers of the region, Antamina has a responsibility to find suitable practices that minimize the socio-environmental impact on the surroundings. Financing is provided from several international lenders and requires rigorous compliance with environmental and social guidelines as adhered to by domestic and international regulations.

1.3 PROJECT OVERVIEW

The research in this thesis is part of an extensive collaborative research project among the University of British Columbia, Compañía Minera Antamina S.A., Teck, and the Natural

Sciences and Engineering Research Council of Canada. The primary objective of the project is to characterize and understand the processes that control the release, mobilization and transport of metals in NRD from waste rock. The intent of the project is to provide a comprehensive characterization of neutral drainage conditions at Antamina and to understand how to use short-time and small-scale testing to predict long-time, large-scale field responses. Improved understanding of NRD leaching will allow Antamina to better manage their waste rock and identify, transport and dispose of it in the most cost-effective fashion with minimal environmental impact in short- and long-term timeframes.

The project involves a suite of experiments ranging from mineralogical analyses and microbiological and geochemical laboratory studies to field-scale experimental waste rock piles that are employed to address the processes governing metal and other solute release, transport and attenuation in this neutral-pH drainage environment (Figure 1.1).

1.4 RELEVANCE TO THE ANTAMINA MINE

The responsibility of monitoring, controlling and mitigating the hydrological vulnerability of its waste rock management practices is critical to Antamina's sustainability. By the end of 2006, nearly one-third of the 1.5 billion tonnes of waste rock estimated to be generated throughout the life of the mine from 2001 to (at least) 2020 was already removed (Golder, 2007a). Antamina's waste rock is sorted into three categories of expected leaching behavior on site based upon elemental and mineral assays from drill cores. Classes A, B and C represent waste rock that will typically produce leachate with solute loads that will require treatment, may require treatment and won't require treatment, respectively.

There are two principal waste rock disposal sites at Antamina, the East Dump and the Tucush Dump. The East Dump is by far the largest dump at Antamina and receives all of the Class A material, and some Class B and C material. The Tucush Dump receives only Class B and Class C waste rock material because it is situated within a partially-karstic valley that has a large potential for rapid solute transport. Both the East and Tucush Dumps are located within different drainage basins.

Several methods are utilized by the mine to re-route, capture and treat a majority of mine effluent water. The East Dump is located upon lower permeability strata that directs most of the poor quality drainage water to a tailings pond. Drainage from the Tucush Dump is expected to be more benign, and is therefore routed through a constructed wetland to attenuate dissolved solids and solutes. Due to a significant variability in Class B waste rock, there is a level of uncertainty surrounding the drainage quality of Tucush effluent and wetland performance. To address this issue, the first test pile in this neutral-pH drainage study was constructed using Class B waste rock.

With better understanding of the metal release and attenuation mechanisms in the Class B material, the mine will be able to manage its waste rock in a more effective manner. This may involve directing more or less Class B waste rock to the Tucush Dump to ensure that the effluent compliance levels are met and the potential impacts of waste water are mitigated.

1.5 THESIS OBJECTIVES

This thesis characterizes the initial 2 years of hydrological and geochemical data obtained from the first experimental waste rock pile (test pile 1) that was built (Figure 1.1). This pile was constructed with 'run-of-the-mine' Class B marble and hornfels waste rock using the same conventional end-dumping method that the mine employs to dispose of the waste rock. Constructed in 2006 by Corazao Gallegos (2007), this 36 x 36 x 10 m (high) pile was designed at an intermediate scale between the laboratory and field cell experiments, and the existent mine waste rock piles. Aranda (2009) examines the leaching characteristics of eight field cells constructed with material from test pile 1. Pile dimensions were decided based on the tradeoff between the largest size to ensure results that are representative of full-scale piles and the most cost-effective way in which to construct the pile. The piles represent the largest sized-experiment within the context of this comprehensive project. Test pile 1 results will be used to address the following research questions:

1. What are the principal mechanisms that control the hydrology, chemistry and solute mass loadings in this Class B waste rock test-pile?

2. How can results from this experiment be related to those from other experiments at different scales and related to the existing mine waste rock piles?
3. How can results be used to improve management of the Tucush Dump?
4. How can results be used to improve short-term mitigation and long-term mine closure strategies?

Although results from the first two years of pile operation do not provide long-term trends in pile behaviour, they are useful in characterizing the initial pile flushing and hydrogeochemistry, and will help in understanding which flow processes are occurring within the pile under certain conditions. This study will be useful in subsequent scale-up investigation and modeling efforts, and can be combined with results from several previously published reports related to this comprehensive project (Corazao Gallegos, 2007; Corazao Gallegos et al., 2007; Bay et al., 2009; Aranda, 2009; Aranda et al., 2009; Conlan, 2009).

1.6 LITERATURE REVIEW

Previous studies have investigated waste rock-water interactions, reactions and weathering rates that control acid generation, sulphate and metal release from mine waste environments. Smith and Beckie (2003) contains a comprehensive summary of hydrological and geochemical transport processes in waste rock, whereas Nichol (2002), Wagner (2004), Corazao-Gallegos (2007), Marcoline (2008) and Neuner (2009) contain detailed reviews of the processes that lead to poor-quality drainage from waste rock environments. The following section examines several important processes that contribute to solute mass loadings in waste rock, with particular attention given to the physical properties of waste rock that determine the nature of and chemical composition of the flow.

1.6.1 What is Waste Rock?

Two principal forms of waste are generated from mining activities: mine tailings and waste rock. Tailings are the fine-grained material left over after mineral processing, whereas waste rock is the low-grade overburden material that surrounds an ore deposit and must be removed in order to access it. There has been a considerable amount of research pertaining to mine tailings (Wunderly et al., 1996; Blowes et al., 1998; Moncur et al., 2005; Petrunic et al., 2005) and heap

leach processes (Brierley and Brierley, 2000; Olson and Clark, 2008; Webb et al., 2008), yet relatively less is known about mine waste rock and the mechanisms responsible for metal release, attenuation and transportation.

Waste rock is produced by the crushing force of blasting, and results in a wide variety of particles that range in size from clay to large boulders. Most waste rock is placed in large disposal sites located near the open pit where they typically remain indefinitely. As Nichol et al. (2005) describe, these waste rock piles are generally thick unsaturated zones tens to hundreds of meters high, and are composed of physically and chemically heterogeneous materials containing a large variability in size, texture, permeability, macropores, fractures and capillary breaks. The internal structure of a waste rock pile is largely dependent on the method in which the material is placed, which itself is dependent on site conditions and equipment availability (Bellehumeur, 2001; Fala et al., 2003).

1.6.2 End-Dumping and Internal Structure

A comparison of different waste rock disposal methods is found in Corazao (2007), the two most conventional being push- and end-dumping. Push-dumping involves dumping material in lifts at the top of a pile and a bulldozer pushing it level whereas end-dumping involves dumping material directly across the crest. Waste rock is segregated in both methods and leads to different internal structures which leads to different flow and chemical transport pathways throughout the pile. Push-dumping generally results in a coarse lower zone and a non-uniform upper zone with horizontal traffic surfaces between lifts. In end-dumping, the conventional waste rock disposal strategy employed at Antamina, material segregation occurs upon the tipping of waste rock from the truck as cobbles and boulders accumulate near the bottom of the slope and silts and sands tend to settle near the top of the pile (Fala et al., 2005). As illustrated in Figure 1.2, this results in a heterogeneous pile that is highly anisotropic with spatially variable hydraulic conductivity (Saretzky, 1998).

An intermediate region is often present between the upper finer zone and the lower coarser zone, and characteristically includes evenly distributed material (Morin et al., 1991). Discontinuous inter-bedded inclining layers of fine- and coarse-grained material, approximately dipping at the

angle of repose ($\sim 37^\circ$), were observed in several waste rock piles as stated by Fala et al. (2005), Stockwell et al. (2006) and Azam et al. (2007). These layers result from the preferential settling (or deposition) of coarser materials underneath finer-grained materials that settle at a slower rate and may lead to flow focusing (Figure 1.2).

The compaction of the top of the pile under the traffic of heavy equipment causes a finer grain-sized, lower-permeability traffic layer in which infiltration is much slower compared to the coarse-grained, unconsolidated pile batters around the edge of the pile (Fala et al., 2005; Bellehumeur, 2001). At the Cluff Lake mine, Saskatchewan, Canada, Bellehumeur (2001) found that an untrafficked waste rock surface consisting of loose gravel, cobble-sized waste rock and a few fines encountered almost immediate infiltration at the surface under the most extreme rainfall events, whereas a finer, compacted traffic surface led to ponding and overland flow. These led to dramatic differences in the hydrological and geochemical regime of the pile and to stratification or channeling of the flow of water.

1.6.3 Waste Rock: Physical Properties

When waste rock is exposed to atmospheric oxygen and precipitation, it may undergo a series of (bio)geochemical reactions that can potentially release contaminants such as heavy metals to the environment. Physical heterogeneities in waste rock (e.g., particle size, texture, lithology, chemical composition, stratification, channeling, segregation, sorption, and permeability) impact the rate, direction and uniformity of flow through waste rock. These flow differences will directly affect the chemical composition and solute mass loadings of the effluent water. In general, the two main factors that control the fluid flow and chemical transport in waste rock are the particle size distribution and texture (Smith and Beckie, 2003).

Waste rock typically exists within a range of grain sizes that spans almost six orders of magnitude, between 1 μm and 1 m, depending on the different processing and depositional methods (Fala et al, 2005). This physical heterogeneity makes the understanding and prediction of flow through unsaturated waste rock material highly complex. To define the relative proportion of fine and coarse fractions in a granular matrix, particle size distributions (PSD) are often used. PSD's may help indicate the tendency of certain types of flow to occur in waste rock,

as water retention generally increases as the particle size and porosity decrease (Aubertin et al., 2003; Fala et al., 2005).

Waste rock texture is a primary control on the infiltration capacity, sorptivity and geometry of fluid pathways. It is typically granular in texture due to the blasting process and often ranges from zones with a fine-grained matrix enveloping large cobbles and boulders to matrix-free clast-supported zones (Nichol et al., 2005). If waste rock consists of a relatively large proportion of fine material (e.g., has greater than 20 % fines less than 2 mm in diameter), it creates a matrix in which the larger cobbles and boulders are likely embedded (Dawson and Morgenstern, 1995; Smith and Beckie, 2003). The waste rock pile is referred to as acting in a 'soil-like' manner (Smith and Beckie, 2003). Conversely, if the waste rock consists of a relatively small proportion of fine material (e.g., less than 20 % fines), the fine-grained material in combination with an assortment of larger particles may create large voids and connected macropores. This type of waste rock is referred to as 'rock-like' (Smith and Beckie, 2003). The flow of water is more channeled in rock-like material and dominated by matrix flow in soil-like material, with implications for discharge quality and quantity.

1.6.4 Waste Rock: Flow Processes

The hydraulic properties of waste rock are a function of the physical properties of the waste rock material. In the finer-grained matrix where capillarity controls flow, this relationship can be expressed by the soil water characteristic curve and the hydraulic conductivity, which may indicate the tendency of one type of flow to occur over another, which has implications for solute mobilization. To understand the processes that lead to solute mass loadings, waste rock flow processes are examined.

1.6.4.1 Soil Water Characteristic Curve

A soil water characteristic curve describes the relationship between particle size, soil moisture content and/or soil water suction (i.e., matric or capillary forces). Yazdani et al. (2000) describe that capillarity is related to the size of the particles within a structure, and that particles with a diameter > 4.75 mm (#4 sieve) exhibit little capillarity regardless of whether they are under loose or dense arrangement. Material < 4.75 mm in diameter will typically exhibit slow and diffuse

matrix flow whereas material with a grain size distribution containing less than 35 % fines (< 4.75mm diameter), rapidly loses its ability to retain water under tension and would typically exhibit macropore-like flow. Herasymuik et al. (1995) use the same distinction to characterize between fine- and coarse-grained materials and serves as a suitable reference to distinguish between these material classes. Yazdani (1995) presents a detailed account of how moisture content (including antecedent moisture and water retention), pore geometry and particle size changes can affect the hydraulic properties of the pile and thus the hydraulic conductivity.

1.6.4.2 Hydraulic Conductivity

In unsaturated waste rock conditions, hydraulic properties are highly dependent on the physical waste rock properties which dictate the amount and connectivity of water-filled pore spaces (Fala et al., 2005). Hydraulic conductivity varies with location, due to depositional processes, and in time, due to variations in saturation and mineral precipitation-dissolution (Morin et al., 1991). Water retention generally increases as particle size and porosity decrease, yet the saturated hydraulic conductivity tends to increase with the average size of the particles (Aubertin et al., 2003; Mbonimpa et al., 2002). However, very large boulders (i.e., > 1 – 2 m in diameter) do not have a bulk porosity and do not contribute to the overall bulk porosity of a waste rock pile (Yazdani et al., 2000; Fala et al., 2003; Neuner, 2009). Due to a large variability in particle size, the infiltration capacity can accordingly vary by several orders of magnitude as explained by Bellehumeur (2001), who found that steady state infiltration was quite different from rapid infiltration at different locations in a waste rock pile, suggesting that a bi-modal permeability was present.

Much like particle size is highly variable in waste rock piles, so too is hydraulic conductivity, which is a function of the particle size and orientation. Morin et al. (1991) state that a single conductivity value cannot be used to accurately represent an entire waste rock pile, and that a range of values should be considered to account for the variations in particle size, rock characteristics, and construction techniques. It is for this reason that highly variable systems are often attributed multi-modal properties (Gerke and van Genuchten, 1993; Diodato and Parizek, 1994; Flury et al., 1994; Tuller and Or, 2002). For simplicity, the hydraulic conductivities for waste rock can conceptually be divided into two types of flow:

1. matrix flow, and
2. preferential flow.

1.6.4.3 Matrix and Preferential Flow

In most unsaturated waste rock, flow is either in the form of matrix or preferential flow (Figure 1.3). In a soil-like waste rock in which a significant proportion of finer-grained particles are present, the fine-grained matrix is generally able to retain and transport water under tension or capillary forces. This is referred to as matrix flow. Conversely, in a rock-like waste rock in which a large fraction of coarse material is present, the dominant flow mechanism may be via non-capillary or gravity-driven preferential flow. Each type of flow can be described using different physical and chemical properties such as porosity, particle size, hydraulic conductivity, matric suction, etc.

Matrix flow typically experiences slow and diffuse, matric (and gravity) force-driven capillary flow throughout both wet and dry periods whereas the coarser grained waste rock will encounter rapid, gravity-driven preferential flow that is generally activated under high moisture conditions. Therefore, matrix flow is typically the dominant flow mechanism in waste rock (Wagner et al., 2006; Neuner, 2009). The fine-grained matrix material has the ability to retain a larger volume of water under matric forces whereas the coarser-grained materials typically retain a lower volume of water.

When the matrix is fully saturated, the specific discharge of water q [m/s] through the material can be described by Darcy's Law, which relates the hydraulic conductivity K [m/s] of a saturated porous medium to the hydraulic gradient, $\partial h/\partial l$ [unitless] in order to determine the specific discharge as described in the following equation:

$$q = -K \left(\frac{\partial h}{\partial l} \right) \quad [1-1]$$

This equation describes the one-dimensional specific discharge of water and assumes that the material is fully saturated and that the flow is laminar. Under unsaturated conditions of waste

rock, the vertical, gravity-driven infiltration flux through the unsaturated zone is a function of matric pressure ψ [kPa] or volumetric water content Θ [unitless] and can be expressed as $K(\psi)$ or $K(\Theta)$ as summarized in Richard's Equation (1931):

$$q_z = -K(\psi) \left(\frac{d\psi}{dz} + 1 \right) \quad [1-2]$$

While matrix flow is subject to Darcy's Law, preferential flow may or may not be, depending on the type of flow (Figure 1.3).

1.6.4.3.1 Preferential Flow

Under certain conditions, clast-supported regions of the pile can often create large voids that may be filled under heavy infiltration events. This can lead to water by-passing the matrix under high saturation conditions and can result in rapid slugs of relatively fresh water penetrating much quicker than flow through the matrix (Nichol, 2002; Smith and Beckie, 2003). Preferential flowpaths generally occur due to collections of connected pores that concentrate flow to certain pathways, and typically result in large variations in the timing, magnitude and volume of the flow response at the base of a waste rock impoundment (Corazao Gallegos, 2007). Since matrix flow is much slower, preferential flow will undoubtedly lead to differences in residence time and can greatly impact water quality. According to Smith et al. (1995), water can infiltrate the entire depth of an experimental waste rock pile in times from within only a few hours to several years, indicating that most waste rock piles have spatially variable hydraulic properties due to variations in moisture content, grain size distribution and/or mineralogy (Fala et al., 2005; Smith and Beckie, 2003). Based on the occurrence of frequent experimental observations of this preferential flow in unsaturated porous media, Flury et al. (1994) explain that this phenomenon is commonly believed to be the rule rather than the exception.

Preferential flow consists of macropore flow, which describes the rapid flow of water through large connected voids, and capillary barrier-flow, which describes the slower movement of water around fine-grained material via capillary contact. Preferential flow likely most often occurs due to capillary barriers that cause flow focusing. Capillary barrier-flow is subject to Darcy's Law whereas macropore flow is not (Figure 1.3).

1.6.4.3.2 Capillary Barrier

Evidence of the preferential flow of water along fine-grained lenses or around large boulders through capillary contact has been observed in several investigations (Diodato and Parizek, 1994; Bellehumeur, 2001; Bussiere et al., 2003; Fala et al., 2005; Stockwell et al., 2006). Under conditions where interbedded fine- and coarse-grained layers are present (i.e., as created from the end-dumping of waste rock), a capillary barrier may be formed in which water may be preferentially retained in the finer-grained material due to capillary forces. This may result in the preferential flow of water that is focused to other regions, likely having implications on solute loadings.

1.6.4.3.3 Macropore Flow

The flow of water through large connected void spaces that is typically activated under high infiltration events and responsible for rapidly channeling of water much faster than the capillary-dominated matrix-flow velocities (up to 5 m over a few hours) is referred to as macropore flow (Germann and Beven, 1981; Eriksson et al., 1997; Newman, 1999; Smith and Beckie, 2003; Nichol et al., 2005; Stockwell, 2006; Marcoline, 2008; Neuner, 2009). Macropore flow is also referred to as non-capillary flow. Due to a higher infiltration rate and subsequent lower residence time, this type of flow typically consists of a lower dissolved load than matrix flow.

1.6.5 Waste Rock: Chemistry

Fala et al. (2005) conclude that the flow of water, transport of aqueous components, and dissolution/precipitation of solid minerals are closely coupled processes in mine waste environments. In the presence of reactive waste rock, these processes often interact in complex ways to generate poor quality drainage. Based on this, waste rock effluent chemistry is ultimately determined by the physical waste rock properties (PSD, texture, structure, mineralogy) and flow through this material.

The leaching of metals and generation of acidic drainage are both common features in waste rock where sulphide minerals are present. Pyrite is the most common sulphide mineral in most mine environments, the oxidation of which has been very well documented (Morin et al., 1991; Pantelis and Ritchie, 1992; Ritchie, 1994; Jambor and Blowes, 1998). The amount of, and time

in which, water is in contact with a sulphide mineral surface (e.g., pyrite) is a significant controlling factor that affects water quality. The release of metals is a complex process that is primarily dependent on the waste rock mineralogy and presence of water and oxygen. Precipitation events lead to the highly variable vertical flow of water through a waste rock pile. Just as the presence of water is a critical component in characterizing pile behaviour, so is the distribution and movement of pile gases such as oxygen. The movement of oxygen in waste rock piles may be influenced by temperature gradients between the pile surface (subject to ambient temperature) and pile interior (mainly due to heat released from pyrite oxidation). While gas transport typically occurs through diffusion, it may be enhanced through thermally-driven gas convection if the material is sufficiently permeable (Lefebvre et al, 2001). Therefore, both oxygen transport and temperature have strong influences on the rate at which geochemical processes proceed.

1.6.5.1 Residence Time: Impact of Flow on Chemistry

There is a general relationship between outflow volume and chemistry in waste rock (Wagner et al., 2006). Slow-moving water through the fine-grained matrix will typically have a higher dissolved load because it has a higher contact time with a greater surface area compared to faster-flowing water through macropores, which is generally associated with rapid slugs of fresher water (Smith and Beckie, 2003). Assuming no distinct chemical differences between material, the finer-grained material will typically undergo the most significant weathering. For example, Strömbererg and Banwart (1999) found that particles < 0.25 mm contributed to nearly 80 % of the sulphide and silicate dissolution at the Aitik Copper mine, Sweden.

Under relatively wet conditions, larger macropores can preferentially flush and channel water rapidly through the unsaturated pile, the shorter residence times generally result in lower dissolved loads. During dry periods, water transport is slow and predominantly exists as matrix-flow and results in a higher dissolved load (Wagner et al., 2006). Effluent water draining from the base of the pile typically represents both types of flow, but can be dominated by one flow or another depending on site conditions, the antecedent moisture content and time of year (Smith and Beckie, 2003; Nichol et al., 2005).

1.6.6 Challenges in Predicting Weathering from Particle Size and Flow Indices

During the deconstruction of a 12-m high waste rock dump, Stockwell et al. (2006) characterized the physical properties that control the flow of water by measuring soil water suction, volumetric water content, grain size distribution and mineral weathering at various locations within the pile. The goal was to relate these physical and chemical characteristics to the tendency for preferential flow and mineral weathering to occur based on the relative fraction of fine-to-coarse grained material. A large fine-grained fraction by weight may indicate a tendency for matrix flow to occur within the pile (more weathering), whereas a relatively coarse distribution may indicate a tendency for macropore-dominated flow to occur more frequently (less weathering). However, Stockwell et al. (2006) was unable to establish a relationship between physical flow indices and chemical weathering characteristics.

1.6.7 Waste Rock: Neutral Drainage

Whereas several investigations have examined the acidic rock drainage of mine environments, relatively less is known about the neutral rock drainage. Blowes et al. (2007) report that neutral-pH conditions exist at several tailings impoundments and open pits. Neutral-pH drainage can result provided there is a sufficient source of acid buffering potential in the gangue minerals to counter the acid generated by sulfide mineral oxidation. Neutralization often occurs in three distinct pH-buffering plateaus that correspond to the dissolution of carbonates (circum-neutral), hydroxides (acidic) and silicates (very acidic) (Blowes and Ptacek, 1994; Moncur et al., 2005). Several studies have examined these pH-dependent acid buffering tendencies in mine tailings, with particular emphasis on laboratory investigations pertaining to the secondary mineralization that forms coatings around mineral surfaces (Petrunic et al., 2006; Moncur et al. 2005; Sherlock et al., 1995; Jambor and Blowes, 1998; Blowes et al., 1998; Lin and Herbert, 1997; Davis and Ritchie, 1986, Ritchie, 1994; Jambor and Blowes, 1998). Other laboratory investigations have focused on the neutralization potential of acidic mine waste water (Sobek et al., 1978; Sherlock et al., 1994, Strömberg and Banwart, 1998). There is limited work pertaining to neutral drainage from waste rock.

Several waste rock experiments across different scales have investigated the mechanisms that lead to acid mine drainage. Only a limited number of experiments at the laboratory scale have

examined the mechanisms that lead to neutral drainage from waste rock. No comprehensive hydrological and geochemical investigation into neutral-pH waste rock drainage from a field-scale test-pile has yet been carried out.

1.6.8 Challenges in Waste Rock Investigations: Scaling Issues

The mechanisms that lead to mineral weathering and acid generation are highly dependent on scale. Since it is never feasible to have detailed characteristics of a given waste rock, various waste rock leaching methodologies spanning several orders of magnitude from μm to 10's of m have been established. Results of these experiments consistently indicate a discrepancy between the mineral weathering rates at the different scales (Malmström et al., 2000). Corazao Gallegos (2007) describes waste rock investigations spanning several scales from the laboratory to the field-scale. The intention is to scale-up or extrapolate from lab to field scale in order to generate reliable correction factors that will enable the prediction of loadings from existing waste rock (Otwindowski, 1995; Eriksson et al., 1997; Malmström et al., 2000; Frostad et al., 2005).

Laboratory settings provide the most manageable, cost-effective way in which to conduct physical, hydrological, chemical, mineralogical and biological experiments on waste rock in a controlled setting. Laboratory experiments are somewhat biased because they do not subject the material to actual environmental conditions. On the other hand, field cells are larger than most laboratory tests and are constructed in the field so that they are exposed to the same atmospheric conditions of the existent waste rock pile. These experiments still demonstrate limitations in predicting metal leaching from the existing waste rock piles based on their limited particle size distribution (e.g., less than 10 cm) and loadings rates, but are useful for validating leaching release rates obtained from laboratory tests (Frostad et al., 2005). Consequently, field-scale test piles are typically constructed with 'run of the mine' waste rock and exhibit trends most similar to the existing waste rock piles.

There is a large discrepancy of several orders of magnitude between the weathering rates reported in the lab and field (Malmström et al., 2000). Empirical, site-specific correction factors can possibly be determined but cannot be applied at different sites. These differences are most likely due to the variation in particle sizes between the different experiment scales as lab

experiments may only range over 2 - 3 orders of magnitude but field experiments may vary by orders of 5 or more. Since surface area decreases with larger particle sizes, the relative abundance of surface site reactions will likely be higher in laboratory experiments.

Due to the complexities involved in characterizing the hydrological and geochemical mechanisms involved in mine waste rock, various 1-, 2- and 3-D flow, transport, and coupled reactive transport models have been generated to better understand waste rock environments (e.g., Lefebvre, 1994; Lefebvre and Gelinas, 1995; Mayer et al., 1999; Sracek et al., 2004; Linklater et al., 2005). Wagner (2004) contains a detailed review of the various models. However, because it is difficult to obtain accurate predictions based solely on numerical models, field and lab experiments that take place over several years are required to make advances towards a more complete conceptual framework.

1.6.9 Waste Rock Test Piles

Numerous investigations of operational waste rock piles at various mines demonstrate that the physical, hydrological and chemical characterization using conventional subsurface methods is often highly complex and leads to large uncertainties in estimating and predicting pile behaviour (Smith et al., 1995; Herasymuik, 1995; Eriksson et al., 1997; Price, 2003; Lefebvre et al., 2001; Sracek et al., 2004; Linklater et al., 2005; Milczarek et al., 2009). The exact flow paths and locations of obstacles encountered along the way, such as a large boulder or a low-permeability layer, are largely unknown and only hypothesized based on inferences from the data. This will also have strong implications on the porewater chemistry. Consequently, these challenges have led to the construction of several field-scale test-pile experiments in various climates throughout the world (e.g., Table 1.1).

Field-scale waste rock piles provide a necessary intermediate link in scale between laboratory and field cell experiments and the full-scale waste rock piles. There are no well-established criteria for waste rock test pile construction. In general, the design of each pile is determined by a balance between practicality and cost. Ideally, each pile is large enough to sufficiently capture all of the field-scale processes while meeting reasonable budget constraints. For example, while the differences between matrix and macropore flow may be evident in a smaller test pile

(perhaps 2 – 3 m high), gas transport dynamics that typically manifest in larger-scale operational waste rock dumps may not be. In these large dumps, oxygen may not be able to penetrate to the centre of the pile whereas a smaller pile may be well-aerated and not entirely representative of the operational dump (Pantelis and Ritchie, 1992). Therefore, all of these considerations are required when designing a waste rock test pile.

1.7 ORGANIZATION OF THESIS

This thesis examines the first two years of data collected from waste rock test pile 1 at the Antamina mine. Relevant data from other parts of the project will be referred to and, if appropriate, compared to the test pile data. Final integration of the test pile data and data from other studies is a future task in the Antamina research project.

This chapter summarized the project scope and motivation and reviewed the pertinent literature about waste rock hydrology and chemistry. Chapter 2 examines the site conditions of the Antamina mine, project design and test pile construction, and physical and chemical properties of the waste rock used in test pile 1. Chapter 3 examines the hydrological characterization of test pile 1, with emphasis on the outflow rates and flow mechanisms. Chapter 4 examines the waste rock effluent chemistry and Chapter 5 integrates hydrology and chemistry with particular emphasis placed on the evolution of the solute mass loadings. Chapter 6 synthesizes selected data from Chapters 2 to 5 to highlight the main mechanisms that contribute to solute mass loadings of test pile 1. Chapter 7 summarizes the major findings and conclusions from each chapter. Future recommendations to improve this investigation and significance for the Antamina mine are also discussed.

TABLES

Table 1.1. Comparison of recent waste rock test piles.

Test Pile Site	Location	Authors	Pile Dimensions [m] (length x width x height)
Cluff Lake Mine	Saskatchewan, Canada	Bellehumeur, 2001 Nichol et al., 2005 Wagner et al., 2006 Marcoline, 2008	8 x 8 x 5
Key Lake Mine	Saskatchewan, Canada	Carey et al., 2005 Stockwell et al., 2006	25 x 25 x 12
Antamina Mine	Ancash Department, Peru	Corazao Gallegos et al., 2007	36 x 36 x 10
Diavik Mine	Northwest Territories, Canada	Neuner et al., 2009	60 x 50 x 14
Cadia Hill Mine	New South Wales, Australia	Rhode & Williams, 2009	~ 200 x 35 x 15
Grasberg Mine	Papua Province, Indonesia	Andrina et al., 2003	480 x 80 x 20

FIGURES

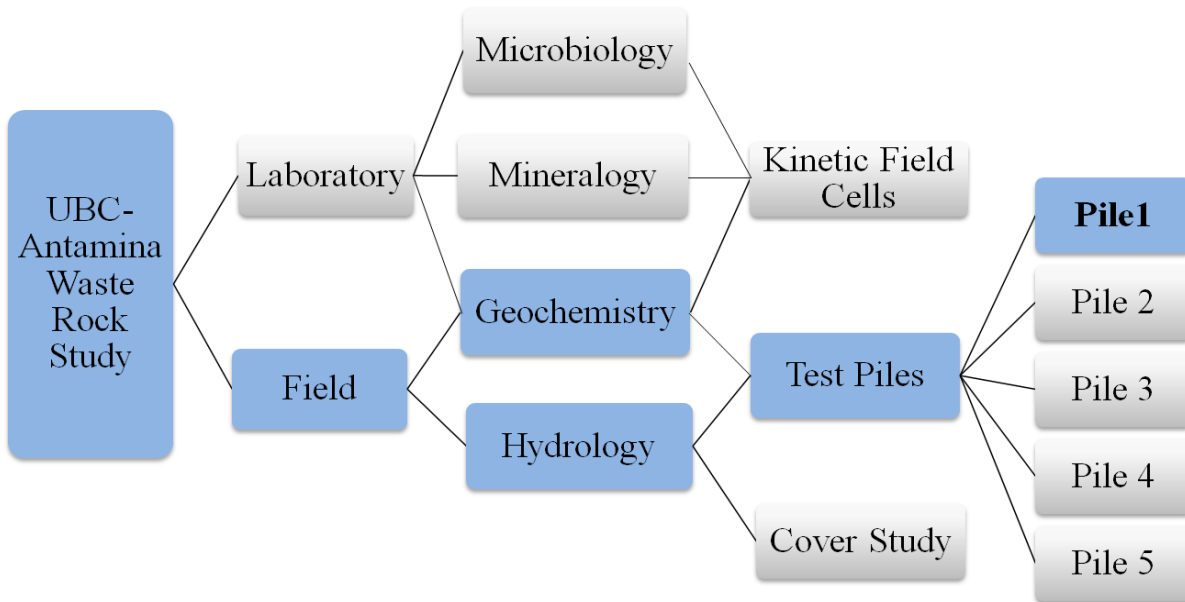


Figure 1.1. Neutral drainage waste rock project. Components relevant to this thesis are shaded in blue.

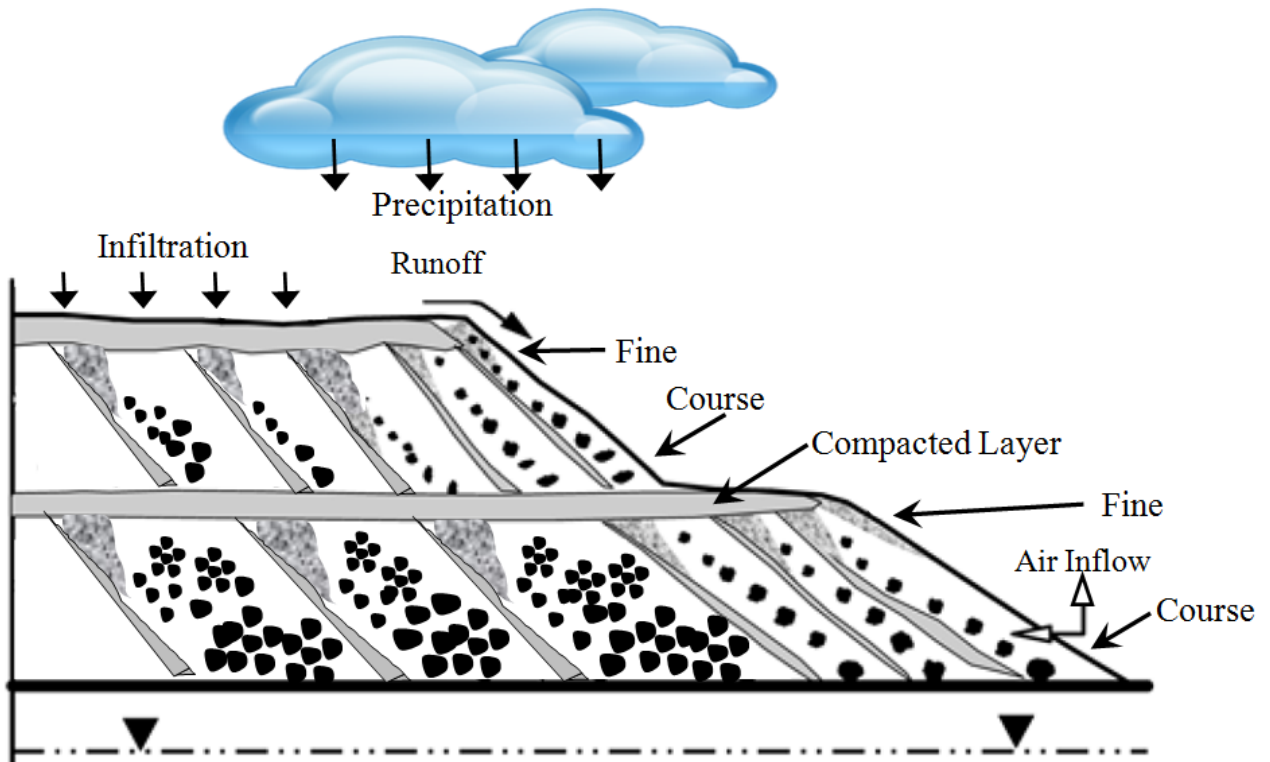


Figure 1.2. Waste rock pile schematic. Modified from Fala et al. (2005).

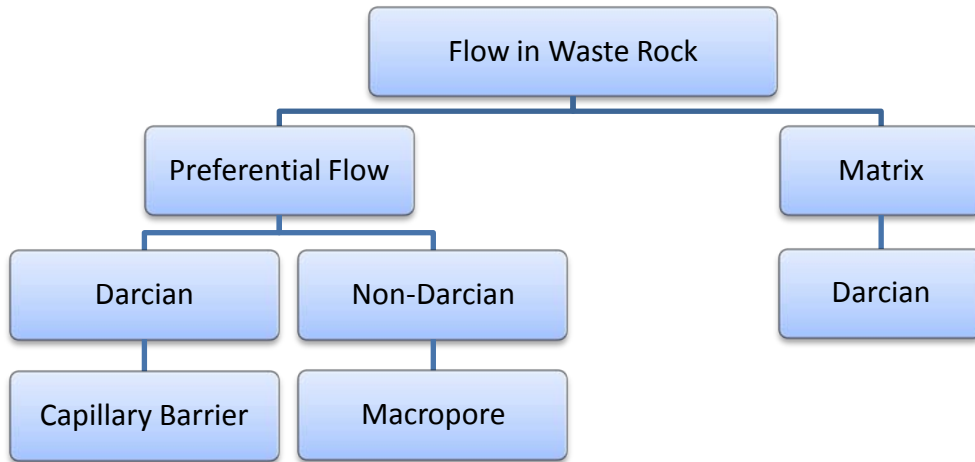


Figure 1.3. Flow processes in waste rock.

2 SITE DESCRIPTION, INSTRUMENTATION, SAMPLING AND MATERIAL CHARACTERIZATION

2.1 LOCATION

The Antamina mine is located, specifically, at 9°32' south and 77°03' west (approx. UTM 274 000 east and 8 945 000 north) at over 4,200 m above sea level, and roughly 270 km north of Lima, Peru (Redwood, 1999; Lipten and Smith, 2004). Situated near the mine is the Huascarán National Park, which is designated as a United Nations Education, Scientific and Cultural Organisation (UNESCO) World Biosphere Reserve and World Heritage site (Figure 2.1).

2.2 CLIMATE

The mine does not reflect a typical tropical or high altitude climate. Mean annual temperature is between 5.5 and 6.0 °C and mean annual precipitation is between 1200 and 1300 mm. The area surrounding the mine is unique in that it constitutes the highest elevation tropical mountain setting in the world. The climate is typically cool and moist throughout the year and bears similarity to an alpine tundra 'ecozone', which is characteristic of shrub and grassland vegetations generally found above tree line. Weather at Antamina is governed by the tropical rain belt, which oscillates about the northern and southern tropics creating distinct 'wet' and 'dry' periods that respectively fall between October – April and May – September. Since meteorological data was first recorded at Antamina in 2000, the maximum reported daily precipitation is 36 mm and the hourly temperatures range between -4 and 23 °C.

2.3 REGIONAL GEOLOGY

On the western coast of South America, the oceanic Nazca Plate is being subducted towards the east under the continental South American Plate. This process of subduction has led to significant folding, faulting, uplift, volcanic and plutonic processes that are responsible for the mineral-rich Andean mountain belt that extends along the western coast of the continent from the southern tip of Chile and Argentina up to Colombia and Venezuela (Figure 2.1).

The Central Peruvian Andes consist of the Western and Eastern Cordillera ranges. The Western Cordillera consists of two smaller ranges: the Cordillera Negra (to the west) and the Cordillera Blanca (to the east). The Antamina deposit is situated along the eastern edge of the Cordillera

Blanca, which is part of a polymetallic belt transecting Peru from 6° to 14° south (Figure 2.1). The area consists of high grade Zn-Pb-Ag-Cu-Au mineralizations with significant Cd, Bi, Mo and As associations (Lipten and Smith, 2004; Love et al., 2004).

The Cordillera Negra and the coastal zone to the west form a magmatic arc that was active from the Late Jurassic to the Tertiary. Further east, thick marine sediments consisting of slates, quartzites, sandstones, shales and coal with marine limestone were deposited from the Late Jurassic to the Late Cretaceous to form the Western Trough (Lipten and Smith, 2004). In the mid-Cretaceous, a marine transgression deposited thick marine carbonates followed by marine shales (113 – 88 Ma and 88 – 84 Ma, respectively; Lipten and Smith, 2004). The Jumasha and Celendin Formations developed during the carbonate and shale depositions, respectively. Later, a multi-phase quartz monzonite porphyry batholith intruded into the Cretaceous-aged sedimentary limestone deposits of the Jumasha Formation, creating the Antamina skarn deposit 5 – 16.5 Ma (Lipten and Smith, 2004; Love et al., 2004). Quartz monzonite is a granitic rock typically comprised of a quartz, plagioclase and potassium-feldspar assemblage that is resistant to weathering.

2.4 DEPOSIT GEOLOGY

The Antamina skarn deposit is rich in copper and zinc and is the source of the Antamina mineral reserve. Subsequent hydrothermal alteration to the Cu-Zn skarn body introduced copper orebodies at the limestone contact, with zinc, lead and bismuth also found in contact with limestone, in addition to metamorphic marble and hornfels (Evans et al., 2005). Ore formation may have been limited due to the fine-grained composition of the hornfels, which results in a low apparent porosity and permeability and, hence trace sulphides consistently below grade level (Lipten and Smith, 2004; Love et al., 2004).

Skarn deposits usually form by a chemical metasomatism of rocks at the contact zone between magmatic granite intrusions into carbonate-rich rocks (e.g., limestones). Figure 2.2 illustrates that the Antamina skarn orebody is elongated (3 km x 1 km x 1 km) in a northeast direction and is situated in the Antamina valley (Redwood, 1999). Approximately 90 % of the skarn deposit is mineralized and contains considerable amounts of copper, zinc, silver and molybdenum, existing

primarily as sulphide minerals. Sulphide zones generally exist at the skarn-limestone contacts and are physically easy to separate. Since the upper reach of the ore body was recently unearthed by Quaternary glaciation, it has not resulted in significant oxidation or enrichment.

Pyrite, chalcopyrite and magnetite are ubiquitous throughout the orebody, with a lesser presence of pyrrhotite and sphalerite. The deposit consists of several mineralization or metal zonations going from the outer layers to the outer rims (Figure 2.3). Specifically, the outer layers consist of intermediate skarn (Cu-Zn-±Mo-±Bi), green endoskarn (Zn-Cu-Ag-Bi-Pb) and mixed brown (Cu-Zn-Ag-Bi) endoskarn, whereas the outer rim consists of marble (±Zn-±Pb-±Ag) and hornfels (Zn-Pb-Ag-Bi) (Lipten and Smith, 2004). In addition, there is a pocket of wollastonite-bornite exoskarn (Cu-Zn-Ag-Bi), and the whole deposit is hosted by limestone. Lipten and Smith (2004) and Love et al. (2004) both contain detailed geological descriptions of the history and composition of the lithographic and metallic composition of the deposit.

2.5 HYDROGEOLOGY

The Antamina mine is located on the eastern edge of the continental divide that separates water from draining to the Pacific or Atlantic Oceans. The mine is located within the Amazon basin, upon the upper catchment of the Marañon River which is a tributary of the Amazon River. It is situated between two steeply dipping limestone ridges that act as geographic and hydrologic boundaries. Nearly 10 % of the surface area of the Peruvian Andes consists of Cretaceous-aged karstic limestone in which a highly inter-connected system of seeps, springs, streams and rivers exists throughout the region. Karstic terrain often contains large conduits that can rapidly transport groundwater over a short time period (Evans et al., 2005).

The bedrock geology of the Antamina region consists of:

1. a lower sequence of clastic sediments consisting of sandstones, quartzites, shales and various carbonates, and
2. an upper sequence of calcareous facies such as limestones and various shales.

The calcareous upper sequence is where the karstic terrain is located, and typically results in low runoff and high infiltration situations. The northeast side of the Tucush Valley is underlain by karstic limestone of the Middle Jumasha that diverts water to the adjacent Ayash watershed. The southern flank of the valley consists of Celendin Formation and Upper Jumasha material, both of which are expected to act as hydraulic barriers (Evans et al., 2005).

Satellite image and air photo interpretation, field mapping, fracture trace analysis, karst surface and spring mapping, and dye-tracing studies have all been carried out to characterize and present a conceptual model of the terrain surrounding Antamina (Evans et al., 2005). At Antamina there are two main waste rock dumps, the East and Tucush Dumps, and one low/marginal-grade stockpile, all of which generate poor quality drainage (Figure 2.4). The East Dump is located in the Huincush Valley, to the east of the open pit and to the west of the concentrator and tailings pond. It is composed of both reactive and non-reactive material, and resides upon less-permeable clayey soils that direct most of the drainage water to the tailings pond. The Tucush Dump is located within the Tucush Valley (4.5 km long, 400 – 600 m deep) and receives non-reactive (Class C) and possibly reactive (Class B) waste rock, which is placed on the southern, less-permeable Celendin Formation and Upper Jumasha regions of the valley.

2.6 DEPOSIT DEVELOPMENT

The terrain surrounding Antamina is composed of rugged, steeply dipping limestone peaks, glacial valleys and lakes and deep canyons. The region is littered with fossils and ruins, showing a rich history of previous inhabitants. The word *Antamina* stems from the Quechua words of ‘*anta*’ and ‘*mina*’, which when translated to English mean ‘copper’ and ‘mine’, respectively. It is believed that copper was mined in the vicinity of Antamina in pre-Colonial times, but the first records of small-scale mining in the area date back to the 1850’s. The first significant exploration effort was carried out nearly a century later by the Cerro de Pasco Corporation in the early 1950’s, who estimated the Antamina grade to be 3 % or approximately one million tons of copper (Redwood, 1999; Love et al., 2004).

Property rights of the mine changed hands several times between the 1950’s and the 1990’s until 1996 when they were finally privatized, leading to the formation of Compañía Minera Antamina

S.A. Feasibility studies increased the deposit's original reserve estimates almost 4-fold. In 2008 the most recent plan indicated that Antamina has a total of 617 million tons of estimated reserves, with 1.23% Cu, 1.03% Zn, 0.029% Mo and 13.7g/t Ag. The amount of ore processed daily is expected to increase from the current 87,000 to a sustained 104,000 tonnes per day. With the newest facilities, the maximum daily capacity of processed ore will be as high as 130,000 tonnes per day (Golder, 2007a).

2.7 WASTE ROCK GENERATION AT ANTAMINA

Mineral ore deposits such as Antamina's quartz monzonite porphyry intrusion exist in transitional zonations of varying ore grades that decrease with distance from the contact zone (Figure 2.2; Figure 2.3). A significant amount of overburden material must be removed in order to access the ore deposit. High-grade ore is sent for processing, whereas material with low- to marginal-grade ore proportions is stockpiled for processing at a later date. The uneconomical overburden material is considered waste rock and is commonly placed near the open pit in large, multi-layered end – dumped waste rock piles.

All of the excavated material at Antamina originates at the open pit mine. Material is blasted apart to allow the mining equipment to gain access to the ore. Based on previously assayed core samples, the blasted material is either processed, stockpiled or disposed of as waste rock. High grade ore material is sent to the primary crusher and SAG (Semi-Autogenous Grinder) mill. At the concentrator, the material is pulverized by a series of ball-mills and then subjected to a series of hydrochemical flotation processes that separate most of the mineral from the host rock. Mineral concentrate is then sent along a 302 km-long pipeline to the coastal port of Huarney, whereas the remaining effluent and tailings are piped to the tailings pond where it is retained by a 300-m + high tailings dam. Marginal- and low-grade ore is stockpiled for later processing (Golder, 2007a).

Waste rock represents an obstacle in mineral extraction and is costly to transport away from the point of extraction. It also has a significant capacity to release a large amount of metals and other elements to the surrounding environment. More reactive waste rock is sent to the East Dump,

whereas less reactive waste rock with a lower metal content can either be sent to the Tucush dump or to the tailings dam where it will be used to fortify and extend the tailings dam.

2.8 WASTE ROCK CLASSIFICATION

Waste rock at Antamina is categorized into 3 general classes (A, B and C) based on rock type, chemical composition and visual attributes (Table 2.1). The most reactive material is Class A, whereas the least reactive is Class C. Class B represents an intermediate reactive material (Golder, 2006).

Of a total projected 1.5 billion tonnes of waste rock estimated to be produced during the life of the mine from 2001 to (at least) 2020, it is estimated that 44 % will consist of Class A, 42 % will consist of Class C and 14 % will consist of Class B.

2.9 TEST-PILE DESIGN

As part of the neutral waste rock drainage study at Antamina, five 36 x 36 x 10 m (high) waste rock test-piles were built between 2006 and 2009, all of which were based on the same design. The construction of the first pile (2006) using Class B material is outlined in detail by Corazao Gallegos (2007). Appendix A includes design plans and photographs of pile construction and instrumentation. The second and third test piles (2007) were built using Class A material with a few modifications from the first test pile (Appendix B). The fourth and fifth test piles (2008) were also built in the same manner. This thesis is based on the data collected from the first two years of operation of the first test pile, referred to as test pile 1.

Each pile consists of a large basal lysimeter with three sub-lysimeters within the basal lysimeter area. The lysimeters collect all drainage from the pile and convey it through pipes to an instrument hut where the flow rate is metered, samples can be collected and the temperature and electrical conductivity are continuously monitored. A number of instruments have also been installed within each pile along a six so-called instrument lines. The detailed description of pile lysimeters and instrumentation follows next.

2.9.1 Site

The experiment site was prepared by constructing three platforms from waste rock. The upper, intermediate and lower platforms have approximate elevations of 4385, 4373 and 4371 m above sea level, respectively. The pile base was constructed on the 4373-platform, and waste rock was end-dumped from the 4385-platform (Figure 2.5). All of the instrumentation lines and drainage pipes placed within the pile are connected to the instrumentation hut located on the 4371-platform. Between 2-February and 9-July-2006, over 26,000 metric tonnes of waste rock material was delivered to site for the construction of test pile 1.

2.9.2 Base Construction Methods

On the 4373-platform, the base of the pile was built with a 3 % gradient, dipping to the southeast corner. A 0.8 m-high protection berm was conformed around the square perimeter, making the pad 36 (l) x 36 m (w) from apex to apex. A 60-mil High Density Polyethylene (HDPE) geomembrane was installed upon the base to capture and prevent any water from penetrating deeper. This catchment area is referred to as the basal lysimeter. Three (3) smaller 4 x 4 x 0.5 m (high) catchments, referred to as sub-lysimeters, were constructed within the basal lysimeter and also lined with HDPE geomembrane. The sub-lysimeters are located along the centre (east-west) axis of the pile (Figure 2.6). A 4" HDPE pipe conveys water from each of the zero-tension lysimeters to an instrumentation hut for continuous water quality/quantity monitoring. Corrao Gallegos (2007) contains more details about the design, construction and instrumentation of the pile base.

A 0.35 m protective layer of 2B rejected material (< 1.5 “), referred to by the mine as ‘lastre’, was placed directly above the geomembrane and compacted. This material consists of a crushed Class C waste rock (almost pure calcium carbonate) that the mine typically uses for road construction. This geomembrane protective layer is referred to as the 2B-protective layer (Appendix A). Within the basal lysimeter, a series of perforated HDPE drainage pipes were placed upon the protective layer to collect basal drainage water and convey it to the monitoring equipment in the instrument hut. The vertical hydraulic conductivity of the compacted 2B-protective layer is roughly two orders of magnitude lower than the anticipated vertical

conductivity rates in the waste rock layer and is believed to represent a relatively impermeable boundary.

To address the possibility that the compacted lastre material would compromise the chemistry of the waste rock effluent, a sump was installed at the lowest (southeast) corner of the pile so that water samples representative of the 2B-protective layer could be collected and compared with lysimeter data.

To protect the geomembrane, instrumentation and drainage network from the force of waste rock that will be end-dumped from 10 m above, approximately 5,560 metric tonnes of Class B black marble waste rock, stockpiled on site since 2-, 3-February-2006, was used to construct a 1.5 m-high protective layer upon the 2B-protective layer (Table 2.2). Since the 2B-protective layer is not constructed with waste rock, it is not included in the protective layer discussion. Throughout the remainder of this thesis, the protective layer will only be in reference to the waste rock protective layer unless otherwise stipulated (Appendix A).

In a parallel field-cell study, Aranda (2009) characterized the mineralogical and elemental properties of materials from the protective layer and three subsequent tipping phases of this pile. The results from Aranda (2009) are summarized in Table 2.3 and Table 2.4.

2.9.3 Pile Construction Methods

The waste rock for the pile was end-dumped from the 4385-platform in 3 separate phases, with a pause after each phase for installation of instrumentation lines 1 - 4 along the progressing pile slope (Appendix A). On 10-May-2006, the first tipping phase (Tipping Phase I) took place with the delivery 6,200 metric tonnes of Class B marble diopside waste rock (Table 2.2). With each subsequent payload discharge, the pile progressed outwards from the anterior slope. Along the centre-line of this slope, a 1 - 2 m-deep trench was excavated for the instrumentation installation (discussed below). All instrumentation was manually protected by fine material or small gravel, depending on the type of instrumentation, and then covered with more material for protection.

The second tipping phase (Tipping Phase II) occurred on June 27 - 28 and consisted of over 6,000 metric tonnes of Class B marble diopside waste rock (Table 2.2). Two 1 - 2 m-deep trenches were excavated at the front of the pile, one located along the centre and line 3 beginning from the same location and extending laterally to the front-corner (northeast) of the base of the pile. Instrumentation placed within these trenches is discussed below.

The third and final tipping phase (Tipping Phase III) took place on 7-, 8-July-2006 and consisted of almost 8,400 metric tonnes of Class B marble diopside and grey hornfels waste rock (Table 2.2). A 1-2 m-deep trench was excavated along the centre of the pile slope and instrumentation was installed and protected in similar fashion to the previous trenches (discussed below).

2.10 INSTRUMENTATION

A total of six instrumentation lines were placed within the pile to characterize the internal pile behaviour (Figure 2.6; Figure 2.7; Figure 2.8). Instrumentation lines 1 - 4 are located within the slope trenches whereas lines 5 and 6 are located within the protective layer. A summary of instrumentation placed in each line is found in Table 2.5, and a discussion of each instrumentation type follows in the following section. GPS coordinates are available for all instrumentation ports except for lines 5 and 6 (Appendix A).

Additional instrumentation was installed in the instrumentation hut to monitor the quality and quantity of water discharging from the base of the pile. Meteorological data was measured on site and throughout the Antamina mine property.

2.10.1 Pile Instrumentation

Instruments used in the pile include thermistors to measure temperature, and Time Domain Reflectometry (TDR) probes to measure moisture content. In the instrument hut, tipping buckets and electrical conductivity (EC) probes continuously measure flow and solution EC from the basal lysimeter and three sub-lysimeters. A rain gauge measures site precipitation, although several other rain gauges are located at different places at the mine. All instruments are all connected to a CR1000 datalogger (www.campbellsci.ca). Energy is supplied by a 56 W solar

panel. Details of pile instrumentation locations within the pile and installation methods can be found in Corazao Gallegos (2007) and Appendix A.

2.10.1.1 Time Domain Reflectometry Probes

Twenty-two (22) Time Domain Reflectometry (TDR) probes were custom-built and installed in the test pile to provide continuous, automated in-situ volumetric water content estimates (Corazao Gallegos, 2007). The TDR probes, capable of accurately measuring moisture content in the high dissolved solid porewater environment expected in the test pile, were built using the design of Young (1998) that was elaborated by Nichol et al. (2002, 2003). These probes are unique because they include a high resistance coating along the centre conductor rod that enables them to function better in the conductive waste rock porewaters (Nichol et al., 2002, 2003). Similar TDR probes have been employed in other waste rock investigations (e.g. Neuner, 2009).

Five TDR probes each were installed in instrumentation lines 1 – 4 (vertical) and one TDR probe was installed in each instrumentation line 5 and line 6 (base) (Table 2.5). Moisture content data provided by the TDR measurements are automated and obtained at 30-minute intervals, and allow for estimates of average wetting front arrival times, variable moisture content and storage fluctuations in response to seasonal variations.

No soil-specific TDR calibration correlating the raw TDR travel time to the in-situ volumetric water content of waste rock in the test pile 1 is available. A soil-specific relationship between similarly-designed TDR probes calibrated in waste rock from the Cluff Lake mine (Nichol et al., 2002, 2005) is used to calibrate the TDR probes at the Antamina test pile. Without a soil-specific calibration, relative changes in moisture content are emphasized over absolute changes.

Appendix F includes more information about the nature of the calibration, data processing steps, and other calibration equations considered.

2.10.1.2 Thermistors

Thirty-six (36) thermistors (RST Instruments, TH0002 2252 ohm 0.01 °C, www.rstinstruments.com) were installed in test pile 1, 32 of which are located within the pile and an additional 4 are located in the instrumentation hut (one per each lysimeter's flow-through conveyance system).

Six thermistors are located in each of instrumentation lines 1 to 4 (pile) and a total of eight thermistors are located in lines 5 and 6 (base) (Table 2.5). Each thermistor was factory calibrated based on their custom-ordered length (pile: 60 – 21 m; outflow drainage conveyance system: 5 m). Thermistor measurements are automated and obtained at 30-minute intervals.

Temperature data provided by the thermistors is principally used to assess whether heat is emitted during sulphide mineral oxidation and to estimate the extent of temperature-driven gas convection. However, several secondary reasons exist, namely: for geochemical speciation modeling and other calculations (i.e., mineral solubility), neutralization capacity (Sherlock et al., 1995), and to affect temperature corrections for TDR and electrical conductivity.

2.10.1.3 Soil Water Solution Samplers

Fifteen (15) soil water solution samplers (Soil Moisture Equipment Corp., www.soilmoisture.com, model #: 1920F1L12B02M2, 12”, 2 bar cup) were installed in lines 1, 2 and 4 (five samplers in each line) to provide point-source water samples at various horizontal and vertical locations throughout the pile (Table 2.5). These samplers have a maximum capacity of 500 ml. Samples are extracted from the water sampling panel located in the instrumentation hut.

2.10.1.4 Gas Ports

A total of sixty-one (61) ports provide gas samples from within the pile. The original pile design included sixty-four (64) gas sampling ports but several (~ 5 - 10) gas tubes were compromised during installation and resulted in the installation of duplicate tubes where possible. 10 ports are located in line 5 and 14 in line 6 (base), and an additional 10 in each of lines 1 to 4 (vertical) (Table 2.5; Appendix A). The gas sampling ports consist of 1.6 mm ID polyethylene tubes (www.new-line.com). One endpoint was covered with a porous geotextile, and placed facing downwards to prevent dust and water from entering the line. It was then covered with pebble-sized material to allow for unobstructed gas flow. The other end extends to the instrumentation hut where it is connected to the gas panel where samples can be extracted.

2.10.1.5 Tipping Buckets

Infiltrating rain water that penetrates the full depth of the pile eventually reaches the base of test pile 1 test pile where the basal lysimeter and three sub-lysimeters are located. Water from the lysimeters then flows to the instrumentation hut via 4" HDPE pipes. Inside the instrumentation hut, water passes through one of four flow-through conveyance cells installed for water quality measurements, and then into one of the four custom-built tipping bucket flow gauges (Corazao Gallegos, 2007). The flow-through conveyance system allows for continuous electrical conductivity and temperature data to be obtained, and a sampling port facilitates sample extraction (Figure 2.9). Tipping buckets, used to measure discharge, are based on designs that have been used in similar experiments to measure the flow rate of water from test piles (Nichol et al., 2005; Andrina et al., 2006; Neuner, 2009).

Water flowing from the basal lysimeter flows to the 'large tipping bucket', which was designed to operate under a maximum flow rate of 60 L/min and a maximum volume-per-tip of nearly 3 L. Water flowing from each of the three sub-lysimeters separately drains to one of three 'small-tipping buckets' which were designed to operate under a maximum flow rate of 16 ml/s and a maximum volume-per-tip of nearly 25 ml. Each tipping bucket is connected to the CR1000 datalogger in the instrumentation hut, which records the time of each tip.

Each tipping bucket was individually calibrated in January-2007 and again in August-2008. The calibration equation converts the raw tip-time (time between consecutive tips) to a corresponding flow rate (Appendix E). The equivalent volume of water during each tip is calculated by multiplying the calibrated flow rate by the reported tip-time. Results are totalled on a daily basis and reported as m³/day. For further information regarding the background, design, installation and initial calibration of these flow tipping buckets, refer to Corazao Gallegos (2007) and Appendix E.

2.10.1.6 Electrical Conductivity Probes

Electrical conductivity is indicative of the concentration of charged species in a porewater solution, whereby higher values correspond to higher ionic strengths and electrical conductivity. A custom-built electrical conductivity (EC) probe was installed within each of the four

lysimeters' flow-through conveyance system (Figure 2.9) and connected to the CR1000 datalogger to provide automated EC measurements at 30-minute intervals. Probes were designed and built at the University of British Columbia (Vancouver, BC, Canada). Corazao Gallegos (2007) and Neuner (2009) describe the theory, design and installation of these inexpensive sensors.

The raw EC data was temperature-corrected to account for temperature variations (Hayashi, 2004):

$$EC_{25} = SC = EC_T [1 + a(t - 25)] \quad [2-1]$$

where EC_t is the measured EC [$\mu\text{S}/\text{cm}$] at a given temperature t [$^{\circ}\text{C}$], EC_{25} is the EC at a standard reference temperature of $t = 25$ $^{\circ}\text{C}$ and referred to as specific conductance (SC). The temperature compensation factor a [$^{\circ}\text{C}^{-1}$] is an arbitrary value (dependent on the TDS-EC relationship) and accounts for increases to EC with temperature increase. A commonly used a value is 2 %, which describes a '2 % increase of EC per 1°C increase of temperature'. Other, more site-specific temperature compensation values have been employed in previous experiments (e.g., 1 – 3 %; Hayashi, 2004).

2.10.1.7 Composite Tank and Flow Splitter

A composite tank was installed to permit weekly mass balance (water) and mass loading (solute) calculations for the entire pile. Serving as a secondary reservoir that retains a proportion of water draining from all four lysimeters, the composite tank allows for a comparison of the entire pile flow and chemistry averaged between sampling intervals with the flow and chemistry from instantaneous samples collected from individual lysimeters.

All of the water draining from the bottom of each of the four tipping buckets converges to a single pipe that directs water to a flow splitter. The flow splitter, 0.8 m long x 0.33 m wide x 0.75 m tall, is designed to separate approximately 6.25 % of the combined effluent water and convey it (under gravity) to the 2.5 m^3 composite tank. Corazao Gallegos (2007) contains details about the design, construction, installation and calibration of the flow splitter.

The composite tank consists of a multi-layered plastic that prevents solar rays from penetrating the plastic (so as not to affect the geochemistry of the water) and a high-resistance outer layer that prevents degradation over time. The 2.5 m³ tank (1.55 m high x 1.60 m wide) was installed at a 3 % gradient towards the direction of the outlet valve roughly located 2 cm above the base of the tank. It is assumed that there is a negligible amount of water or sediment remaining in the tank after it is drained. For precaution, a roof is located above the tank to prevent any damage from occurring (Corazao Gallegos, 2007). Further detail can be found in Appendix G.

2.10.2 Meteorological Instrumentation

2.10.2.1 Precipitation

Precipitation at the test pile site is measured using a Rainnew 111 Tipping Bucket Wired Rain Gauge (+/-1% accuracy) from RainWise Inc. (www.rainwise.com) connected to a Campbell Scientific CR1000 datalogger. The rain gauge is located on the roof of the instrumentation hut. Another six tipping bucket rain gauges (Campbell Scientific TR-525 rain gauge; $\pm 1\%$ accuracy; www.campbellsci.ca) are located within 5 km of the study site. Each tip is equivalent to 0.254 mm of rainfall. Assuming that the rain is spatially uniform, the rainfall can be multiplied by the horizontal surface area of the pile in order to estimate the total volume of water falling on the pile surface. Due to a mean annual temperature of 5.5 – 6.0 °C, almost all precipitation is in the form of rain. When it does snow, it typically melts within hours to days.

2.10.2.2 Evaporation

A ‘Class A’ pan located less than 4 km from the study site at the Yanacancha meteorological station provides pan evaporation (E_{pan}) measurements. Free-water E_{pan} measurements represent an integrated proxy of the actual evaporation that occurs due to transient climatological conditions such as net radiation, air temperature, humidity and wind speed. Allen et al. (1998) describes the pan evaporation set up in detail. This is further explained in Appendix D.

2.10.2.3 Air Temperature, Relative Humidity, Wind Speed and Direction.

See Appendix C.

2.11 WATER SAMPLING

Twenty-one (21) water quality monitoring locations exist in test pile 1, 15 sampling ports and 6 sampling stations. The 6 sampling stations are located outside the pile (pile exterior) and consist of the lysimeters, composite tank and sump. The 15 sampling ports are located inside the pile (pile interior) where the soil water samplers (SWS) are located along instrumentation lines 1, 2 and 4 (Appendix A).

The 6 sampling stations are located outside the pile and monitor drainage from each the basal lysimeter, three sub-lysimeters, composite tank and sump. The sampling stations from each of the three sub-lysimeters (A, B and C) and the basal lysimeter (D) are located in the flow-through lysimeter conveyance cell in the instrumentation hut (Figure 2.9). The composite tank (E) is located adjacent to the instrumentation hut and is sampled at the outflow valve. Water is sampled from the sump (F) via a hose protruding from the pile's south eastern corner.

2.11.1 Water Quality Parameters

The samples were collected at weekly, bi-weekly, monthly, bi-monthly or semi-annual intervals. The frequency depends on the station, parameter, time of year, and pile maturity. Field parameters, described next, are obtained for each sample.

2.11.1.1 Field Parameters

Field parameters include temperature (± 0.1 °C), pH (± 0.03 units), specific conductance (± 0.05 % $\mu\text{S}/\text{cm}$) and dissolved oxygen (± 0.05 % mg/L). These parameters are measured with a handheld multiparameter instrument (WTW Multi 340i). Field parameters are measured on a weekly basis for the sampling stations due to their inexpensive cost and ease of measurement. The 15 sampling ports (i.e., SWS) were analyzed weekly during the first year and bi-weekly thereafter, depending on the time of year.

2.11.1.2 Lab Parameters

Lab samples were analyzed weekly for all 4 lysimeters and composite tank, with samples analyzed bi-weekly for the sub-lysimeters after the first year. It should be noted that the sub-

lysimeters do not always flow in the dry season at Antamina in which case sampling can be intermittent or non-existent. Samples from the sump are extracted and analyzed every 6 months.

Samples from the 15 SWS were obtained weekly during the first year, and every 2 to 4 months thereafter, depending on the time of year. Suction lysimeter samples can only be collected when a sufficient volume of water is available (discussed below). In situations when insufficient solution volume for complete analysis is available, samples are sent to the lab in order of priority; dissolved metals, total metals, anions, alkalinity, and nitrogen species.

All samples are refrigerated to an optimal storage temperature of 4 °C during transport from the field to the laboratory in Lima. Samples are analyzed by Envirolab Peru S.A.C. by inductively coupled plasma mass-spectrophotometry (ICP-MS) for pre-determined solutes. The suite of analyzed constituents is described below. Corzaao Gallegos (2007) describes the analytical method and parameter detection limits.

2.11.1.2.1 Dissolved Metals

Dissolved metals have the highest priority for analysis. When 250 ml of a sample are obtained, the following dissolved metals will be tested for : Al, Sb, As, Ba, Be, Bi, Bo, Cd, Ca, Co, Cr, Cu, Sr, Sn, P, Fe, Li, Mg, Mn, Hg, Mo, Ni, Po, Ag, Pb, Se, Na, Ta, Ti, V, Zn. At the time of collection, samples intended for dissolved metal analysis are filtered and preserved with nitric acid to reduce the pH to less than 2.

2.11.1.2.2 Total Metals

When 500 ml of a sample are obtained, the same constituents that are tested for dissolved metals are tested for total metals. Total metal samples are not filtered, but are preserved with nitric acid, similar to dissolved metals.

2.11.1.2.3 Other parameters

Other parameters include non-metals and nutrients, etc. When 1000 ml of a sample are obtained, total alkalinity, chloride, fluoride, pH, sulphate, ammonium, nitrate and nitrite are all analyzed

(recall that the soil water samplers have a maximum capacity of 500 ml). Anions are not preserved.

2.12 GAS SAMPLING

Gas samples were obtained every six months: April-2007, November-2007 and August-2008. Samples were analyzed using an OmniStar Quadrupole Mass Spectrometer and a Varion 4200 Gas Chromatograph.

2.13 WASTE ROCK PROPERTIES

A detailed characterization of the physical waste rock properties is critical in understanding the hydrological and chemical processes occurring within the waste rock pile. The solid phase mineralogical and elemental composition, particle density and acid-base accounting of the waste rock is presented based on field cell analyses by Aranda (2009). (Note, for the purpose of this investigation, it is assumed that the mineralogical proportions measured in the field cells represent the same proportions in the test pile). A particle size distribution was performed on selected material from end-dumped pile material. Saturated hydraulic conductivity is measured on the compacted, top surface of the pile. The bulk porosity of the waste rock is estimated based on the mass and volume of test pile 1.

2.13.1 Solid Phase Mineralogical Composition

The black marble, marble diopside and grey hornfels waste rock used in the construction of this test pile originated from the Jumasha Formation (Section 2.3). This material was classified as Class B waste rock based on the element-based assays employed by the mine (Table 2.1). Mineralogical composition analyzed using Mineral Liberation Analysis (MLA). The MLA uses a Scanning Electron Microscope equipped with sophisticated software that performs an automated, systematic, quantitative evaluation of the abundance, association, size and shape of minerals within a given sample. Results of this analysis show that average pile composition consists of 48.4 % silicate, 47.5 % carbonate, and 2.2 % sulphide minerals (Aranda, 2009). The remaining 1.9 % consists of phosphate, oxide, sulphate and other minerals. Nearly 56 % all sulphide minerals consists of pyrite (1.2 % of the total pile), and 95 % of all sulphide minerals when combined with chalcopyrite (20.2 % of sulphides), pyrrhotite (10.2 % of sulphides) and

sphalerite (8.2 % of sulphides). Calcite is the dominant carbonate mineral. Tipping Phase II material has the highest sulphide and silicate and the lowest carbonate proportions. Tipping Phase II has the highest carbonate content. Table 2.3 summarizes MLA results from Aranda (2009).

2.13.2 Solid Phase Elemental Composition

Whole-rock elemental analysis was conducted on material from the protective layer and three tipping phases by the ALS Chemex Laboratory Group using the ICP-MS61 methodology. Average pile sulphur (S) content is approximately 0.61 wt. %, with 27.1 % wt calcium (Ca), 1.7 % wt. iron (Fe), 0.09 % wt. zinc (Zn) and 0.06 % wt. copper (Cu). The high Ca content indicates a significant buffering capacity of the waste rock (Table 2.4). Tipping Phase II has the highest Fe and S proportions and Tipping Phase III has the highest Ca and Zn proportions. Refer to Aranda (2009) for more detailed attributes of this material.

2.13.3 Acid Base Accounting

Sobek et al. (1978) provided the earliest methodology for acid base accounting (ABA), which the mining industry uses to obtain an initial characterization for predicting acid rock drainage. ABA is used to quantify the constituents of the material under study to determine how much acid it can produce when oxidized or how much acid it can neutralize. The acid potential (AP) is determined in a static test by calculating the theoretical amount of acid that can be produced if all of the total sulfur is oxidized to sulfuric acid and is expressed as kg CaCO₃/tonne. The neutralization potential (NP) is determined experimentally by digestion of hydrochloric acid, followed by a titration to determine the amount of acid consumed, expressed in kg CaCO₃/tonne (Sobek et al., 1978; Lawrence and Wang, 1996). Results are typically presented in the form of a Neutralization Potential Ratio (NPR) which is the NP-to-AP ratio. A higher ratio value means a larger the neutralization potential. Any value less than 2 most likely 'acid-generating' and higher than 4 is most likely 'non-acid generating' (Price, 1997).

Acid base accounting was conducted on waste rock from the protective layer and all three tipping phases to provide a preliminary assessment of how strongly the waste rock can buffer the generated acidity when exposed to weathering under natural conditions. The NPR ratios range

between 5 and 291, with material from Tipping Phase II having the lowest ratio (NPR ~ 5) and Tipping Phase III having the highest ratio (NPR ~ 5). By this definition, all of the waste rock placed in the pile is non-acid generating. Further details can be found in (Aranda et al., 2009).

2.13.4 Particle Size Distribution

Waste rock particle size distributions (PSD) generally encompass size fractions that range over several orders of magnitude. Regardless of the coarse proportions, the waste rock PSD curves typically exhibit a long tail at the fine size fractions (Smith and Beckie, 2003). The most common way to perform a grain size analysis is by sieve separation which physically separates the material based on different sieve sizes.

Five particle size distribution tests were performed on the test-pile waste rock by Golder Associates using the ASTM D 5519 methodology. The first three tests were performed on material randomly selected from 26 truckloads of stockpiled material and the additional two tests were performed on one individual truckload dumped adjacent to the pile during Tipping Phase I and II. Nearly 450 tonnes of waste rock was used for the PSD on material from Tipping Phases I and II, and was removed from the total mass of material placed in the pile (Table 2.6). The average PSD curve for the protective layer (stockpiled material) is shown in Figure 2.10 along with those from Tipping Phase I and II.

Very large boulders in the waste rock necessitated the use of excavators and other mechanical equipment to separate larger particle sizes (Corazao Gallegos, 2007). It is important that PSD analyses are performed shortly after material deposition at site to avoid any compaction, settling, or dissolution in rain. Material for the concurrent field cell investigation by Aranda (2009) was randomly selected from these stockpiles using 25-kg ‘grab-bags’.

The material is relatively coarse and heterogeneous, with sizes extending across more than four orders of magnitude. There is a long tail of fine material, and 15 – 25 % of the material is larger than 1 m in diameter. Another way to characterize PSD curves is through the uniformity coefficient C_U which describes the ratio between the diameter of the size fraction that represents nearly 60 % of the total sample (D_{60}) over the 10 % size fraction (D_{10}). Morin et al. (1991) report

that although typical waste rock has a widely distributed grain size, the $C_U (D_{60}/D_{10})$ is always at least 20. The average uniformity coefficient for the five PSD curves measured on this waste rock is $C_U = 330 \text{ mm} / 10 \text{ mm} = 33$.

2.13.5 Hydraulic Properties

The hydraulic properties of waste rock are heavily determined by the PSD (Chapter 1). Yazdani et al. (2000) determined that particles with a diameter $> 4.75 \text{ mm}$ no longer have significant capillarity under unsaturated conditions. Based on the PSD (Figure 2.10), approximately 5 - 10 % of the pile is made up of material $< 4.75 \text{ mm}$ in diameter, indicating that the pile is relatively coarse and that preferential (i.e., macropore) flow may be present along with matrix flow.

Eight fixed-ring infiltrometer tests were performed at several locations of the top, compacted layer of the pile to measure the one-dimensional (vertical) saturated hydraulic conductivity. Methods were similar to those outlined in Bouwer (1986). Results varied by two orders of magnitude from 1.2×10^{-4} (10 m/day) to 3.7×10^{-6} m/s (0.3 m/day), and an average saturated hydraulic conductivity is 2.7×10^{-5} m/s (2.3 m/day). No direct hydraulic conductivity tests were conducted along the less consolidated, coarser batter although empirical methods are used to provide indirect estimates of hydraulic conductivity in Chapter 3.

2.13.6 Dry Bulk Density

The dry bulk density of the stockpiled protective layer was measured (using a water replacement method) before it was placed in the pile (Corazao Gallegos, 2007). The stockpiled material was compacted in a similar manner to its placement in the protective layer of the pile and tested. Results indicate that the stockpiled material had a dry bulk density of $\rho_b = 1845 \text{ kg/m}^3$. Dry bulk density test was not measured on the end-dumped material from Tipping Phases I, II and III.

The amount of material compaction can affect porosity and the overall flow regime. As Nichol (2002) indicates, flow from a 5 m-high waste rock pile can vary by several orders of magnitude with a density increase of 40% due to compaction. It is for this reason that it is important to consider the way in which the waste rock material was handled and minimize handling to simulate actual waste dump conditions. The stockpiled material was flattened and likely

compacted to a degree resulting in a slightly higher than expected density. Nearly three months after the waste rock was stockpiled and the density measured, the material was finally placed in the protective layer. During this time the material could have settled, reacted with atmospheric conditions of the wet season, and some finer material may have been washed away. Based on these factors, results of the bulk loose density test on the stockpiled protective layer could not be used as a proxy bulk density of the pile and another method was utilized. An uncertainty of up to 30 % was attributed to this estimate, resulting in a dry bulk density of $\rho_b = 1845 \pm 550 \text{ kg/m}^3$.

A second way bulk density estimated was performed based on the mass and volume of test pile 1. Using GPS data, the volume of waste rock that was delivered to site is estimated to be 11,600 m^3 . However, both mass and volume estimates have to account for the amount of material that was dumped at the back slope of the pile (i.e., the first tips of Tipping Phase I) but was not included in the 36 x 36 m pile footprint (1,600 m^3 or 3,200 tonnes). In addition, approximately 2,600 tonnes of waste rock was removed from the bottom perimeter of the pile after completion to conform to the initial pile design dimensions and to allow access to the three exposed sides of the pile. Accounting for the material removed for the PSD (Section 2.13.4) and material removed from the protective berm during the last tipping phase (Corazao Gallegos, 2007), the mass of waste rock placed in the pile is estimated to be 20,000 \pm 4,000, with a total estimated volume of 10,000 \pm 2,000 m^3 (Table 2.6). Based on the mass and volume of test pile 1, the resulting bulk density is estimated at 2,000 \pm 400 kg/m^3 . Based on the shape of the pile, the top compacted layer represents 24 % of the total pile surface area and the batters make up the remaining 76 %.

2.13.7 Porosity

The bulk porosity n of a porous medium can be difficult to estimate accurately without *in-situ* measurements. Due to a wide variety of material sizes ranging from fine sand and silt to large boulders in waste rock, it is difficult to determine an accurate, representative porosity value without more specific information and intimate knowledge of the complex relationships between grain sizes in the existing sample. Obtaining actual porosity measurements would significantly disturb the pile so instead porosity was estimated.

Bulk porosity is estimated based on the void volume V_v and total volume V_T , or the dry bulk density ρ_b [kg/m^3] and specific gravity/particle density G_s [kg/m^3] of a porous medium:

$$n = V_v/V_T = 1 - \rho_b/G_s \quad [2-2]$$

where $\rho_b = 2000 \pm 400 \text{ kg}/\text{m}^3$. The specific gravity of a material can be measured experimentally and compared to an equal volume of pure water. Particle density was measured for the kinetic field cell waste rock (Aranda, 2009). An average particle density value of $2894 \pm 60 \text{ kg}/\text{m}^3$ was obtained for all field cells. Waste rock from Tipping Phase II (FC-2) has the highest average particle density of $3140 \text{ kg}/\text{m}^3$, and material from Tipping Phase III (FC-4) has the lowest particle density of $2747 \text{ kg}/\text{m}^3$. The experimental results are rather consistent with results of whole-core density analyses for limestone/marble and hornfels performed by AMEC (AMEC, 2008).

Using the two bulk density ranges of $1845 \pm 550 \text{ kg}/\text{m}^3$ (empirical) and $2000 \pm 400 \text{ kg}/\text{m}^3$ (calculated), the calculated porosity ranges between $0.15 < n < 0.42$. However, the presence of large boulders may decrease bulk porosity because while they contribute to the total pile mass but not the total void volume (Neuner, 2009; Fala et al., 2003). Therefore, it is assumed that any boulders with a diameter larger than 0.5 - 1 m would not contribute to the overall porosity. Based on the PSD (Figure 2.10), approximately 15 to 25 % of the waste rock contributes to the final mass and volume, but not the void volume. The resulting total volume V_{Tn} that contributes to porosity is estimated to be 75 – 85 % of V_T . The final bulk porosity is therefore estimated to be 0.45 ± 0.15 based on the bulk density of the protective layer and 0.4 ± 0.1 based on the total pile mass and volume.

2.14 SUMMARY

This chapter described the climate, geography, geology and hydrogeology of the Antamina mine. A brief history of the mine history and the mining activities was described in order to provide a history of waste rock used in this study. Different waste rock types are classified based on their chemical content and the Class B (possibly-reactive) waste rock material was used in the pile. The pile design and construction was also described, including the dimensions, instrumentation

and timeline for construction. The physical properties of the waste rock placed in the pile were examined and will serve as the foundation for understanding the hydrological and solute release behaviour of the pile.

TABLES

Table 2.1. General classification of waste rock types from the Antamina mine.

Class	Rock Type	Metal Limits/Restriction			
		Zn (ppm)	As (ppm)	Sulphides (%)	Visible Oxides (%)
A	Hornfels, Limestone, Marble, Skarn, Intrusive	>1500	>400	>3	>10
B	Hornfels, Limestone, Marble	700 – 1500	<400	<2-3	<10
C	Hornfels, Limestone, Marble	<700	<400	<2-3	minimal

Table 2.2. Test pile 1 construction timeline.

Construction Stage	Beginning	End	Type	Initial Mass [metric tonnes]	Initial Bulk Moisture Content (%) ¹	Observations (qualitative)
Waste Rock Protective Layer Stockpile	2-Feb	3-Feb				
Geomembrane Installation	3-Mar	10-Mar				Wet and rainy
2B-Protective Layer	11-Mar	3-Apr				Wet and rainy
Sub-Lysimeter (material, geomembrane and 2B Protective Layer)	5-Apr	17-Apr				Wet and rainy
Protective Layer	4-May	10,11-May	Black Marble	5,740	3.1%	-
Tipping Phase I	10-May	11-May	Marble Diopside	6,400	2.1%	Sunny, dry
Instrumentation Line 1 Installation and Covering	12-Jun	26-Jun				Mainly sunny and dry, some clouds
Tipping Phase II	27-Jun	27-Jun	Marble Diopside	6,120	1.7%	Sunny, dry
Instrumentation Line 2 & 3 Installation and Covering	29-Jun	6-Jul				Mainly sunny and dry, some clouds
Tipping Phase III a ³	7,8-Jul	9-Jul	Marble Diopside	5,775	1.9% ²	Sunny, dry
Tipping Phase III b ³	7,8-Jul	9-Jul	Grey Hornfels	2,765		Sunny, dry
Instrumentation Line 4 Installation and Covering	20-Jul	24-Jul				Mainly sunny and dry, some clouds
Perimeter Adjustment	5-Aug	6-Aug				

* based on Corazao Gallegos (2007)

¹ as measured during particle size distribution

² estimated based on water content of Tipping Phase I and II.

³ two different tipping phases that are views as one.

Table 2.3. Solid phase mineral composition of waste rock.

Phase Type	Protective Layer Black Marble	Tipping Phase I Marble Diopside	Tipping Phase II Marble Diopside	Tipping Phase III Marble Diopside/ Grey Hornfels	Pile
Mass [t]	5,560	2,835	5,385	5,780	19,560
Mineral	% Material Placement Phase by weight ¹				
Sulphide	0.5	2	4.5	1.9	2.2
Carbonate	55.6	47.5	11	73.8	47.5
Silicate	41	49.6	82.2	23.6	48.4
Phosphate	1	0.3	0.4	0.24	0.5
Oxides	1.2	0.4	1.3	0.30	0.8
Sulphates	0.3	0.1	0.3	0.14	0.2
Others	0.4	0.1	0.1	0.17	0.2
Total	100	100	100	100	100

¹ based on field cell material 10-840 mm in diameter as determined by MLA on (Aranda, 2009)

² weighted average

Table 2.4. Solid phase elemental composition of waste rock.

Solute	Unit	Protective Layer	Tipping Phase I	Tipping Phase II	Tipping Phase III	Pile ²
Mass	tonnes	5,560	2,835	5,385	5,780	19,560
As	ppm	134.0	67.9	44.0	30.5	69.1
Ca	%	30.0	26.7	18.2	32.7	27.1
Cu	ppm	588.0	819.4	715.1	410.4	604.0
Fe	%	0.87	1.27	3.5	1.14	1.72
Mg	%	0.88	1.23	1.7	0.99	1.18
Mo	ppm	5.65	92.6	44.2	46.8	41.0
Na	%	0.12	0.09	0.27	0.09	0.15
Pb	ppm	553.5	309.2	822.0	470.0	567.3
Zn	ppm	1267.5	645.0	498.0	983.9	882.2
S	%	0.24	0.29	1.21	0.57	0.61

¹ based on field cell material 10-840 mm in diameter as determined by ICP-MS (Aranda, 2009)

² weighted average of whole pile

Table 2.5. Summary of instrumentation.

Instrumentation	Line	Line	Line	Line	Line	Line	Instrumentation Hut	Total
	1	2	3	4	5	6		
TDR	5	5	5	5	1	1	0	22
Thermistor	6	6	6	6	5	3	4	36
Gas	10	10	10	10	10	14	0	64
SWSS	5	5	0	5	0	0	0	15
Electrical Conductivity Probe	0	0	0	0	0	0	4	4
Tipping Bucket	0	0	0	0	0	0	4	4

Table 2.6. Final mass calculation.

Stage	Density ² [kg/m ³]	Mass [metric tonnes]					Final
		Initial Mass ¹	Particle Size Distribution	Exterior	Berm	Pile Adjustment	
Protective Layer	2770	5,560					5,560
Tipping Phase I	2910	6,260	-225	-3,200			2,835
Tipping Phase II	3140	6,010	-225		-400		5,385
Tipping Phase III	2850	8,380				-2,600	5,780
Final Pile Mass							19,560

¹ initial mass dumped on site according to Antamina Mining Operations

² Aranda (2009)

FIGURES

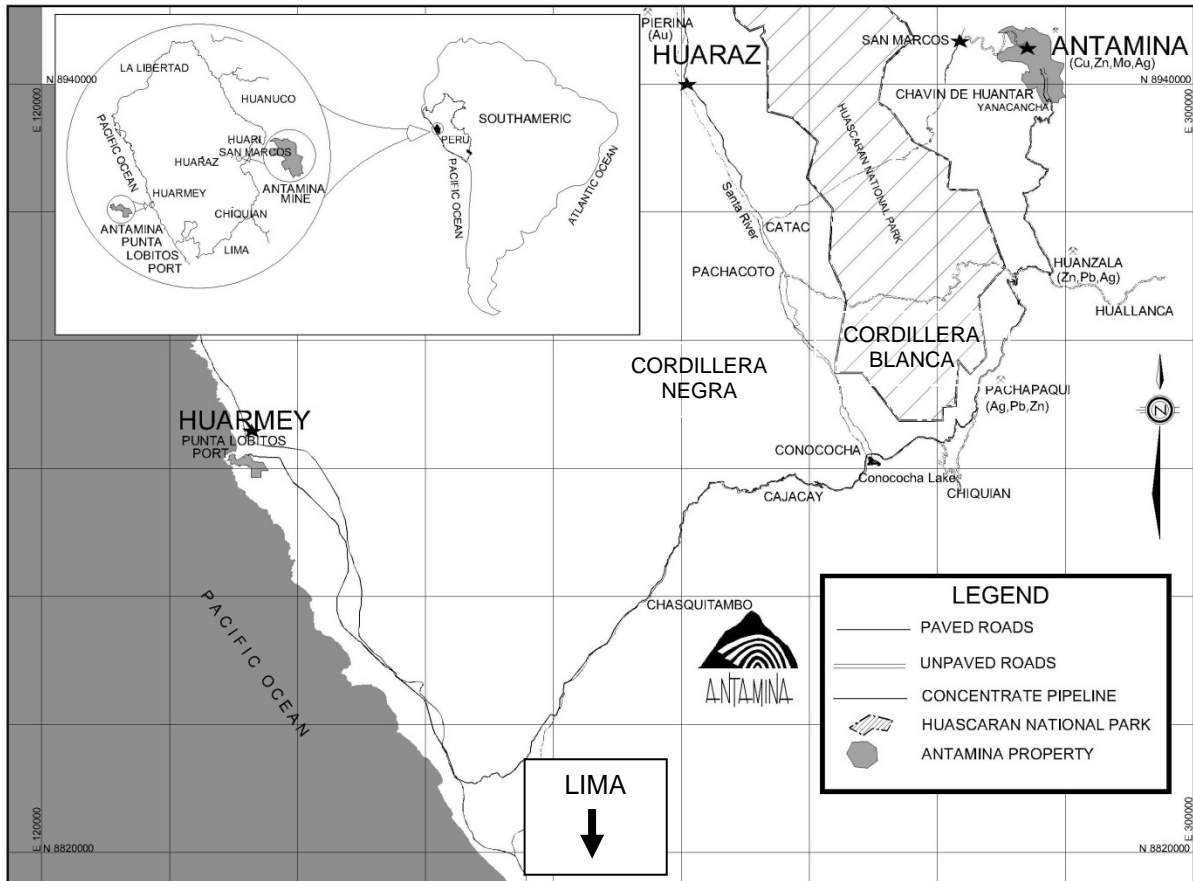


Figure 2.1. Map of mine location. Modified from Aranda et al. (2009).

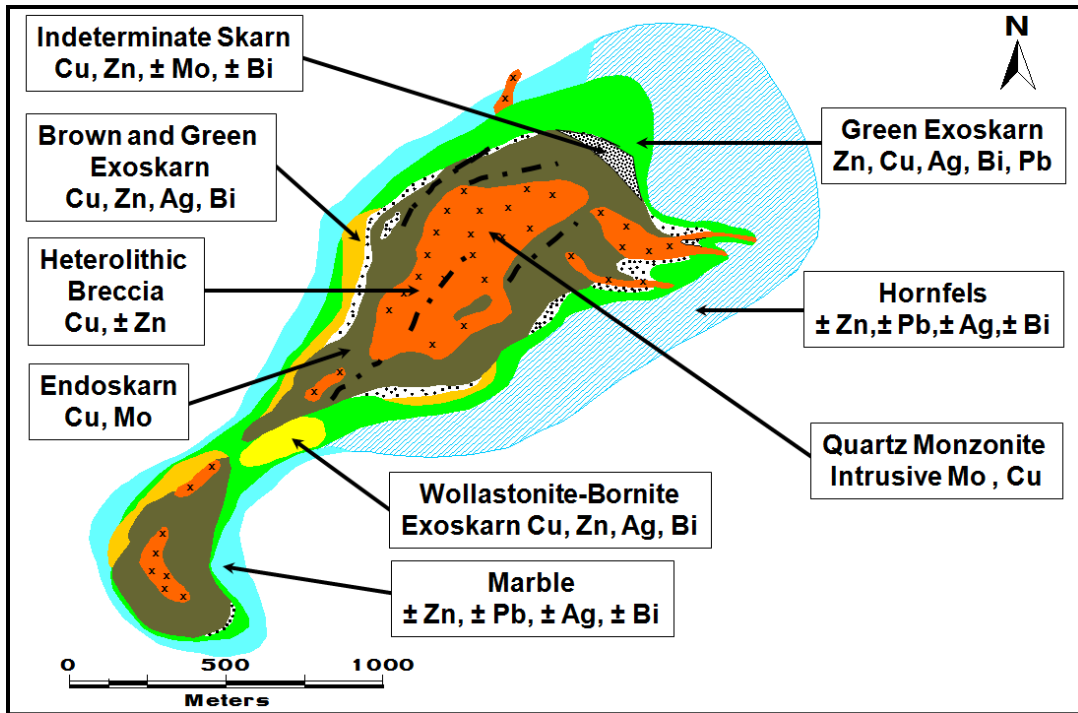


Figure 2.2. Plan view of schematic lithology of the Antamina deposit. (Antamina, 2003).

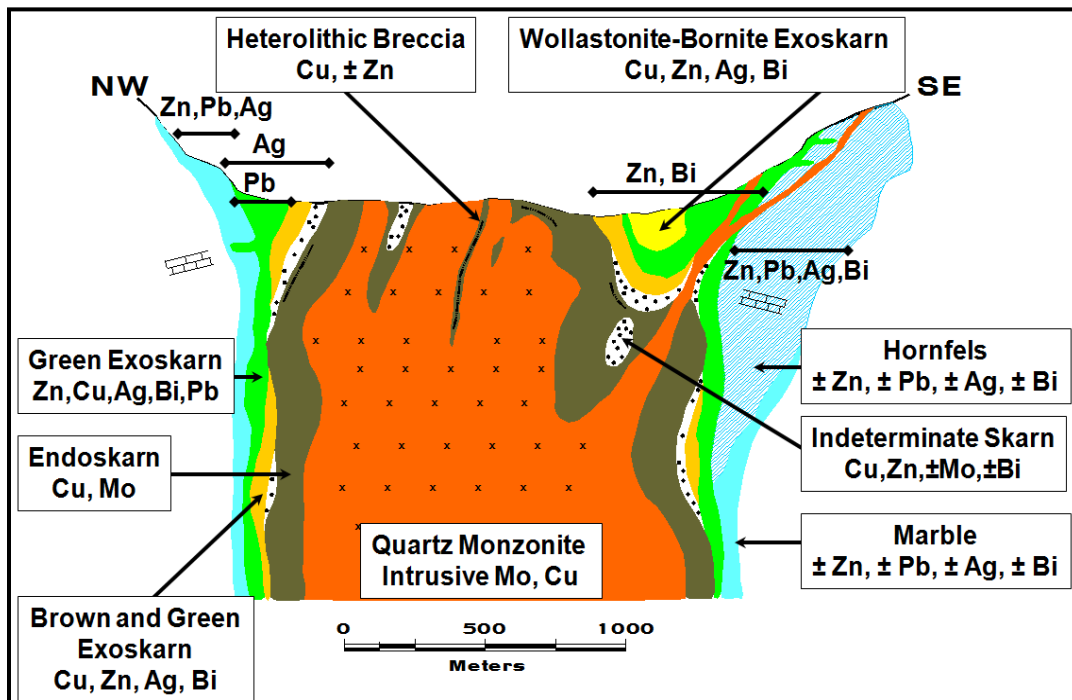


Figure 2.3. Schematic lithology and metal zonation of Antamina (Antamina, 2003).



Figure 2.4. Map of the Antamina mine.

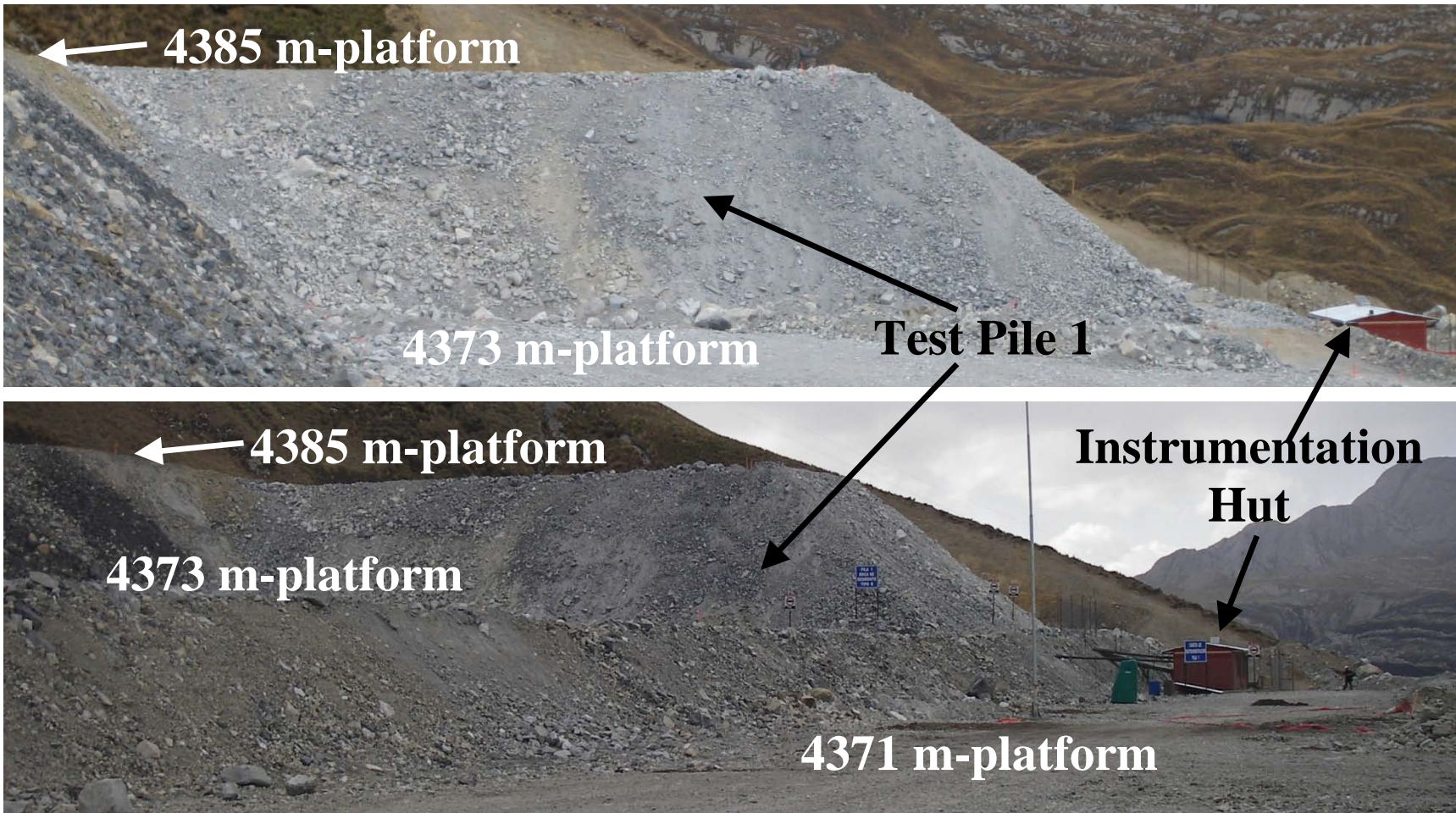


Figure 2.5. South view of completed test pile 1 and platforms.

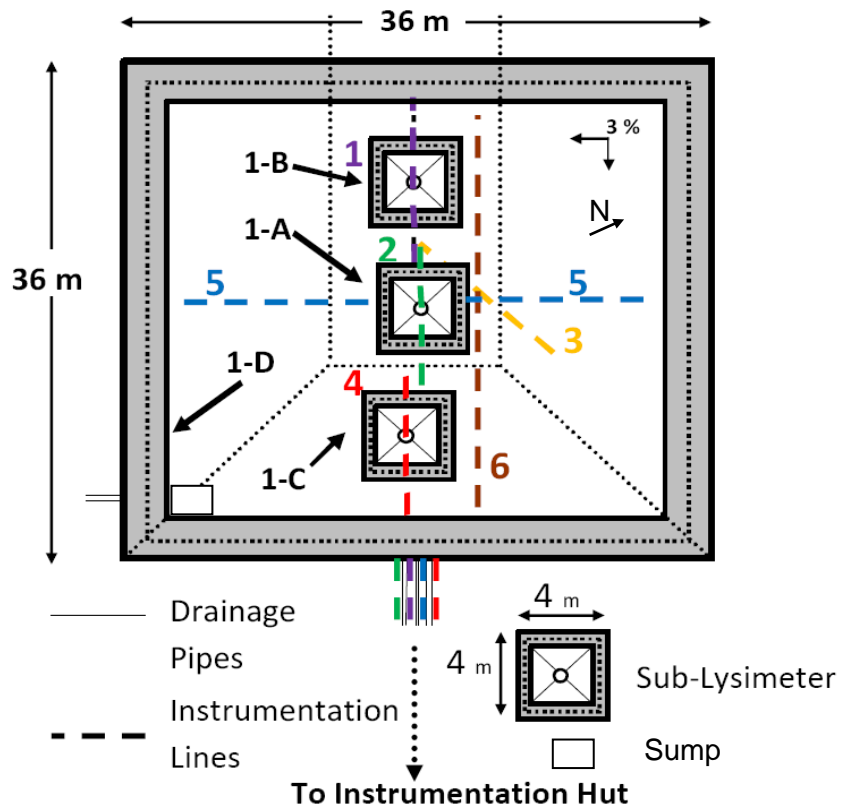


Figure 2.6. Test pile 1 base design and instrumentation schematic (plan view).

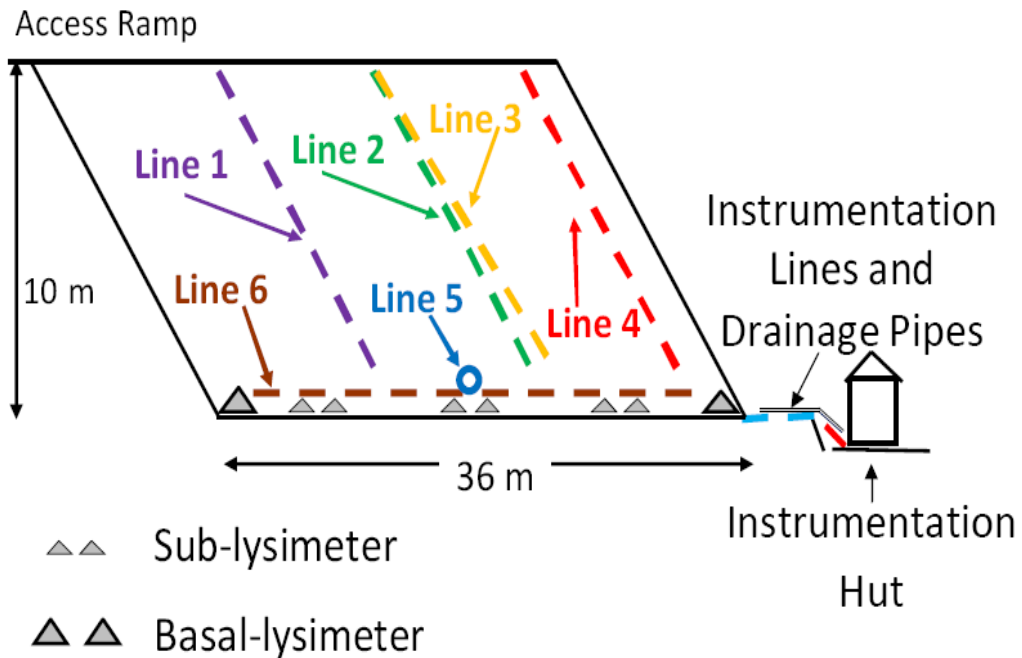


Figure 2.7. Test pile 1 side profile and instrumentation schematic (cross section).

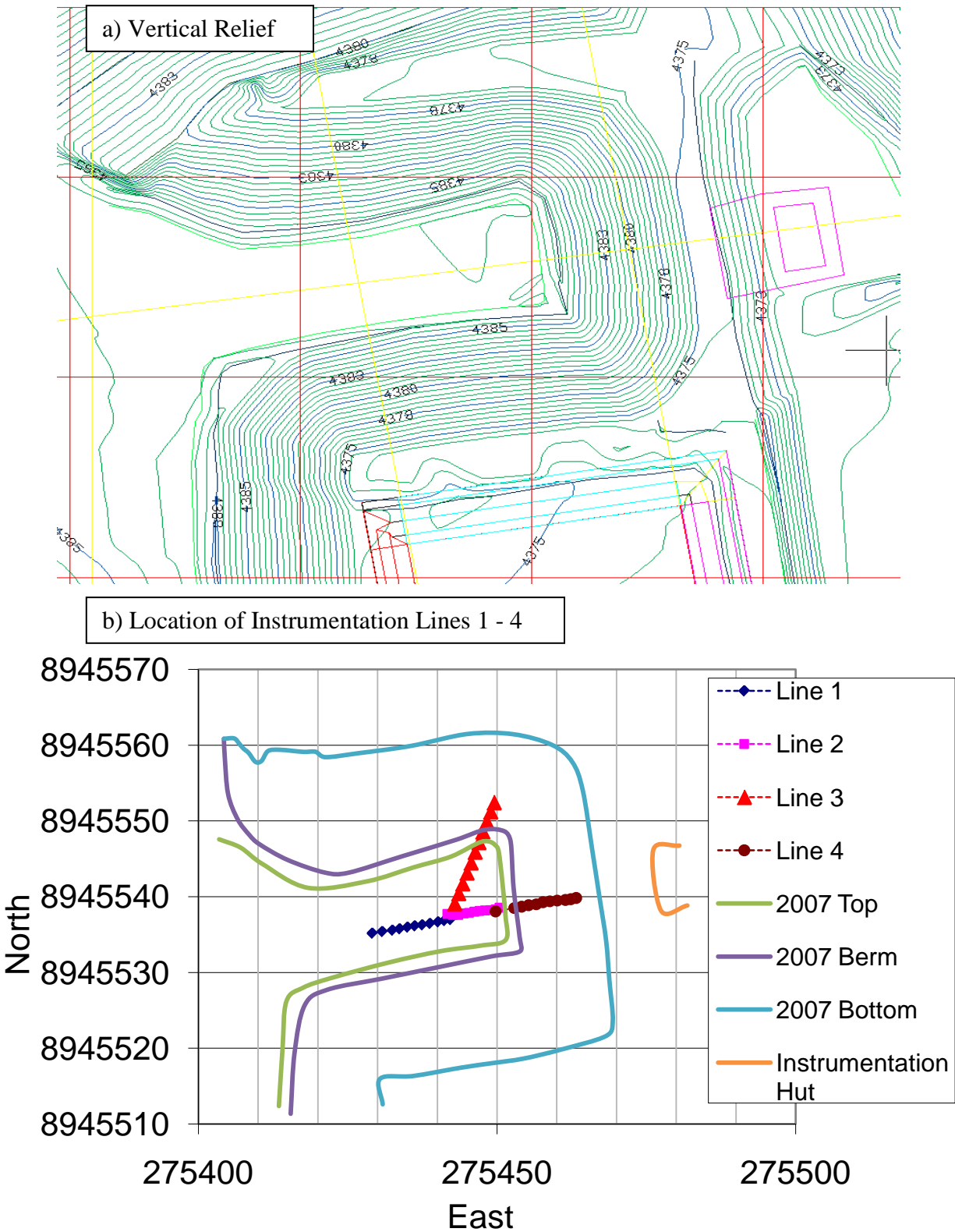


Figure 2.8. Plan view location of instrumentation points in relation to pile exterior.

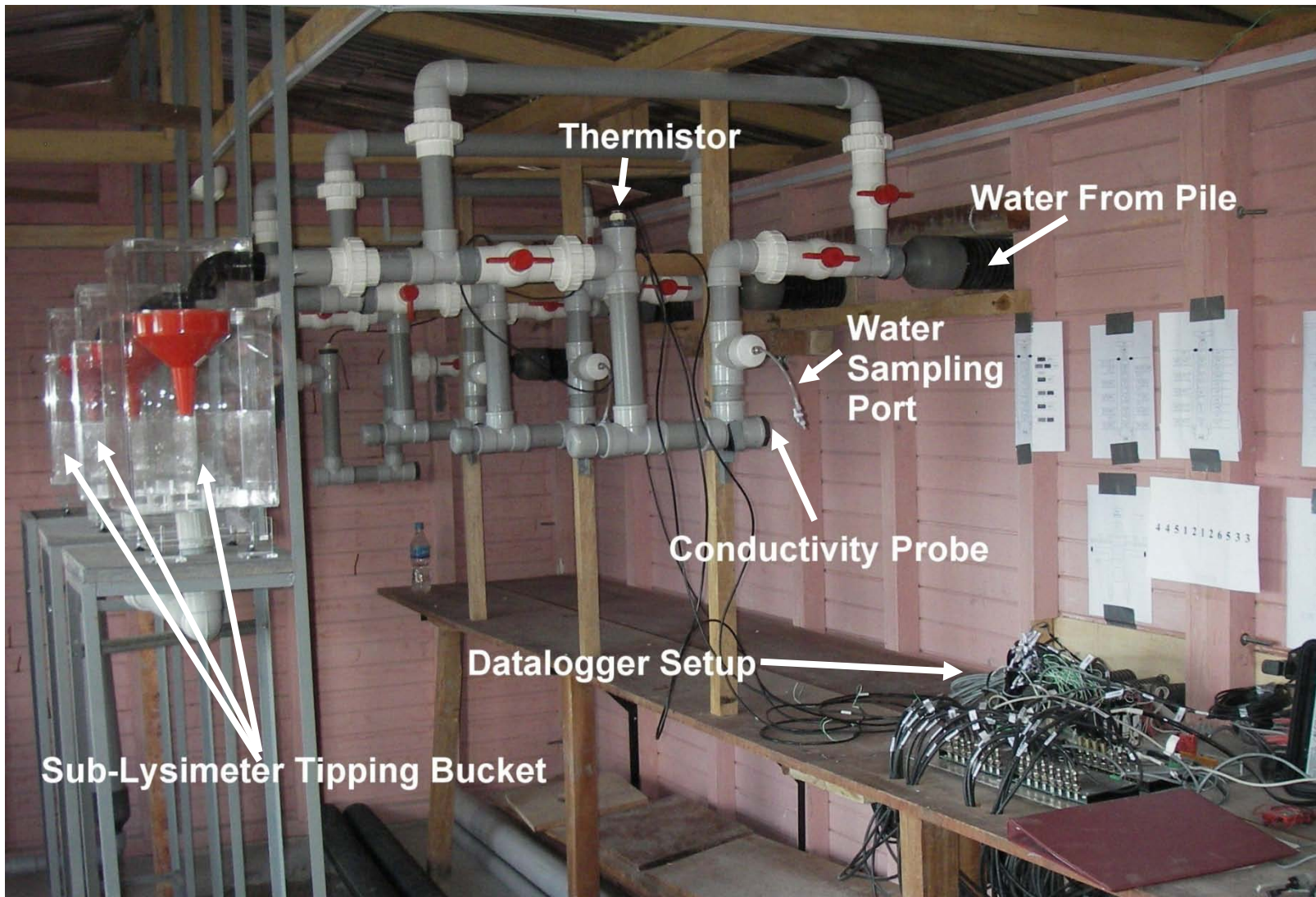


Figure 2.9. Inside the instrumentation hut.

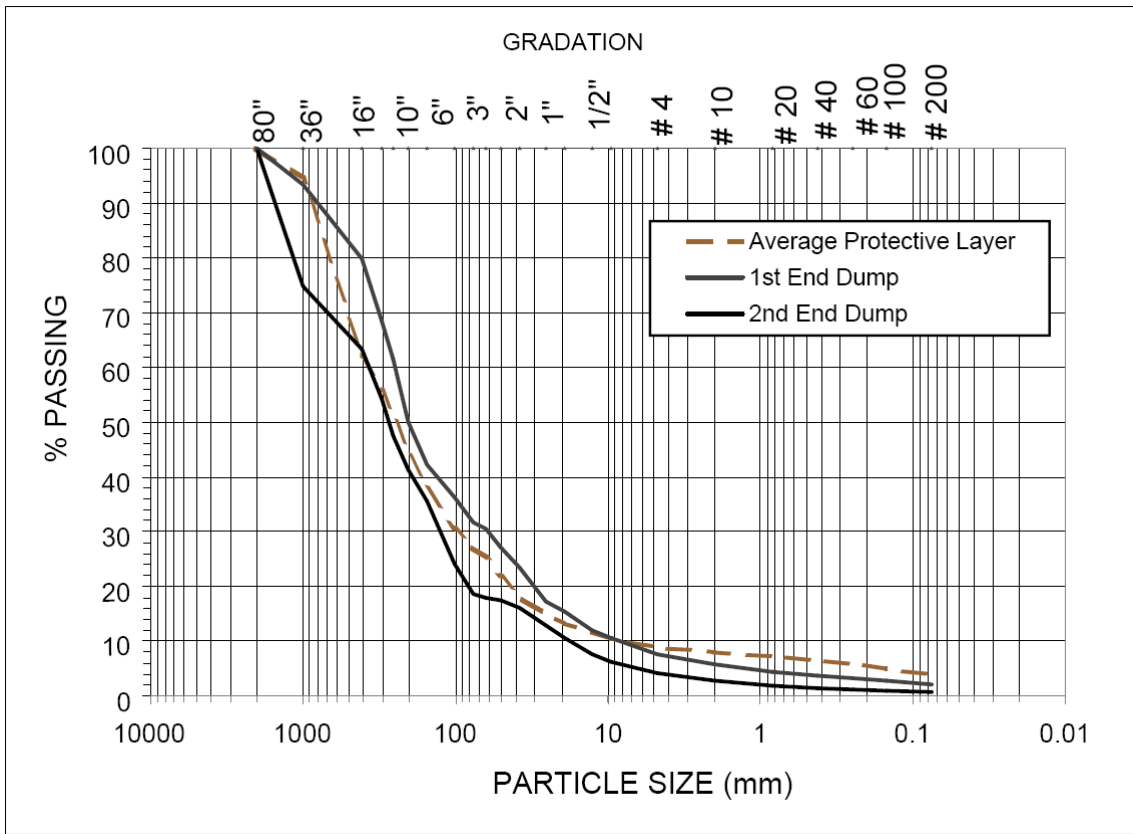


Figure 2.10. Particle size distribution of waste rock material placed in the pile.

3 RESULTS: TEST PILE HYDROLOGY

This chapter characterizes the water balance of the 36 m x 36 m x 10 m-high waste rock test pile 1 during the first 21 months of operation from 18-Jan-2007 to 30-Sept-2008. By examining each component of the water balance equation in test pile 1, this chapter will identify:

1. the percentage of precipitation that infiltrates through the test pile,
2. spatial and temporal flow differences,
3. what flow mechanisms are prevalent,
4. average linear groundwater and wetting front velocities, and
5. moisture content changes.

The water balance equation for test pile 1 is:

$$P - R - \Delta S - ET - G - Q = 0 \quad [3-1]$$

where precipitation P , runoff R , change in storage ΔS , evapotranspiration ET , groundwater seepage G , and basal outflow Q are typically expressed in m^3/day or a time averaged flux of mm/day . Since test pile 1 is free of any vegetation, there is no transpiration and evaporation E need only be considered. When ponding is observed on the compacted traffic surface at the top of the pile, the ponded water does not run off and eventually evaporates or infiltrates, or may generate small-scale runoff that infiltrates in areas of higher permeability. Runoff is further prevented by a 0.5 m berm that is placed around the top surface of the pile. A French drain installed on the natural slope that abuts test pile 1 intercepts groundwater flow and prevents subsurface flow from entering the pile (Corazao Gallegos, 2007). The only source of water into test pile 1 is precipitation falling on the top and side of the pile. The water balance equation 3-1 is then rearranged:

$$P - E = \Delta S + Q \quad [3-2]$$

3.1 PRECIPITATION

A total of 1526 mm of precipitation P is reported by the site rain gauge during the 21 month period between 18-January-2007 and 30-September-2008. This amount corresponds to 1978 m³ of precipitation across the horizontal surface area of the test pile (1296 m²). A clear seasonal variability is apparent, as a significant proportion of the annual rainfall occurs within nearly one half of the year (wet season), leaving the other half relatively dry (dry season). Due to a poor rain gauge-datalogger connection from February- to June-2008, rainfall at the study site during this period is estimated based on measurements made at Antamina rain gauges located within 5 km of the site (Appendix C).

3.1.1 Estimation of Missing Precipitation Data

Using meteorological data from several weather stations located throughout the Antamina property (Figure 3.1), 375 mm of precipitation is estimated to have fallen at test pile 1 during the period of missing rain data between February- and June-2008. Weekly precipitation data is used for this estimation because it provides the best compromise between monthly (low resolution, low standard error) and daily (higher resolution, higher standard error) analyses. The 123-day long gap is reduced to 119 days (17 weeks) because the partial week after the gap in which rain data is obtained registers a higher amount of precipitation than estimated, and is used because it represents rain recorded by the rain gauge. Conversely, 10.2 mm of rain is registered during the partial day in which the rain gauge stopped working. When this amount of rain is accounted for, the total reported site precipitation becomes 1516 mm (1526 – 10.2 mm).

The following section summarizes the steps used to estimate the missing site precipitation. Appendix C outlines these steps in greater detail.

3.1.1.1 Local Gauges and Linear Least Square Regression Analysis

Precipitation reported by the site rain gauge is compared to precipitation reported by six Antamina rain gauges (Figure 3.1). Based on data from the entire study period, the site rain gauge is best correlated with the Yanacancha rain gauge ($r^2 = 0.85$) situated approximately 4 km away and 200 m lower in elevation, and Quebrada Antamina ($r^2 = 0.84$) situated less than 5 km

away and 300 m higher. Based on precipitation data from these two stations, the missing site precipitation (u_N) is estimated using a least squares analysis:

$$f(u_N) = a_1(M_{x_N}) + a_2(M_{y_N}) + d \quad [3-3]$$

where N is the number of data points in each basis function (i.e., the number of weeks; $N = 1, 2, 3, \dots, 17$); $f(u_N)$ is the estimated mm of rainfall at the test site at a given week N ; M_x and M_y are the Yanacancha and Quebrada Antamina basis functions during at a given week N ; a_1 and a_2 are the Yanacancha and Quebrada Antamina parameters (i.e., correlation factors to site data); and d is the offset term. Based on calculations outlined in Appendix C, the a_1 and a_2 parameters are calculated to be 0.510 ± 0.017 and 0.354 ± 0.015 , respectively, and the d offset is calculated to be 2.76 ± 0.17 . Accounting for error, a total of 375 ± 15 mm of precipitation is estimated to have fallen in the period during which the datalogger failed to record rainfall at the test site.

3.1.2 Estimation Validity

An examination of the precipitation, wind direction, temperature and relative humidity for the period of missing site precipitation shows no clear departure from normal variability dating back to 2001 (Appendix C). The precipitation estimate proved to be a suitable substitute for the missing site precipitation because:

1. results from applying equation 3-3 to estimate precipitation at the test site over the entire study period (and not just during the period of missing precipitation) are similar to the measured precipitation over the same time period (see below), with only a 6 % difference between cumulative totals (Figure 3.2), and
2. cumulative precipitation from a second rain gauge (Campbell Scientific TR-525, same as the Antamina gauges) installed on site (28-Sept-2008) has a similar shape to the cumulative precipitation of the first site rain gauge during the same period 135-day period (see below), with a 4 % difference between cumulative totals (Figure 3.3).

In the first case, the linear regression analysis is extended to estimate rainfall at the test pile over the entire study period from 18-Jan-2007 to 30-Sept-2008 based on the weekly Yanacancha and

Puente Juprog rain data (Figure 3.2). The cumulative measured site precipitation (rain gauge) and cumulative estimated precipitation (equation 3-3) over the entire study period shows that they are quite similar in shape. The total measured precipitation during this period (1516 mm) is approximately 6 % lower than the total estimated precipitation during the same period (1607 mm), indicating that the least squares analysis provides a close approximation to the reported site rainfall. For comparison, cumulative rainfall reported at the Yanacancha and Quebrada Antamina stations is also presented.

In the second case, a comparison of overlapping daily rainfall data is carried out between the site rain gauge and a backup rain gauge installed on top of the test pile on 28-Sept-2008, at the end of the study period. For the purpose of this analysis, performance of the two gauges extends beyond the study period and 135 days of data (28-Sept-2008 to 12-Feb-2009) is compared between both gauges (Figure 3.3). Precipitation from this period is not included in the water balance calculations referred to throughout the remainder of this investigation. The total measured precipitation during this period for the primary site gauge (780 mm) is approximately 4 % higher than the backup gauge (747 mm). These differences may be the result of:

1. natural variability in total weekly precipitation i.e., spatial heterogeneity of precipitation particularly in mountainous regions (Buytaert et al., 2006).
2. slight manufacturing differences between the primary rain gauge (RainWise) and the backup rain gauge (Campbell Scientific).

Nevertheless, results indicate that there is an expected variability in precipitation even over a small area (i.e., 10's of m), regardless of whether they are based on weekly or daily data. Since cumulative site precipitation (measured and estimated) is based on weekly data and is within the same range of variability as the two site rain gauges which are based on daily data (± 5 %), this indicates that the result of the linear regression model is acceptable for the purpose of this investigation and can be used in the succeeding water balance calculations (Section 3.2.2; Section 3.5.1)

3.1.3 Uncertainty in Precipitation Measurements

It is possible that a number of rain gauge tips were not recorded by the datalogger due to the way in which the datalogger prioritizes the data being recorded (Appendix E). This would result in an underestimation of precipitation. Due to the nature of the precipitation data, it is nearly impossible to estimate the extent of unrecorded or ‘missed’ tips at site. That the reported site precipitation fell within the range of precipitation reported at other Antamina sites indicates that the amount of missed tips can be assumed to be insignificant for the purpose of this study.

Appendix C discusses the differences between the site rain gauge and the Antamina rain gauges, but does not consider the uncertainty involved in using rain gauges in general. In a study of local errors resulting from tipping bucket rain gauges, Ciach (2003) reports that while tipping bucket rain gauges are convenient and reliable tools they are subject to systematic errors (calibration, wetting-evaporation losses, etc.) and random instrumentation errors (heterogeneous distribution, time sampling, hydrodynamic flow instabilities in the pivot bucket mechanism, turbulent wind, etc.). These errors are typically unknown and largely ignored.

Furthermore, Ciach (2003) states that the magnitude of rain gauge errors is highly dependent on local rainfall intensity and the time interval over which the rainfall is examined. In examining moderate rates (10 mm/hr) over 5- to 60-minute time intervals, Ciach (2003) attributes errors between 3 – 5 % based on small time-scale intervals, and the errors continue to decrease as the time interval in which rainfall is recorded increases. It is likely that these errors are inherent to some degree in the site rain gauge data.

Error is also introduced in the linear calibration equation relating tips to precipitation rates or equivalent volumes of water. Experimental observations by Rain Wise Inc. demonstrate that while the theoretical volume of water to trigger a tip is 8.2 mL, the actual volume that triggers a tip is approximately 10 % less than theoretical. The empirical calibration of 7.4 mL/tip is thus recommended by the manufacturer because it accounts for splashing effects and residual water droplets that remain after a tip due to surficial tension, despite the application of certain Teflon-based sprays meant to reduce this. The relationship, however, is not linear because variable precipitation intensities will result in variable rainfall fluxes. Experimental observations by the

manufacturer indicate that when the flow rate does not exceed 75 mm/hour, the varying intensity can be corrected for by subtracting 3 % from the total precipitation. Since the hourly precipitation never exceeds this rate (Section 3.1.4, below), the 3 % correction can be applied to this rain gauge data. However, because there is no empirical evidence in the current literature that supports this 3 % correction, it cannot be applied to the data with sufficient reliability.

Therefore, while most rain gauge manuals attribute a ± 1 % accuracy error arising from instrumentation errors, an uncertainty range of ± 5 % is attributed to the reported site precipitation due to all of the above-mentioned factors.

3.1.4 Final Site Precipitation and Reported Trends

In the 499 days in which site rain gauge data is available, a total of 6008 tips are reported by the gauge, which corresponds to a total of 1526 ± 76 mm of reported rain over the 21-month period. Accounting for the 375 ± 15 mm of precipitation estimated to have occurred during the 119-day period of missing site data, approximately 1891 ± 91 mm of rain is estimated to have fallen on site (after removing 10.2 mm described in Section 3.1.1). Site precipitation that is based on both measured and estimated precipitation is referred to as the final site precipitation. Figure 3.4 shows the cumulative estimated precipitation [mm] over the entire period along with the daily reported precipitation. Since the study period does not include two full years of data, the annual precipitation was calculated based on the first and last 365 days of the 21 month-long study period. For example, annual precipitation is 1224 mm/year between 18-Jan-2007 and 17-Jan-2008, whereas it is 1370 mm/year during between 1-Oct-2007 and 30-Sept-2008. Both values are within the range of annual precipitation reported at other Antamina rain gauges.

There is a significant difference between the amount of rain during the wet and dry seasons, with the wet season typically extending from October through April and the dry season from May through September (Figure 3.4). The period of missing rain data extends across both of these periods with approximately 70 and 53 days in the wet and dry season periods, respectively. Based on measured precipitation throughout the entire 21 month-long study period (except for Feb- to Jun-2008), the average precipitation flux is 1.3 mm/day during the dry season and 4.6 mm/day during the wet season. Total dry season precipitation is 25 % of the total wet season

precipitation. There is nearly 25 % more precipitation in 2008 than during the same number of days in 2007 (Table 3.1).

Of the 499 reported days in which site rain data is available, 343 of these days (69% of the total days) report rain, with a maximum flux of 27.9 mm/day on 25-Apr-2007. This value does not account for varying intensities and durations of precipitation throughout the day. For example, it does not display whether all of this precipitation fell over 30 minutes or 12 hours, or whether most of it occurred during the morning, afternoon, or night. To better understand the variability in precipitation, this 499-day period is examined for 12-, 6-, and 1-hour intervals.

In general, the variability in precipitation increases with shorter time-intervals (Figure 3.5). Precipitation is reported in 52 % of the 12-hour periods (maximum flux of 18.3 mm/12 hr on 2-Jan-2008), 38 % of the 6-hour periods (maximum flux of 16.3 mm/6 hr on 27-Nov-2007) and 14 % of the 1-hour intervals (maximum flux of 8.9 mm/hr on 24-Jun-2008). The highest precipitation flux is 1.02 mm/min on 25-Apr-2007 (not surprisingly the same day as the maximum daily precipitation). While the maximum recorded precipitation at 24-hour and minute-intervals are coincident with the same rain event, the highest recorded precipitation rates measured at 12-, 6- and 1-hour intervals are observed at other times of the year, regardless of whether it is the wet or dry season. This indicates that precipitation is highly variable at this site.

3.2 EVAPORATION

Evaporation E that is used in the water balance (equation 3-2) is estimated using the pan evaporation (semi-empirical), Penman-Monteith (theoretical), SoilCover (model), and large-scale pan lysimetry (empirical water budget) approaches during two periods:

1. the study period (i.e., the first 21-months of pile operation) from 18-Jan-2007 to 30-Sept-2008, and
2. one complete water year from 1-Oct-2007 to 30-Sept-2008.

Pan evaporation measurements (E_{PAN}) from the Yanacancha meteorological station (Figure 3.6) are converted to the site-specific bare soil conditions of test pile 1 by using a 0.65 bare soil pan

correction factor K_{pan-BS} (Appendix D). The results are referred to as corrected pan evaporation. The Penman-Moneith approach requires a calculated bare soil correction of $K_{BS} = 0.8$ to convert ET_{ref} to an estimated bare soil evaporation E_{BS} (Appendix D). Results from the SoilCover model and large-scale pan-lysimetry water balance methods are only examined in the context of one water year (Table 3.2). Further details can be found in Appendix D.

Evaporation during the entire study period is examined first, followed by evaporation during the water year.

3.2.1 Evaporation: Study Period

Over the entire study period, the pan evaporation approach (E_{PAN}) estimates total evaporation at test pile 1 to be 1423 mm (75 % of 1891 mm of total precipitation) whereas the Penman-Monteith approach (E_{PM}) estimates total evaporation at 1617 mm (86 % of total precipitation). That the Penman-Moneith estimate is higher than the corrected pan evaporation estimate is consistent with other comparisons between the two models (Wilson et al., 1997; Allen et al., 1998; Swanson et al., 2003).

The study period (Jan-2007 through Sept-2008) does not span a representative time period. It is likely that the pile had not fully adjusted to the disturbances experienced during pile construction, which likely results in a moisture content less than residual saturation due to evaporation from the blasting process and during end-dumping. Since the 21 month-long study period consists of two complete dry seasons but one full and one partial wet season, it could not be easily compared to other results. Therefore a more detailed examination of the data during one water year, which includes one complete wet and dry season, is more representative of pile behaviour and can be more easily compared to results from other investigations.

3.2.2 Evaporation: 2007-2008 Water Year

The water year period extends from 1-Oct-2007 (beginning of the 2007-08 wet season) through 30-Sept-2008 (end of the 2008 dry season). This period is examined because:

1. nearly one year has passed since the test pile construction was completed and the pile is no longer affected by post-construction disturbances (i.e., waste rock has retained additional moisture content that it lost through evaporation during the end-dumping process),
2. flow at the end of the dry season is at a minimum compared to the rest of the year (further explained in Section 3.3.4), and
3. the net change in storage can be assumed to be $\Delta S \sim 0$, which is important for water balance calculations (Section 3.4.4).

Evaporation estimates during the water year are presented below.

3.2.2.1 Pan Evaporation and Penman-Monteith Estimates

Table 3.2 indicates that evaporation based on E_{PAN} measurements yields an estimate of 887 mm (68 % of the 1297 mm of precipitation during the water year), whereas the E_{PM} approach yields an estimate of 972 mm (75 %) during the water year. The average daily E_{PAN} and E_{PM} fluxes during the water year are relatively similar, with values of 2.4 and 2.7 mm/day, respectively. However, E_{PM} is much more variable than E_{PAN} (Figure 3.7) and average E_{PAN} and E_{PM} estimates are 5 to 10 % higher during the dry season compared to the wet season. For example, average wet season evaporation fluxes are 2.4 and 2.6 mm/day for E_{PAN} and E_{PM} , respectively, and the corresponding dry season averages are 2.5 and 2.8 mm/day, respectively. A higher relative humidity during the wet season (Appendix C) likely results in more similar vapour pressures between the waste rock surface and the adjacent air mass, whereas the vapour pressure gradient increases during the dry season (which has a lower average relative humidity) and promotes higher evaporation rates.

The average daily precipitation rate during the water year is 3.5 mm/day, with an average of 5.1 mm/day during the wet season and 1.4 mm/day during the dry season (Table 3.1). Average precipitation-to-evaporation ratios ($P:E$) approximate 2 and 0.5 during the wet and dry season, respectively, for both E_{PAN} and E_{PM} . These ratio differences indicate that precipitation is greater than evaporation during the wet season and precipitation is less than evaporation during the dry season, and that there is a shift in dominance depending on the season (Figure 3.7).

These two approaches have limitations. Accurately characterizing evaporation at any given site can be highly complex. Allen et al. (1998) explain that no weather-based calculations can be expected to perfectly predict evapotranspiration under every climatic situation due to simplification in formulation and errors in data measurement. While pan evaporation data provides the closest proxy for daily potential evaporation, correcting the data from an open pool of water to a bare soil surface creates uncertainty in achieving accurate results. Pan evaporation methods are susceptible to the microclimatic conditions under which the pans are operating and the rigour of station maintenance among other factors (e.g., location, design specifications, material and measurement frequency). Although pan evaporation measurements are recorded daily at the Yanacancha weather station, they do not occur at the same time each day and the height of water in the pan is only refilled once per week. Allen et al. (1998) determined that, in general, a $\pm 15\%$ error should be attributed to pan evaporation data. This error range is applied to the pan evaporation data for test pile 1.

The Penman-Monteith approach is also useful in predicting evaporation based on meteorological conditions, but typically overestimates evaporation under unsaturated conditions and under low evaporation conditions, even with precision instruments and excellent environmental conditions (Wilson et al., 1997; Allen et al., 1998; Swanson et al., 2003). These estimates are also further complicated by several factors such as the soil, particle size distribution, moisture content, surficial permeability, infiltration rate, occurrence of ponding, aeration, etc. Allen et al (1998) reported error estimates as high as 20 % when using this approach. This error range will also be applied to the Penman-Monteith estimates for test pile 1.

3.2.2.2 Modeled Evaporative Fluxes: SoilCover

The SoilCover evaporative flux model estimates evaporation to range between 32 and 41 % of the total precipitation during the water year, depending on the material properties (Table 3.2). This is approximately half of the evaporation estimated using the previous two approaches.

Estimates produced from this model proved too unreliable due to the lack of several soil property parameters that are required in order to achieve accurate results. This model is thus too unconstrained and could not be calibrated.

3.2.2.3 Lysimetry Water Balance Estimate

The final approach used to estimate evaporation is based on the pan-lysimetry water balance method. Conducting a water balance calculation that includes P (Section 3.1, above) and outflow Q (Section 3.3, below), and assuming no net change in storage ($\Delta S \sim 0$) over the course of one water year, water balance equation 3-2 can be rewritten to calculate evaporation E :

$$E = P - Q \quad [3-4]$$

Using equation 3-4 and assuming that there is no net change in storage ($\Delta S \sim 0$), a total of $E_{WB} = 766$ mm (59 % of site precipitation) is calculated to have evaporated from the pile during the water year (Table 3.2). This approach integrates several factors that the other approaches fail to address, one of the most important factors being the difference in evaporative flux between the rubble-based batters and fine-grained, compacted top of the pile (Figure 3.8). The lysimetry water balance approach provides the most reliable integration of climatic variables and material properties, particularly with regards to the differences between the top surface layer and the batter. However, it does not quantify these differences (i.e., separate evaporation from the batter vs. top of pile), and cannot be used to provide a higher-resolution evaporation estimate (i.e., daily, weekly, monthly). In addition, this approach heavily relies on the accuracy of the precipitation and outflow measurements and that no net change in storage occurred over the water year. All three of these components are based on a combination of reported data, interpolations and assumptions. Nevertheless, this approach is more reliable than the other quasi-empirical and mathematical approaches in estimating evaporation at test pile 1.

3.3 OUTFLOW

Pile construction was complete by September-2006 but the automated data collection system did not become operational until 18-Jan-2007, mid-way into the wet season. Chapter 2 introduced the 36 x 36 m basal lysimeter D, and the three 4 x 4 m sub-lysimeters A, B and C located within

the basal lysimeter along the centre line (Figure 2.6). The combined flow from these four lysimeters is the outflow component Q in the water balance equation 3-2.

Based on qualitative observations of when water first began flowing from the base of the pile, it took approximately three to four months for the pile to ‘wet up’ after construction was complete (Corazao Gallegos, 2007; Bay et al., 2008). Discharging water is first observed from basal lysimeter D nearly three months after pile construction was complete, whereas flow did not start draining from the interior sub-lysimeters A and B until nearly four months after pile construction. In general, water penetrates the batters more rapidly than it does the full 10 m-depth of the pile. Once the pile began draining during this initial wetting up period, the rate of drainage clearly became affected by the rate and intensity of precipitation. The term ‘wet-up’ is used to describe the initial period after pile construction in which the waste rock moisture content (likely below residual saturation) increased to attain a state of dynamic equilibrium over a one-year timescale (e.g., a water year).

3.3.1 Correcting Tipping Bucket Data: RANSAC

Four tipping buckets are used to measure the rate of discharging water from each of the four lysimeters (Chapter 2). Each tipping bucket was calibrated to convert the ‘tip-time’ to a corresponding flow rate (Appendix E). Shortly after the tipping bucket flow gauges were calibrated and began collecting data in January of 2007, it became clear that there was a problem with the tipping bucket data. Due to a software problem, the datalogger randomly failed to record tips from each of the four tipping buckets. These missed tips are accounted for by using the Random Sample Consensus (RANSAC) model, which is typically applied to datasets in which significant outliers are present (Fishler and Bolles, 1981). This model identifies the outliers in the data that result from unrecorded tipping bucket tips, and allows for the subsequent correction. Appendix E contains a detailed description of how this was accomplished, a summary of which is provided next.

Based on a set of user specified parameters, the RASNAC model assigns each data point (i.e., tip-time) an ‘inlier’ or ‘outlier’ value. Inliers represent data whose distribution can be explained by a set of model parameters, i.e., can be fitted to a line, and represent the ‘base case’ or ‘field-

observed' flow rate. Once identified, inlier points are placed in the inlier 'bin'. Outliers represent data points that do not fit the model and can consist of both noise and erroneous measurements. Missed tips are associated with higher tip-times than base case tips. They are subsequently assigned m -integer values depending on how many missed tips the model estimates that they are associated with, and are then placed in the corresponding 'bin' level. For example, if the base case tip-time tt is 30 seconds, the tip-time may be around 60, 90 or 120 s at $m = 1, 2$ or 3 missed tips, respectively. Since the 'tip-time to flow-rate' calibration equation is non-linear, the resulting flow rates do not change by the same corresponding factor e.g., at $tt = 30$ s, the flow rate $q = 5.9$ L/min and at $tt = 120$ s, the flow rate $q = 1.4$ L/min. See Appendix E for further explanation.

Results of the RANSAC model indicate that the proportion of base case data points within the total interpreted dataset range between 65 and 80 %. This means that 20 to 35 % of the data in the interpreted datasets originate from missed tips, depending on the tipping bucket and the flow rate (i.e., there are more missed tips at higher flow rates). Since the hydrological characterization is based on this interpolated data, flow data is attributed an error of ± 20 to 35 %, depending on the lysimeter. Appendix E includes further discussion.

Despite some relatively large error values in the resulting dataset, results of the RANSAC model are determined to be applicable for the purpose of this investigation. Unless otherwise stated, interpolated outflow is considered as outflow data for the remainder of this discussion.

3.3.2 Total Pile Discharge

A total of 1175 m³ of water drained from the base of the pile throughout the study period from 18-Jan-2007 through 30-Sept-2008. An additional 59 m³ of water is accounted for based on data points removed due to maintenance or whole periods in which the datalogger did not record data from a given tipping bucket but field observations confirm that the tipping bucket was flowing (Appendix E). A total outflow of $Q = 1234$ m³ of water is estimated to have discharged from the base of the pile during the entire 21 month study period. A majority of this outflow is reported by basal lysimeter D, but the sub-lysimeters allow for the investigation of smaller-scale (i.e., higher resolution) processes that occur within the context of a larger waste rock volume. A summary of

lysimeter contribution and accounting for any removed or estimated flow at each lysimeter is given in Table 3.3.

Of an estimated total of 1234 m³ of pile outflow over the entire study period, basal lysimeter D contributes $Q_D = 1202 \pm 231$ m³, whereas sub-lysimeters C, B and A contribute $Q_C = 23.4 \pm 7.1$ m³, $Q_B = 2.8 \pm 0.7$ m³ and $Q_A = 6.4 \pm 1.4$ m³, respectively. The source of the errors is described in Appendix E. The basal lysimeter represents 97.4 % of the total pile effluent, whereas sub-lysimeters C, B and B represent 1.9, 0.2 and 0.5 %, respectively.

3.3.3 Outflow Hydrographs

Outflow from the basal lysimeter and three sub-lysimeters is presented as unit hydrographs that show the evolution of outflow [m³/day] over time (Figure 3.9). Each hydrograph illustrates peak discharges in response to heavy precipitation events, and both the rising and receding limbs that result on either side of a significant outflow peak. Outflow from the base of the pile is nearly 50 % of the total precipitation over the entire study period and 41 % of the precipitation during the 2007-08 water year (Table 3.2).

All four outflow hydrographs demonstrate highly variable flow rates that differ by several orders of magnitude depending on the location and time of year. A strong seasonal response in outflow is apparent, with high- and low-flow periods generally corresponding to the wet and dry seasons (October through April and May through September, respectively). All lysimeters respond to event-driven precipitation inputs, with a variable lag time depending on the lysimeter location and height of material above it. Each lysimeter also illustrates a characteristic drying period during which the pile is draining to near-residual saturation. This is particularly apparent in the basal lysimeter hydrograph (Figure 3.9d). Aside from some similarities between lysimeter hydrographs, each lysimeter exhibits its own distinct characteristic response to precipitation (Figure 3.9a).

The average pile flow rate over the entire study period is approximately $Q = 2.0$ m³/day, with wet and dry season averages of nearly $Q = 3.0$ and 0.5 m³/day, respectively. Lysimeter flow

results exhibit similar characteristics to those in a 5 m high waste rock test pile in northern Saskatchewan presented by Nichol et al. (2005) in which:

1. peak flow rate (magnitude and timing) was different among lysimeters,
2. lysimeters with the highest flow rate showed the most rapid response to precipitation whereas those with the lowest flow rates showed the slowest response, and
3. various flow mechanisms (matrix flow, macropore flow, displacement, etc.) are reflected in the data

These observations are discussed throughout the remainder of this chapter.

3.3.4 Hydrograph Variability

Total wet and dry season outflow Q [m^3], weekly outflow rates [m^3/week] and average outflow flux [mm/day] for each lysimeter is compared to the total precipitation during the same period (Table 3.1). Since the wet and dry seasons consist of 7 and 5 months respectively, results are presented as time-averaged values. In addition, because the study period begins in the middle of the 2006-7 wet season (Jan-2007), data for that season is incomplete and unrepresentative of the entire wet season. A larger volume of water from precipitation corresponds to a larger volume of discharging water. This is not a direct correlation, as each lysimeter responds differently to precipitation events.

Outflow response to precipitation events is observed anywhere between a few hours and several weeks after a high-intensity precipitation event. The maximum outflow rates during the 21 month study period is $Q_D = 14.7$ and $Q_C = 0.44 \text{ m}^3/\text{day}$ for basal lysimeter D and sub-lysimeter C, respectively, on 25-Feb-2008 (Figure 3.9). Unfortunately, there is no site precipitation data available at this time (Section 3.1.1; Appendix C). Nearly 4 km away, 75 mm of rain was measured at the Yanacancha rain gauge during the entire week, which is much higher than the average weekly wet season site precipitation of 45 mm/week (Table 3.1). For the study period, a maximum of $Q_B = 0.038 \text{ m}^3/\text{day}$ is reported for sub-lysimeter B on 27-Feb-2008 and $Q_A = 0.038 \text{ m}^3/\text{day}$ for sub-lysimeter A on 27-Jan-2008.

These maximum values represent daily flow rate averages and do not explicitly indicate the maximum observed flow rate that could have been sustained for shorter periods of time within the day. For example, basal lysimeter D reaches an equivalent flow rate as high as $Q_D = 21.6 \text{ m}^3/\text{day}$ that is sustained for a few hours and is 50 % higher than the maximum calculated daily flow rate. This is based on the highest outflow measured by the large tipping bucket, $Q_D = 15 \text{ L/min}$. Similarly, sub-lysimeter C reaches equivalent flow rates as high as $Q_C = 0.8 \text{ m}^3/\text{day}$ (0.54 L/min) for a few hours, which is a 75 % increase over the maximum calculated daily flow rate. Sub-lysimeters A and B both report maximum flow rates of $Q_A, Q_B = 0.052 \text{ m}^3/\text{day}$ (0.036 ml/s). These maximum flow rates are important when comparing the area-normalized flow behaviour between the lysimeters (below). Additionally, this information will be useful in subsequent hydrological models in which it is important to know the maximum outflow volumes expected from this test pile.

It is difficult to calculate a minimum flow rate for the lysimeters, since all four lysimeters have gaps in the data due to instrumentation maintenance/problems or periods in which no water drained to the lysimeters. Site observations confirm that all three sub-lysimeters stopped flowing during certain periods of the dry season, whereas the large lysimeter could flow continuously throughout the year (if maintenance was not required). The lowest reported flow rate at basal lysimeter D is slightly more than $Q_D = 100 \text{ L/day}$ ($0.1 \text{ m}^3/\text{day}$), and is observed at the end of both dry seasons (i.e., September/October of 2007 and 2008). The lowest reported sub-lysimeter flow rate (greater than 0 ml/s) is nearly $Q = 0.15 \text{ L/day}$ ($1.5 \times 10^{-4} \text{ m}^3/\text{day}$), and occurs near the end of the dry season (Figure 3.9).

When all four lysimeters are flowing, the basal lysimeter outflow response is representative of the entire pile response, and can be conceptualized as a composite average of the spatially-variable sub-lysimeter responses. When any or each of the three sub-lysimeters cease to flow, the basal lysimeter response is assumed to be an approximate representation of the entire pile because D contributes a majority of the pile response (Section 3.3.2).

3.3.5 Lysimeter Net Infiltration

Lysimeter responses are compared against one another by normalizing the flow rate by the area footprint ($q = Q/A = \text{mm/day}$; sub-lysimeter area = 16 m^2 , and basal lysimeter area = 1248 m^2). The resulting discharge flux represents the cumulative net infiltration at each lysimeter. For example, Table 3.3 presents the cumulative volume of water that is recorded at each lysimeter during the course of the 2007-08 water year. Based on this data, the net cumulative infiltration calculated at the basal lysimeter is $q_D = 540 \text{ mm/year}$, whereas sub-lysimeter C has a higher value of $q_C = 890 \text{ mm}$, and B and A have $q_B = 110$ and $q_A = 280 \text{ mm/year}$, respectively. For comparison, the net precipitation during the water year is $q_{Pile} = 1297 \text{ mm/year}$ (Table 3.2). Similarly, the daily infiltration flux for each lysimeter is also calculated and compared to the daily precipitation flux (Figure 3.10).

In response to a heavy precipitation event, basal lysimeter D and sub-lysimeter C experience larger, more rapid infiltration fluxes than sub-lysimeters A and B, which experience more attenuated flux responses. These differences are likely due to the effect of the batter, which permits rapid, less attenuated flow responses to precipitation. The daily infiltration flux at sub-lysimeter C is almost an order of magnitude higher than sub-lysimeters B and A, and reaches up to 150 % of the maximum daily infiltration flux reported at basal lysimeter D, particularly in response to two large precipitation events in Jan- and Feb-2008 (Figure 3.10a). During these two events, the daily infiltration flux for sub-lysimeter C is larger than the precipitation flux, possibly indicating that flow is focused from other parts of the pile to C. The flow response of the batters disproportionately affects the spatially- and temporally-variable hydrogeological response of the pile. This behaviour is also observed at a 5 m-high waste rock test pile at the Cluff Lake mine, Saskatchewan, Canada (Nichol et al., 2005).

3.3.6 Effect of Antecedent Moisture Content

In dry soils, matric forces usually dominate over gravitational forces. In response to a precipitation event, a significant proportion of water is drawn into the unsaturated matrix to replenish the moisture content (Baver et al., 1972). Surficial infiltration rates are highest at the start of a rainfall event (or wet season) as high matric forces (capillary, adsorption) combine with gravity to induce strong infiltration rates until moisture content stabilizes and the unsaturated

hydraulic conductivity is roughly equal to the infiltration rate (Smith and Beckie, 2003). Therefore, antecedent moisture content is an important consideration when examining the hydrological behaviour of a given material.

Pile construction was completed in Sept-2006 and the data was online in Jan-2007 (Chapter 3). The waste rock was likely extremely dry (i.e., below residual saturation) due to drying from the blasting process and further evaporation during the end-dumping process. (Note. this is not the case for the protective layer which was stockpiled on site for up to 3 months (Chapter 2) and likely had a moisture content above residual saturation). The wet-up period of 3 - 4 months confirms that the pile was initially dry and that a large proportion of infiltration was taken up into storage in the few months after pile construction was complete. It is for this reason that the water year was set to begin almost one year after pile construction was complete and the pile is assumed to have adjusted to any construction disturbances.

Based on site precipitation and the hydrograph response of the basal- and sub-lysimeters in the test pile (Figure 3.4; Figure 3.9d), the pile is at its driest point at the end of the dry season or beginning of the wet season (September/October). This is further confirmed by the Time Domain Reflectometry (TDR) moisture content data discussed below (Section 3.4). When the wet season rains begin, the pile is at its driest and a considerable proportion of the infiltrating water is retained under the high initial matric forces. Since the volume of water entering the pile is greater than the volume of water discharging from the base of the pile, the overall water storage of the pile begins to increase (as indicated by the TDR data discussed below). The extent at which this will occur is dependent on the pile dimensions as well as moisture content, hysteresis, material wilting point and field capacity, relative proportion of fine-grained material in the pile and net infiltration, all of which control the flow of water through the pile and how much moisture the pile material can store (Smith and Beckie, 2003).

Lysimeter discharge rates are accordingly lowest at the end of the dry season/beginning of the wet season. Discharge rates increase days to weeks after the onset of the wet season, depending on the location within test pile 1. For example, beginning on 24-Feb-2007, nearly 280 mm of rain is introduced during 50 near-consecutive days of rain after an uncharacteristically dry

February (Figure 3.10b). Nearly 7 days after this high-precipitation period begins, the daily infiltration rate at basal lysimeter D responds on 2-Mar, whereas sub-lysimeter C infiltration responds nearly 3 - 4 days after the basal lysimeter on 6-Mar. Both continue to experience increasing flow rates for the next 2 - 4 weeks, after which they attain relatively high flow rates. Flows to sub-lysimeters A and B are more attenuated and do not respond until almost 19 to 22 days after the onset of the 50-day precipitation period. Nearly one week after, they reach relatively high, sustained flow rates (Figure 3.10).

Similar trends at the onset of the 2007-08 wet season (i.e., Oct-2007) are observed in basal lysimeter D fluxes, which show delays up to 2 weeks after the wet season begins (Figure 3.10a). No sub-lysimeter data are available for this period and it is likely that they were dry during a portion of this period. Flow to sub-lysimeter C indicates higher infiltration rates at the end of October, whereas sub-lysimeters A and B do not experience significant increases until December.

3.3.7 Wet Season Responses

Once the pile has reached a state of dynamic equilibrium over a one year time scale (i.e., has wet-up and water contents always exceed residual saturation) and flow at all four lysimeters exhibit high flows that are representative of the wettest pile conditions over the course of a water year, several flow responses become evident in the data. These include preferential macropore flow, pressure-wave responses and non-vertical flow.

3.3.7.1 Preferential and Macropore Flow

The nonspecific descriptive flow that occurs in certain areas at faster rates than normal in response to a rainfall event is called 'preferential flow', and is believed to occur due to collections of large connected pores or obstacles that concentrate flow to certain pathways. Preferential flow is typically activated under high-intensity and high-infiltration precipitation events when the matrix water content is high and matric pressures are relatively low (Chapter 1). During these events, water can penetrate to depth at velocities much higher than would be expected for matrix flow alone.

Based on lab and field-scale experiments, Fala et al. (2005) observed that preferential flow can be caused by continuous macropores, or by capillary flow through vertical, horizontal or inclined layers of relatively high hydraulic conductivity, and that it has the ability to control the movement of water within a pile. Capillary flow is typically subject to Darcian principles and occurs in the finer-grained matrix, whereas macropore flow is typically referred to as non-capillary flow, is not subject to Darcian principles, and generally occurs within the coarser-grained pile regions. Preferential flow that occurs over timescales of days to weeks is typically associated with capillary flow, whereas non-capillary flow generally occurs over hourly timescales. Macropores have been reported to rapidly channel water much faster than the capillary-dominated matrix-flow velocities (Germann and Beven, 1981; Eriksson et al., 1997; Newman, 1999; Nichol et al., 2005).

While the antecedent moisture condition is shown to be an important consideration in characterizing pile hydrology (Section 3.3.6), the intensity of a precipitation event can also play a critical role in pile response. Based on a qualitative examination of the outflow data from test pile 1, there is a clear response in outflow (particularly near the surface) any time in which the daily precipitation exceeds 8 - 10 mm/day. This is also observed in the moisture content data (Section 3.4), and can sometimes be resolved in the water chemistry as the chemical signature of macropore flow is typically fresher and has a lower dissolved load than the typical matrix pore water (as discussed in Chapter 4). The following section will examine the evidence of preferential flow in the test pile in further detail.

Wagner et al. (2006) observed that matrix flow was the dominant type of flow during periods with low or moderate infiltration, and that the macropores were only episodically wet. Similarly, for the Antamina test pile, only when sub-lysimeters A and B report larger sustained flow rates during the latter half of the wet season did basal lysimeter D and sub-lysimeter C show direct responses to precipitation events (i.e., when precipitation \geq 8-10 mm/day). It is hypothesized that when sub-lysimeters A and B encounter high sustained flow rates characteristic of mid- to end-of the wet season, this indicates that the pile matrix has reached a state in which the moisture content is relatively high compared to the rest of the year. Throughout the remainder of this discussion, when the pile attains this condition it will be referred to as the 'wet season wet-up'

that describes the wettest conditions that the pile experiences when under a dynamic equilibrium over a one year time scale. Only when the pile has attained the ‘wet season wet-up’ state and ponded water is available at the surface (to provide free water), can macropores may be activated under high intensity precipitation events. Even if the pile has achieved the ‘wet season wet-up’ state, if there is no ponded water at the surface then macropores will act as barriers to flow.

Sharp responses to precipitation events are apparent in basal lysimeter D and sub-lysimeter C data. Basal lysimeter D consistently shows the first response to a precipitation event, shortly followed by C which typically exhibits a higher flux compared to basal lysimeter D (Figure 3.10). A faster response in the basal lysimeter is likely caused by a rapid infiltration of water at the pile edges, whereas water has to infiltrate (or be displaced by a pressure wave, see below) further to get to sub-lysimeter C (6 - 9 m) at the base. Sub-lysimeter C typically has a higher infiltration rate than basal lysimeter D in response to peak events, which may be explained by non-vertical flow paths that focus water into a preferential pathway.

Between 15- and 23-Mar-2007, sub-lysimeter B also reports a flux rate increase from $q_B = 0.14$ to 1.5 mm/day, and sub-lysimeter A reports a flux increase from $q_A = 0.22$ to 1.7 mm/day between 15- and 27-Mar-2007. Under these conditions, the pile is described as attaining the ‘wet season wet-up’. During the next month, in response to a 32 mm-precipitation event between 8- and 10-Apr-2007, basal lysimeter D and sub-lysimeter C fluxes begin to increase rather sharply (Figure 3.10b). The gradient of the rising limbs of both C and D fluxes is nearly identical (which is not usually the case), and both experience very rapid flux rate increases over the two days of heavy sustained precipitation (by as much as 250 % from their respective fluxes a few days prior). As basal lysimeter D and sub-lysimeter C fluxes are increasing, both sub lysimeter A and B fluxes are decreasing, and don’t begin to increase until 4 (sub-lysimeter B) to 7 (sub-lysimeter A) days after the rain event began. During the following 6 - 8 weeks, sub-lysimeters A and B maintain relatively high sustained flow rates, and D and C fluxes experience rapid responses to large precipitation events greater than 8 - 10 mm/day. Similar observations are also reported during the 2008 wet season.

3.3.7.2 Pressure-Wave Displacement of Water through the Pile

The maximum observed pile outflow flux (i.e., a combination of the basal lysimeter and three sub-lysimeters) is 12 mm/day. Based on this, it would take water over 800 days to travel through the complete 10 m-depth of the pile and over 80 days to travel through a 1 m-deep edge of the pile (i.e., pile toe). These calculations do not account for porosity or water content (Section 3.5.3, below). However, the previous section explained that outflow responses at the base of the pile are observed only a few days after a large precipitation event. While it is likely that a proportion of this outflow water results from macropore flow, it is also likely that the rapid outflow responses to precipitation events (after the pile has attained the ‘wet season wet-up’ state) are due to a ‘pistoning’ or displacement of water through the pile that result from a pressure-wave. This means that water reporting at the base of the pile is likely pre-event water (i.e., water already stored in the pile) and does not include the same water molecules that originated from that precipitation event just a few days prior. This applies more to the pile interior (10 m height) than it does to the more permeable batters (variable height). Similarly, Nichol et al. (2005) observed that despite calculated macropore flows as high as 5 m/day, a majority of outflow from an applied tracer at the Cluff Lake waste rock pile consisted of pre-event water. These displacement mechanisms in response to high-intensity precipitation events after a period of wet conditions may be the result of a pressure-induced wave that is discussed further using soil moisture data from the Time Domain Reflectometry probes (Section 3.5.2, below).

3.3.7.3 Non-Vertical Flow

The heterogeneous nature of waste rock leads to non-uniform flow. While the general direction of water movement is downwards, it also includes a horizontal flow component. Under high infiltration events, an increase in the vertical flow component may result in an increase in the magnitude of the horizontal component as well, increasing the collection area (or footprint) of a given flow pathway. It is also possible that flow with a considerable horizontal component can occur due to structural differences such as obstacles (i.e., a large boulder) or interbedded fine- and coarse-grained layers. These interbedded layers are typically a result of the way in which the waste rock material was placed (i.e., end-dumped), and create/facilitate capillary barriers and/or transport pathways (Chapter 1). When infiltrating water exhibits a relatively significant horizontal flow component, it can lead to a situation where the outflow of a given collection area

is greater than the expected outflow based on the precipitation flux for the same area over the same time period (Neuner, 2009). This suggests evidence of behaviour that is referred to as non-vertical flow. There is evidence of this type of flow in the test pile hydrology, particularly under relatively large precipitation events.

Flow to sub-lysimeter C reports infiltration fluxes that exceed the daily precipitation flux at several points during Mar-2007, whereas basal lysimeter D is consistently below the precipitation flux (Figure 3.10b). During the following wet season, basal lysimeter D continues to remain below the precipitation flux, and sub-lysimeter C only exceeds the precipitation flux under heavy sustained precipitation periods centered on 16-Jan and 27-Feb-2008 (Figure 3.10c). For example, on 16-Jan-2008, the net infiltration flux at C is 27 mm/day, while basal lysimeter D approaches almost 9 mm/day. Precipitation is near 10 mm/day. No daily precipitation is available for the 27-Feb event (Section 3.1), but it is likely that the flow to sub-lysimeter C also exceeds the precipitation flux on this day as well based on the nature of the response of sub-lysimeter C.

That the daily infiltration flux at sub-lysimeter C exceeds the daily precipitation flux at select times indicates that water may be focused to certain locations of the pile and non-vertical flow mechanisms may be active within the pile under high precipitation events. While there is a possibility that that these large peaks may be overestimations of the actual flow based on the way in which the flow data is interpolated (Appendix E), this analysis assumes that these large peaks are representative of pile outflow.

3.3.8 Difficulty Identifying Different Flow Pathways and Multiple Arrivals

Nichol et al. (2005) found that several spatially distinct flow paths were identifiable in the outflow data from a 5 m-high waste rock pile at the Cluff Lake mine (Chapter 1). The different flow paths were described as occurring due to spatial heterogeneity, non-capillary flow, saturation or presence of boulders. While it is most probable that multiple flow paths are present in the Antamina test pile, they could not be resolved in the outflow hydrographs (even at higher resolution e.g., shorter time intervals). This may be due to the data interpolation and filtering

(smoothing) schemes in which the data is processed and the way in which it is presented (Appendix E).

Another possible explanation (though unlikely) is due to the lysimeter design. Outflow that reports to the 36 x 36 m basal lysimeter or one of the three 4 x 4 m sub-lysimeters likely consists of water originating from various matrix and (possibly) macropore flow paths. Matrix flow is generally more uniform and diffuse compared to the sporadic, more rapid, smaller-scale pulses of water associated with macropore flow. Due to a large collection area of the lysimeters, outflow can be conceptualized as spatially averaging the different matrix and macropore (if activated) flow pathways. That various flow pathways cannot be distinguished may also be due to the fact that a 1.5 m-thick waste rock protective layer (slightly compacted by heavy machinery during placement) may have dissipated the macropore slug making it harder to resolve in the lysimeter data.

3.3.9 Uncertainty

It has already been explained that a large range of error is associated with the outflow data due to a considerable amount of missed tips in the tipping bucket data (Section 3.3.1; Appendix E). However, there is another level of uncertainty that results in less reliable data at higher flow rates. This primarily applies to the recording system that measures outflow from sub-lysimeter C, which does not function optimally under very high flow rates (Appendix E). Based on a 3-second scanning resolution, the datalogger reports each tip in 3-second intervals, regardless of when the tip occurs. Based on tipping bucket design (funnel aperture, chamber capacity; Appendix E) it is nearly impossible for two tips to occur within one 3-second interval. Nevertheless, when plotted on a 'tip-time vs. time' graph, this creates contiguous, coarse resolution flow data under high flow rates. In reality, the tips do not occur at three second intervals, yet it is nearly impossible to determine at what point within a given interval the tip actually occurred. (Note, this scanning resolution interval has subsequently been changed to 0.125 seconds).

In probability and statistics, the *continuous uniform distribution* is a family of probability distributions that describes a statistical situation in which it is equally probable to have a tip at any time within a given interval. Applied to the tipping bucket data, it states that there is an equal

probability that a tip will occur at any point in the 3-second interval. For a random variable such as a tip, the expected value m is calculated as:

$$m = \frac{a+b}{2} \quad [3-5]$$

where the minimum and maximum interval bounds are a and b respectively. When applied to the tipping bucket data, a is always 0 seconds and b is always 3 seconds, resulting in an expected value of $m = 1.5$ seconds. Therefore, flow data is corrected by adding 1.5 seconds to each interpolated tip-time (interpolated time between consecutive tipping bucket tips) before it is converted to a flow rate (Appendix E). Since this data represents an average between the minimum and maximum bounds, it is referred to as the ‘expected’ flow data. It is possible that the tip-time did not always occur midway between a and b , so the minimum and maximum flow rates are used to represent the lower and upper flow rate bounds. The interpolated data represents the lower bound of a given interval (i.e., $a = 0$) and the upper bound (estimated maximum) flow rate (recall that, in general, there is an inverse relationship between tip-time and flow rate; Appendix E). Conversely, the upper bound of a given interval (i.e., $b = 3$) requires that 3 seconds is added to each tip-time and represents the lower bound (estimated minimum) flow rate. All of the results previously presented in this chapter were based on the ‘expected’ flow dataset. A summary of the expected, upper and lower bound estimates at each lysimeter is presented in Table 3.3.

Due to the nature of the calibration equation (Appendix E), the upper and lower bound flow rates (a and b in Equation 3-5) diverge during higher flow rates and converge during lower flow rates, effectively illustrating that there is a larger error bound at very high flow rates. Departure from the expected value is asymmetric due to the nature of the calibration equation, with the upper bound exhibiting a larger departure from the expected value than the lower bound. Figure 3.11 illustrates how the error bounds relate to the expected volumetric flow data for basal lysimeter D and sub-lysimeter C. Note that sub-lysimeter C has a much higher range in values at the highest observed flow rates (i.e., upper bound is twice the value of lower bound flow rate), indicating the lowest reliability for this tipping bucket data under very high flow rates (Figure 3.11b). To note, this means that despite assuming a uniform probability of a tip falling within a given 3-second

interval, the resulting flow rate will not exhibit a uniform distribution based on the non-linear nature of the calibration equation (Appendix E). Even still, the flow pattern does not change dramatically between the upper and lower bounds.

Based on the entire study period, the cumulative upper and lower bound estimates for basal lysimeter D are 3.3 and 3.0 % higher and lower than the expected flow, respectively. The upper and lower estimates for sub-lysimeters A and B do not vary by more than 1 %, whereas the lower bound sub-lysimeter C estimate is 7 % less than the expected flow, and the upper bound is 10 % higher. This indicates that flow rates at sub-lysimeter C are mostly affected by the coarse scanning resolution of 3 seconds. These error bounds are not as large as those presented based on the data interpolation scheme ($\pm 20 - 35$ %; Section 3.3.1), and will not be discussed further.

3.4 MOISTURE CONTENT

The change in moisture content of an unsaturated porous medium provides insight into the flow behaviour and storage capacity of that medium. Time Domain Reflectometry (TDR) probes were therefore installed to characterize the moisture regime of test pile 1.

3.4.1 Time Domain Reflectometry Data

Twenty-two TDR probes were installed inside the pile to provide continual moisture content data (Corzaao Gallegos, 2007). Each probe is connected to a Moisture Point MP-917 TDR instrument (www.esica.com) located within the instrumentation hut. When instructed, the MP-917 box directs a pulse to a single TDR probe, calculates the travel time difference, and then outputs the result to the datalogger. An incorrect setting in the TDR instrument resulted in unrecoverable TDR data from the first day of the study period until 8-May-2008 (the beginning of the 2008 dry season), when the wrong setting was corrected (Appendix F).

Since the study period for this investigation extends until 30-Sept-2008, this means that the available TDR data during this 145-day period only occurs during the 2008 dry season. During this time, TDR data indicates that the pile is draining water but does not show any considerable responses to precipitation because no significant rain events occur during this period. Therefore, for the purpose of examining the moisture content regime of the pile, the study period is

extended to include TDR data from 1-Oct-2008 through 22-Jan-2009, as this is sufficient to observe the re-wetting of the pile (i.e., as it achieves the ‘wet season wet-up’ state) during the beginning of the 2008-9 wet season. Approximately 585 mm (760 m³ water) of precipitation and 225 mm (292 m³) of outflow from the basal lysimeter are calculated during this additional period (based on similar methodology used for the previous data). Raw TDR data (travel time offset in nanoseconds) is calibrated to m³/m³ (volume of water/bulk volume), but is generally presented as a volumetric water content percentage (% VWC).

3.4.2 TDR Probe Response

Two TDR probes are located in instrumentation lines 5 and 6 near the base, approximately 10 m below the surface (Appendix A). The remaining twenty are located in 4 near-vertical instrumentation lines (5 probes in each) at average depth intervals of 1.75 m below the surface (Appendix A). These probes are used to track a wetting front of moisture content as it penetrates to depth. The wetting front is estimated based on the time between the peak precipitation and the peak increase in moisture content (measured as the average between the upper and lower moisture content inflection points associated with that wetting front signal). TDR data is used to corroborate observations that were previously discussed in this chapter.

3.4.2.1 Protective Layer

Two TDR probes were installed within the 2B-Protective Layer of the pile base in instrumentation lines 5 and 6 (Appendix A). It was decided to place these probes in the 2B material to determine the moisture variability of the 2B-Protective Layer to gain a better understanding of the effect of the protective layer on the flow in the pile and chemistry. On physical grounds, it would be expected that the 2B-Protective Layer largely remains saturated because the drainage system is 0.35 m above this 2B-Protective Layer and water has no place to exit from.

The TDR probe in line 5 consistently exhibits a high moisture content $\theta = 45$ % VWC that does not vary throughout the study period, possibly indicating that:

1. the probe is not functioning properly,

2. the calibration does not work well for the 2B crushed material, or
3. the 2B-Protective Layer is saturated.

Since this is the lowest probe in the pile, it may possibly indicate that the 2B-Protective Layer is saturated and the probe is below a water table. A VWC of 45 % is higher than expected, but falls within the calculated porosity range of $n = 0.4 \pm 0.1$ for test pile 1 waste rock (Chapter 2). No porosity is known for the 2B-Protective Layer. While it is possible that this probe is located below the water table (if one is present), no conclusions can be confirmed until more data is obtained and a soil-specific TDR calibration equation is obtained for the test pile waste rock (Appendix F) and possibly the 2B-Protective Layer.

The line 6 TDR probe shows more of a seasonal response, with $\theta = 25$ % VWC in October and begins to increase shortly after in response to precipitation inputs until a maximum of $\theta = 31$ % VWC is attained on 22-Jan-2009. That water content of this probe is variable likely indicates that it is above the water table (if one is present).

3.4.2.2 Compacted Surface

The shallowest TDR probes in the pile (i.e., the highest TDR in lines 1 - 4) are located 1.6 – 2.4 m below the surface (Appendix A). The VWC for these shallow probes ranges between 11 - 30 % VWC, with the lowest values (11 – 18 % VWC) in September/October and the highest values (18 – 30 % VWC) in January/February (Figure 3.12).

Consecutive days of precipitation that are characteristic of the wet season begin in the second week of Sept-2008, yet these probes do not register a moisture content increase until 9-Oct, nearly 5 weeks after the rains begin. At this point, moisture content begins to increase relatively rapidly over the next few days in response to 30 mm of precipitation that falls over the course of 4 days (Figure 3.12). In order for these responses to occur, they need:

1. a sufficient volume of infiltrating water is required prior to these responses, and

2. a significant precipitation event (or consecutive events) to trigger a sharp response in moisture content. Without these event(s), infiltrating water from prior events will not likely result in a sharp increase in moisture content.

The highest probe in line 4 (L4TDR5) responds much earlier because it is under the batter (explained in the following section). That these TDR probes do not show any responses until 5 weeks after the heavy precipitation events began indicates that:

1. the permeability of this material is relatively low compared to the rest of the pile, particularly compared to the batters (Figure 3.8),
2. the rain water is initially taken up by matric forces to replenish the moisture content, which influences the rate at which the wetting front can propagate (Section 3.3.6),
3. matrix flow is dominant here,
4. water may be by-passing the TDR instruments, and/or
5. only a large rain event (> 10 mm/day) will lead to identifiable short-term changes in moisture content.

It has already been discussed that this material is relatively fine (due to preferential settling during the end-dumping process) and compacted (due to the heavy dump truck traffic during pile construction) compared to the rest of the pile. TDR data supports these observations and indicates that this material has a relatively low permeability compared to the pile batters (Chapter 2). In addition, that the shallow probes from instrumentation lines 1, 2 and 3 all indicate rather sharp rises in moisture content at around the same time indicates that the wetting front moves relatively uniformly through the upper 1.6 – 2.4 m of the pile, with an average wetting front velocity v_{wf} of 0.06 m/day (7×10^{-7} m/s). Recall that results of the infiltrometer (Chapter 2) demonstrate that the average hydraulic conductivity of this material is 2.3 m/day (3×10^{-5} m/s). That these two rates differ by almost two orders of magnitude is due to the differences in methodology and the fact that they are both at different points of the ‘hydraulic conductivity – moisture content’ characteristic curve. For instance, the infiltrometer test was conducted in March, more than halfway into the wet season, and the material is likely the wettest it is throughout the entire year. Conversely, the TDR wetting front velocities are calculated based on

data from September/October, which is the beginning of the wet season when the material is relatively dry and some of the infiltrating water is taken up by matric forces.

It is also likely that no large moisture content changes are evident in the first 5 weeks of precipitation because no large precipitation events (> 10 mm) occur. Some moisture contents do respond a few days after a large precipitation event of 12 mm occurs on 7-Oct-2008.

3.4.2.3 Batter

Instrumentation line 4 is located at the front of the pile, under the pile batter (Appendix A). Since each of these four TDR probes (the fifth does not function) are approximately 1 - 2 m below the surface, they are also 'shallow' probes. However, these probes differ from the probes at the top of the pile (above) because the batter consists of much coarser material than the top of the pile (Figure 3.8). Due to these differences in material, moisture contents are very different under the batter.

Line 4 experiences the largest variation in moisture content, which varies between 13 and 35 % VWC (Figure 3.13). TDR probes under the batter report clear and distinct responses to a 10 mm-precipitation event on 9-Sept, which is preceded by 3 days in which 10 mm fell. These probes responded almost one month prior to responses under the top layer. This corresponds to wetting front velocities as high as $v_{wf} = 0.5$ m/day, which is one order of magnitude higher than calculated for the upper compacted layer. This wetting front velocity is similar to those calculated at two other waste rock test piles in which Marcoline (2008) and Neuner (2009) report the wetting front velocity to range between $v_{wf} = 0.1$ and 1 m/day, and $v_{wf} = 0.1 - 5$ m/day, respectively, using similar TDR probes.

TDR probes near the bottom of line 4 (L4TDR1 and L4TDR2 in Figure 3.13) show an increase from 13 % VWC near the end of the dry season (1-Sept-2008) to 36 % VWC during the wet season (19-Jan-2009). TDR probes near the top of line 4 (L4TDR4 and L4TDR5; L4TDR3 does not function) increase from 18 to 30 % VWC over the same period. All four probes show rapid responses to intermediate- and large-precipitation events, with the highest volumetric water change of nearly 3 % observed over the course of one day. Nearly six weeks later, these probes

reach maximum moisture contents, and remain near these levels for the remainder of the period (Figure 3.13). That L4TDR1 and L4TDR2 moisture contents differ from each other by almost 8 % throughout the period whereas L4TDR4 and L4TDR5 probes exhibit very similar responses likely indicates the heterogeneous nature of the waste rock pile.

3.4.2.4 TDR Variability

TDR results are generally similar to Nichol (2002); Nichol et al. (2003), Marcoline (2008) and Neuner (2009), all of which report highly heterogeneous flow through waste rock and higher wetting front velocities than fluid velocities. Results show that, in general, the deepest probes encounter the highest sustained water contents compared to the shallowest probes under the top layer of the pile, which typically report the driest values and experience the largest range in moisture contents. Deeper probes also respond several weeks after the onset of the wet season, whereas probes under the unconsolidated batter respond only a few days after the onset of the wet season. These observations are generally consistent with Nichol (2002) who reports that water content changes from TDR probes near the surface are generally larger (of a 5 m-high waste rock pile at the Cluff Lake mine) in comparison to deeper probes where water content changes in response to the largest rainfall events are less. That some shallow probes report higher moisture contents than deeper probes at test pile 1 is likely a result of:

1. material heterogeneity surrounding each probe,
2. by-passing of water around TDR probes, and/or
3. preferential and/or non-vertical flow.

Based on a moisture content range between 11 and 36 % VWC, the residual saturation can be expected to be around 11 % VWC. The average moisture content measured during the particle size distribution was 3 %. Although the TDR probes measure the water content of the matrix and not the entire range of particle sizes, these moisture content differences indicate that the waste rock moisture content was below residual saturation during pile construction and explains why there was an initial delay in wetting-up during the 2006-7 wet season (Section 3.3.6).

3.4.3 Wetting Front Propagation and Evidence of Preferential or Non-Vertical Flow

An example of the wetting front propagation to depth is illustrated using line 1 TDR responses (Figure 3.14). The shallowest TDR probe (L1TDR5) is 2.4 m below the surface, and shows a rapid increase in moisture content on 9-Oct that is likely triggered by a 21 mm-precipitation event on 6- and 7-Oct. Over the course of a few days, the moisture content experiences a steady increase of 10 % VWC from 17 % to almost 27 % VWC. Nearly twenty days later, the closest functioning probe (L1TDR3) at a depth of 5.8 m below the surface, begins to respond. Shortly after, the next closest probe at a depth of 7.3 m (L1TDR2) begins to respond to increasing moisture content, followed by the deepest probe (L1TDR1) at a depth of 9.3 m during the second week of November. That the moisture contents increases in order with depth to surface effectively illustrates the wetting front as it propagates to depth during October and November of the 2008-09 wet season.

While TDR probes may not report macropore flow, it is still possible for them to report preferential and/or non-vertical flowpaths in the matrix. Another example of wetting front propagation to depth that provides evidence of preferential flow is illustrated using line 2 TDR responses (Figure 3.15). The shallowest TDR probe (L2TDR5) is located 1.6 m below the surface, and shows a rapid increase in moisture content on 10-Oct that is likely triggered by 21 mm of precipitation during 6- and 7-Oct. Nearly three weeks later on 1-Nov, both L2TDR4 (3.2 m depth) and L2TDR1 (7.9 m depth) moisture contents begin to increase. Since L2TDR1 moisture content increases before the two probes above it at depths of 4.9 (L2TDR3) and 6.5 m (L2TDR2), this provides evidence of preferential or non-vertical flow. It is likely that the heavy precipitation during the week prior to this increase in moisture content activates some macropores or other flow paths that channel water to depth while by-passing the middle TDR probes. This is supported by Smith and Beckie (2003) who report that because TDR probes are installed in a fine-grained matrix, they may not be able to indicate the presence of preferential flow through large macropores.

The presence of wetting fronts in response to high-precipitation events are more evident near the onset of the wet season when the pile is relatively dry compared to towards the end of the wet season when the pile is relatively wet. This indicates that:

1. antecedent soil moisture condition influences the wetting front propagation time,
2. TDR probes are of limited use in tracking fluid flow in wet waste rock, and/or
3. TDR probes preferentially sample from the matrix material in which they are installed and do not likely measure the macropore flow that by-passes the matrix regions.

3.4.4 Change in Storage

Based on observations of a 5 m-high waste rock test pile at Cluff Lake, Nichol (2002) and Marcoline (2008) observed that test pile moisture content returns to similar levels over the course of one water year, and that it can be assumed that there is no net change in storage ($\Delta S \sim 0$) over that time period. No Antamina test pile TDR data yet is available over the course of one water year, so the actual change in storage ΔS could not be determined. However, due to very similar recession curves of the basal lysimeter D hydrograph and a return to minimum flow rates of nearly $0.1 \text{ m}^3/\text{day}$ at the end of both the 2007 and 2008 dry seasons (Figure 3.9d), it is assumed that the pile returns to similar moisture conditions after one water year (i.e., returns to a dynamic equilibrium steady state) and that $\Delta S \sim 0$ over the course of one water year that fully encompasses a wet and a dry season (1-Oct to 30-Sept).

Without moisture data throughout the entire water year, the maximum and minimum water storage limits are estimated based on the 7.5 month-long data in which the TDR data is examined (May-2008 to Jan-2009). The following calculations are only included to provide a relative idea of the potential change in water content of the pile, and should not be considered absolute. Large uncertainty is expected, and is discussed after the calculations are presented.

Based on the available data, the pile is assumed to be at its driest point on 1-Sept-2008 and the wettest on 11-Jan-2009. For the purpose of water balance calculations, the pile volume is conceptually divided into individual discrete volumes, each one centered around a single TDR probe. Average wet and dry volumetric water contents are applied to each volume to obtain a representative water content of the entire pile during the two representative periods. TDR probes in line 1 and 2 are used to provide internal pile moisture contents whereas probes in line 4 are used to provide representative moisture contents along the front batter as well as the north- and

south-facing batters. Instrumentation lines 3, 5 and 6 are omitted for simplicity. When no TDR data is available (e.g., L1TDR4 and L4TDR3 do not function) linear approximations are made using nearby probes. Average moisture contents of $\theta_d = 18\%$ and $\theta_w = 25\%$ are estimated on the driest and wettest days, respectively, and result in an estimated change of storage of $S = 850\text{ m}^3$. This corresponds to an estimated change in storage of 8.5 % of the entire pile volume ($10,000\text{ m}^3$) over the entire 7.5 month period of study.

It should be reiterated that these calculations are only meant to present the relative differences in moisture content between wet and dry periods, and should not be used as any absolute values until further data is obtained. One of the principal flaws with these calculations is that the TDR data is assumed to represent moisture content of the entire pile when it is already discussed (above) that TDR data only measures the moisture content of the matrix. The presence of boulders and large voids leads to lower moisture contents for the entire pile than that of the matrix (see porosity calculations, Chapter 2). To account for the large boulders, Neuner (2009) multiplied the TDR moisture content by the proportion of fine-grained material to estimate the large-scale moisture content of the entire pile. While this is not relevant for calculating change in storage, it is useful in calculating flow velocities.

3.5 DISCUSSION

3.5.1 Water Balance

Water balance calculations are conducted over the course of one water balance year and include one complete wet and dry season (Table 3.2). The water year extends from 1-Oct-2007 to 30-Sept-2008 as explained in Section 3.2.2. Evaporation estimates from waste rock piles are highly complex and can vary considerably depending on the methodology applied. Nevertheless, there is relative agreement when the error ranges are incorporated.

Test pile 1 discharge Q represents 41 % of estimated precipitation P over one water year, which is slightly higher than the discharge observed at a similar investigation ($Q = 44 - 55\% P$ over three consecutive water years) conducted on a 5 m-high uncovered waste rock pile at the Cluff Lake mine in northern Saskatoon, Canada (Marcoline, 2008). At this waste rock test pile site, the

M.A.T is $-0.3\text{ }^{\circ}\text{C}$, with the average daily temperature greater than $0\text{ }^{\circ}\text{C}$ for 5 months of the year. Average annual precipitation (including snow) is 460 mm. Even though the climate of the Cluff Lake mine is very different from that of the Antamina mine, that the percentage of evaporation and outflow is relatively similar indicates that behaviour at test pile 1 is relatively typical of a waste rock test pile.

Based on the available data, the maximum estimated change in storage is calculated over a 4.5 month period (and not the preferred water year). Given the large error estimate attributed to the flow data, the storage value of $S = 850 \pm 298\text{ m}^3$ roughly corresponds to the total volume of water estimated to have discharged from the base of the pile $Q = 670 \pm 235\text{ m}^3$. This is conceptually easy to understand. According to the steady state constraint over the water year, any water that is added to storage must eventually be removed to comply with $\Delta S = 0$. This means that over the course of the water year, ΔS should theoretically be equal to Q (longer-term trends may vary). That there is relatively good agreement between these two figures provides strong support that:

1. the instrumentation (tipping bucket, precipitation, moisture content) is functioning properly,
2. the data was accurately calibrated/interpolated/analyzed, etc.,
3. the assumptions made throughout this chapter are reasonable, and
4. there is no leak in the lysimeter catchment system.

3.5.2 Pore Water Displacement and Macropore Flow Velocity

Smith and Beckie (2003) report that outflow responses in test piles are typically observed prior to TDR responses, indicating that the maximum pore water fluid velocity (i.e., through macropores) generally exceeds the wetting front velocity recorded by the TDR probes. TDR responses are typically slower than lysimeter outflow peak discharges and indicate that the spatially distinct preferential flow paths at high flow rates do not correspond to the majority of TDR probe locations (Nichol, 2002). Marcoline (2008) further states that the outflow flux is the best estimate of pore water velocity while TDR probes represent biased velocity ranges based on the fact that they preferentially sample from only the matrix and are not representative of the

overall pile behaviour. Similar results are observed in the Antamina test pile data, but only once the pile has sufficiently attained the ‘wet season wet-up’ state. Otherwise moisture contents near the top of the pile increase from days to weeks before outflow fluxes begin to increase after a considerably dry period (i.e., start of the wet season).

The pore water velocity v_{pw} [m/s] in an unsaturated porous medium is related to the pore water flux q [m/s] and water content Θ [m³/m³] in the following equation (presented in Chapter 2):

$$v = q / \Theta \quad [3-6]$$

The highest flux of water calculated for basal lysimeter D is $q = 12$ mm/day ($Q = 14.7$ m³/day). Based on the average ‘wet season’ moisture content of the test pile ($\Theta = 25$ % VWC), the pore water velocity is calculated using equation 3-6 to be $v_{pw} = 0.05$ m/day. Conversely, the lowest basal lysimeter flux is $q = 0.088$ mm/day ($Q = 0.11$ m³/day), and corresponds to $v_{pw} = 5 \times 10^{-4}$ m/day at the ‘dry season’ water content of $\Theta = 18$ % VWC. Calculated using moisture contents from the bottom of the pile (e.g., L1TDR1 and L2TDR1 (L4TDR1, L5TDR1 and L6TDR1 are excluded (see above) and L3TDR1 is not functioning properly)), the ‘wet season’ porewater velocity is $v_{pw} = 0.04$ m/day ($\Theta = 32$ % VWC) and the ‘dry season’ porewater velocity is $v_{pw} = 3 \times 10^{-4}$ m/day ($\Theta = 26$ % VWC).

Smith and Beckie (2003) state that wetting-front velocities three to four orders of magnitude faster than the median water velocity have been observed in waste rock piles. Comparing the maximum pore water velocity ($v_{pw} = 0.05$ m/day) with the maximum wetting front velocity ($v_{wf} = 0.5$ m/day) for test pile 1, the maximum wetting front velocity is 1 order of magnitude higher than the pore water velocity. This supports the previous statement that rapid outflow fluxes in response to a heavy precipitation event largely consist of pre-event pore water that is displaced through the matrix of the pile (Section 3.3.7.2). This displacement mechanism may be described as a kinematic or pressure wave that moves through the unsaturated profile much faster than the maximum pore water velocity (Rasmussen et al., 2000; Neuner, 2009).

The pressure wave mechanism consists of distinct, rapid increases in moisture that propagates to depth in an unsaturated zone in response to precipitation inputs (Neuner, 2009). These waves are analogous to a garden hose - in which opening the tap causes an almost instantaneous increase in outflow well before the water entering at the higher flow rate reaches the end of the hose - and typically displaces pore water when activated. In test pile 1, infiltrating water into the unsaturated zone will typically propagate downwards in the form of a wetting front, which is defined as the interface between the region of higher water content and fluid velocity, and the underlying region with lower water content and fluid velocity (Smith and Beckie, 2003). Using pressure tensiometers to track the pressure wave in response to precipitation events, Neuner (2009) explains that pressure waves are quite common in unsaturated flow conditions, even under relatively minor rainfall events. The pressure wave is dependent on moisture content and will propagate more effectively if the porous medium is fully saturated.

These pressure waves should not be confused with the rapid velocities associated with macropore flow. In the case of macropore-flow, the wetting front may contain particles that travel at the speed of the wave, but wetting fronts are more often in the form of pore water displaced by a propagating pressure wave that results from the presence of infiltrating water. Since Rasmussen et al. (2000) explain that pressure wave diffusivity increases with depth, this likely explains why more displacement is observed in basal lysimeter D and sub-lysimeter C, and that the pressure wave signal may have been largely dissipated by the time it penetrates the full 10 m of the pile (sub-lysimeters A and B).

Results indicate that macropore flow is likely activated under high intensity rainfall events and that flow from pressure-induced matrix water displacement is also likely occurring. A lack of moisture content data throughout the study period does not allow the moisture content to be examined during the high outflow events that were previously examined. In addition, without any pressure data (i.e., from tensiometers) the direct confirmation of pressure waves can only be inferred and cannot be further investigated in this study. Additional work is required to fully characterize flow through the unsaturated zone, as this will affect the evolution of water quality over time.

3.5.3 Effects of the Batter on Pile Hydrology

Results demonstrate that evaporation from, and infiltration into, the fine-grained, traffic-compacted top layer of the pile is very different from the coarse-grained, non-compacted batter. Water can pool on the top surface of the pile and be exposed to higher evaporation and lower infiltration rates, whereas higher infiltration rates can occur on the porous slope of the pile and lead to more net infiltration and less evaporation (recall no significant runoff has been observed at the pile). The compacted top surface of the pile represents only 21 % of the total surface area of the pile. This indicates that a majority of the surface area of the pile is dominated by the batter. However, evaporation from the batters may be further complicated because:

1. the sloping nature of the batters leads to a larger exposed area in which rain may fall, and may be less concentrated so infiltration may not be as high (assuming vertical rainfall),
2. there is a higher proportion of internal evaporation at the course, well-aerated batters as wind-driven advection is likely occurring, bringing fresh (i.e., less humid) air into the batters (particularly the front), and/or
3. it is difficult to obtain accurate evaporation estimates for both the unconsolidated batters and compacted top of pile (e.g., Carey et al., 2005).

It is for these reasons that the most reliable evaporation estimate is that from the water balance method, as it is based on empirical calculations that integrate both climatic and meteorological properties.

3.6 SUMMARY

Using the suite of available data from meteorological data and in-situ pile instrumentation, this chapter characterized the hydrological behaviour of test pile 1. A reasonable agreement between the water balance components is attained, indicating that the data analysis methodology was suitable for the purpose of this investigation. In addition, this chapter has shown that:

1. infiltration to test pile 1 is approximately 41 % of annual precipitation, and evaporation is 59 %,

2. flow is spatially and temporally variable, as evidenced by the basal and sub-lysimeter hydrographs,
3. the hydrological response of the pile is clearly dominated by the less consolidated batter compared to the less permeable top of the pile,
4. the average linear porewater velocity ranges from $v_{pw} = 0.2$ m/year in the dry season to $v_{pw} = 17$ m/year in the wet season,
5. the highest calculated wetting front velocity ($v_{wf} = 0.5$ m/day), is one order of magnitude higher than the porewater velocity ($v_{pw} = 0.05$ m/day),
6. evidence of preferential flow, macropore flow, non-vertical flow, and pressure-wave pistoning is prevalent in the data, and
7. average moisture contents at the end of the 2008 dry season are $\theta = 18$ % VWC.

TABLES

Table 3.1. Total estimated volume, weekly rate, and daily flux of precipitation and lysimeter outflow.

		Estimated Precipitation			Lysimeter Outflow											
		[m ³]	[m ³ /week]	[mm/day]	[m ³]				[m ³ /week]				[mm/day]			
					D	C	B	A	D	C	B	A	D	C	B	A
2006-7	Wet ¹	561	38.1	4.2	437	8	0.8	1.5	29.7	0.54	0.06	0.1	3.4	4.86	0.51	0.92
	Dry	209	9.6	1.1	95	1.1	0.1	0.4	4.3	0.05	0.006	0.02	0.49	0.44	0.05	0.18
2007-8 ²	Wet	1379	45.3	5.1	604	13.5	1.5	3.9	20	0.45	0.05	0.13	2.29	3.99	0.45	1.15
	Dry	303	13.9	1.4	67	0.8	0.2	0.5	3	0.03	0.01	0.02	0.35	0.31	0.09	0.21
Average Wet ³		749	41.7	4.6	38.1	10.7	1.2	2.7	24.8	0.5	0.05	0.12	2.84	4.42	0.48	1.04
Average Dry		197	11.7	1.3	9.6	0.9	0.2	0.5	3.7	0.04	0.008	0.02	0.42	0.37	0.07	0.19
Total		2452	27.6	21.2	1202	23.3	2.7	6.3	13.5	0.26	0.03	0.07	1.54	2.34	0.27	0.63

¹wet season data is not representative of complete wet period because the study period began on 18-Jan-2007

²this is the 2007-8 water year

³calculated over entire period

Table 3.2. Summary of evaporation estimates throughout the study period and water year.

	mm	m ³	% of Precipitation	% Error
Study Period (18-Jan-2007 to 30-Sept-2008)				
<i>P</i>	1891	2450	100	± 5
<i>E_{PAN}</i>	1423	1760	75	± 15
<i>E_{PM}</i>	1617	1890	86	± 20
<i>Q</i>	949	1230	50	± 20 – 45
<i>ΔS</i>	N/A	N/A	N/A	N/A
Water Year (1-Oct-2007 to 30-Sept-2008)				
<i>P</i>	1297	1681	100	± 5
<i>E_{PAN}</i>	887	1150	68	± 15
<i>E_{PM}</i>	972	1260	75	± 20
<i>E_{WB}</i>	766	990	59	± 25 – 50 ¹
<i>Q</i>	532	690	41	± 20 – 45
<i>ΔS</i>	~ 0	~ 0	~ 0	N/A

¹water balance estimate error combines precipitation and outflow errors.

Table 3.3. Cumulative interpreted flow for each lysimeter.

Volume of Water [m ³]								
Collection Area	Interpreted ¹			Manually Removed ²	Estimated Unrecorded ³	Total ⁴		
	Lower Bound	Expected	Upper Bound			Lower Bound	Expected	Upper Bound
A	3.86	3.91	3.97	0.005	2.47	6.34	6.39	6.45
B	2.55	2.58	2.60	0.026	0.19	2.77	2.79	2.82
C	19.05	20.74	23.15	0.022	2.6	21.68	23.36	25.77
D	1114	1148	1186	2.5	51	1167	1202	1239
Entire Pile	1139	1175	1216	2.6	56.3	1198	1234	1274

¹ resulting dataset from RANSAC interpretation

² equivalent volume of water of data points removed prior to correcting for missed tips due to maintenance, etc. (Appendix E)

³ estimated volume of water not recorded by the datalogger during periods in which site observations confirm lysimeter was flowing

⁴ sum of reported outflow, equivalent volume manually removed, and estimated unrecorded flow during gaps in lysimeter data

FIGURES

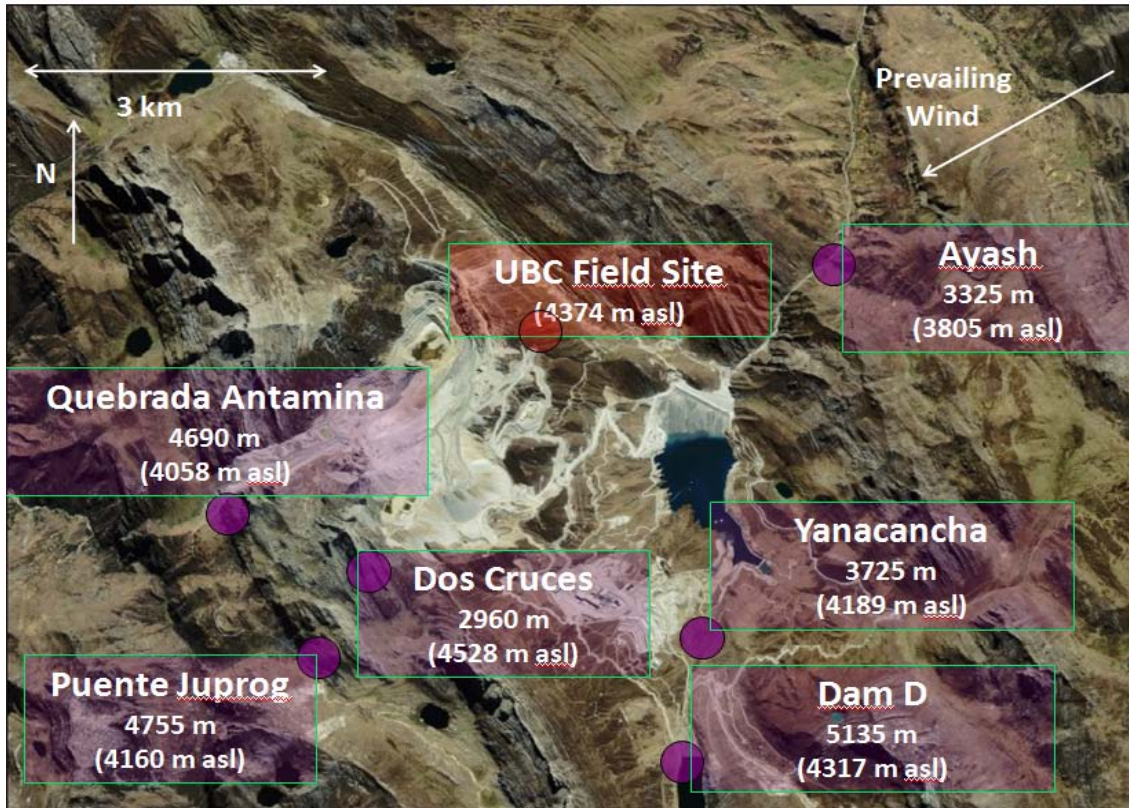
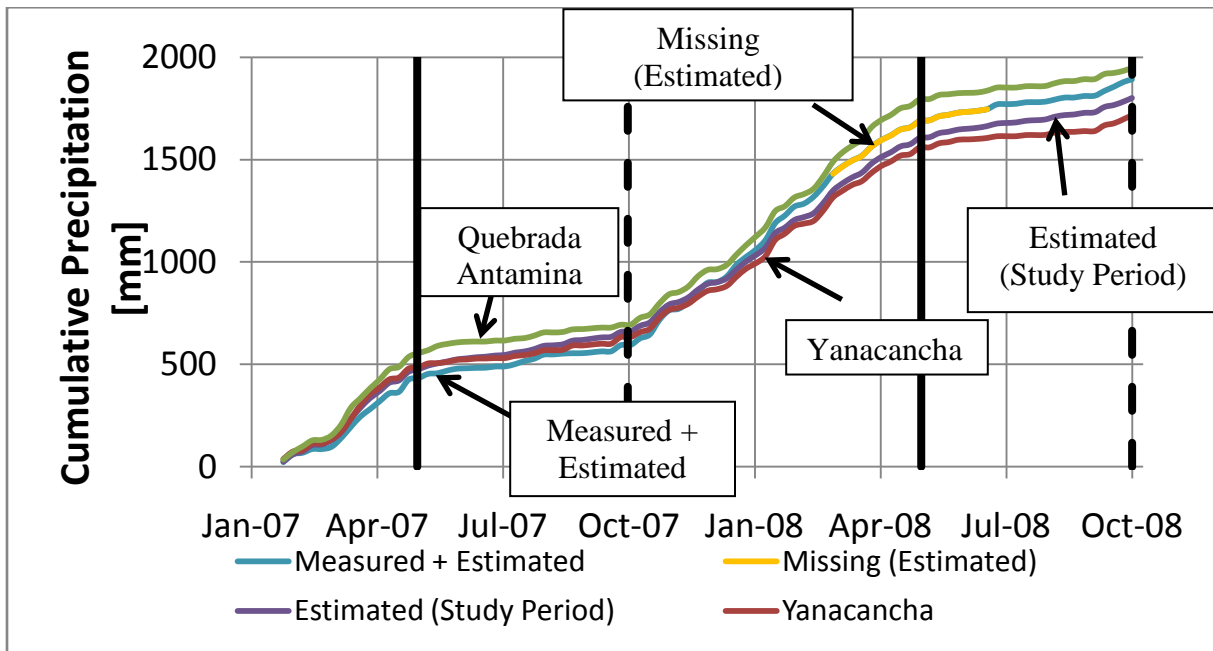


Figure 3.1. Antamina rain gauge locations with respect to the study site (elevation above sea level in brackets).



*black solid line = wet-dry season transition; black dotted line = dry-wet season transition

Figure 3.2. Reported and estimated cumulative rainfall compared to the Antamina precipitation.

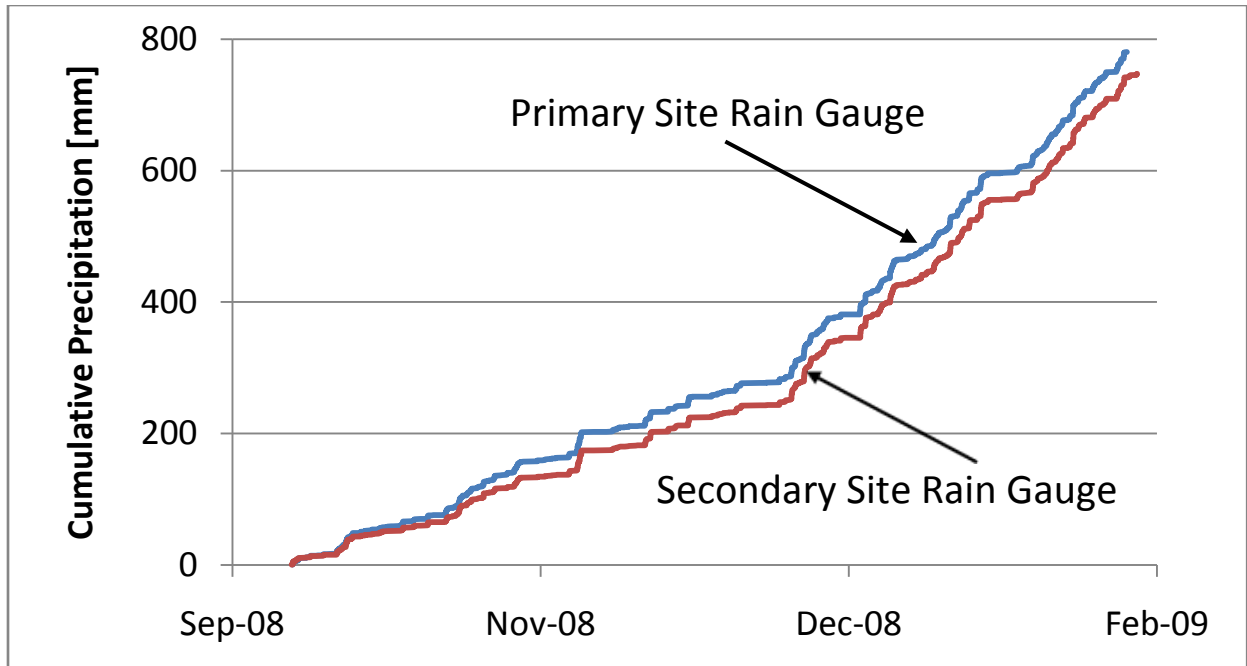


Figure 3.3. Rainfall comparison between the two site rain gauges.

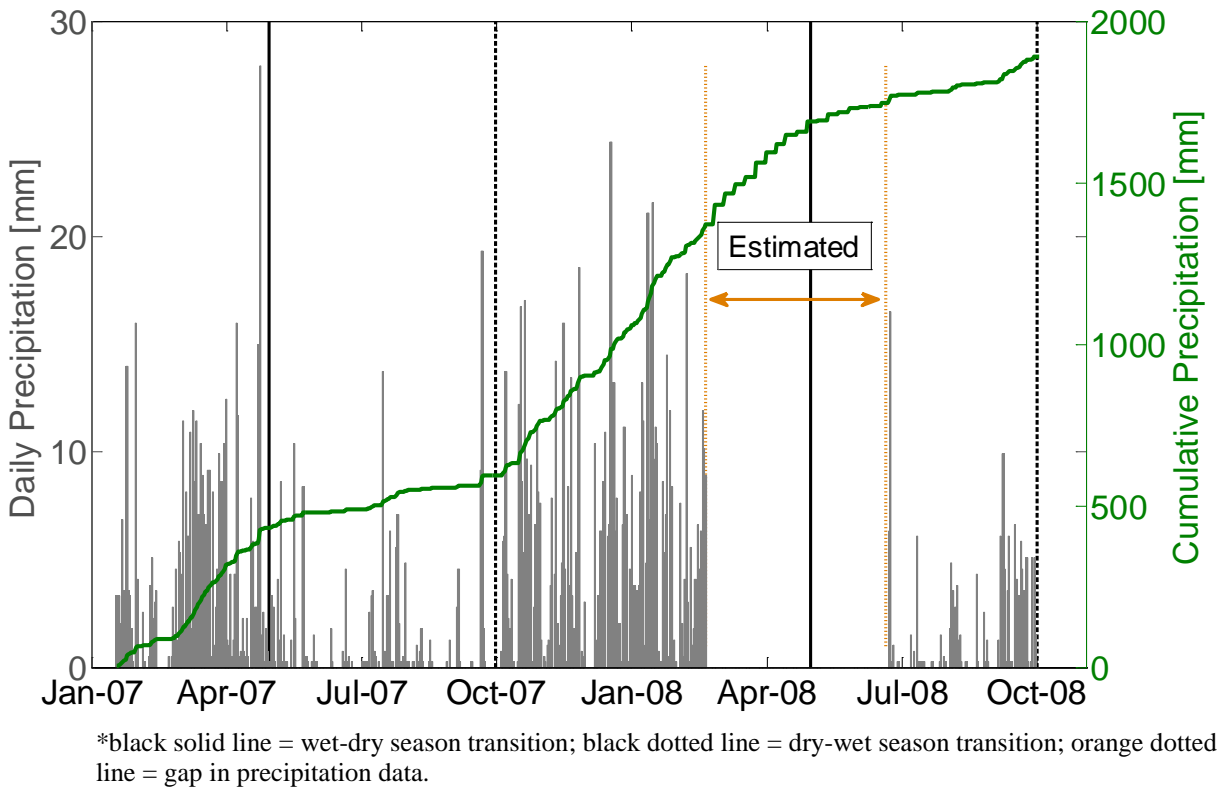


Figure 3.4. Daily and cumulative estimated precipitation.

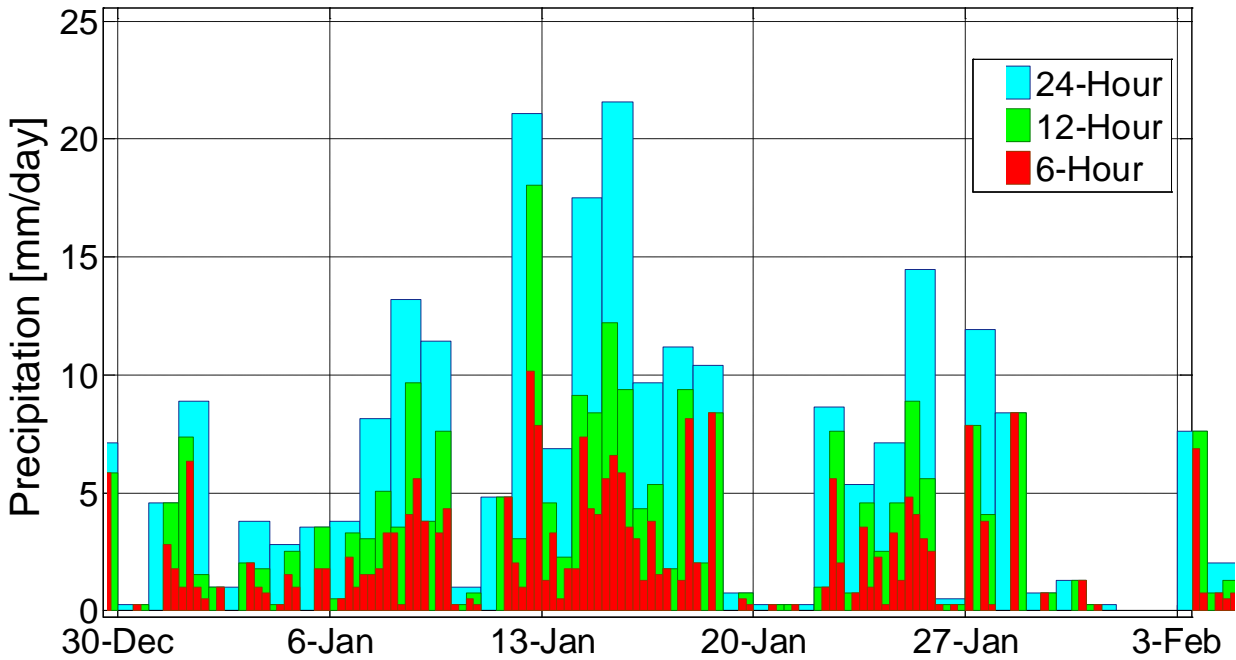


Figure 3.5. Variability of rain as measured by site rain gauge during Jan-2008

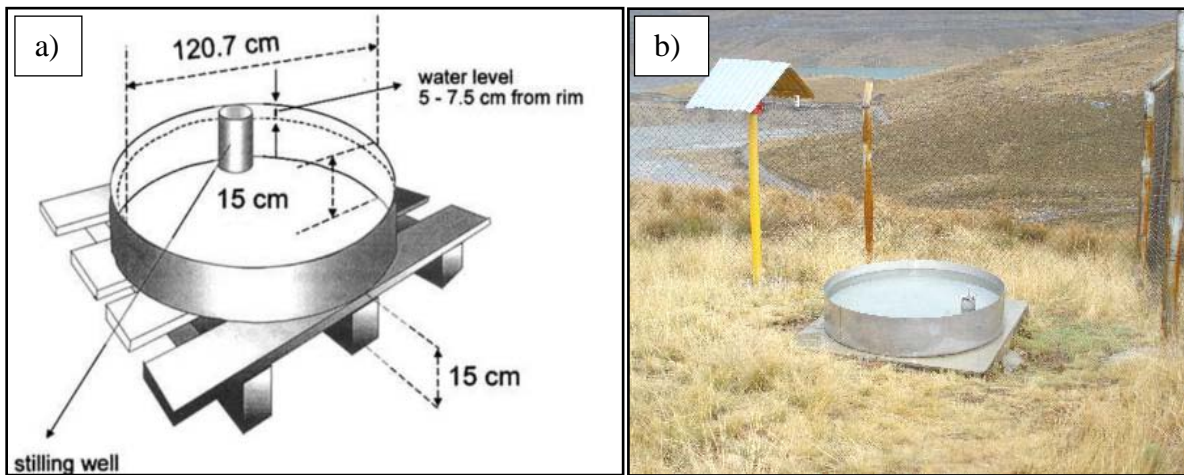


Figure 3.6. Class A Pan evaporation a) schematic and b) Yanacancha station, Antamina.

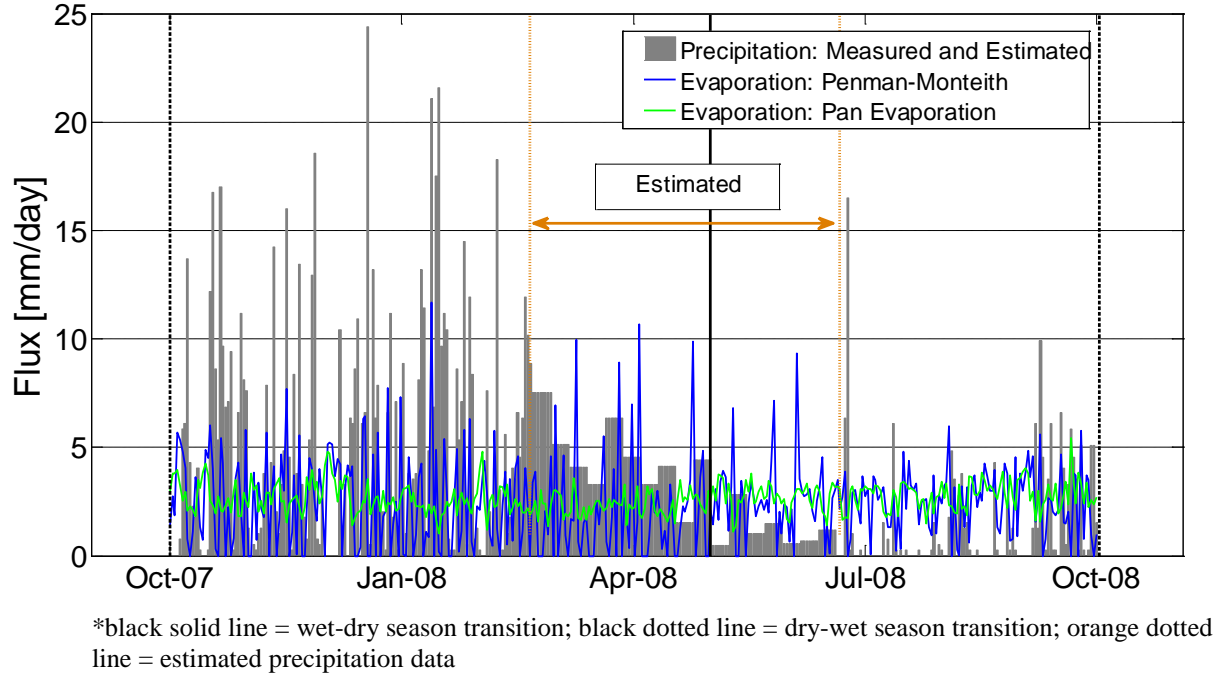


Figure 3.7. Daily precipitation (measured and estimated) and evaporation (Penman-Monteith and Pan Evaporation).

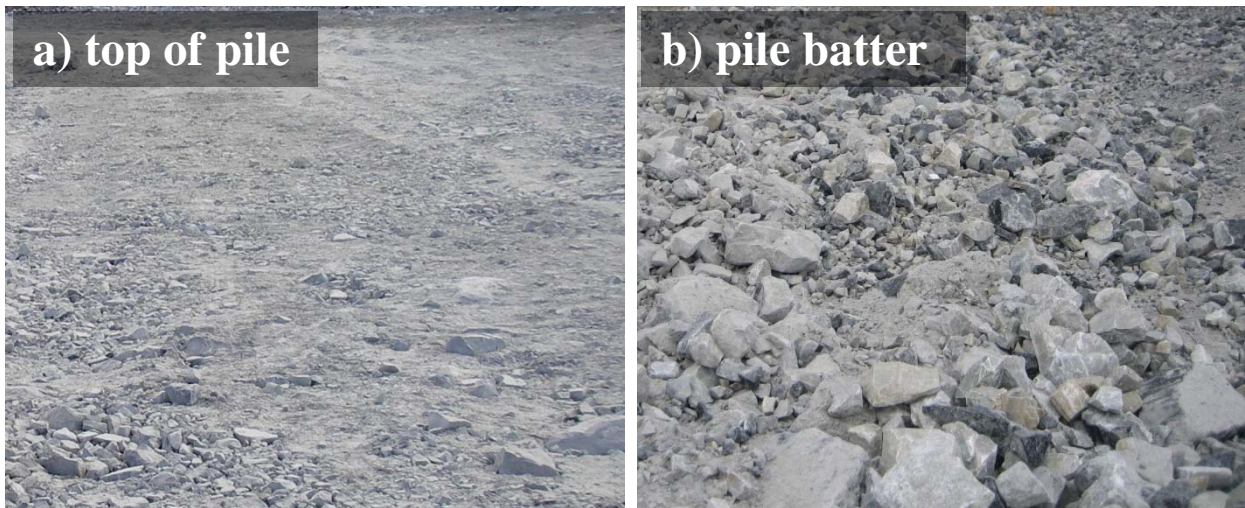
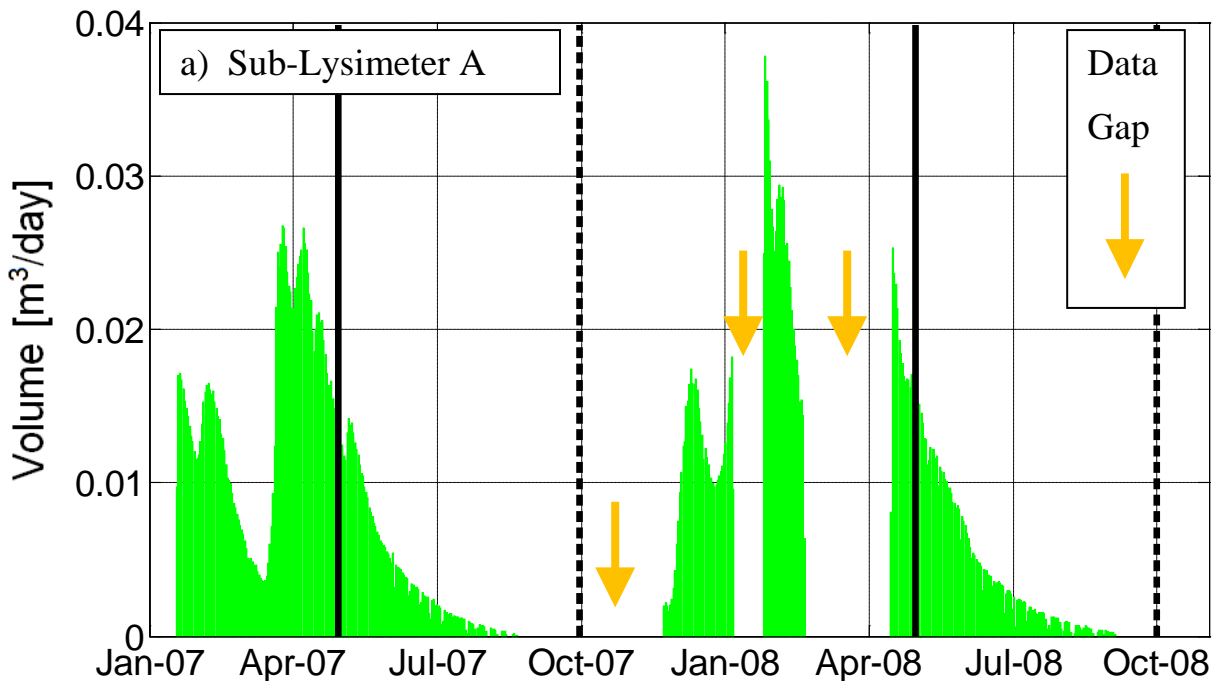
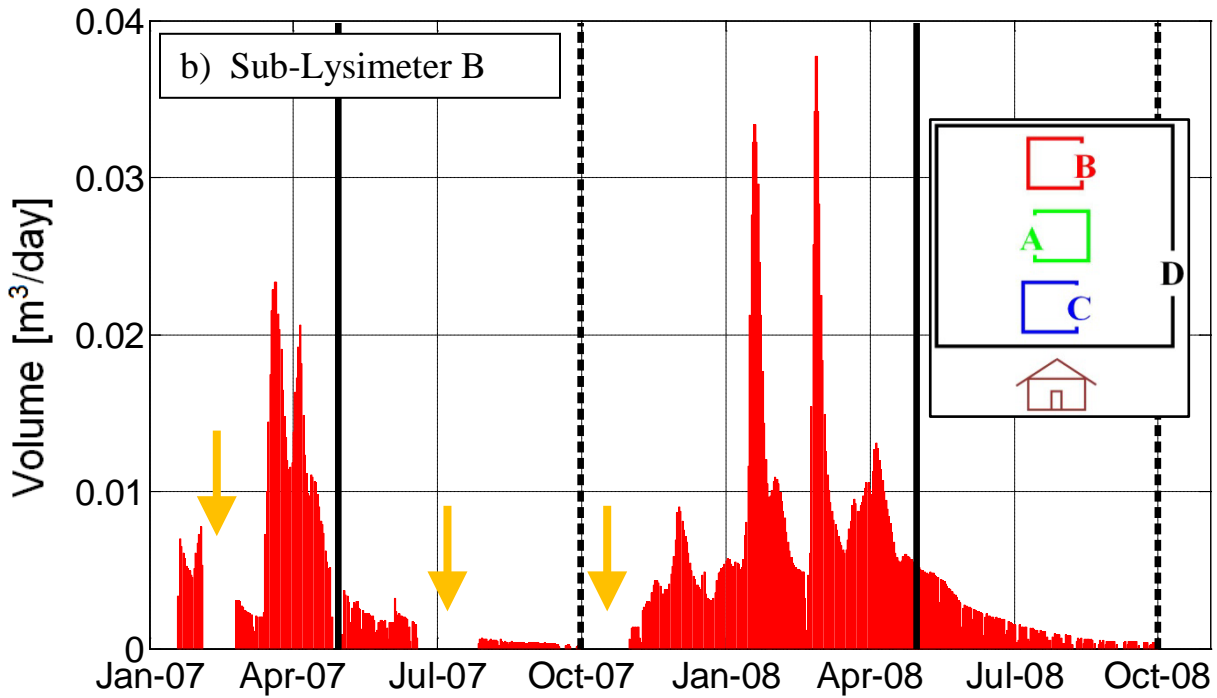


Figure 3.8. Comparison between a) top and b) batter of pile.

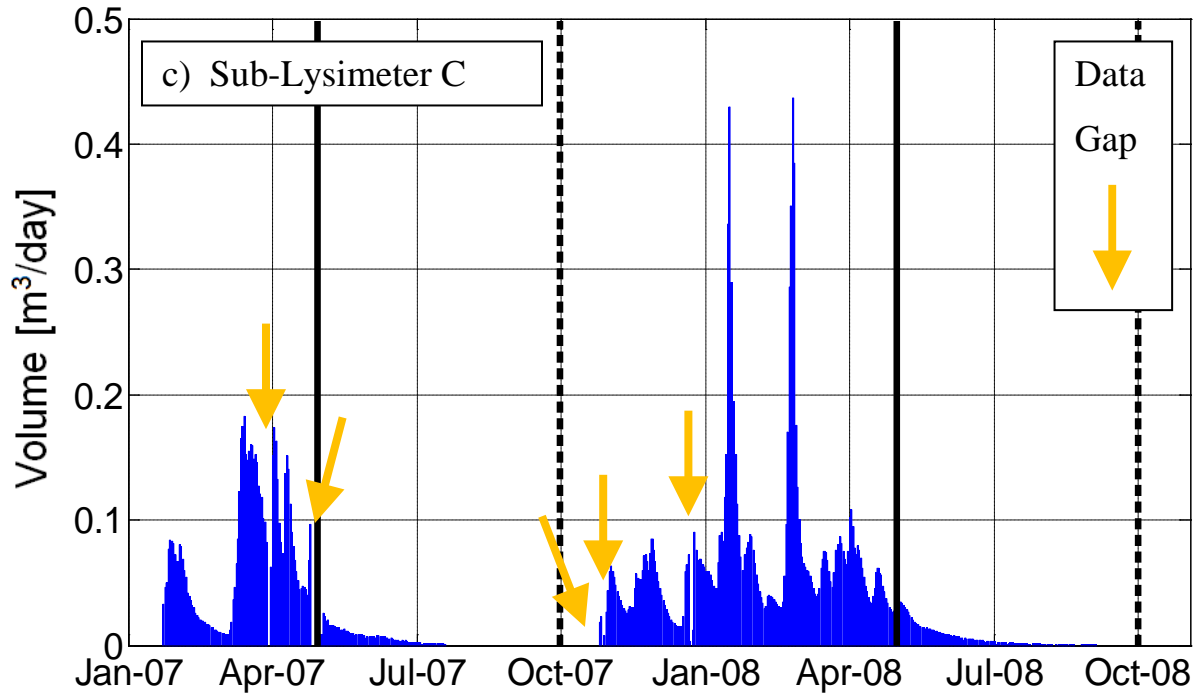


*black solid line = wet-dry season transition; black dotted line = dry-wet season transition.

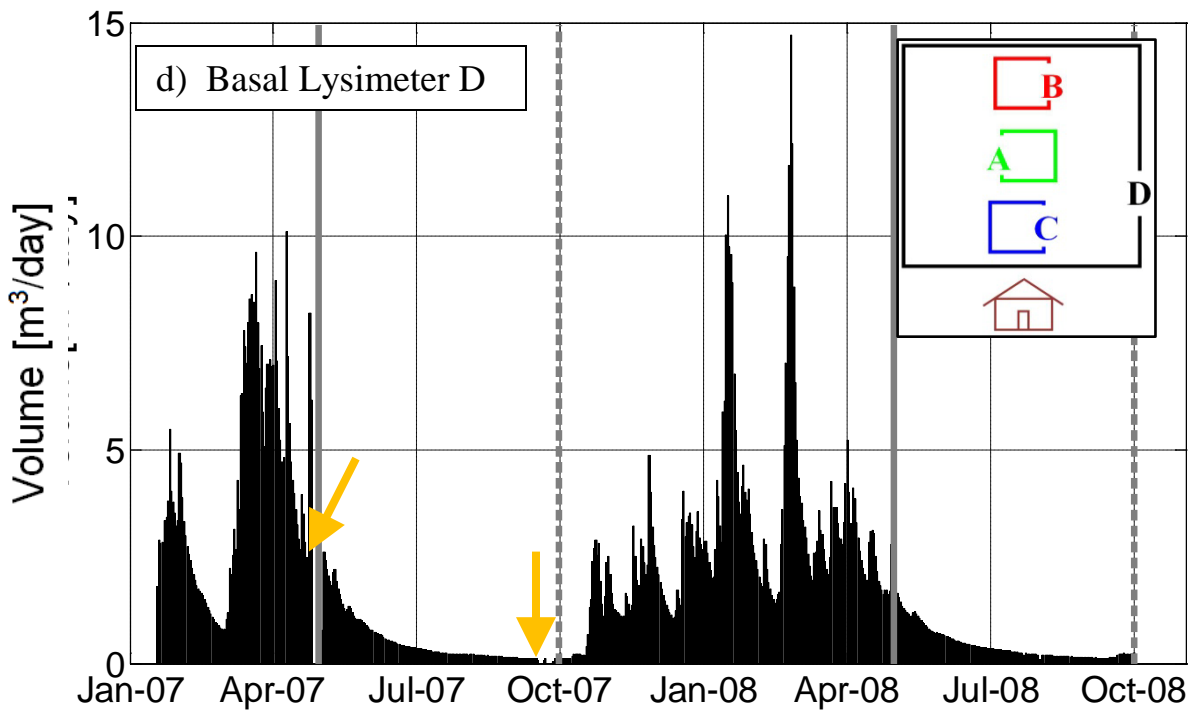


*black solid line = wet-dry season transition; black dotted line = dry-wet season transition.

Figure 3.9. Outflow hydrograph for: a, b, c) the sub-lysimeters and d) basal lysimeter (continued on next page).

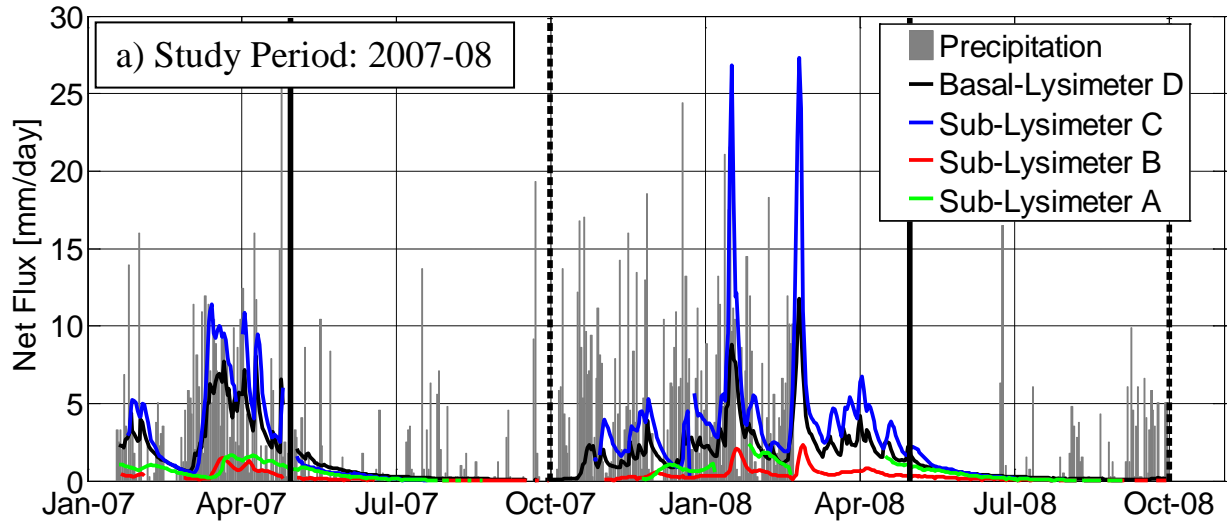


*black solid line = wet-dry season transition; black dotted line = dry-wet season transition.



*black solid line = wet-dry season transition; black dotted line = dry-wet season transition.

Figure 3.9. Outflow hydrograph for: a, b, c) the sub-lysimeters A, B and C, respectively; and d) basal lysimeter D (continued from previous page).



*black solid line = wet-dry season transition; black dotted line = dry-wet season transition

**note. missing precipitation from Feb – June, 2008

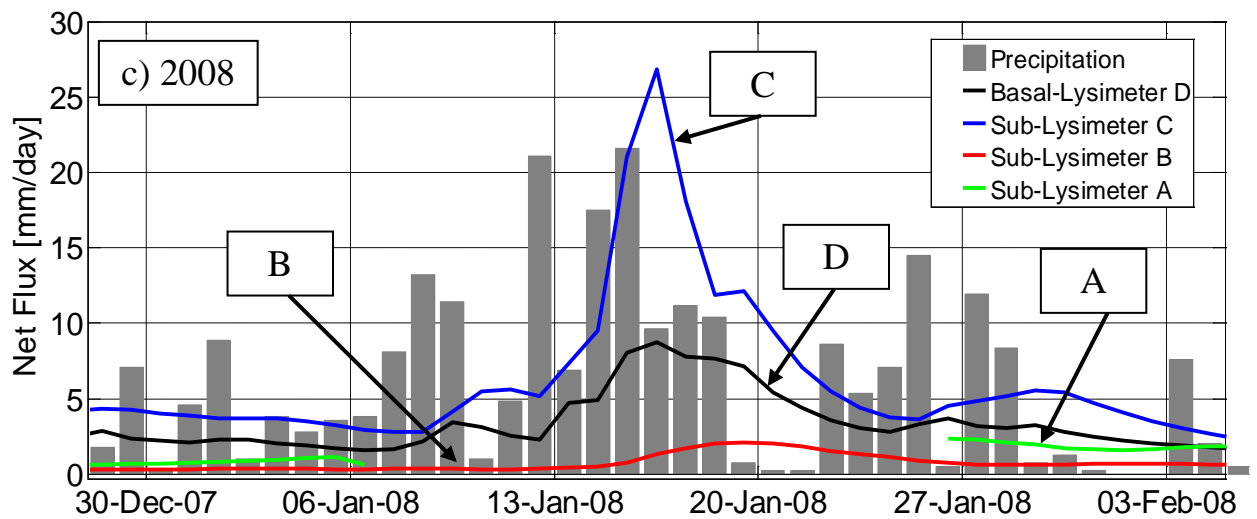
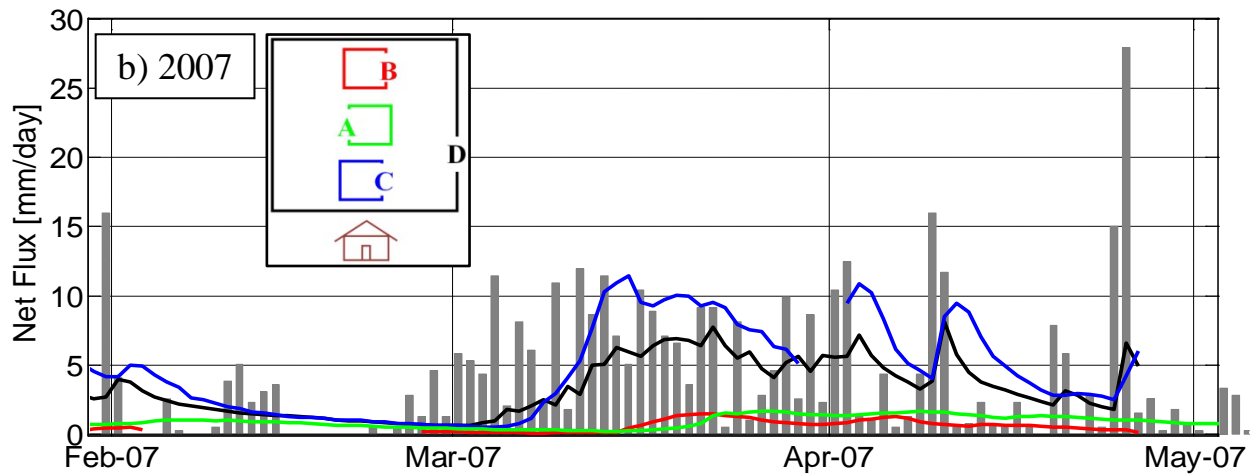


Figure 3.10. Precipitation and lysimeter fluxes for a) the study period b) February-May, 2007, and c) Jan-2008.

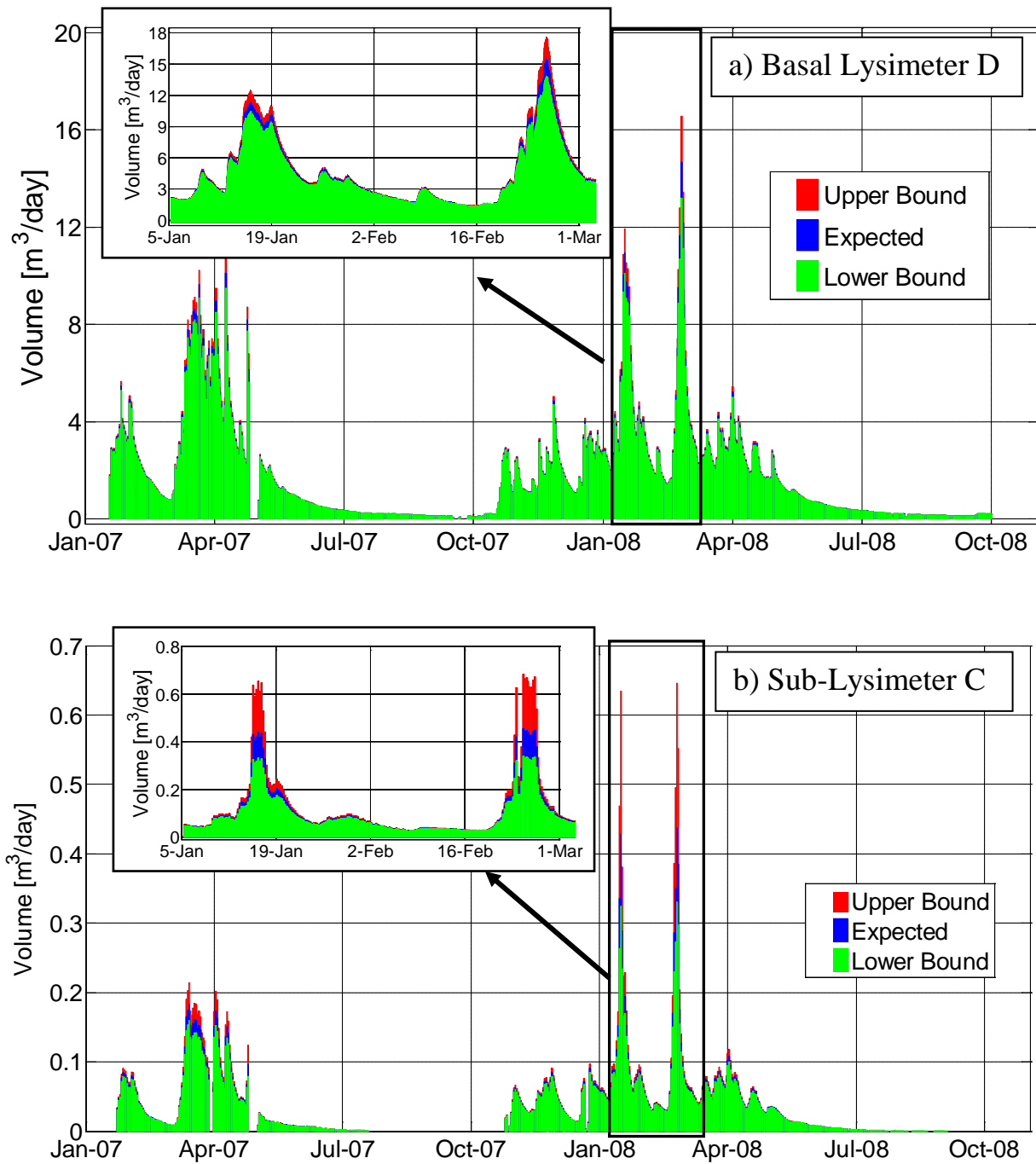


Figure 3.11. Upper, lower and expected flow for basal lysimeter D and sub-lysimeter C.

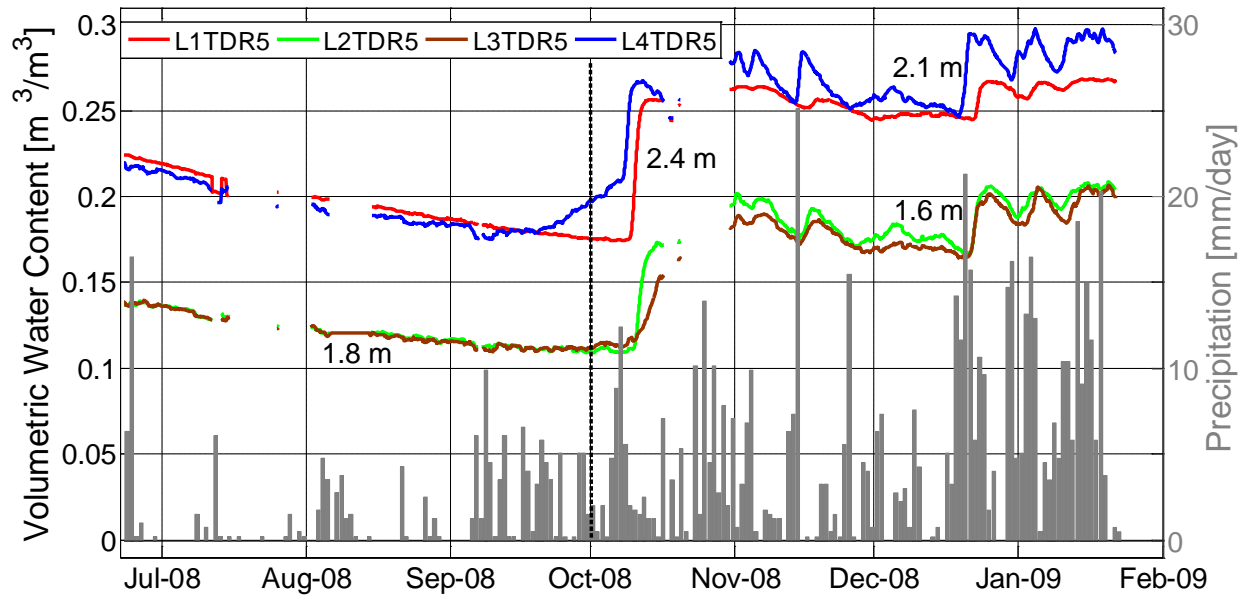
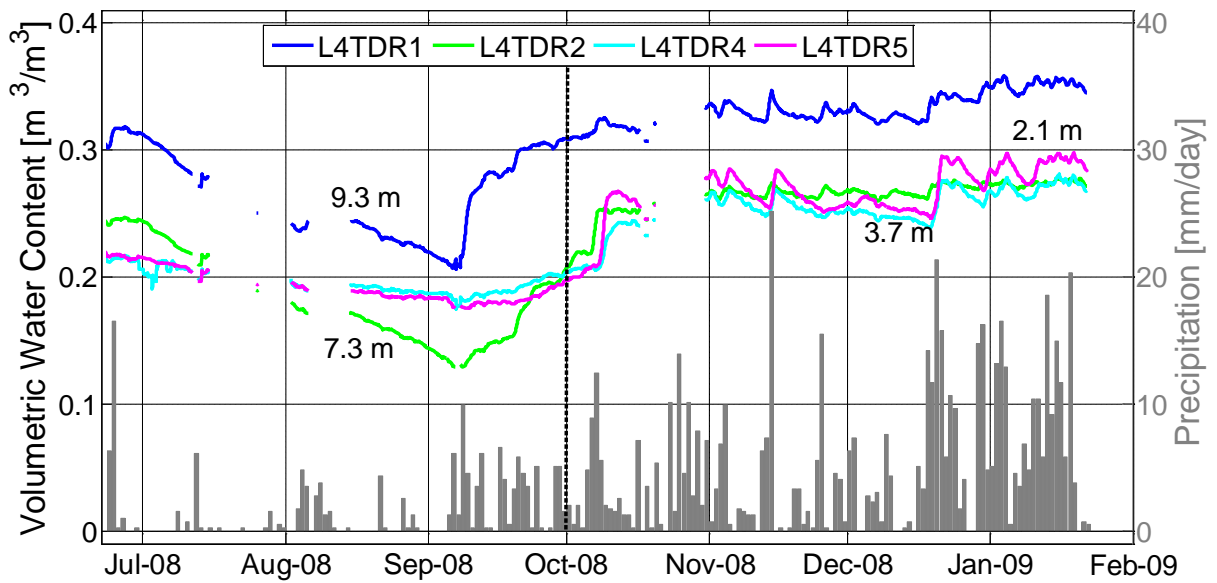


Figure 3.12. Shallow TDR moisture content and precipitation in mm/day.



*L4TDR3 (5.4 m depth) not functioning

Figure 3.13. Line 4 TDR moisture content response (under front batter).

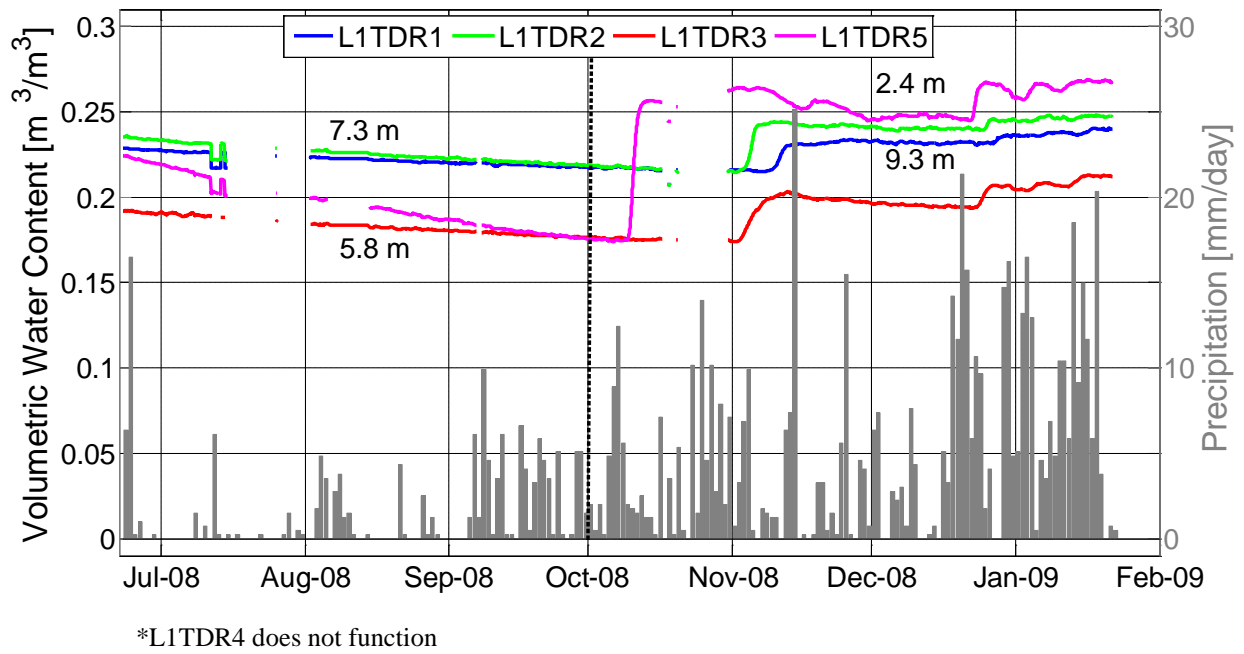


Figure 3.14. Line 1 TDR moisture content and precipitation.

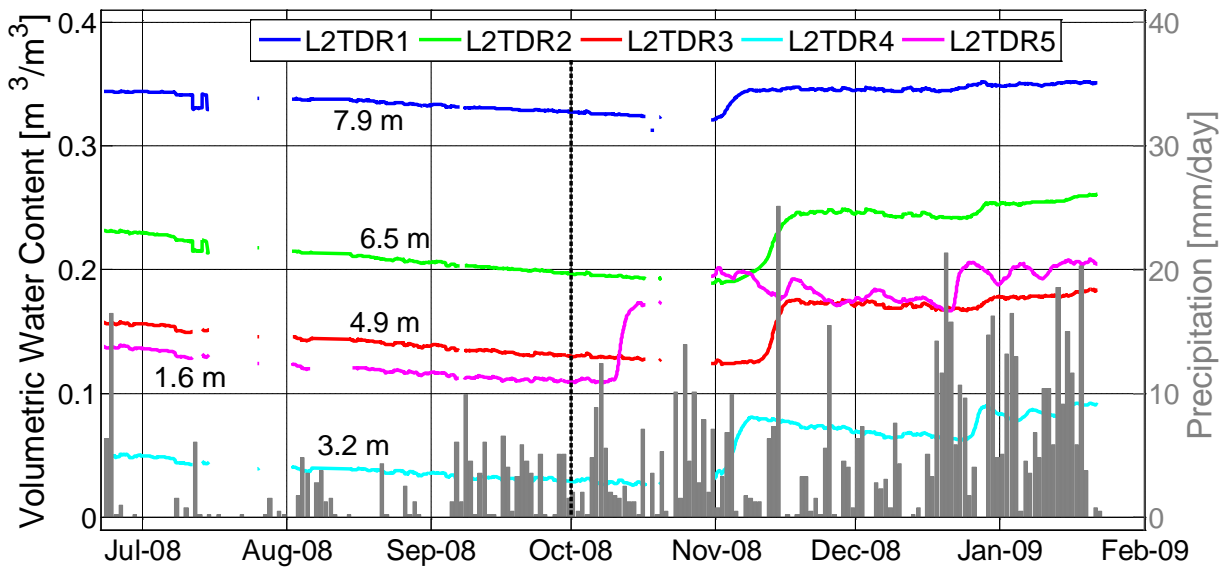
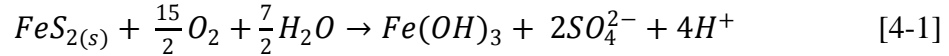


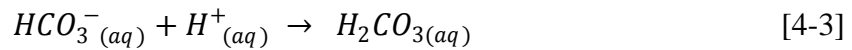
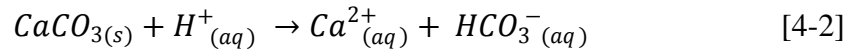
Figure 3.15. Line 2 TDR moisture content and precipitation.

4 RESULTS: TEST PILE GEOCHEMISTRY

It is often the case that sulphide minerals found in mining environments will lead to the creation of Acid Rock Drainage (ARD). Pyrite is a common sulphide mineral associated with ARD, the chemical oxidation of which generates acidic waters according to the following pathway (Blowes et al., 2007):



In some cases, acid generated from sulphide oxidation reacts with the gangue material. If the gangue material includes a carbonate mineral, it can buffer the acidity and create Neutral Rock Drainage (NRD):



Previous analyses have shown that there is a considerable buffering capacity in the Antamina host rock (Golder 2007a, Golder 2007b; Aranda et al., 2009) whereby acid generated from sulphide mineral oxidation is rapidly neutralized by carbonate mineral dissolution. Recall that nearly 2.2 % of the pile consists of sulphide minerals (mainly pyrite) and that 48 % of the entire pile consists of carbonate minerals (Table 2.3). As a result of these buffering reactions, effluent chemistry is pH-neutral, and most metals are immobile under these conditions. However, select metals such as zinc remain mobile under circum-neutral conditions, while the mobility of metals present as oxyanions, such as arsenic (as As(V)), increases. These conditions differ considerably from the majority of mine sites within Canada, which contain mostly acid-generating waste rock. Sulphide oxidation and acid neutralization involve several factors that contribute to the complexity of understanding and predicting acid and neutral rock drainage.

This chapter evaluates the chemical evolution of the neutral-pH drainage pore and outflow waters of test pile 1 between 18-Jan-2007 to 30-Sept-2008 by:

1. characterizing the geochemical composition of porewater and outflow waters,
2. examining the spatial and temporal variability of solute concentrations,
3. assessing the correlation between flow path length and concentration,
4. determining metal release mechanisms and possible attenuation mechanisms, particularly for mobile metals such as zinc,
5. providing supporting evidence for observations from hydrology (e.g., matrix vs. macropore flow), and
6. comparing effluent chemistry between test pile 1 and field cell experiments.

A comprehensive instrumentation network of real-time, continuously logged data, point-source chemistry data from within the pile, and effluent chemistry data are employed to better understand the internal processes and chemical evolution of test pile 1. Approximately 270 water samples were obtained from the sub-lysimeters, basal lysimeter, composite tank and sump and an additional 540 samples were obtained from the soil water samplers.

4.1 ELECTRICAL CONDUCTIVITY

4.1.1 Lysimeters

Continually-logged electrical conductivity (EC) data from the four lysimeters is converted to specific conductance (SC) as described in Chapter 2 (Section 2.10.1.6). The EC probes used in the pile are functional, but experience degradation with time and result in several periods of missing data, particularly for the discharging water from basal lysimeter D. The highest SC values of 6000 $\mu\text{S}/\text{cm}$ are reported at the beginning of the study period, which likely coincide with the initial flushing of weathering products of the most reactive material. Near the end of the study period, SC values typically range between 1000 and 3000 $\mu\text{S}/\text{cm}$. Basal lysimeter D effluent ranges between 1500 and 3500 $\mu\text{S}/\text{cm}$ and is representative of the overall pile specific conductivity.

The high-resolution SC data (obtained at 30-minute intervals) indicates responses to large precipitation events (i.e. low SC values with high precipitation values), but does not register

smaller-scale, rapid fluctuations derived from specific wetting front arrivals via different flow paths (Figure 4.1). The best evidence of rapidly changing chemistry, in response to precipitation, is observed in lysimeter D and the front sub-lysimeter C, where sharp increases in flow result in sharp decreases in SC e.g., in March 2007 (Figure 4.1). This behaviour indicates the activation of macropore flow under heavy precipitation events (as described in the previous chapter) that results in higher discharge rates and a lower dissolved solute load. A similar response is anticipated in 2008 but is not as evident in the data due to incomplete EC-probe data.

Pile batters represent nearly 75 % of the horizontal surface area of the pile and will play an important role on pile response. Near the end of the first week in March-2007, the SC from basal lysimeter D drops from 3500 to 1700 $\mu\text{S}/\text{cm}$ in less than 10 days, whereas sub-lysimeter C drops from 2600 to less than 2000 $\mu\text{S}/\text{cm}$ over nearly the same period. Sub-lysimeters A and B do not show sharp responses, though slight dips observed on 22-Mar and 16-Mar (respectively) correspond to higher pile discharge rates.

Sub-lysimeter A (centre of the pile) reports the highest SC levels which are nearly twice as high as those reported at sub-lysimeter C (front batter of pile). Basal lysimeter D is representative of the entire pile, and reports intermediate levels with the largest seasonal variation (i.e., similar SC levels to A and B during the dry season and similar SC values to C during the wet season). Recall that the highest flow of water is reported from the batters and that a significant amount of the total pile flow occurs during the wet season (Chapter 3). This indicates that more macropore flow is mainly prevalent during the wet season, which is reflected in lower SC values compared to the dry season.

The weekly, manually-obtained field data is also plotted for comparison (Figure 4.1). Since SC values do not undergo rapid changes over the course of a few hours, this provides evidence that a significant portion of the effluent water originates from matrix flow. As matrix water is usually slow and diffuse (e.g., Chapter 1, 3), it is typically associated with higher dissolved loads compared to characteristic macropore flow. Comparing results from sub-lysimeters A and B (matrix dominated) with sub-lysimeter C and basal lysimeter D (stronger contributions from macropore flow) confirm this hypothesis. Recall that that the 4 x 4 m sub-lysimeters are

conceptualized as representing effluent water that spatially averages over matrix and macropore (if activated) flow pathways. The same applies to the 36 x 36 m basal lysimeter flow and chemistry, which averages over various flow and chemistry differences that result from the pile batter and the pile interior.

4.1.2 Composite Tank

The composite tank chemistry follows similar seasonal trends to the lysimeters, with higher reported values during the dry season (Figure 4.1). A regression comparison of SC between the composite tank E and the basal lysimeter D indicates that there is a reasonable correlation (Figure 4.2a). Average wet and dry season SC values for E are compared to those of D and indicate that average composite tank SC values are 5 % higher during the wet season but nearly 4 % lower during the dry season (Table 4.1). Further details about the composite tank are discussed in Appendix G.

4.1.3 Pile Interior

Fifteen (15) soil water samplers (SWS) were installed in instrumentation lines 1, 2 and 4 to provide chemistry data at various vertical points throughout the pile. Five soil water samplers (SWS) were placed at depth in near-vertical intervals of 1.5 m, and Figure 4.3 indicates that concentration changes with depth, similar to findings presented by Wagner (2001). Recall from Chapter 2 that test pile 1 was constructed by end-dumping waste rock in three stages, with Tipping Phase I at the back of the pile, Tipping Phase II in the middle and Tipping Phase III at the front of the pile (Figure 4.4).

The largest variability and highest SC values in response to the initial flushing of weathered products occurs in Tipping Phase II, in which instrumentation line 2 and sub-lysimeter A are located (Figure 4.4). SC values reported at sub-lysimeter A reach 6000 $\mu\text{S}/\text{cm}$ at the beginning of the study period and drop below 3000 $\mu\text{S}/\text{cm}$ towards the end (Figure 4.3). The SC values in line 2 range between 2000 and 3500 $\mu\text{S}/\text{cm}$ at 1.9 m below the surface, and between 2000 and 4500 $\mu\text{S}/\text{cm}$ 8.9 m below the surface. (Note, some data points report up to nearly 8000 $\mu\text{S}/\text{cm}$ but are believed to be the result of improper data recording as they are one order of magnitude higher than the samples from the same location around that time and will be excluded from the general

discussion). SC values indicate slight seasonal variability, but the initial flushing of weathered products makes this pattern harder to resolve.

Conversely, the lowest SC values are reported in Tipping Phase III, in which sub-lysimeter C and instrumentation line 4 are located (Figure 4.4). SC values in sub-lysimeter C range between 1200 and 2600 $\mu\text{S}/\text{cm}$, with a strong seasonal signal that is rather consistent throughout the study period (i.e., reaches same general values during same time in 2007 and 2008) that is not observed towards the pile interior. There do not appear to be any strong differences in SC values at depth, with most values ranging between 500 and 2000 $\mu\text{S}/\text{cm}$. Since the instrumentation and sub-lysimeter in this region both have the shortest flow path and highest flow volumes compared to the other two sub-lysimeters (Chapter 3), it consequently has shorter porewater residence times as supported by evidence of a lower dissolved load.

4.1.3.1 Changes at Depth

In general, SC values increase with depth in lines 1 and 2 as the infiltrating rainwater acquires a higher dissolved load along the flow path. Since average SC values at each SWS port in lines 1 and 2 generally increase with depth, this possibly indicates that no significant solubility controls are present at this time and that the pile is not tall enough to express these controls (i.e., the average specific conductivity may eventually flatten out if the pile was 100 m high, likely due to the presence of solubility controls). SC values in line 1 generally report higher values than the corresponding sub-lysimeter B during the first wet season, but report similar if slightly lower values a few months into the study period. Conversely, SC values in line 2 are almost consistently lower than SC values reported in the corresponding sub-lysimeter A. All SC values in line 4 are lower than those reported in the corresponding sub-lysimeter C. However, since SC values are relatively constant with depth and show similar values at the same time throughout the year, this possibly indicates that this region is subject to different chemical controls compared to lines 1 and 2 based on the fact that this material is closest to the surface and reasonably well aerated. It is also possible that these differences are due to preferential flow or heterogeneities in composition. These themes are discussed later in this discussion.

Each sub-lysimeter lies directly under one or two SWS's, typically the middle ones, indicating that the highest and lowest SWS's will not reflect similar concentrations to the corresponding sub-lysimeter. This may be further complicated by non-vertical flow effects discussed in the previous chapter. Further discrepancies between the SWS and lysimeter chemistries may result from the fact that the SWS's extract a sample from the matrix (higher dissolved load) whereas the sub- and basal lysimeters collect the total flow of water that averages over matrix and macropore flow (lower dissolved load). The SWS's extract point measurements and each sampler has a maximum capacity of only 500 ml that is extracted from an estimated region of influence that is up to 10 - 15 cm in diameter. In comparison, the 4 x 4 m sub-lysimeters have a much larger region of influence and integrates over a larger area.

4.2 TEMPERATURE

Thirty-six (36) thermistor probes were installed at various locations within the pile and instrumentation hut (Chapter 2; Appendix A). Temperature data provided by thermistors is principally used to assess whether heat is emitted during sulphide mineral oxidation and to estimate the extent of temperature-driven gas convection. However, several secondary reasons exist, namely for: geochemical speciation modeling and other calculations (i.e., mineral solubility), neutralization capacity (Sherlock et al., 1995), and to affect temperature corrections for TDR and EC. Temperature data also contributes in explaining flow anomalies observed in the sub-lysimeters during the cooler dry season months. The mean annual temperature (M.A.T.) ranges between 5.5 and 6 °C during the study period (18-Jan-2007 to 30-Sept-2008) and is 5.6 °C during the water year (1-Oct-2007 to 30-Sept-2008).

4.2.1 Lysimeters

In the instrumentation hut, a thermistor probe is installed in each of the four water conveyance systems from each lysimeter (Figure 2.9). Since the conveyance pipes are partially exposed outside the instrumentation hut, lysimeter outflow temperature ranges (-0.6 to +23 °C) are more pronounced than temperatures from inside the pile (see below) due to meteorological diurnal fluctuations. These observations do not provide any indication of the weathering behaviour but help to explain some anomalies in the outflow behaviour.

Water draining from the three sub-lysimeters exhibits very similar diurnal temperature responses, with temperatures generally ranging from approximately 3 - 14 °C during the wet season months and 2 - 18 °C during the dry season months (although temperatures extend beyond these ranges, resulting in short-lived periods in which temperatures drop to below zero and near 20 °C). Higher flow rates during the wet season correspond to a tighter temperature range. Throughout most of the year (although more pronounced in the wet season), the temperature range of sub-lysimeter C is slightly more constrained than that of sub-lysimeters B and A (by up to 2 - 3 °C). This pattern is even further evident in basal lysimeter D flow data, which experiences a significant difference in temperature ranges throughout the year. In the dry months, temperatures range from as much as -0.5 to 23.0 °C and as little as 6 - 8 °C in the 2007 wet months.

Temperature variations in the outflow water do not have any implications to weathering characteristics inside the pile, but do help to explain an anomaly in the flow behaviour. During the cooler low-flow periods of the dry season, the large diurnal temperature range is found to effect sub-lysimeter flow and create abnormal diurnal ‘pulsing’ of rapid water flow during the day and no flow at night. It is hypothesized that this is caused by the freezing of water in the exposed conveyance pipes. To prevent this from occurring, an insulating material was placed around the exposed pipes in November-2007. Consequently, the 2008 wet season temperature fluctuations for basal lysimeter D converge to a constricted range as tight as 6 to 6.5 °C from 2 to 15 °C at the end of the 2008-09 dry season. The range of temperatures decreases by up to 4 °C (in total) for the sub-lysimeters, and at no time does sub-lysimeter drop to freezing temperatures (min ~ 1 °C except for 11-Sept-2008 which registered 0.2 °C). To note, the range in sub-lysimeter C is more constrained by up to 4 °C compared to the other two sub-lysimeters. Despite these differences, the diurnal pulsing is still observed in the sub-lysimeter effluent during the next low-flow period (i.e., 2008 wet season). Based on the minimal volume of water associated with this behaviour, it is insignificant compared to the overall pile outflow and is not discussed further.

4.2.2 Pile Interior

Seasonal and spatial temperature variability is evident throughout the entire study period in test pile 1 (Figure 4.5). Temperature trends towards the pile interior indicate that while the

temperature regime is cyclical (i.e., seasonal variation), temperatures are all 0.5 – 1 °C cooler in 2008 compared to 2007. This may be explained by a small decrease in reactivity later in the pile lifetime as the highly reactive particles react first (releasing energy as a by-product of sulphide mineral oxidation). This may also indicate that the pile may not have reached dynamic thermal equilibrium soon after construction was completed.

4.2.2.1 Internal vs. External Temperatures

Based on 30-minute data, internal pile temperatures range between 0.3 and 12 °C, which is much more constrained than the outflow temperature ranges, indicating the thermal insulating properties of the waste rock (Figure 4.5). Thermistors along the outer shell of test pile 1 respond to short-term meteoric changes whereas temperature probes located in the interior of the pile show more attenuated and subdued temperature variations and respond to long-term meteoric trends (Figure 4.5).

During the water year (1-Oct-2007 to 30-Sept-2008; Chapter 3), temperatures measured from the ‘deep probes’ (> 6 m from the top of the pile in lines 1 - 4, > 15 m from the outer perimeter for lines 5 and 6) in test pile 1 range between 4.5 and 7.5 °C, with a mean temperature of 5.8 °C (Table 4.2). The subdued temperature variations occur because of the insulating properties of waste rock which attenuate the short-term atmospheric signals. The ‘shallow probes’ (< 6 m from the top of the pile in lines 1 - 4, > 15 m from the outer perimeter in lines 5 and 6) exhibit a larger temperature range of 3 - 10 °C with a mean annual temperature of 7.6 °C, during the water year (Table 4.2). The mean annual air temperature (M.A.T.) during the water year is 5.6 °C.

A comparison of mean annual temperature calculated based on daily thermistor data in lines 2 and 3 during the water year (1-Oct-2007 to 30-Sept-2008) is summarized in Table 4.2. During this period, average temperatures near the top of the pile (i.e., shallowest probes) are 1.7 - 1.8 °C higher than the bottom. During the wet season (1-Oct-2007 to 30-Apr-2008) the temperature range is nearly the same (1.7 °C), but the difference slightly diverges during the dry season (2.0 °C). The M.A.T. is very stable during the wet and dry season (Table 4.2), and is very similar to the bottom pile temperatures (± 0.2 °C). This temperature difference (warm surface - cool interior) is the inverse of patterns observed or modeled in other more mature and reactive waste

rock piles, and may have implications on gas transport (Sracek et al., 2004; Andrina et al., 2006; Linklater et al., 2005; Marcoline 2008). It is hypothesized that the highest reported temperatures exist at the top of the pile because:

1. this material is the most reactive (i.e., finer grained due to compaction of heavy machinery and preferential settling of finer material near the top of the pile during end-dumping process) and generates the most heat during exothermic sulphide mineral (pyrite) oxidation,
2. heat-driven gas convection transports heat through the relatively well-aerated pile, and/or
3. solar radiation heats the top of the pile.

The latter item is most probable, but more comprehensive data and thermal modeling is required to form any solid conclusions.

4.2.2.2 Spatial Variability in Temperatures

During the water year the average temperature in instrumentation lines 1, 4, 5 and 6 ranges between 5.5 and 5.9 °C, whereas instrumentation lines 2 and 3 exhibit a mean annual temperature of 6.7 °C. That the mean annual temperature in both lines 2 and 3 is more than one degree higher than the other instrumentation lines may be indicative of higher chemical oxidation rates in the material from Tipping Phase II in which lines 2 and 3 are situated (Figure 4.4). Figure 4.6 presents a cross-sectional profile of average temperatures in lines 1, 2 and 4 during the water year and indicates that temperatures are coolest near the bottom and increase with elevation in the pile.

4.2.2.3 Evidence of Advection and/or Evaporation from Front Batter

Due to its proximity to the surface, each thermistor in line 4 displays fluctuations in response to atmospheric temperature changes and indicates that the waste rock material in the batter will likely undergo stronger temperature fluctuations compared to internal thermistors found in lines 1, 2 and 3. Line 4 thermistors located near the base register cooler and more variable temperatures than thermistors located closer to the top of the pile, which is the opposite trend

observed in the rest of the pile. This likely indicates that when a portion of the overburden above line 4 was removed to conform with initial design specifications, it created a situation where the deepest probes (7 and 8.9 m below surface) became situated closest to the surface at the pile toe (Figure 4.6). That average temperatures at 1.9 and 3.6 m below the surface in line 4 (4.5 and 4.8 °C, respectively) are below the mean annual temperature by one degree likely indicates that this region of the pile is well-aerated (e.g., wind-driven advection) and that energy is likely lost via evaporation (i.e., latent heat of vapourization) and leads to cooler average temperatures. While these differences may result from precision and calibration issues, based on performance of all of the thermistors, a one-degree difference is considered to be indicative of a significant temperature trend within the pile.

4.3 PH

In general, pH values range between 7 and 8.5, with the majority of the values between 7.5 and 8. Sampling station (lysimeters, composite tank) and interior (SWS) pH values are similar, and both exhibit a seasonal variation in response to precipitation. Based on equations 4-2, 4-3 and 4-4, higher pH values typically indicate that porewaters approach more open-system conditions (i.e., atmospheric CO₂ near surface) whereas lower pH values approach more closed-system conditions (i.e., depleted CO₂ towards pile interior).

4.3.1 Lysimeters

A seasonal variation in pH is apparent, with decreasing values during the dry season and increasing pH values during the wet season. There are several explanations for these trends:

1. the rate of sulphide mineral oxidation is slightly higher than calcite dissolution during the wet season, which results in lower pH values,
2. higher infiltration and discharge rates during the wet season result in lower porewater residence times which means that they have less time to equilibrate with calcite before exiting from the bottom of the pile, and/or
3. preferential and/or macropore flow are more prominent in the wet season and have less time to equilibrate with calcite before exiting from the bottom of the pile.

It is also apparent that pH values are nearly 0.5 pH points higher in 2008 than the same period in 2007, likely indicating that the pile is slightly less reactive during 2008. Due to the seasonality of the data, it is difficult to make any conclusions of pH trends based on this data at this time.

4.3.2 Composite Tank

Composite tank E pH values follow similar seasonal trends to the lysimeters. A regression analysis of the weekly and/or bi-weekly pH data between E and basal lysimeter D indicates that there is a relatively weak correlation (Figure 4.2b), which is largely due to the sensitivity of the parameter and the instruments required to measure it (Table 4.1). A relatively close range is observed between the two stations, as average pH values are 4 % higher in the composite tank during the wet season, and 7 % higher during the dry season. Basal lysimeter D pH values are lower during the dry season than during the wet season, and results in larger pH differences between D and E during the dry season (pH difference: ~ 0.5) compared to the wet season (pH difference: ~0.3).

Water collected in the composite tank generally has a higher pH than water collected directly from the lysimeter discharge. This is because water draining from the pile interior likely has a high dissolved CO₂ concentration that exceeds atmospheric levels and releases CO₂ gas as it attempts to equilibrate with atmospheric CO₂ concentrations in the composite tank (and when passing through the flow splitter), which consequently raises the pH according to equation 4-4. A poor correlation between E and D may be the result of the fact that E includes a mixture of water from all four lysimeters.

4.3.3 Sump

Based on two samples (28-Nov-2007, 1-May-2008) an average pH of 7.5 was reported for the sump. These levels are within the lower range of pH values observed throughout the pile (Figure 4.7), possibly indicating that sump porewaters are approaching closed-system behaviour. This is expected based on the sump and 2B-Protective Layer design.

4.3.4 Pile Interior

Soil water sampler data indicates that pH remains relatively stable in lines 1 and 2 and increases with depth in line 4 (Figure 4.7). Line 1 and 2 pH values are generally the lowest reported pH in the pile, and likely indicates that these regions are representative of partially-closed systems within the pile. In general, pH reported in all 3 instrumentation lines (1, 2 and 4) is within a similar range to that reported in the sub-lysimeters, and basal lysimeter D is representative of the variability expressed in the three sub-lysimeters. At the lowest depth in line 4 (i.e., 8.9 m below the surface), pH is 0.5 units higher than the reported pH of the SWS above it (i.e., at 7 m depth). Recall that this SWS is closest to the pile toe and is likely covered by the least amount of material (Figure 4.7). While the higher pH may be due to a lesser amount of sulphide mineral oxidation occurring in this region compared to the rest of the pile, it is possible that the higher pH is due to the degassing of CO₂ in this region in which wind-driven advection is responsible for keeping it well-aerated.

Preliminary gas analyses indicate that CO₂ concentrations (in the gas phase) reach as high as 5 times atmospheric toward the pile interior, but are only 10 % higher than atmospheric in the well-aerated line 4. In the liquid phase, dissolved porewater CO₂ content will equilibrate with the CO₂ concentration in the pore gas. As water from the interior of the pile (elevated CO₂ partial pressure) moves towards more aerated regions (lower CO₂ partial pressure), it equilibrates with atmospheric CO₂ and leads to degassing (equation 4-4). A PHREEQC analysis indicates that an approximate 0.4 unit increase in pH will result during the transport of porewaters from internal to external locations (i.e., moving from closed- to open-systems) while maintaining equilibrium with calcite. This indicates that pH changes may result from sulphide oxidation (which produces H⁺ ions, and decreases pH. A reduction in pH is limited by calcite dissolution, which in turn raises CO₂ – under closed system conditions) and/or CO₂ degassing (which removes CO₂ and increases pH – under open system conditions).

4.4 SOLUTES

This section evaluates the porewater and effluent water solute concentrations. All solute concentrations exhibit seasonal variability, which increase during the dry season and decrease during the wet season (which is opposite to pH). Recall that 250 ml of a sample is required to

analyze the dissolved metals, 500 ml is required for total metals, and 1000 ml is required for the remaining solutes. Each SWS has a capacity of only 500 ml (Chapter 2).

For the interest of this investigation, Antamina's discharging and receiving limits can be found in Table 4.3. The discharging limits refer to the solute concentrations that are allowed to leave the mine (and be mixed with re-directed river discharge) and the receiving limits are the maximum concentrations allowed at sampling stations downstream from the mine.

4.4.1 Metals

Dissolved arsenic (As), copper (Cu), molybdenum (Mo), iron (Fe), lead (Pb), and nickel (Ni) concentrations are at, or near, detection limits (i.e., < 0.05 mg/l). As is primarily released from arsenopyrite, enargite, realgar, tennantite and watanabeite; Cu is associated with chalcopyrite and iron oxyhydroxide, iron sulphate and apatite; Mo is largely from molybdenite but also from some iron sulphates; Pb is mainly associated with galena, but also Fe-oxyhydroxide, chalcopyrite and Fe,Cu-silicates (Aranda, 2009). The only metal above detection limits in this pile is dissolved zinc (Zn), although total Cu and Fe are elevated in the sump (consistent with slightly lower pH levels in the sump).

4.4.1.1 Zinc

Sphalerite is the principal source of Zn in this test pile, but other sources include Fe-oxyhydroxide, Fe-sulphate and apatite (Aranda, 2009).

4.4.1.1.1 Lysimeters, Composite Tank and Sump

Dissolved Zn concentrations in the lysimeter drainage range between 0.5 and 2.5 mg/L (Figure 4.8). There is a clear seasonal variation, with concentrations increasing during the dry season and decreasing during the wet season. The lowest Zn concentrations occur at the end of the wet season and the highest concentrations occur at the end of the dry season. Figure 4.8 illustrates that Zn concentrations are highest at sub-lysimeter B (1-2.5 mg/L), and lowest in sub-lysimeter C (0.5 to 1 mg/L). Concentrations reported at D are typically between these two values except for the end of the 2008 dry season where values increase sharply to match B values.

Zinc concentrations in composite tank E exhibit similar seasonal fluctuations as observed in the lysimeters, with higher concentrations during the dry season. A regression comparison indicates that there is a strong correlation between E and basal lysimeter D, with slightly lower Zn concentrations in the composite tank (Figure 4.2c). Average Zn concentrations in the composite tank are roughly equal to basal lysimeter D concentrations during the wet season, but are nearly 15 % less during the dry season (Table 4.1).

Sump (F) Zn concentrations are similar to those observed in D and E. The sump produces the highest total Fe and copper Cu concentrations reported throughout the entire pile. Dissolved Fe and Cu levels are largely at or near detection limits (Figure 4.9). It is hypothesized that the area around the sump is saturated (Chapter 3) which would create relatively anoxic conditions compared to the rest of the pile thus explaining these high total Fe and Cu concentrations.

4.4.1.1.2 Pile Interior

Zinc concentrations (< 2.5 mg/L) in lines 1 and 2 increase with depth (Figure 4.8) and remain below their respective sub-lysimeter (B and A, respectively) concentrations (see Section 4.1.3 for explanation). The opposite is true for line 4 and sub-lysimeter C. The trend in line 4 is more difficult to resolve, with values reaching as high as 5.5 mg/L at the shallowest soil water sampler at the beginning of the wet season. The highest reported values (> 3 mg/L) occur over a few weeks only and may be the result of:

1. analytical errors,
2. Zn attenuation mechanisms present throughout the rest of the pile may not be present here,
3. release of Zn from a high Zn-bearing region,
4. higher oxidation rates in this region, and/or
5. evaporation of porewaters, resulting in higher relative Zn concentrations during the dry season.

These differences highlight the highly heterogeneous nature of the pile, and that the highest Zn concentration in the effluent waters (2.5 mg/L) may likely increase in time. With the limited data

available for line 4, no definitive conclusions can be made with regards to Zn. Longer term monitoring is required before any conclusions can be drawn.

4.4.2 Cations

Dissolved calcium (Ca), sodium (Na), magnesium (Mg), and potassium (K) all have large concentration ranges, with maximum values of 1200 mg/L, 110 mg/L, 75 mg/L, and 60 mg/L, (respectively). The abundance of Ca indicates that calcite dissolution is significant; however, the presence of Na and K indicates that weathering of the waste rock is not limited to carbonate mineral dissolution as there is a considerable amount of silicate minerals in the pile (e.g., pyroxene, biotite, plagioclase, K-felspar; Aranda, 2009). Ca is also present in Ca-Mg-silicates (diopside) and the calcium silicate minerals of hornfels (Aranda, 2009).

4.4.2.1 Lysimeters, Composite Tank and Sump

The highest cation (Ca, Na, Mg, and K) concentrations are reported in sub-lysimeter A and the lowest concentrations are reported in sub-lysimeter C (indicating chemical differences between pile batter and the interior), and concentrations reported at sub-lysimeter B and basal lysimeter D are typically found in between (Figure 4.10, Figure 4.11, Figure 4.12, Figure 4.13). While seasonal variability is reported in each lysimeter, cation concentrations generally appear to be decreasing over time. This is particularly the case for Na, Mg and K, which indicates that the minerals containing these elements are not weathering as rapidly (silicate minerals generally weather more slowly than carbonate minerals).

Calcium concentrations exhibit a strong seasonal variation with increasing concentrations during the dry season and decreasing concentrations during the wet season, which is opposite to pH. These differences are likely due to the fact that, in equilibrium, an increase in H^+ concentrations (decreasing pH) will result in an increase in Ca concentrations (equation 4-2). Although calcite solubility is affected by both temperature and equilibrium pH, temperature changes between the wet and dry season are not enough to affect these changes and that the likely driver of these seasonal differences is the concentration of Ca. A higher concentration of Ca that results from a higher porewater residence time during the dry season (which increases the dissolved load) leads

to decreasing pH values, and vice versa (equation 4-2). A slightly lower pH will thus enhance calcite solubility.

Cation concentrations in the composite tank E exhibit similar seasonal fluctuations as observed in the lysimeters, with higher concentrations during the dry season. A regression comparison indicates that there is a strong correlation between Ca measured at E and basal lysimeter D (Figure 4.2d). Average cation concentrations in E are slightly higher (< 4 %) than D concentrations during the wet season, but exhibit a larger difference during the dry season. For example, the average Ca concentration at E is 5 % less than D, whereas Na is nearly 9 % higher and Mg is 4 % lower during the dry season (Table 4.1).

Calcium concentrations in the sump (F) are slightly higher than concentrations observed in basal lysimeter D and composite tank E, which is supported by a lower pH in the sump (Figure 4.9).

4.4.2.2 Pile Interior

Cation concentrations measured in the soil water samplers in line 2 report the highest concentrations found throughout the pile during the initial pile flushing in 2007. For example, Figure 4.11 indicates that Na concentrations along Line 2 and measured in sub-lysimeter A effluent are much higher in 2007 (55-110 mg/L) compared to 2008 (25 -55 mg/L). A depth trend for these metals cannot be discerned, as line 2 concentrations are much higher than any other concentrations reported at other pile locations. The soil water samplers also indicate a seasonal trend (Figure 4.10, Figure 4.11, Figure 4.12, Figure 4.13).

4.4.3 Trace Metals

Antimony (Sb) concentrations are less than 0.25 mg/L. Likely sources are stibnite and watanabeite (Aranda, 2009). However, the SWS's in line 1 experience higher than average concentrations in the suction lysimeters located at 7 and 8.9 m depth during the wet season. Interestingly, comparable values are not reported in sub-lysimeter B effluent. Similarly, manganese (Mn) concentrations reported in the SWS's of line 2 are nearly twice as high as its corresponding sub-lysimeter A. Overall, the mobility of trace metals other than Zn from Pile 1 is low.

4.4.4 Major Ions

Major ions such as alkalinity, sulphate, and nitrate are only analyzed if a 1000 ml sample is obtained. This was not usually a problem for the sampling stations (lysimeters, composite tank and sump), but was not possible for the internal pile data as the SWS's are not capable of producing water samples of this size (maximum capacity of ~ 500 ml). Therefore, only major ions are only analyzed for the lysimeters, composite tank and sump.

4.4.4.1 Dissolved Sulphate

Dissolved sulphate is an important solute to monitor because it indicates that the chemical oxidation of sulphide minerals such as pyrite (equation 4-1), chalcopyrite, pyrrhotite and sphalerite (to a lesser extent) is occurring. Concentrations range between 500 and 2000 mg/L and exhibit seasonal trends similar to other solutes with maximum values near the onset of the wet season and lowest values near the onset of the dry season (Figure 4.14). The highest concentrations are found in A and the lowest concentrations are found in C. Basal lysimeter D exhibits high concentrations matching A at the onset of the wet season, and matches the low C concentrations at the onset of the dry season.

Sulphate concentrations in the composite tank E exhibit similar seasonal fluctuations as observed in the lysimeters, with higher concentrations during the dry season (Figure 4.14). Sulphate concentrations measured in the basal lysimeter are strongly correlated to (and slightly higher than) those of the composite tank (Figure 4.2e). Average SO_4 concentrations in the composite tank are roughly equal (2 % higher) to basal lysimeter (D) concentrations during the wet season, but are nearly 9 % lower during the dry season (Table 4.1).

Sulphate concentrations measured in the sump (F) are 500 mg/L higher than the composite tank on 28-Nov-2007 (1675 mg/L) and 100 mg/L higher on 1-May-2008 (1030 mg/L). This indicates that the porewater in the 2B-Protective Layer experiences longer residence times, which is expected based on the location of the sump.

4.4.4.2 Alkalinity

Under the neutral-pH conditions of test pile 1, it can be assumed that almost all of the alkalinity is in the form of bicarbonate (HCO_3^-). Similar to Ca (and opposite to pH), alkalinity experiences seasonal variations in which alkalinity values increase during the dry season and decrease during the wet season (equation 4-2). These trends are also explained by a higher residence time during the dry season, which drives calcite dissolution (increasing Ca and HCO_3^-) and decreases pH (Section 4.4.2.1).

The highest alkalinity values are reported at the end of the observation period (100 mg/L), whereas the lowest values are observed at the start of the period (60 mg/L; Figure 4.15). Alkalinity values from peak 2008 dry season values are 20 % higher than those values from the peak 2007 dry season, although this is likely not indicative of any long-term trends because of the initial flushing of weathered products from the most reactive material. However, if alkalinity in the pile was decreasing over time, this would likely indicate that pH values will be increasing over this period. That HCO_3^- tends to be increasing while Ca concentrations tend to decrease over the study period likely indicates that there is a solubility control of Ca, most likely the precipitation of calcite (equation 4-2).

Composite tank E exhibits similar alkalinity values to those of the lysimeters, with higher concentrations during the dry season (Figure 4.15). Average alkalinity concentrations in the composite tank are nearly 3 % lower than basal lysimeter D concentrations during the wet season, and nearly 9 % lower during the dry season (Table 4.1).

Alkalinity concentrations measured in the sump are 9 mg/L higher than the composite tank on 28-Nov-2007 (83 mg/L) and 3 mg/L higher on 1-May-2008 (79 mg/L).

4.4.4.3 Nitrate

Nitrate is not present in the host rock, but is found in high initial concentrations because it is used in the explosives that the mine uses in blasting. Early time pile concentrations nearly reach 300 mg/L, but drop to 100 mg/L at the end of the observation period. Basal lysimeter D values begin at 120 mg/L but quickly drop to nearly 20 mg/L, indicating that the nitrates are largely

being flushed out. That nitrates are still present in the pile indicates that some porewater is likely retained as residual saturation in the matrix (i.e., relatively immobile).

Nitrate concentrations measured in the sump are 22 mg/L higher than the composite tank on 28-Nov-2007 (63 mg/L) and 1 mg/L higher on 1-May-2008 (7 mg/L).

4.5 PORE GASES

Pore gas analyses provide evidence that sulphide mineral oxidation is occurring based on the pathway described in equation 4-1 whereby oxygen is consumed, carbon dioxide is enriched, sulphate ions are produced and acidity is generated. Results indicate that the outer shell of the pile is reasonably well-aerated. Oxygen concentrations decrease with depth (towards pile interior), with the lowest oxygen concentrations at 85 % atmospheric levels. Conversely, carbon dioxide concentrations increase with depth (towards pile interior), with the most enriched samples containing up to 5 times atmospheric concentrations.

Gas data generally confirm observations described above (e.g., temperature, pH, Ca, alkalinity, etc). The interior of the pile behaves more like a partially-closed system in which higher CO₂ gas concentrations result in higher dissolved CO₂ gases in the porewaters and lower pH values (equations 4-3 and 4-4). The more-aerated pile exterior acts like an open system where CO₂ partial pressures are lower in the pore fluids (gas and water) and results in a higher pH and possible CO₂ degassing (equation 4-4). Wind-driven gas advection is likely the dominant process in these pile regions. The areas with the highest CO₂ and lowest O₂ gas concentrations coincide with instrumentation lines 2 and 3, which exhibit the highest average annual temperatures (Section 4.2.2). Since pyrite oxidation is exothermic, this provides reasonable evidence that significant sulphide mineral (pyrite) oxidation is taking place within test pile 1.

The highest temperatures recorded in lines 2 and 3 are near the top of the pile whereas the highest CO₂/lowest O₂ concentrations are at the bottom of lines 2 and 3 (Tipping Phase II; Figure 4.4). This provides evidence that gas advection (e.g., 'chimney effect') may not be able to penetrate to the pile interior and other gas-transport mechanisms (e.g., diffusion) may prevail. It is also possible that these differences could result in physical heterogeneities in:

1. composition (i.e., higher sulphide contents near the surface), and/or
2. particle size (e.g., finer particle size will likely have a higher water content and result in less oxygen available for pyrite oxidation),

Other indications that lines 2 and 3 are hot spots for sulphide mineral oxidation include the fact that SO_4 concentrations in the effluent waters are highest for sub-lysimeter A (below line 2) and pH values are relatively low compared to the rest of the pile. While this provides good evidence that the middle of the pile (sub-lysimeter A, instrumentation lines 2 and 3) exhibits the largest sulphide mineral oxidation rates and that the top of the pile around lines 2 and 3 may be a 'hot spot', further analysis is still required to determine the principal mechanisms involved and to determine any long-term trends. This is further examined in Chapter 6.

4.6 GEOCHEMICAL MODELING

Outflow geochemistry from basal lysimeter D was analyzed with PHREEQC v. 2.15 using the following parameters: temperature, pH, Alkalinity (as CaCO_3), S(6) as SO_4 , Cl, N(5) as NO_3 , N(-3) as NH_3 , F, Al, Sb, As, Ba, B, Cd, Ca, Cr, Co, Cu, Fe, Pb, Mg, Mn, Hg, Mo, Ni, K, Se, Si, Ag, Na, Sr and Zn. Several species were below or near the detection limit (e.g., Al, Cd, Cr, Co, Cu, Fe, Pb, Hg, Mo, Ag) but were included to remain consistent with similar geochemical modeling of the field cells (Aranda, 2009). Modifications were made to PHREEQC's Wateq4f database in order to account for Mo thermodynamics not included in the database (e.g., Carroll et al., 2006; Stollenwerk, 1998) as per Conlan (2009).

Chemical modeling of basal lysimeter D shows that, with the exception of 4 samples, charge balance errors are within an acceptable range of $\pm 10\%$ (Figure 4.16). Based on the fact that minerals will tend to precipitate when the saturation index (SI) > 1 , dissolve at SI < -1 , and are 'in equilibrium' when $-1 < \text{SI} < 1$ (Sherlock et al., 1995; Golder, 2007), speciation calculations indicate that the effluent is near saturation with respect to gypsum and calcite. These are anticipated due to the known abundance of carbonate minerals and presence of sulfide minerals within the pile. Gypsum SI values exhibit a seasonal variability, with increasing SI values during the dry season and decreasing values during the wet season. It would also be expected that

porewaters are undersaturated with respect to gypsum near the top of the pile but approach saturation further along the flowpath, near the bottom of the pile where gypsum precipitation may occur. This can only be hypothesized because no consistent SO_4 data is available from the soil water samplers (Section 4.4.4.1).

Gypsum SI values are almost entirely < 0 except for brief periods in August/September during 2007 and 2008 when $\text{SI} > 0$ (Figure 4.17). During the dry season, gypsum may form coatings around minerals found in dry pockets, and may be first to dissolve when moisture returns to these areas, resulting in concentration spikes during the initial wet season flushing. Calculated saturation indices for calcite show a slight increasing trend with time (Figure 4.18). Gypsum and calcite SI in composite tank E indicate that while gypsum remains similar between basal lysimeter D and E, calcite is reportedly higher in E (i.e., $\text{SI} > 0$) providing supporting evidence that CO_2 may be degassing, or solid phase calcite may be accumulating in the composite tank.

In addition to calcite and gypsum, several other minerals are at or approaching saturation (Table 4.4). These minerals include sulphates, carbonates, and oxides, and do not contribute significantly to the assemblage of primary minerals found in the pile. The presence of these minerals may indicate that secondary mineral formation and attenuation mechanisms may be occurring. The sulphate minerals exhibit seasonal trends similar in fashion to gypsum whereas carbonate and oxide SI values are all increasing towards saturation much like calcite. The silica in the oxides is likely present from the silicate minerals in the pile. Phases that exhibit increasing SI values may eventually start to precipitate if they continue on this trend.

4.7 DISCUSSION

4.7.1 Gypsum Precipitation and the $\text{SO}_4^{2-}/\text{Ca}^{2+}$ Ratio

Pyrite oxidation and calcite dissolution/acid buffering pathways will proceed as described in equations 4-1, 4-2, 4-3 and 4-4. Pyrite oxidation can drive the dissolution of carbonates through the production of hydronium ions. As such, for every mole of pyrite oxidized (in the presence of calcite), 2 moles of sulphate and 4 moles of calcium are produced.

An examination of basal lysimeter D effluent concentrations is useful in determining the release and attenuation mechanisms that are occurring within the pile. Figure 4.19 indicates that the effluent water is dominated by SO₄ (anion) and Ca (cation) ions. Geochemical modeling indicates that the porewater at the base of the pile is saturated with respect to gypsum (Section 4.6), and will lead to the precipitation of gypsum under the following pathway:

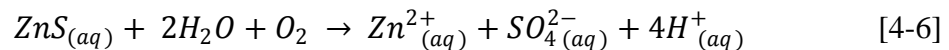


A regression analysis comparing the molar concentration of calcium and sulphate illustrates that there is a near proportional positive molar relationship ($r^2 = 0.62$) between Ca²⁺ and SO₄²⁻ (Figure 4.20), which is consistent with the sulphate release by pyrite oxidation and calcite dissolution, and pH buffering (equations 4-1 and 4-3). These results indicate that CO₂ is degassing (equation 4-4). On the other hand, the precipitation of gypsum includes a 1:1 removal of Ca and SO₄ ions, and does not affect the SO₄:Ca ratio. That the molar ratio is consistent indicates that there are no other primary sources or sinks of Ca and/or SO₄.

In an open, pH-neutral system where HCO₃⁻, H₂CO₃, and CO₂ are at equilibrium, the dissolution of calcite by acid produced from sulphide oxidation may result in an increase of dissolved CO₂ which can lead to a release of CO₂ gas (equation 4-4). This dissolution pathway is supported by the observed CO₂ gas enrichment with depth (5 times atmospheric) which indicates that the pile is not entirely behaving like an open system and that the interior is likely behaving more like a partially-closed system. Although CO₂ concentrations are not as high as reported in other waste rock piles (e.g., Pantelis and Ritchie, 1992; Wels et al, 2003; Sracek et al., 2004), this indicates that CO₂ enrichment is generally occurring towards the pile interior.

4.7.2 Zinc: Source and Attenuation Mechanisms

The primary source of zinc in test pile 1 pore waters is from the chemical oxidation of sphalerite [(Zn, Fe)S] according to the following pathway:



Note that although the chemical oxidation of sphalerite generates sulphate ions and acidity, due to a small proportion of sphalerite present in the waste rock compared to pyrite, pyrite is still considered to be the principal source of acidity, heat and sulphate ions within test pile 1 porewaters.

Based on the spatial and temporal variability of Zn (Figure 4.8) and results of chemical modeling, there is no clear evidence that any attenuation mechanisms are active that would remove a considerable amount of Zn from the porewaters. Zinc concentrations generally increase with depth and experience seasonal variability, and geochemical modeling indicates that no Zn-bearing mineral phases are near saturation. Furthermore, Figure 4.21 illustrates that while there is a reasonable trend between sulphate and zinc in C, D and E, there is no strong trend in A or B at this time.

A possible attenuation mechanism for Zn may be the sorption of Zn on carbonate minerals (Conlan, 2009), but there is no strong evidence of this in the test pile data. In addition, it is also possible that Zn may be retained in secondary mineralization (if it is occurring), but this also cannot yet be confirmed.

4.7.3 Spatial Variability

Instrumentation lines 1, 2 and 4 each correspond with a sub-lysimeter based on location within the pile. It is observed that concentrations do not always increase with depth and do not always correspond well with the sub-lysimeter data, suggesting that internal chemistries may be higher than reported flowing out of the base of the pile. The following list postulates some possible explanations:

1. heterogeneity of mineral composition (similar material classification, but originates from different areas of the pit at different times and has different compositions),
2. mineral availability/reactivity (e.g., how much is occluded and how much is suitable for reaction sites),
3. heterogeneity of particle size,

4. spatial and temporal flow variability (variable porewater travel times and scales, effluent from sub-lysimeters is a combination of matrix and macropore flow),
5. porewater pathways (assuming vertical flow of water, may pass through 2 or possibly 3 different types of waste rock before reaching the base of the pile i.e., Tipping Phase I and II, or II and III +/- the protective layer),
6. biased sampling of soil water samplers (i.e., sampling from matrix and can overestimate surrounding porewater chemistry due to unknown macropore saturation),
7. sample volume (i.e., soil water samplers vs. sub-lysimeter),
8. soil water samplers do not always lie directly above a lysimeter, and
9. unequal rates of sulphide mineral oxidation and calcite dissolution.

4.7.4 Comparison to Field Cell Chemistry

A brief comparison of effluent chemistry between field cells constructed by Aranda (2009) using the same material as used in the construction of test pile 1 is examined over the entire study period. Seasonal field cell solute trends are generally consistent with the test pile in which concentrations increase during the dry season and decrease during the wet season, indicating that the dissolved load is also a function of the porewater residence time in the field cells. Field cells also indicate an initial flushing of the weathering products from the most reactive materials early in the study period.

Based on the pH, Ca and alkalinity evidence, the field cells are well aerated. For example, a majority of the field cell pH values range between 7.5 and 9 (compared to 7 and 8.5 for test pile 1), and higher pH values are more indicative of open system conditions. High pH values (for field cells and pile at the end of the wet season) correspond to higher Ca concentrations (equation 4-2). Ca concentrations range between 300 and 450 mg/L (end of dry season) to 150 mg/L (end of wet season). In comparison, Ca levels in test pile 1 reach up to 1200 mg/L earlier on, but decline to 700 mg/L at the end of the study period. Alkalinity (as CaCO₃) in the field cells ranges between 30 and 60 mg/L, which are similar to pile levels (consistent with relatively well-aerated system where CO₂ is degassing).

Further evidence of sulphide mineral weathering is found in the electrical conductivity (i.e., specific conductance) and SO_4 levels (which are relatively well correlated, as described in Chapter 5). Field cell SC varies between 200 and 1000 $\mu\text{S}/\text{cm}$, but reaches as high as 1000 - 2000 $\mu\text{S}/\text{cm}$ (at the end of the dry season and in the black marble and marble diopside samples in particular). Test pile SC values reach up to 6000 $\mu\text{S}/\text{cm}$ at the beginning of the study period, but decline to maximum values of 3000 $\mu\text{S}/\text{cm}$ at the end of the study period. This signifies that the accumulation of weathering products (dissolved) along the pathway is decreasing over time, likely indicating an overall decrease in waste rock weathering rates (solid phase). Higher EC values correspond to the black marble and marble diopside material. Test pile SO_4 concentrations range between 500 mg/L (end of wet season) up to 2000 mg/L (end of dry season) whereas the field cells range between 200 - 300 (end of wet season) to 700 - 900 mg/L (end of dry season).

The largest discrepancy in effluent chemistry between the field cells and test pile 1 occurs with zinc concentrations. Test pile Zn concentrations range from 0.5 – 2.5 mg/L in the effluent and up to 5.5 mg/L in the internal porewaters as measured by the soil water samplers. On the other hand, field cell Zn concentrations range between 0.4 to 17 mg/L, with the highest concentrations occurring in the marble diopside field cells. These high concentrations may be the result of the chance selection of high Zn-bearing materials, or perhaps due to the reasons previously described in Section 4.4.1.1.2.

That the test pile and field cell pH and alkalinity values are generally similar is rather expected based on open-system conditions. That specific conductance values for test pile 1 are 3 – 6 times higher than those of the field cell, despite the fact that the test pile is almost 10 times taller than the field cells, indicates that there is an accumulation of weathering products along the pathway, but that there is not a linear proportion between test pile and field cell SC values. That these results are non-linear may be a function of:

1. particle size differences,
2. preferential flow,
3. mixing,
4. continuous release,

5. oxygen availability, and/or
6. solubility controls (e.g., sorption, secondary precipitation, etc.).

Previous Class B field cells constructed by Golder (2006) indicate that there is a large variety in mineralogical composition of Class B waste rock at Antamina. Zinc concentrations in marble, hornfels and limestone field cells range between 0.002 and 0.2 mg/L (Golder, 2007b), which is 2 orders of magnitude below the test pile 1 field cells (Aranda, 2009). This large discrepancy between solute concentrations in various Class B effluent indicates that further mineralogical classification is required to distinguish between the more and less reactive sub-classes of this waste rock material. Further work is required to determine whether other Class B material will leach such high Zn concentrations.

4.8 SUMMARY

The following are the most salient conclusions from test pile 1 data:

1. test pile 1 chemistry results support evidence of sulphide mineral oxidation and a subsequent buffering of the generated acid,
2. chemistry shows distinct spatial and temporal variability in the pile with the outer region of the pile behaving like an open system whereas the internal pile behaves more like a partially-closed system,
3. elevated porewater solute concentrations and increased temperatures during the first wet season indicate an initial flushing of the weathering products of the most reactive particles. Increasing concentrations typically correlate with longer flowpath lengths, but the observed variability suggests the presence of pockets of elevated oxidation and dissolution rates, and reactive mineral contents,
4. concentrations do not change dramatically, which suggests that chemistry will evolve slowly over time (i.e., days and weeks and not hours or minutes),
5. pile structure and instrumentation location lead to variations in pile chemistry that are further complicated by transient flow mechanisms (matrix vs. macropore),
6. concentrations generally increase with depth in lines 1 and 2, and remain the same or actually decrease at depth in line 4, the latter is likely due to location differences (batter).

The effects of the pile batters and initial waste rock composition have direct results on effluent chemistry, with line 4/sub-lysimeter C showing the lowest concentrations, line 2/sub-lysimeter A showing the highest and line 1/sub-lysimeter B showing intermediate concentrations. Basal lysimeter D typically shows a range that is representative of all three sub-lysimeters,

7. despite the coarse nature of the waste rock, matrix-flow is the dominating flow mechanism in this pile (e.g., concentrations do not undergo rapid changes over a few hours), but SC data provides evidence that suggests macropore flow is present e.g., sharp increases in basal lysimeter D and sub-lysimeter C outflow result in sharp decreases in specific conductance. Further evidence of macropore flow is evident in the pH and Ca data,
8. temperature data indicates that sulphide mineral oxidation is occurring, and slight increases in some pile regions provides additional support that the heterogeneous pile will experience varying rates of pyrite oxidation that may result in creating local 'hot' spots of higher sulphide mineral oxidation,
9. despite Cu, Fe, Pb and other metals present in the waste rock (Chapter 2), these are all rapidly immobilized upon dissolution, indicating that the only metal in which attenuation mechanisms are not significantly present is zinc (i.e., exceeds receiving and discharging limits,
10. test pile 1 is relatively young and it is likely that conditions are not providing an optimal environment (pH, sulphide oxidation, temperature, etc.) for the establishment of significant microbial consortia that catalyze sulphide mineral oxidation (Lin and Herbert, 1997),
11. there is little evidence of thermal-induced convection, which may indicate that most of the gas exchange between the pile and the atmosphere is supported through wind-driven advection near the outer shell and diffusion-dominated transport towards the interior, and
12. initial pore gas analyses indicate that oxygen remains at near-atmospheric levels throughout the pile, signifying that either sulphide mineral oxidation is occurring at low levels or there is rapid replenishment of oxygen succeeding these reactions. Based on the presence of sulphate ions in solution, it is evident that sulphide mineral oxidation is occurring and that oxygen is being replenished to some extent.

TABLES

Table 4.1. Parameter comparison between basal-lysimeter and composite tank.

		Average							
		Specific Conductance	pH	Zn	Ca	Na	Mg	SO4	Alkalinity
		(Field) uS/cm	(Field)	Dissolved mg/L	Dissolved mg/L	Dissolved mg/L	Dissolved mg/L	Dissolved mg/L	Total mg/L
Wet	D	2251	7.716	1.19	504.3	10.9	20.5	1081.2	72.1
	E	2369	8.055	1.20	509.2	11.3	20.4	1102.9	69.7
Dry	D	2606	7.595	1.50	592.6	12.4	23.2	1390.6	81.6
	E	2505	8.120	1.27	561.5	13.5	22.3	1263.4	74.3

Table 4.2. Temperature comparison between top and bottom of pile.

		Mean Temperature [°C]		
		Water Year (1-Oct-2007 to 30-Sept-2008)	Wet Season (1-Oct-2007 to 30-Apr-2008)	Dry Season (1-May-2007 to 30-Sept-2008)
	Top of Pile	7.6	7.6	7.7
	Bottom of Pile	5.8	5.8	5.7
	Difference	1.8	1.7	2.0
	Air Temperature	5.6	5.7	5.5

*based on temperature data from instrumentation lines 2 and 3

Table 4.3. Solute discharging and receiving limits

Parameter	Units	Discharge Limit ¹	Notes	Receiving Limit ¹	Notes
As - dissolved	mg/L	0.5 – 1	MEM ²	0.2	GWL-III ⁵
Cu - dissolved	mg/L	0.3 – 1	MEM ²	0.022 – 0.025	CMA-RW ⁶
Fe - dissolved	mg/L	1 – 2	MEM ²		
Pb - dissolved	mg/L	0.2 – 0.4	MEM ²	0.1	GWL-III ⁵
pH - field	pH Unit	6 - 9	MEM ²	6 – 9	GWL-III ⁵
Mo - dissolved	mg/L	–	–	0.2	ECT ⁷
Zn - dissolved	mg/L	0.5 – 1	CMA ³ /WB ⁴	0.13 – 0.21	GWL-III ⁵ , ECT ⁷
S	mg/L			0.002	GWL-III ⁵

¹ as of 2006 (Golder, 2006)

² MEM: Peruvian Ministry of Environment and Mines

³ CMA: Compañía Mineral Antamina standards

⁴ WB: World Bank.

⁵ GWL-III: General Water Law – Class III

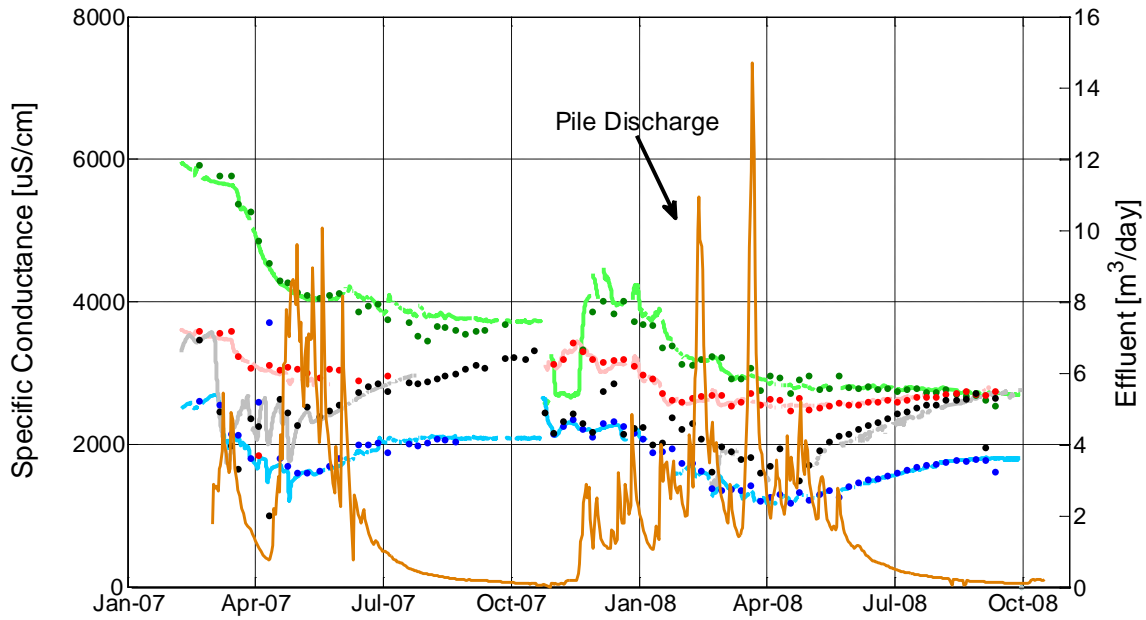
⁶ CMA-RW: Dissolved Cu and Zn to replace CMA Total Cu and Zn.

⁷ ECT: eco-toxicity test performed by Stantec.

Table 4.4. Minerals modeled to be near saturation in basal lysimeter effluent.

Mineral Type	Mineral Name	Mineral Composition
Sulphate	Anhydrite	CaSO ₄
	Barite	BaSO ₄
	Celestite	SrSO ₄
Carbonate	Aragonite	CaCO ₃
	Dolomite (ordered and disordered)	CaMg (CO ₃) ₂
	Smithsonite	ZnCO ₃
Oxide	Chalcendony	SiO ₂
	Cristobalite	SiO ₂
	Quartz	SiO ₂
Other	Fluorite	CaF ₂
		Zn(OH) ₂ (γ),
		ZnCO ₃ ·H ₂ O
		ZnO(active).

FIGURES



*solid lines indicate wet-dry season transition; dotted lines indicate dry-wet transition.

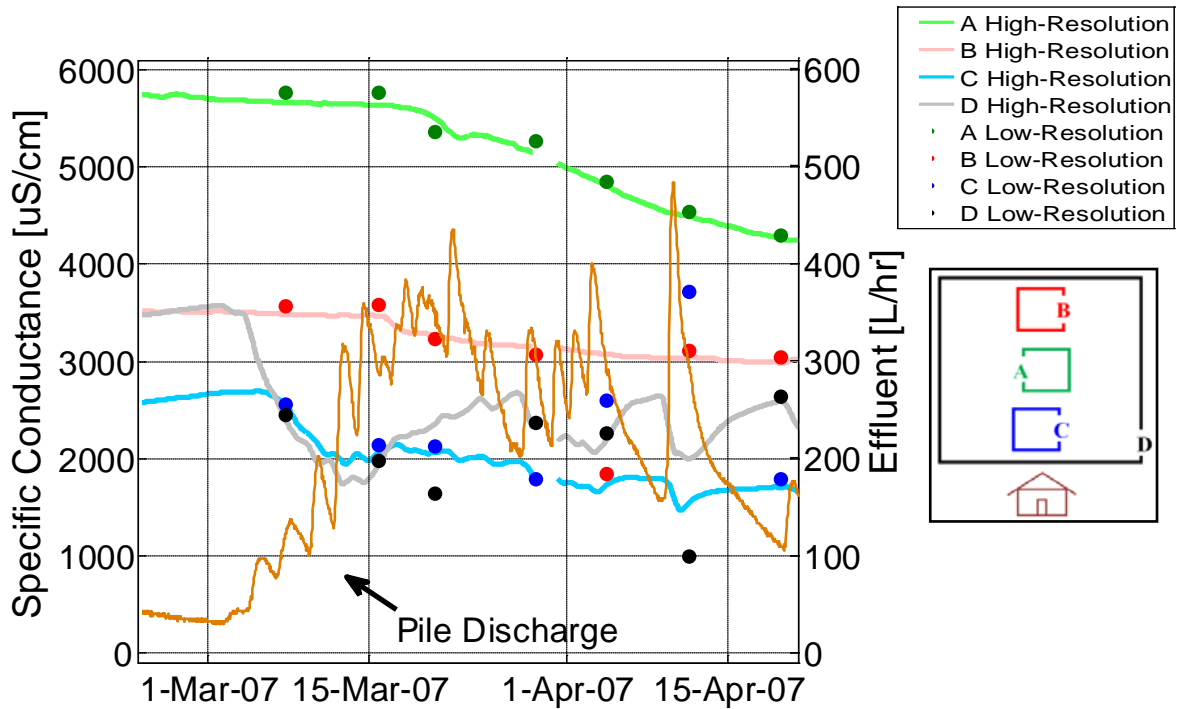


Figure 4.1. Continual and weekly-obtained specific conductivity vs. and pile discharge.

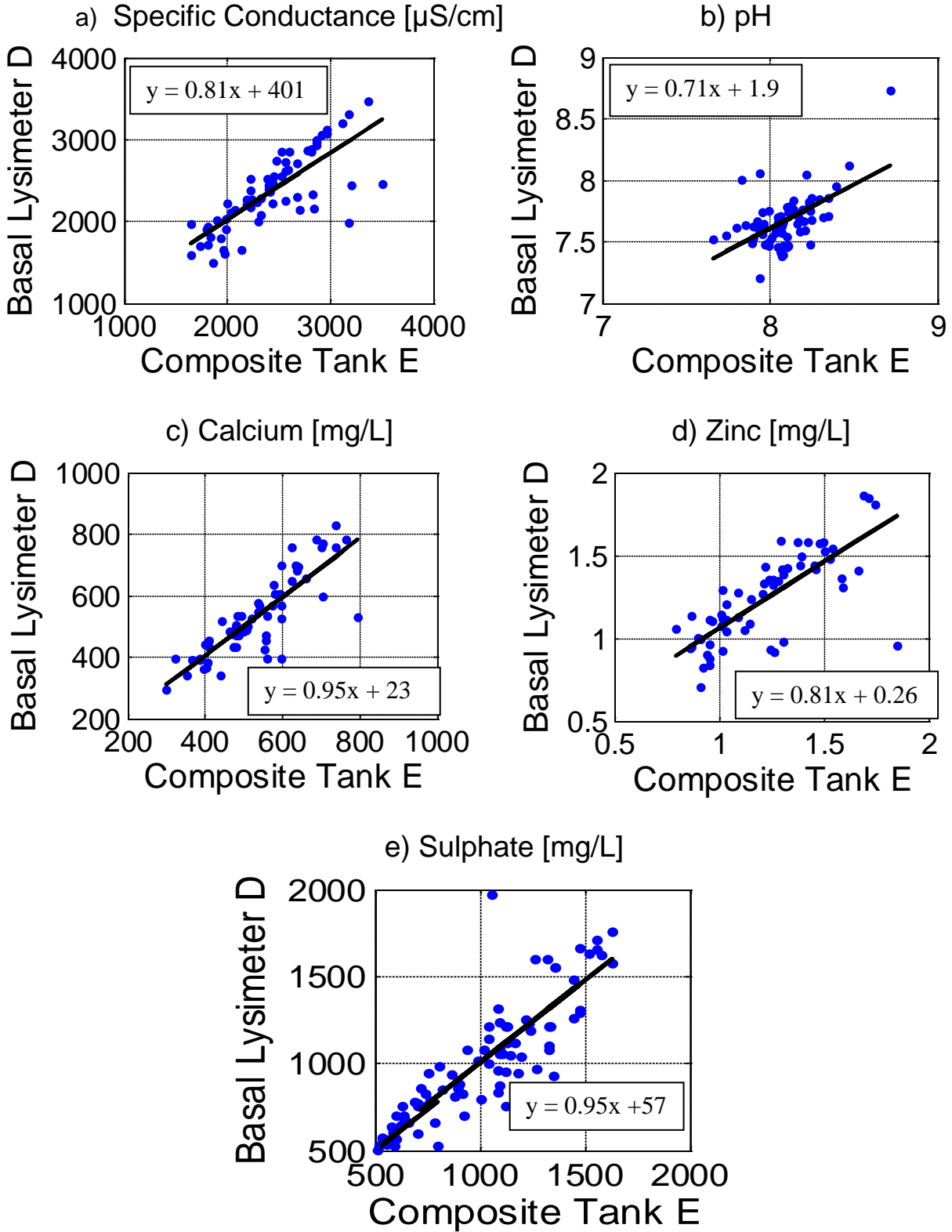
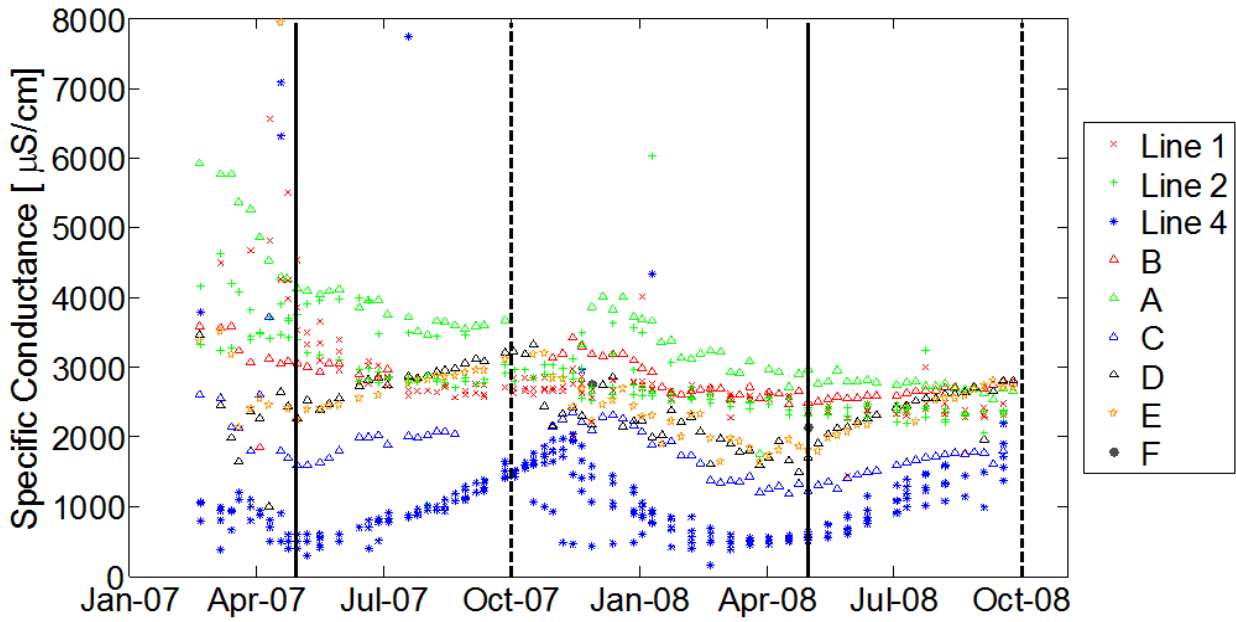


Figure 4.2. Parameter comparison between basal lysimeter and composite tank.



*solid lines indicate wet-dry season transition; dotted lines indicate dry-wet transition.

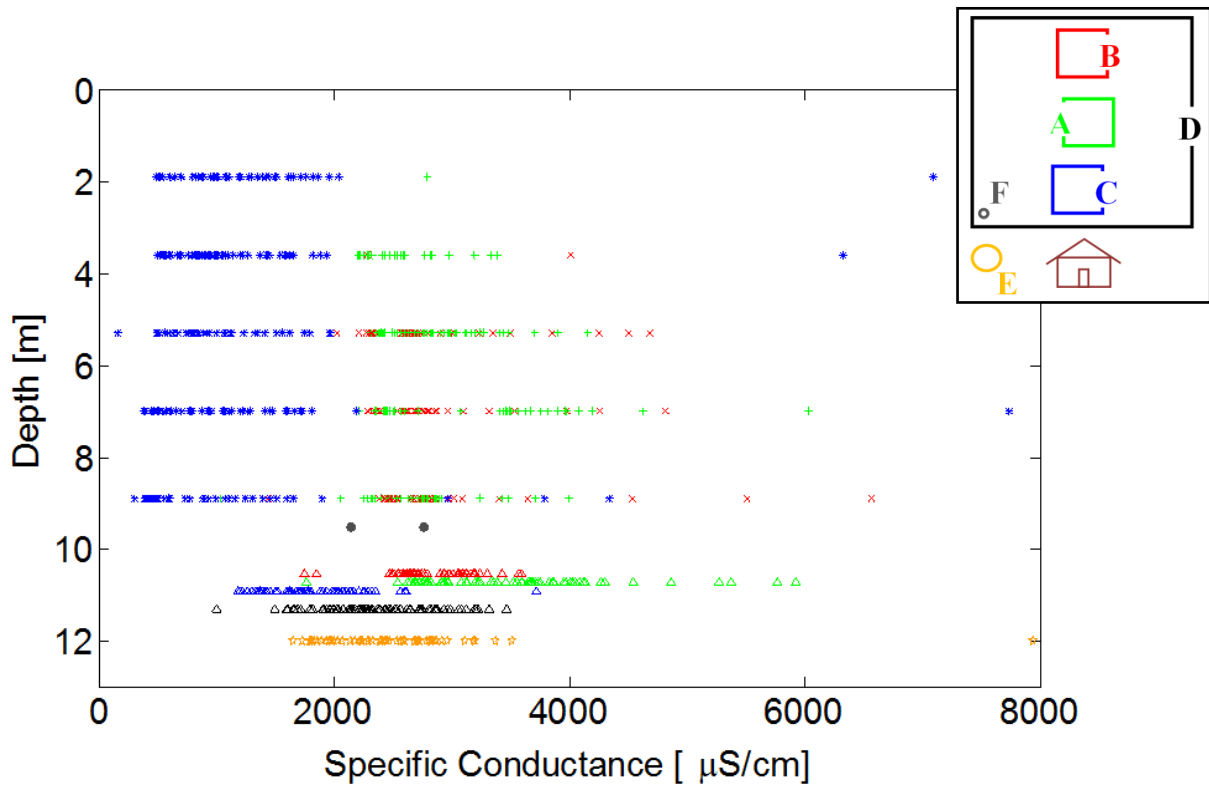


Figure 4.3. Temporal and spatial distribution of specific conductance.

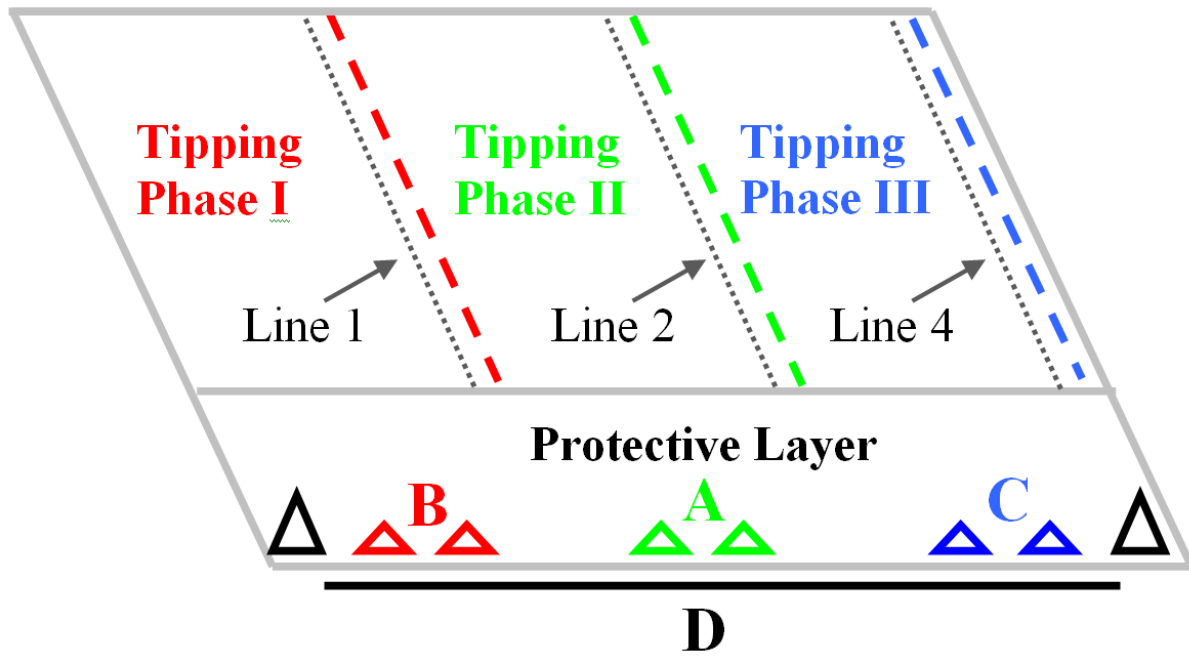
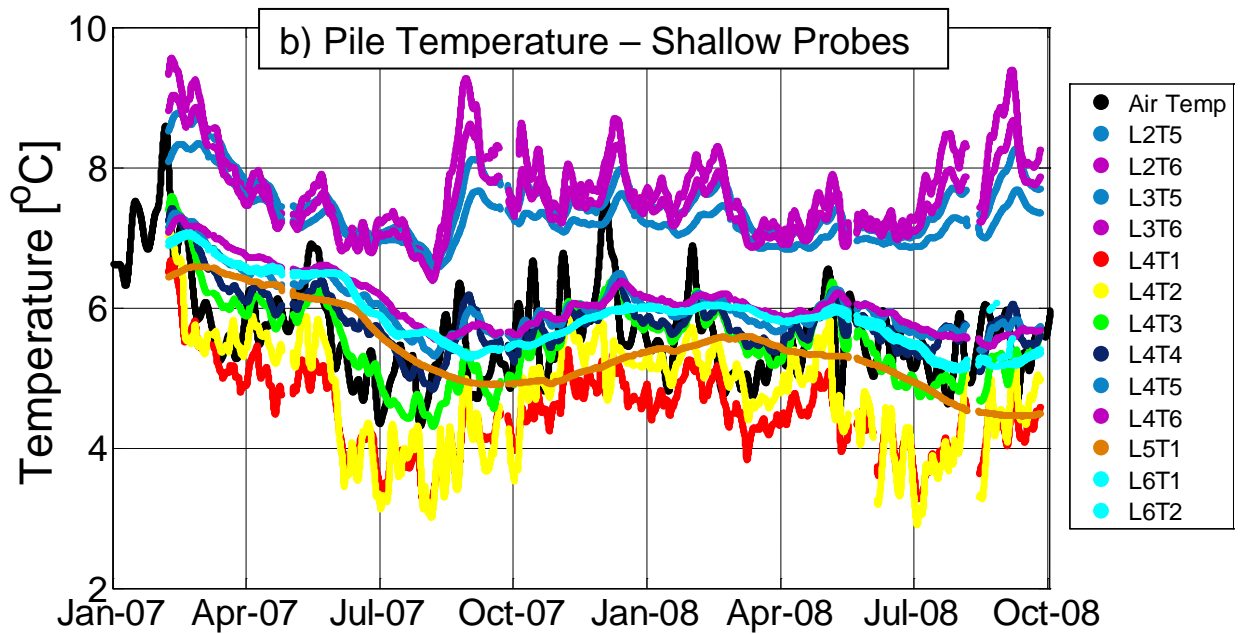
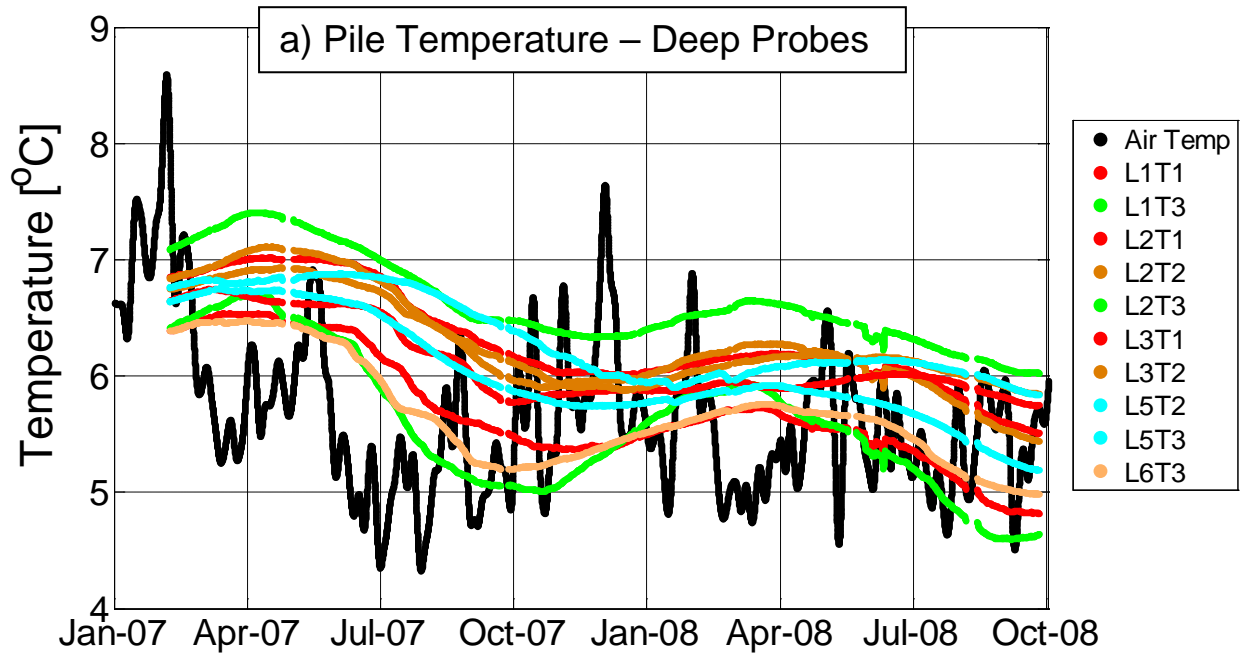


Figure 4.4. Cross-sectional diagram of four construction stages and four lysimeters



*all temperature probes are located within test pile 1

Figure 4.5. Internal and external pile temperature variation.

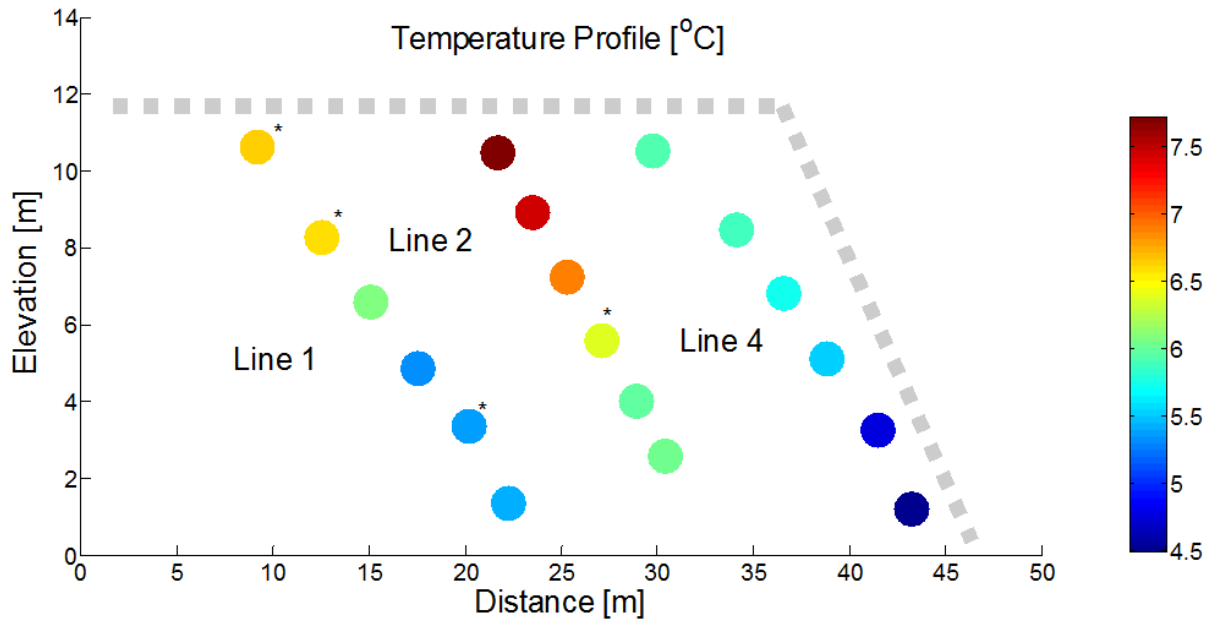
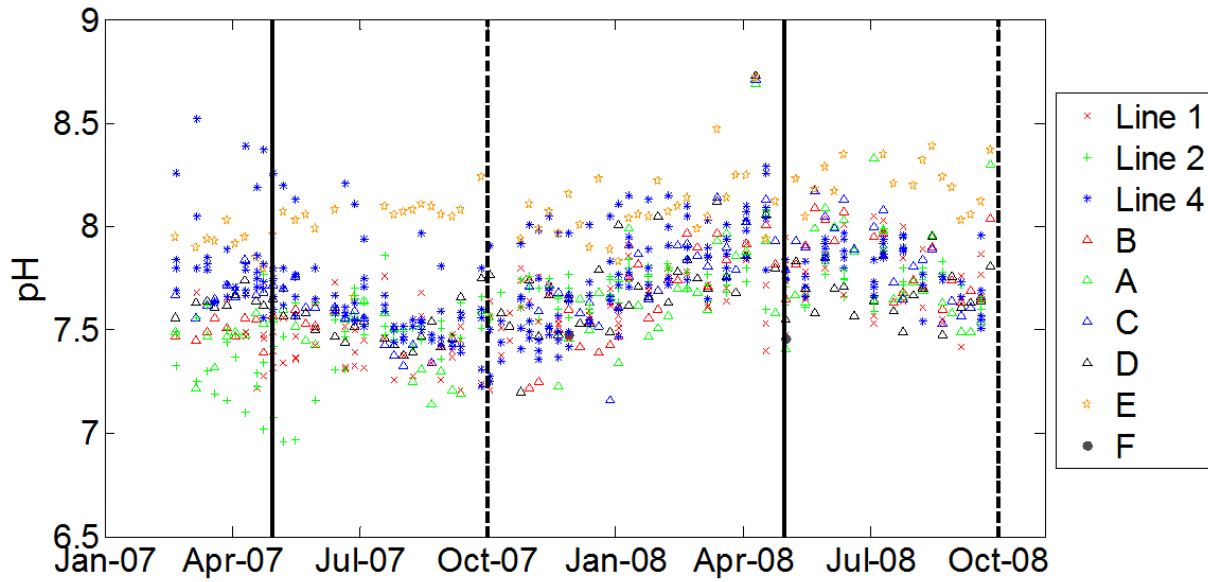


Figure 4.6. Average temperatures in lines 1, 2 and 4 over the water year.



*solid lines indicate wet-dry season transition; dotted lines indicate dry-wet transition.

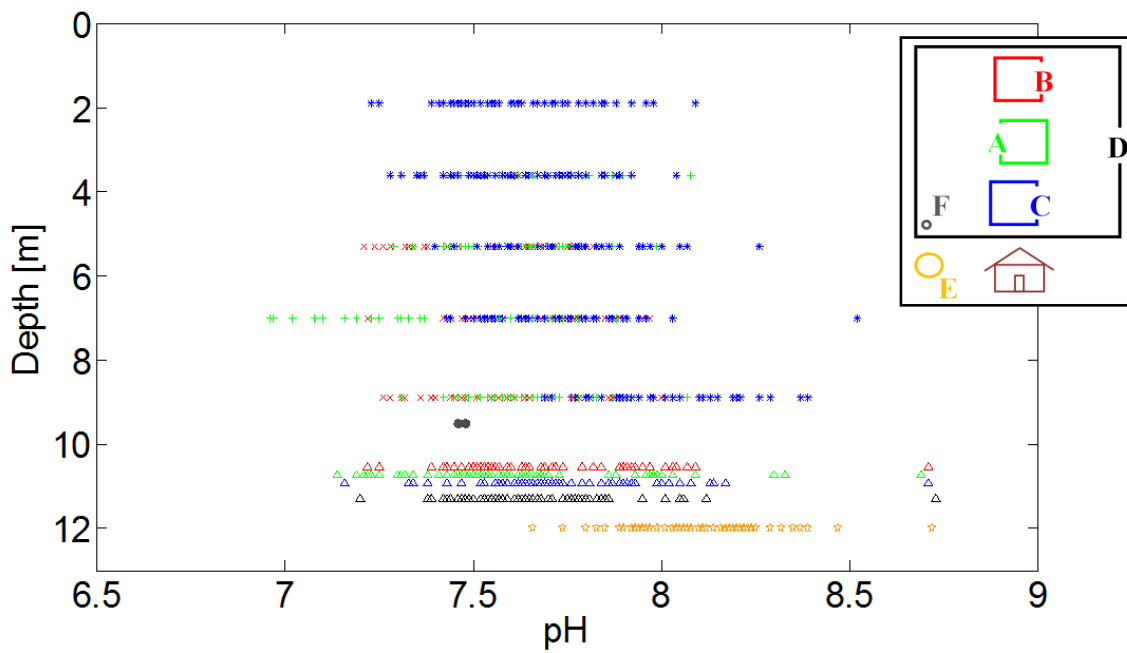
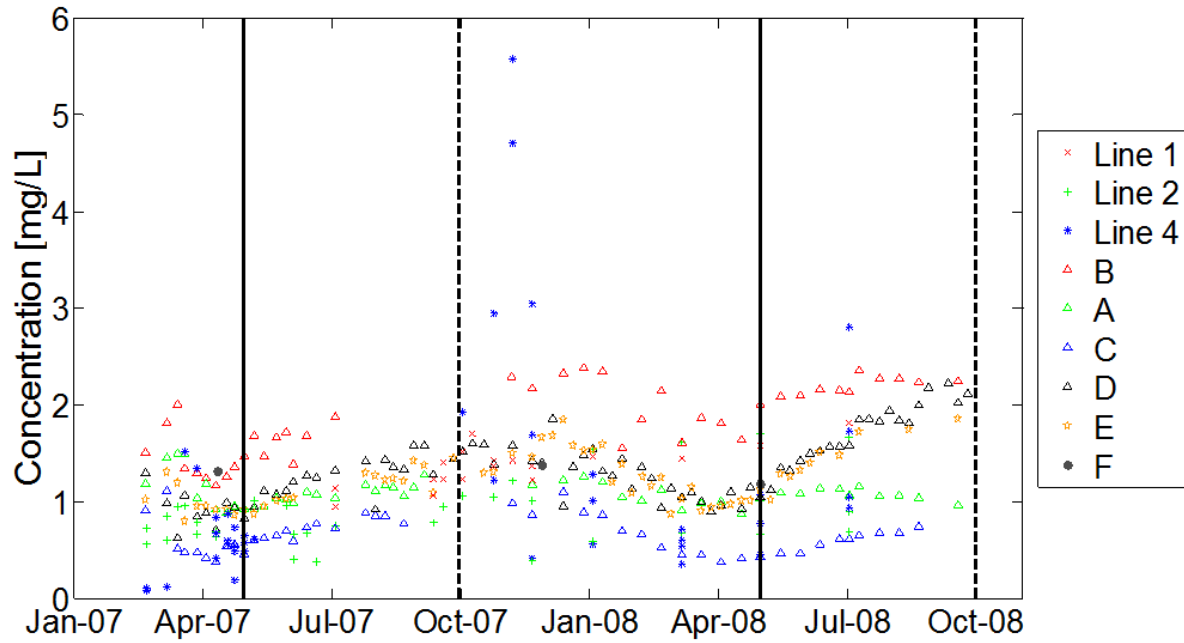


Figure 4.7. Temporal and spatial distribution of pH.



*solid lines indicate wet-dry season transition; dotted lines indicate dry-wet transition.

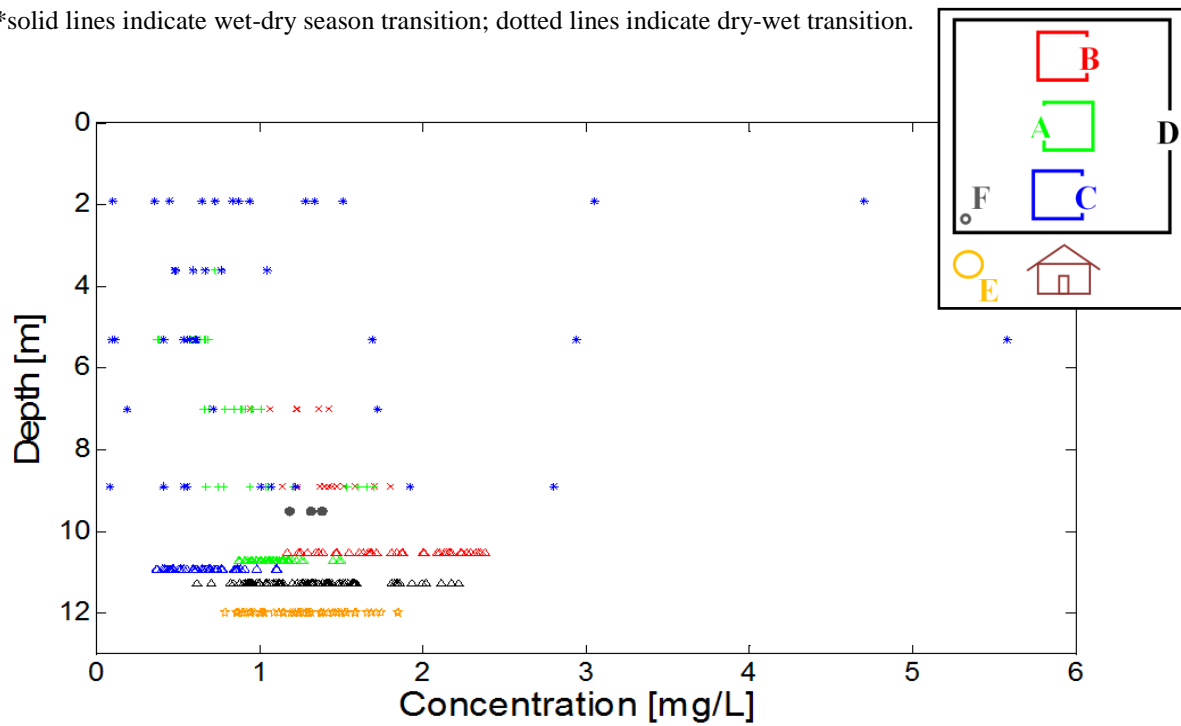


Figure 4.8. Temporal and spatial distribution of Zn.

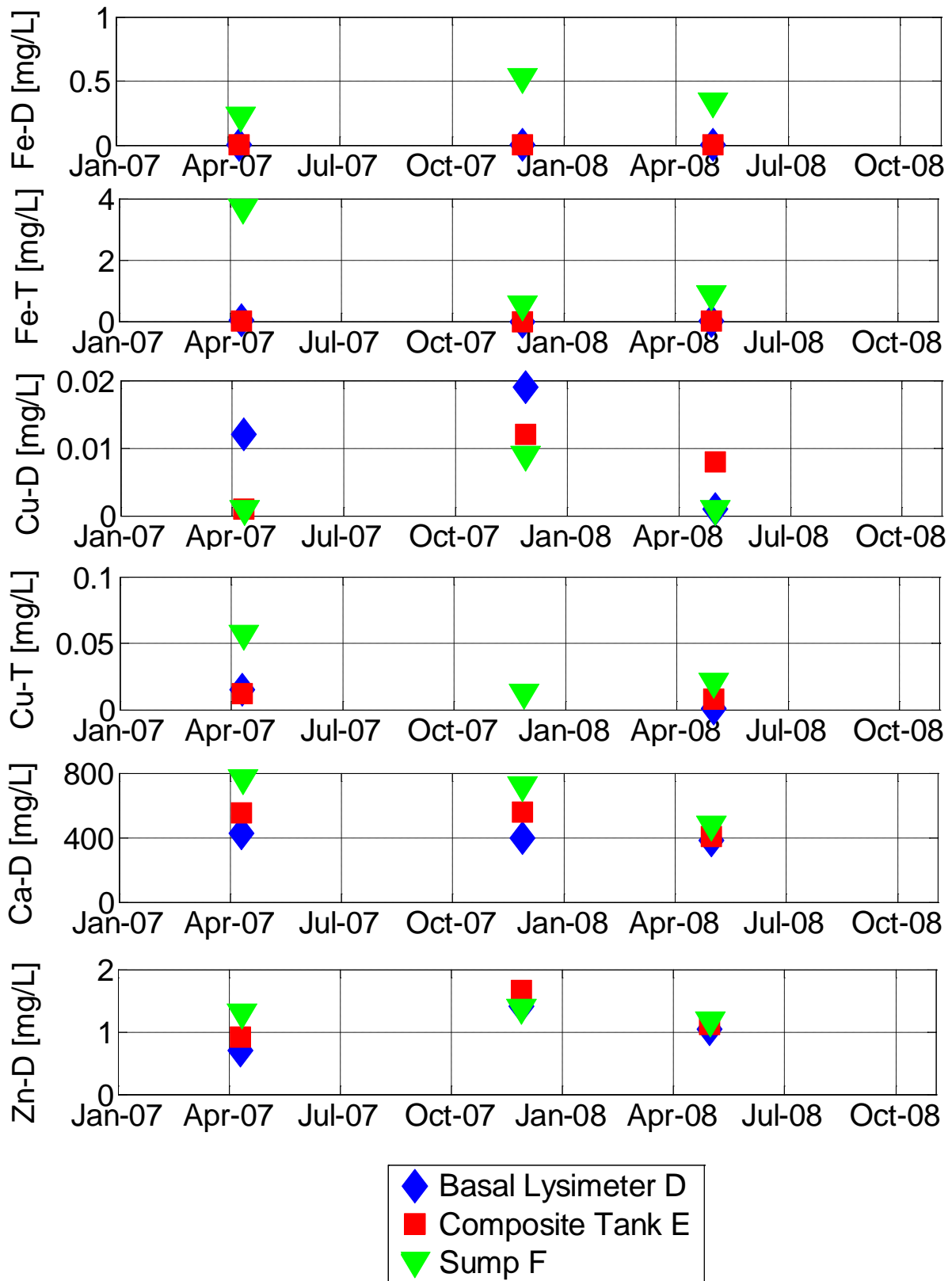
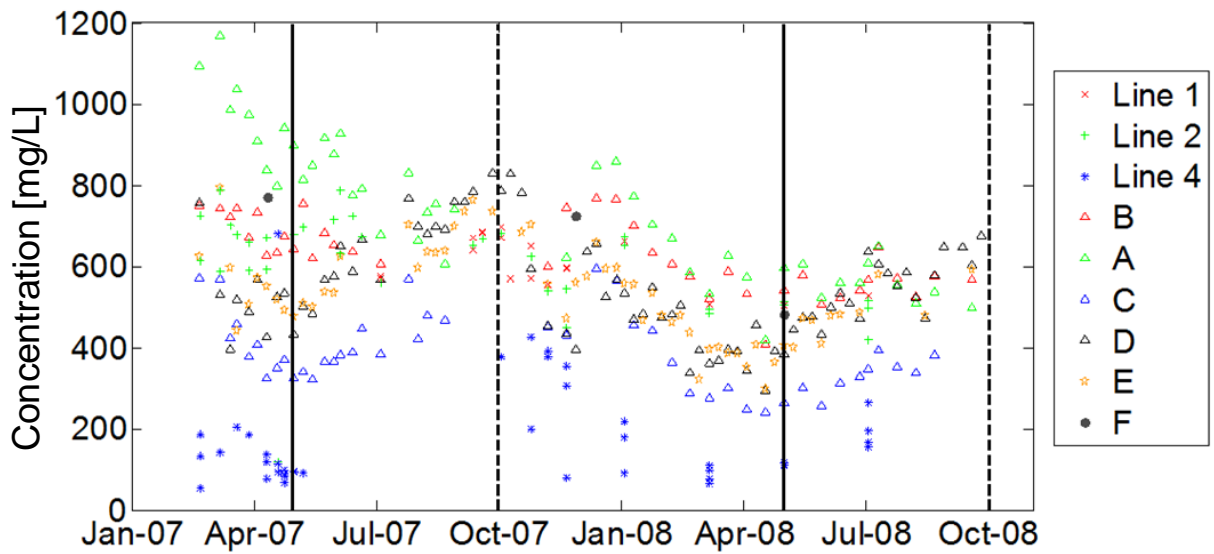


Figure 4.9. Sump comparison to basal lysimeter and composite tank.



*solid lines indicate wet-dry season transition; dotted lines indicate dry-wet transition.

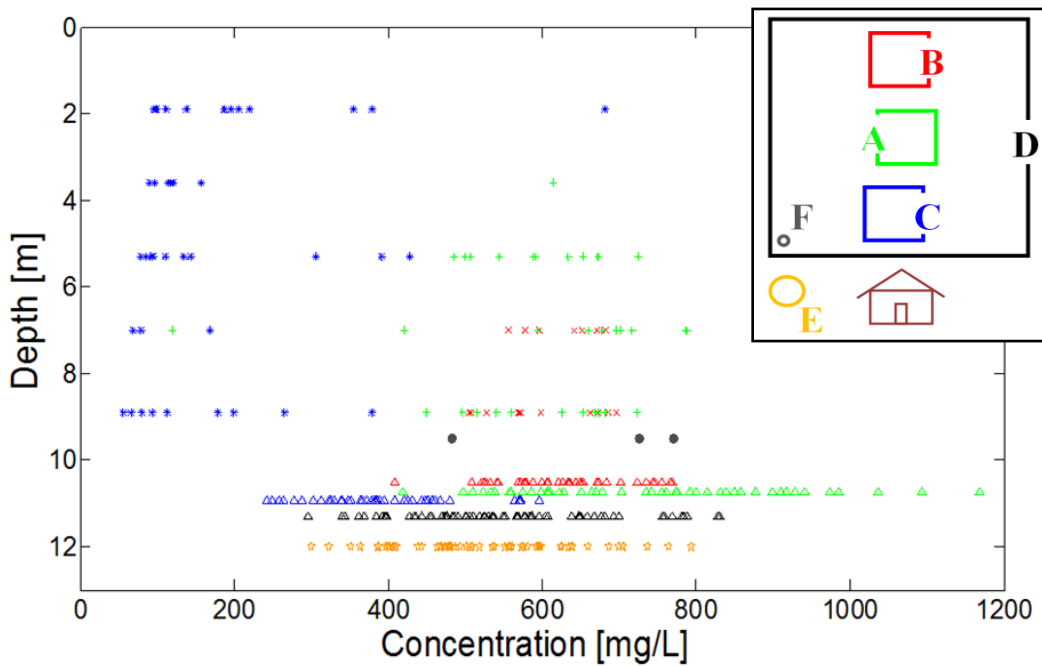
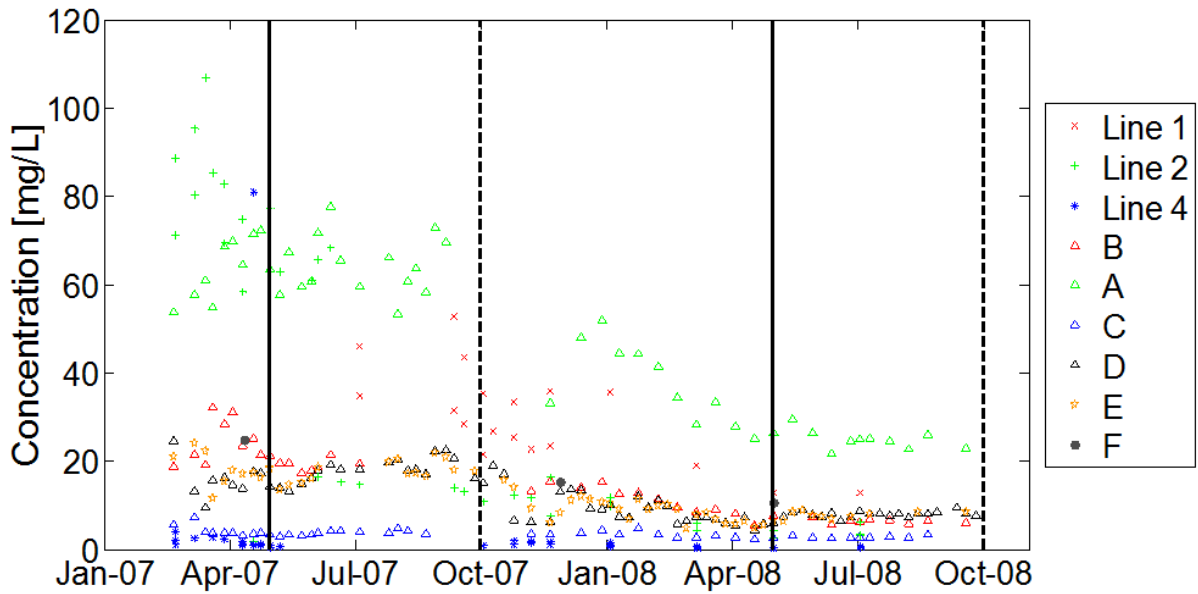


Figure 4.10. Temporal and spatial distribution of Ca.



*solid lines indicate wet-dry season transition; dotted lines indicate dry-wet transition.

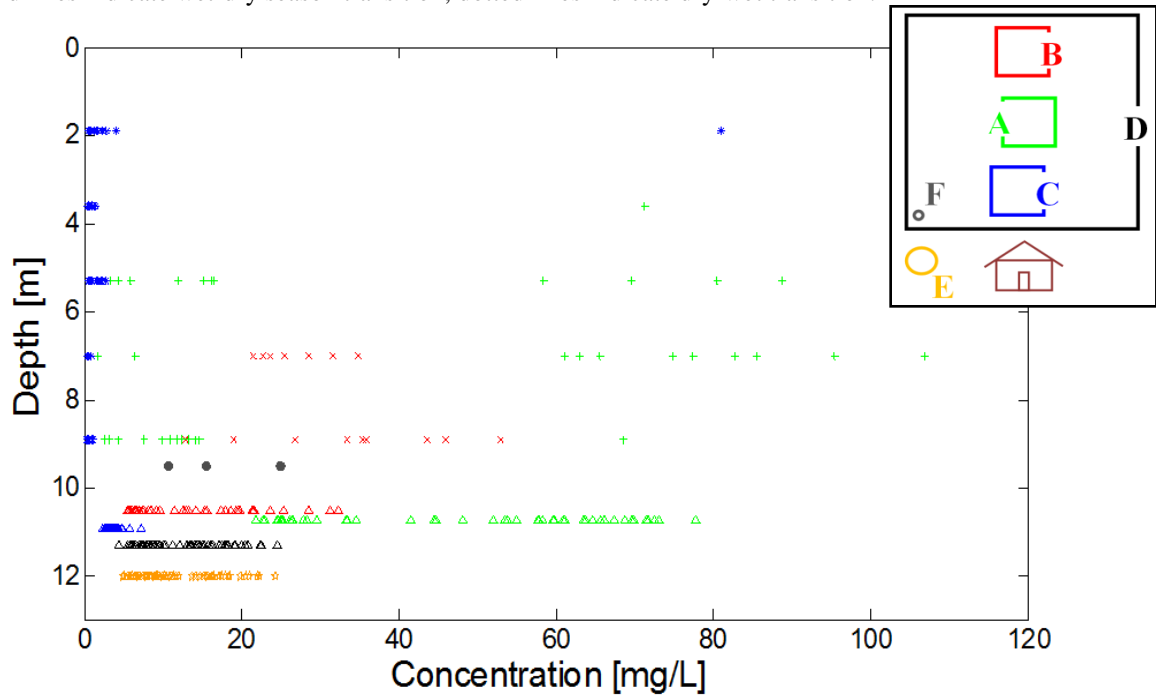
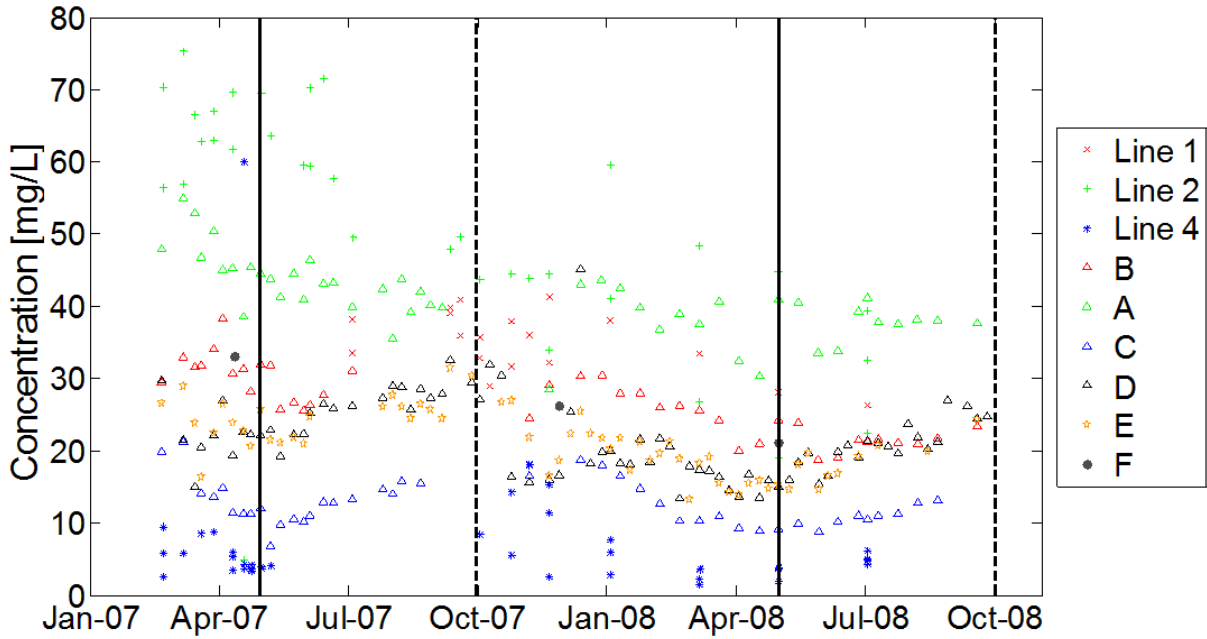


Figure 4.11. Temporal and spatial distribution of Na.



*solid lines indicate wet-dry season transition; dotted lines indicate dry-wet transition.

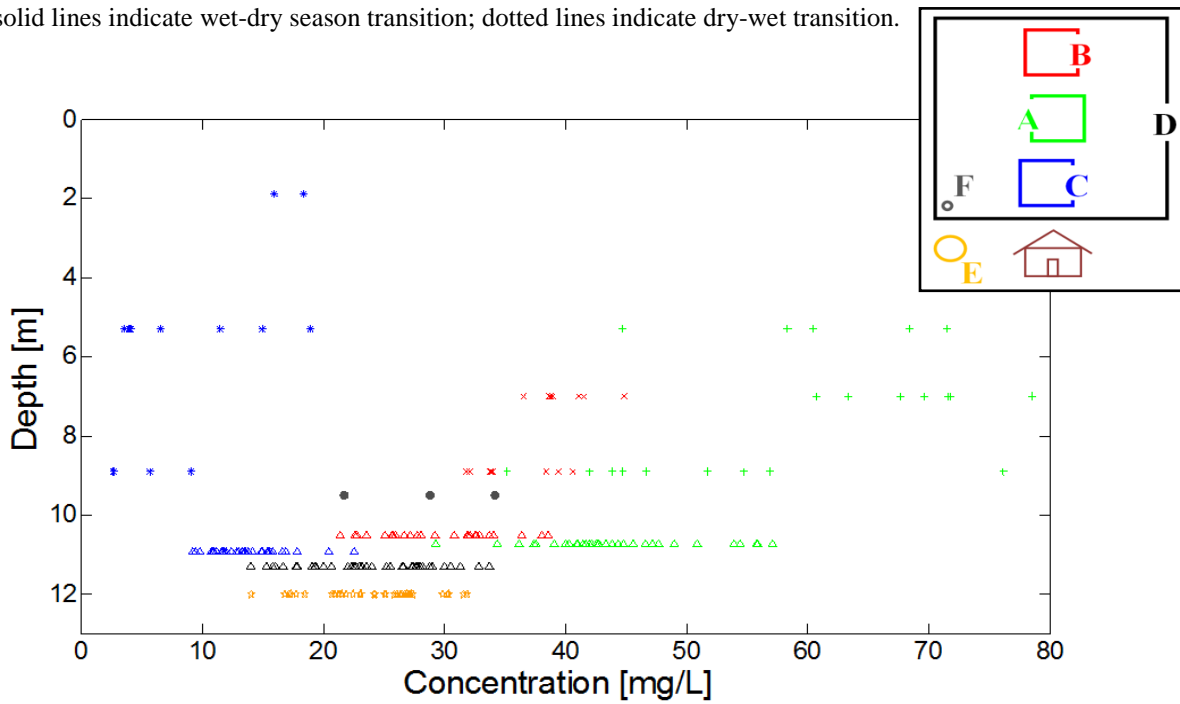
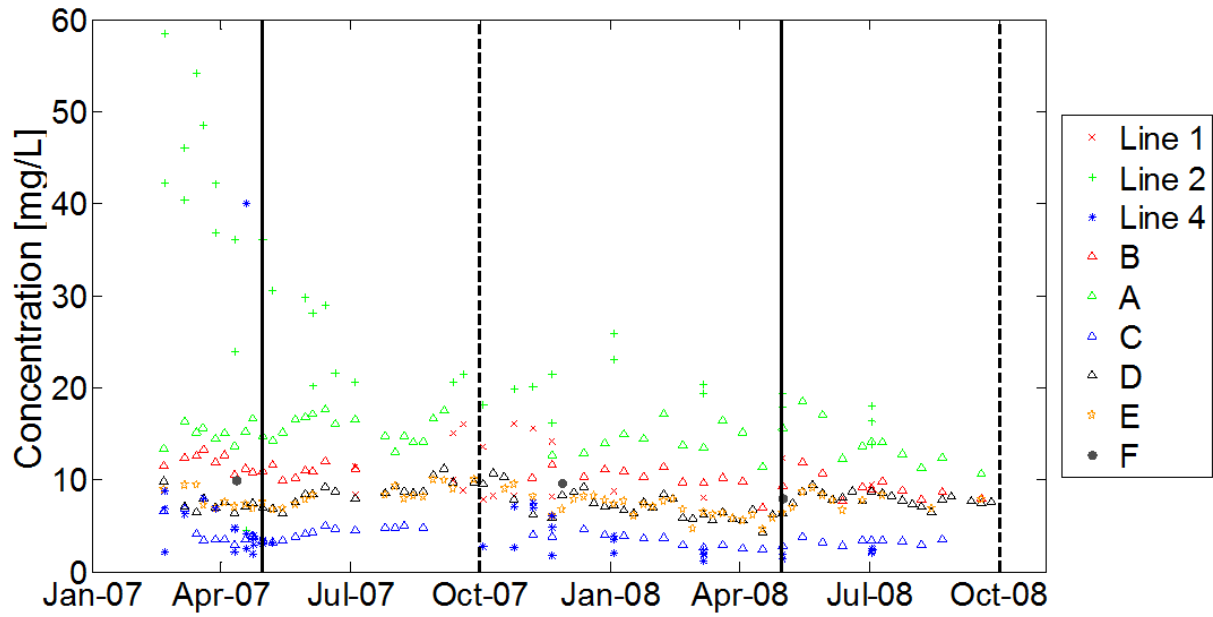


Figure 4.12. Temporal and spatial distribution of Mg.



*solid lines indicate wet-dry season transition; dotted lines indicate dry-wet transition.

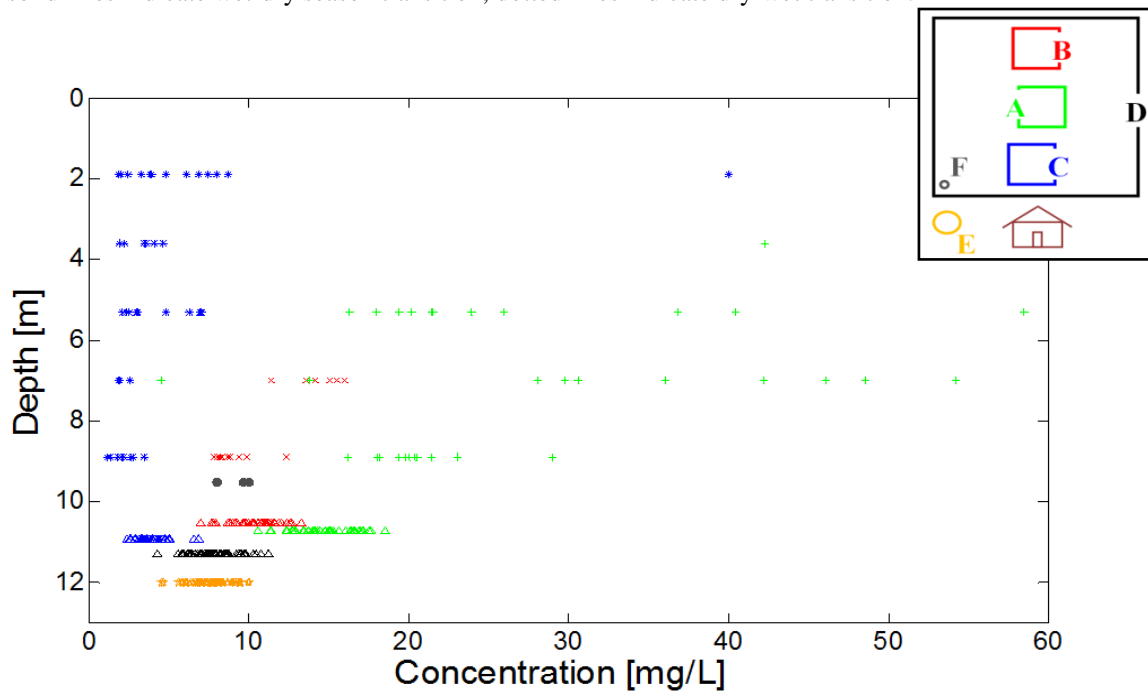
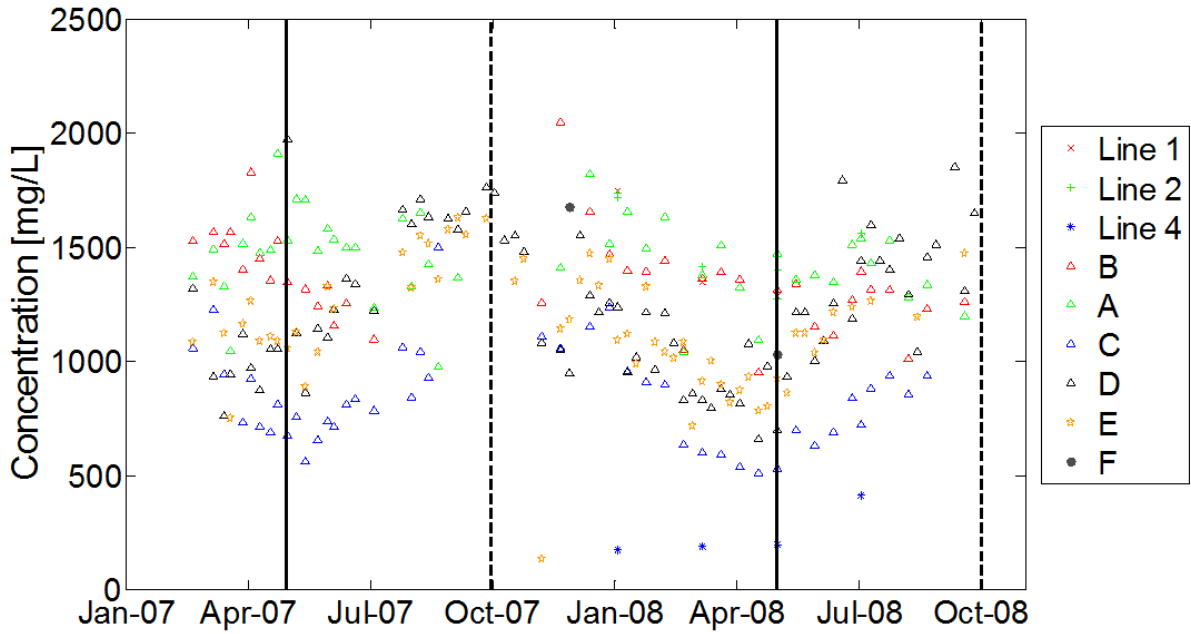
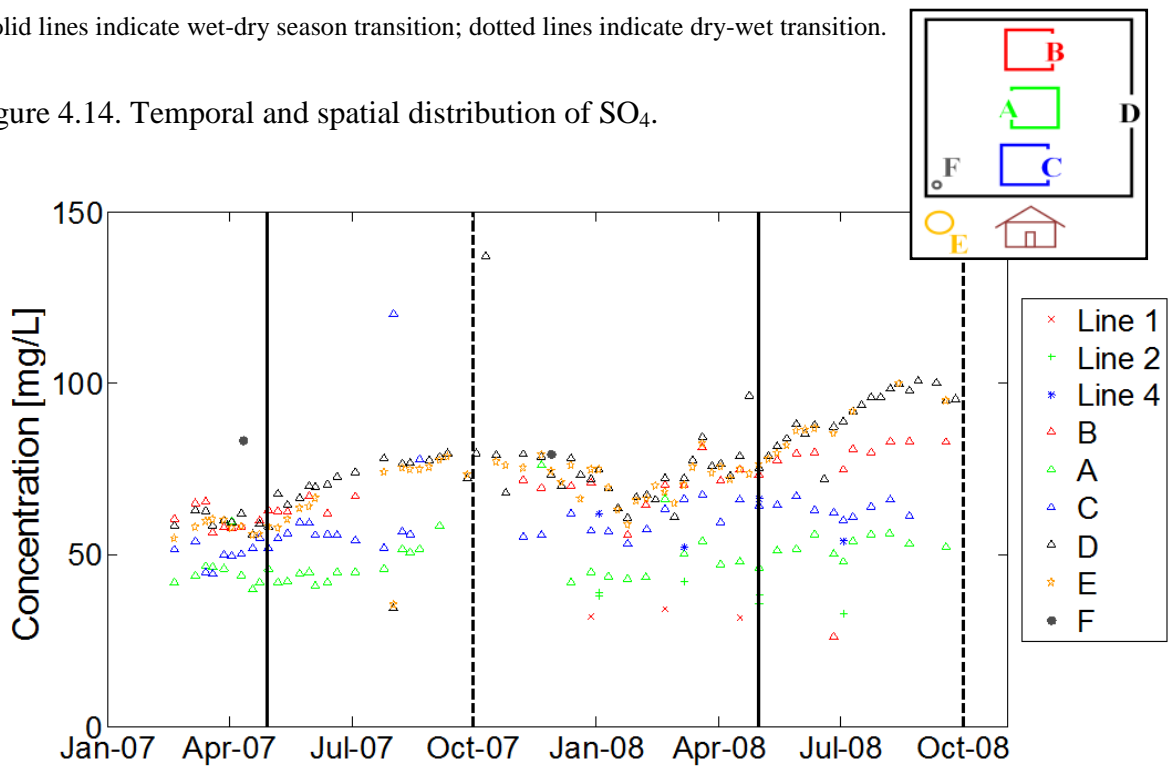


Figure 4.13. Temporal and spatial distribution of K.



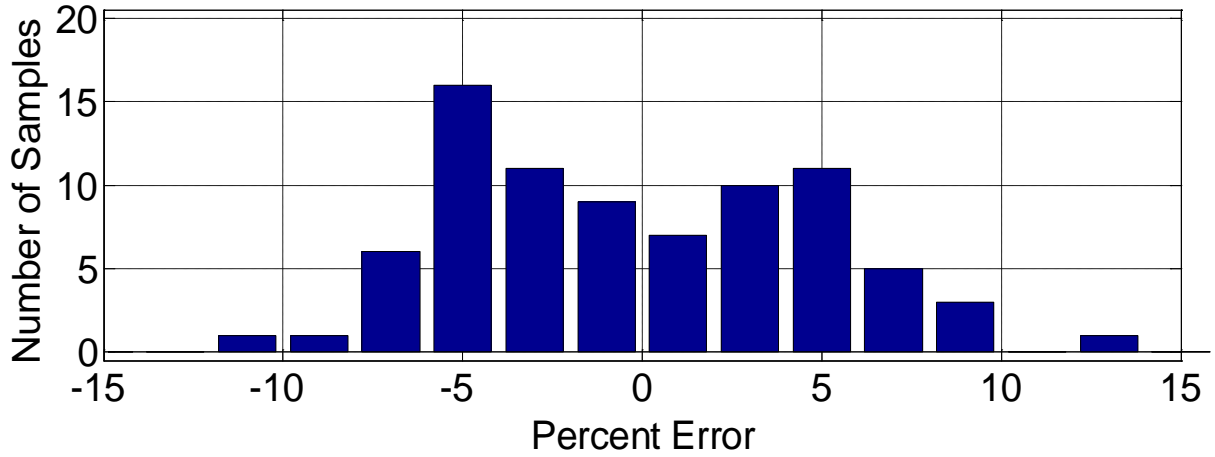
*solid lines indicate wet-dry season transition; dotted lines indicate dry-wet transition.

Figure 4.14. Temporal and spatial distribution of SO₄.



*solid lines indicate wet-dry season transition; dotted lines indicate dry-wet transition.

Figure 4.15. Temporal and spatial distribution of alkalinity.



*the largest absolute error is 41 %.

Figure 4.16. Percent charge balance error of PHREEQC model of basal lysimeter data.

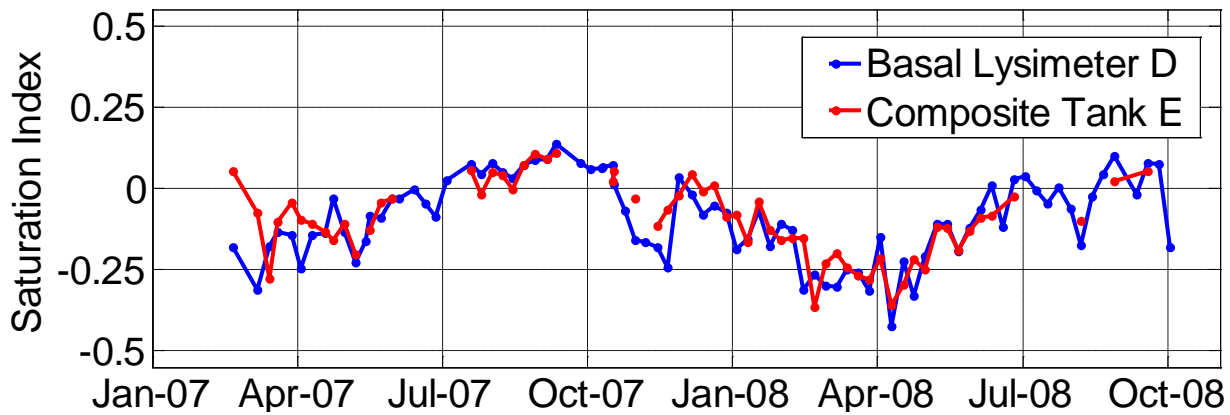


Figure 4.17. Gypsum SI for the basal lysimeter D and composite tank E.

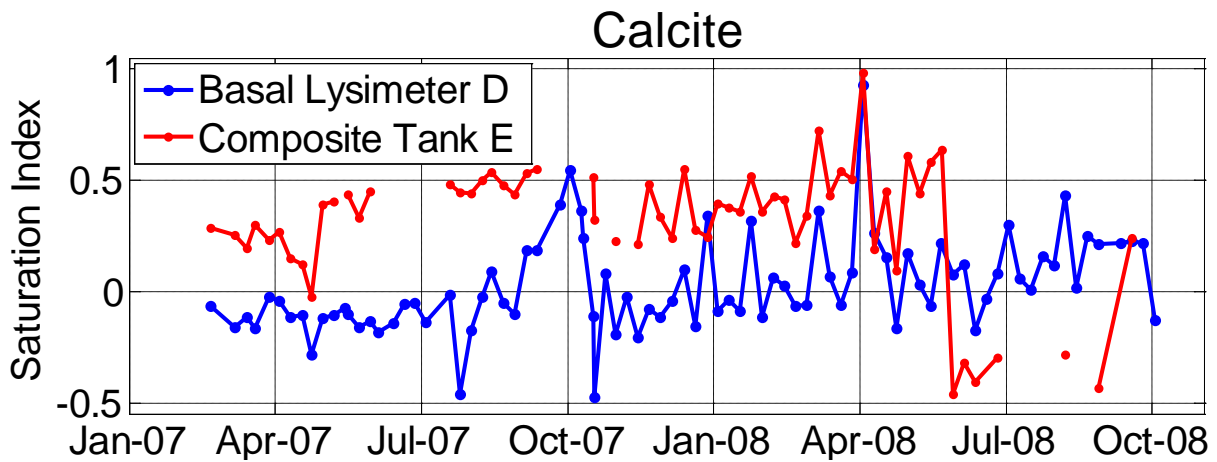


Figure 4.18. Calcite SI for the basal lysimeter D and composite tank E.

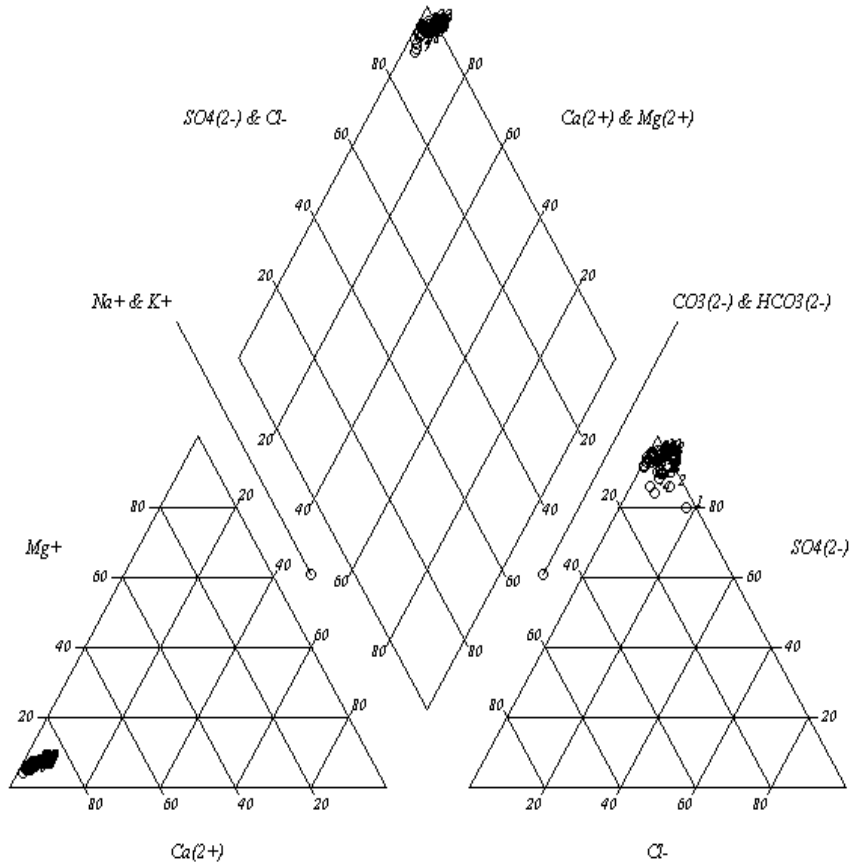


Figure 4.19. A trilinear Piper Plot of basal lysimeter D effluent

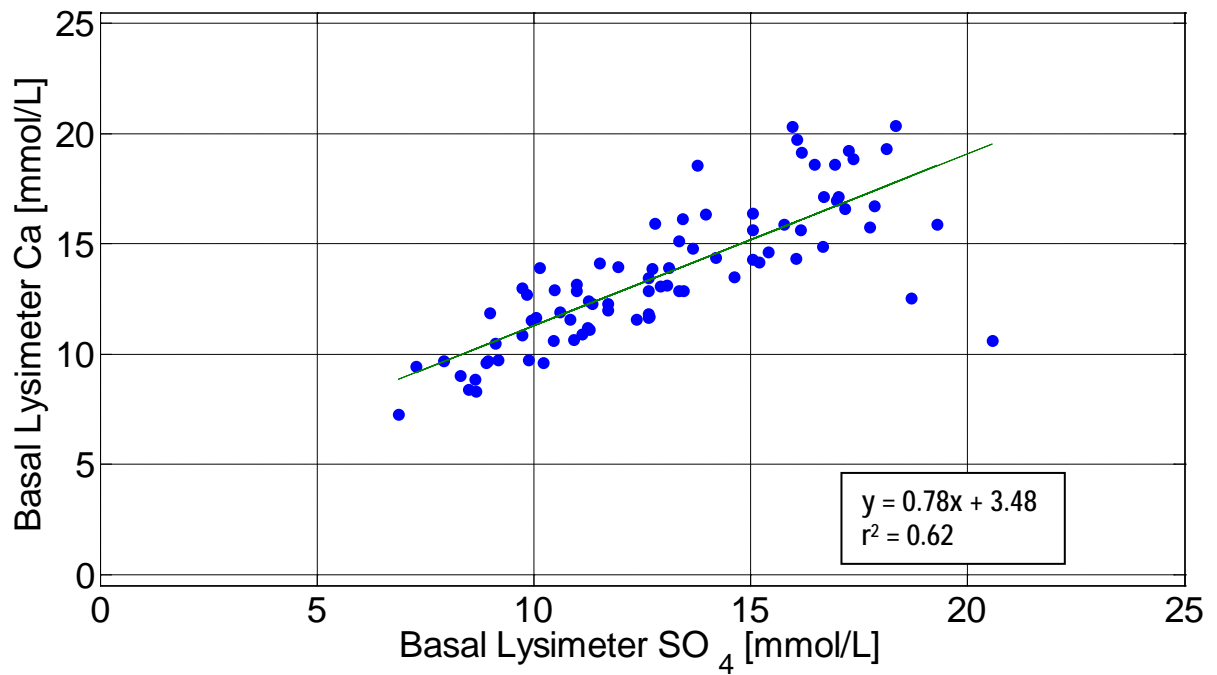


Figure 4.20. Regression analysis of Ca and SO₄ at basal lysimeter D.

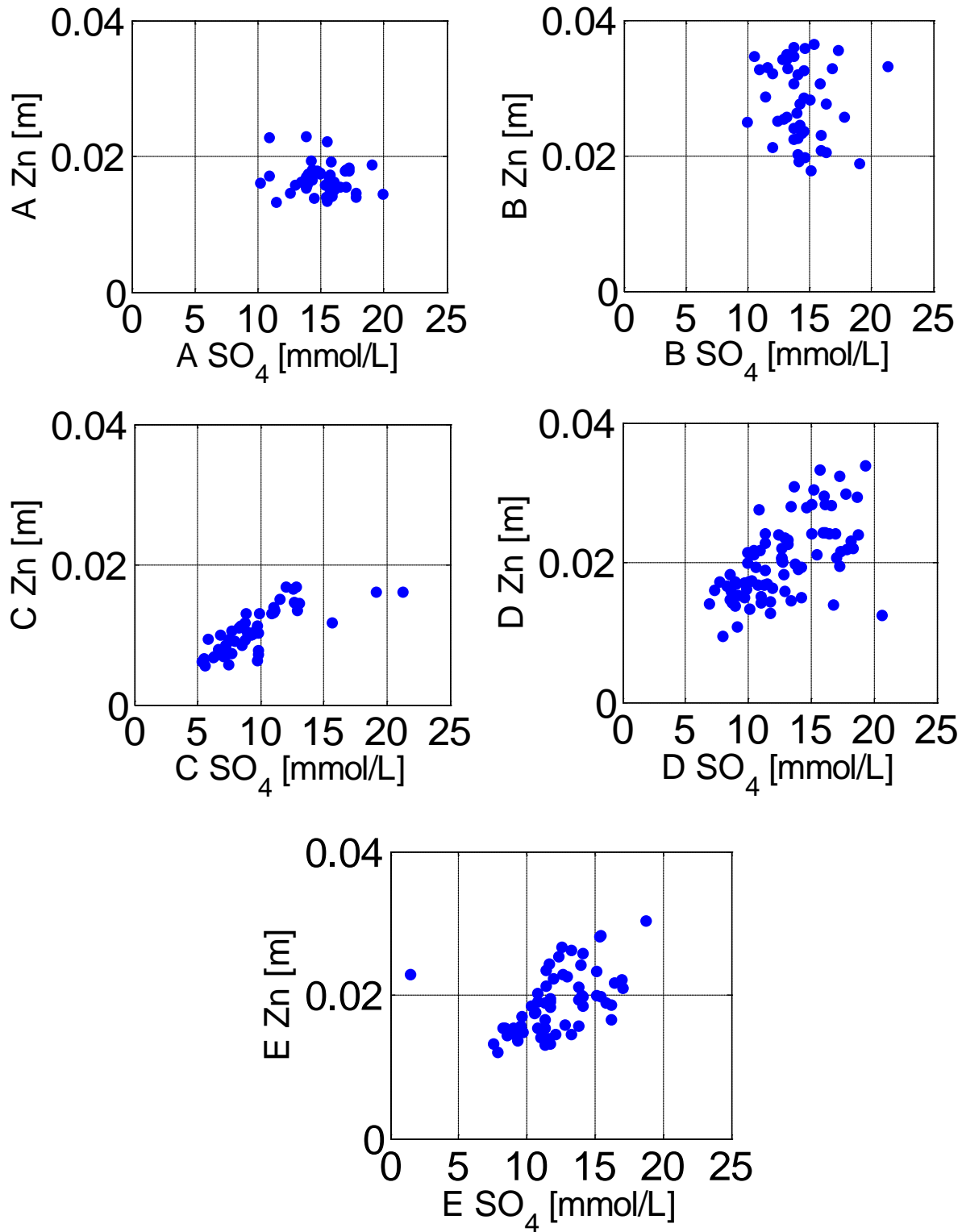


Figure 4.21. Correlation between SO_4 and Zn at sub-lysimeters A, B & C, basal lysimeter D, and composite tank E.

5 RESULTS: TEST PILE MASS LOADINGS

Solute mass loadings represent a critical component in understanding and predicting the metal release capability of a waste rock environment. The solute mass loading behaviour of test pile 1 is examined based on flow and chemistry results presented in Chapters 3 and 4, respectively. This chapter will:

1. examine the relationships between flow, chemistry and solute mass loading of test pile 1,
2. determine solute-specific correlations to specific conductance at various lysimeters,
3. compare low- and high-resolution mass loading estimates for SO₄, Ca and Zn,
4. determine mechanisms that control solute mass loadings,
5. develop first-pass estimations of metal depletion rates that will aid in characterizing the relative strength of metal release mechanisms dominating the first 2 years of pile operation, and
6. compare test pile 1 loading rates with those from field cells of the same material.

5.1 INITIAL PILE COMPOSITION

The solid-phase elemental composition of waste rock placed in the pile from each of the four material placement stages (protective layer and Tipping Phases I-III) is summarized in Table 2.4. The average elemental mass is calculated using the solid phase elemental concentration s [%] and mass M [kg] of waste rock associated with each placement stage. When normalized by the total pile mass M_T [kg], the average proportion of each element in the pile, s_P [%], is calculated using the following weighted average calculation:

$$s_P = [(s_1 * M_1) + (s_2 * M_2) + (s_3 * M_3) + (s_4 * M_4)]/M_T \quad [5-1]$$

where materials used in the protective layer, Tipping Phase I, Tipping Phase II and Tipping Phase III are denoted by subscripts 1, 2, 3 and 4, respectively. The most notable results indicate that calcium, sulphur and zinc make up nearly 27.1 and 0.61 and 0.09 % of the pile by weight, respectively (Table 2.4).

5.2 SOLUTE MASS LOADINGS

Solute mass loading is a transient term based on transient flow and variable effluent chemistry. Mass loading M_L [mg/week] is calculated from the volume of water Q [L/week] and solute concentration c [mg/L] at a given time based on the following relationship:

$$M_L = Q * c \quad [5-2]$$

Using equation 5-2, the solute mass loading of this test pile is calculated using two different approaches:

1. a 'low-resolution' approach (Section 5.2.1, below), and
2. a 'high-resolution' approach (Section 5.2.2, below)

The former approach is based on near-weekly geochemical sampling and flow, whereas the latter is based on continually-logged electrical conductivity and flow measurements. The resulting mass loading rates are presented in mg/week. Loadings are then normalized by the waste rock mass of the pile ($M_T \sim 20,000$ metric tonnes; Chapter 2) to obtain a mass loading M_L [mg/kg/week] described as 'mg of solute released per kg of waste rock per week'. To obtain mass loading rates for each of the four lysimeters, the loadings rates are normalized by the estimated mass of waste rock lying directly above the 36 x 36 m basal lysimeter or 4 x 4 m sub-lysimeters.

Solute mass loadings are based on the flow estimates presented in Chapter 3, where methods used to account for data gaps in flow are explained, and chemistry presented in Chapter 4. Sulphate is the dominant anion with the highest concentration in the effluent waters, calcium is the dominant cation, and Zn is the only trace heavy metal found at any level of interest (e.g., above the discharge limit). Calcium is an indicator of acid neutralization by carbonates. These three solutes serve as the basis for the following loading discussion. Based on the sampling schedule described in Chapter 2, weekly chemistry data is not available for all lysimeters (e.g., only when they are flowing). For the following low-resolution mass loading calculations, chemistry values are interpolated between the nearest points before and after the given date.

5.2.1 Low-Resolution Mass Loadings

Low resolution mass loadings M_L are calculated using weekly Q_L totals that correspond to the chemistry sampling days in which the c_L values are obtained (refer to Chapter 4). Table 5.1 presents the cumulative and weekly-averaged flow and loadings separated into wet and dry periods. It is observed that pronounced wet and dry periods result in significantly different effluent and loading trends. Average weekly discharge and loadings rates are calculated to account for differences in sampling frequency and period length (i.e., wet and dry seasons are 7 and 5 months long, respectively). Average cumulative wet season loadings and time-averaged loading rates are larger than the average dry season loadings by a factor of at least 6. For example, the average wet season SO_4 loading rate is 1.45 mg/kg/week and the dry season loading rate is 0.23 mg/kg/week (Table 5.1). Discharge volume differences vary by nearly the same factor. This indicates that flow is of greater influence to mass loadings compared to solute concentration, and is consistent with trends reported by Wagner (2004).

5.2.1.1 Cumulative Loadings

The cumulative SO_4 , Ca, and Zn loadings for the entire period are shown in Figure 5.1 and indicate that 1343 kg, 613 kg and 1.4 kg (respectively) are released from the pile throughout the entire study period. These figures include combined loadings from the three sub-lysimeters and the basal lysimeter. All three curves exhibit the same shape as the total estimated precipitation (Chapter 3), which indicates that the seasonal change between wet and dry seasons are the dominant influence governing these mass loadings at this site and that the greatest proportion of the loadings is released during the wet season.

5.2.1.2 Time-Averaged Loading Rates

Average weekly mass loadings are calculated based on the outflow from each lysimeter. Results are then normalized by the estimated mass of waste rock associated with each respective lysimeter (assuming only vertical flow). For example, pile mass is estimated at 20,000 tonnes of waste rock (Chapter 2), of which an estimated 326 tonnes lie directly above sub-lysimeter A, 330 tonnes lie above B, and 240 tonnes lie above C. These masses are estimated based on a 4 x 4 vertical prism of waste rock that lies directly above each sub-lysimeter (assumes vertical flow). A significantly larger amount of material (~ 19,104 tonnes) contributes to the flow from basal

lysimeter D. The time-averaged, weekly-normalized loading rate [mg/kg/week] is referred to throughout the remainder of this investigation as the weekly loading rate.

The weekly SO₄, Ca and Zn loading rates calculated at each lysimeter are presented in Figure 5.2. All lysimeters exhibit strong seasonal variations in loadings that vary by 2 - 3 orders of magnitude. Sub-Lysimeters A and C exhibit similar mass loading behaviour to basal lysimeter D, with maximum wet season SO₄ loading rates between 4 and 6 mg/kg/week, Ca loadings between 2 and 3 mg/kg/week and between 0.003 and 0.005 mg/kg/week for Zn. Sub-lysimeter B wet season solute loading rates do not reach similar levels. This is likely due to both the flow behavior and composition of the material in this region of the pile. All lysimeters exhibit relatively low loading rates in the dry season. Differences between sub-lysimeter B and sub- and basal lysimeters A, C and D, respectively, as well as seasonal differences are further explained in the following chapter.

5.2.1.3 Flow vs. Chemistry

Weekly SO₄, Ca and Zn loading rates exhibit opposite seasonal trends from the respective solute concentrations (Figure 5.3). Despite decreasing solute concentrations during the wet season, mass loadings continue to increase, indicating that flow rate has a larger influence on mass loading behaviour than solute concentrations. This is explained by flow rates (Q) that vary by up to three orders of magnitude whereas solute concentrations (c) decrease by a factor of 2 to 5 (equation 5-2). In a similar investigation on a 5 m-high waste rock pile at the Cluff Lake mine, Wagner et al. (2006) report similar trends except for the period directly after the onset of large infiltration events where a short but rapid increase in concentration is reported. This is explained by a flushing effect where weathering products that have accumulated over a period of relative dryness are easily dissolved under large precipitation events, and lead to higher dissolved loads in the porewater. Over a larger time frame (e.g., monthly) results of the 5 m test pile indicate that flow rates and dissolved metal concentrations are positively correlated, which is the opposite of data presented for Antamina's test pile 1.

Chapter 4 explains that the solute concentrations are in part dependent on the residence time of porewater in the pile, and Chapters 3 and 4 explain that the different transport pathways (i.e.,

matrix vs. preferential flow) also affect solute concentration and loading behaviour. In similar investigations, long-term mass loading behaviour is found to be generally dominated by matrix-flow water, with peak mass loadings resulting from preferential flow during periods of high-intensity infiltration (Wagner et al., 2006; Neuner, 2009). Similar to these investigations, in response to large precipitation events, the chemistry of test pile 1 continues to increase until a (relatively) fresh slug of water penetrates to depth and decreases the dissolved load of the effluent water. Test pile 1 thus responds similarly to large precipitation events, however the dataset contains some uncharacteristically high solute concentrations during periods of high flow (e.g., SO_4 concentrations associated with basal lysimeter D on 1-May-2007; Figure 5.3).

5.2.1.4 Specific Conductance-Solute Correlations

Weekly solute concentrations are correlated to the weekly-measured specific conductance (SC) reported in Figure 4.1. Figure 5.4 provides an example of the correlations calculated based on basal lysimeter D effluent, and Table 5.2 summarizes the SC- SO_4 , -Zn and -Ca correlations (and r^2 values) calculated at each lysimeter. Solute concentrations are estimated based on the correlation equations provided in Table 5.2. For example, the SC- SO_4 correlation is:

$$[\text{SO}_4] = 0.532 * \text{SC} - 37.3 \quad [5-3]$$

where, sulphate concentrations ($[\text{SO}_4]$) are given in mg/L and the specific conductance (SC) is given in $\mu\text{S}/\text{cm}$. Table 5.2 indicates that correlations between SC and SO_4 , Zn and Ca range from strong ($r^2 = 0.86$) to non-existent ($r^2 = 0.01$). Basal lysimeter D exhibits a strong SC-Ca relationship ($r^2 = 0.82$), with a moderate correlation for SC- SO_4 ($r^2 = 0.56$) and a weak correlation for SC-Zn ($r^2 = 0.19$). Sub-lysimeter C has the best SC-solute correlation and all lysimeters have relatively weak SC-Zn correlations. Poor SC-Zn correlations (Figure 4.21) are likely a result of the fact that Zn is a trace metal and has little effect on the SC, which is largely dominated by SO_4 and Ca ions.

These correlations are used in the following section to estimate high-resolution solute concentrations and mass loadings.

5.2.2 High-Resolution Mass Loadings

Under certain conditions (e.g., in response to a large precipitation event), solute concentrations may change over a short period of time (Wagner et al., 2006). High-resolution mass loadings are therefore required to monitor the short-term fluctuations in mass loadings that the previous (low-resolution) method does not account for.

High-resolution mass loadings M_H are calculated using solute correlations to specific conductivity (Section 5.2.1.4) to estimate c_H , and flow measurements Q_H are presented for the same time interval. One of the principal benefits of installing custom-made EC probes is that they provide high-resolution SC data (i.e., 30-minute intervals) that can show rapid responses to precipitation inputs. The continual SC data is similar to the weekly, manually collected SC data (Figure 5.1).

5.2.2.1 Basal Lysimeter SO_4 Loading

Using the regression correlations provided for basal lysimeter D in Table 5.2 and the continuous SC data, SO_4 loadings are estimated over three (3) separate weeks during the 2006-07 wet season (7- to 15-Mar-2007, 7- to 15-Apr-2007 and 8- to 15-May-2007). Results are compared to flow, specific conductance and estimated sulphate concentrations (Figure 5.5; Table 5.3). These time periods are chosen because all of the chemistry (lab, field, and continual SC data) and flow data are present. For data processing purposes, SC and flow data are reduced to hourly intervals. Estimated hourly solute concentrations [mg/L] are multiplied by hourly lysimeter flow [L/hr] to obtain a loading rate that is converted to an equivalent kg SO_4 /day.

The inverse relationship between flow rate and solute concentration (Section 5.2.1.3) also applies to mass loadings and specific conductance, indicating that flow rate and mass loadings are linearly proportional to each other much like SC and solute concentrations are to one another (Section 5.2.1.4). However, SC and solute concentration both respond slower and less proportionally than flow rate and mass loadings (due to magnitude in changes, Section 5.2.1.3). For example, under extreme events, flow and loading rates can increase by more than 50 % over one day whereas SO_4 and SC experience less proportional, more attenuated responses (Figure 5.5).

5.2.2.2 Lysimeter SO₄, Ca and Zn Loadings

Whereas Section 5.2.2.1 examines the SO₄ loadings at D, results presented in this section compare the SO₄, Ca and Zn loading rates at each lysimeter during an 8-day period during the week of 11- to 19-Apr-2007.

Weekly sub-lysimeter C and basal lysimeter D loading rates are higher than A and B for SO₄, Zn and Ca (Figure 5.6). The total pile flow from all four lysimeters over the course of the period is also included, and illustrates that sub-lysimeter C and basal lysimeter D loading rates are more responsive to the changing discharge compared to sub-lysimeters A and B, which experience much more gradual, attenuated responses. Basal lysimeter D responds more rapidly than sub-lysimeter C. The highest SO₄ and Ca loading rates are found at the front of the pile (sub-lysimeter C), whereas the lowest loading rates are found towards the pile interior (sub-lysimeter B). There is a poor SC-Zn correlation for all lysimeters (Table 5.2), which possibly explains why basal lysimeter D has a higher Zn loading rate than sub-lysimeter C. Otherwise, loadings are generally consistent among the three solutes as measured at the four lysimeters, and the relative difference in loading rates between lysimeters is consistent with the flow patterns reported in Chapter 4.

5.2.3 Comparison Between Low- and High-Resolution Loadings

Low- and high-resolution loading rates are compared. High-resolution data indicates that significant changes in effluent chemistry are occurring that the low-resolution (weekly) data is not effectively capturing.

Section 5.2.2.1 examines SO₄ loadings at basal lysimeter D over three one-week periods. The high-resolution specific conductance and SO₄ concentrations are averaged over the entire period to enable a comparison with low-resolution parameters. In general, both approaches produce similar results with SO₄ concentrations and SC values having inverse behaviours to increasing flow and mass loading rates.

Section 5.2.2.2 compares the low- and high-resolution solute mass loading estimates for each lysimeter during 11- and 19-Apr-2007. Both methods (low and high) produce similar results, with minor differences (Table 5.4). With the exception of SO₄ at sub-lysimeter A, this trend (low-resolution result < high-resolution result) is observed for all three solutes at each lysimeter. High- and low-resolution loading rates are similar for SO₄ (i.e., 10.6 (low-resolution) and 12.7 (high-resolution) mg/kg/week at basal lysimeter D) and Ca (5.3 (low) and 5.5 (high) mg/kg/week at D). Low-resolution SO₄ rates are nearly 85 % of the high-resolution rates, whereas low-resolution Ca rates are 97 % of the high-resolution rates. Zn experiences the largest discrepancy between low and high resolution solute loading values (i.e., 0.010 and 0.015 mg/kg/week), and low-resolution rates are roughly 70 % of the high-resolution rates. The larger discrepancy from Zn likely arises from a poor SC-Zn correlation (Table 5.2).

Based on Table 5.3 and Table 5.4, average high-resolution SO₄ concentrations are up to 50 % higher than the low-resolution values, whereas high-resolution Ca and Zn loadings are 2 - 8 % and 30 - 50 % higher than the low-resolution loadings, respectively. It is difficult to determine whether the low-resolution approach underestimates loadings or whether the high-resolution approach overestimates loadings. Comparing solute correlations between the basal lysimeter and composite tank (Figure 4.2), this suggests that the low-resolution approach likely produces more accurate results than the high-resolution approach. This is because each composite tank sample represents an integration of flow from all four lysimeters over the course of the week, whereas the basal lysimeter sample represents an instantaneous (weekly) snapshot of concentration that is not indicative of how concentrations varied since the last sample (Appendix G). Since weekly fluctuations in the basal lysimeter concentrations are not significant on the overall pile loadings (Figure 4.1), this suggests that the low-resolution approach likely produces more accurate results than the high-resolution approach, which is based on an empirical relationship and introduces even more error.

5.2.4 Comparison to Field Cells

To determine the weathering characteristics of waste rock in a more controlled domain than the test pile and to isolate distinct rock types which are mixed within the pile, eight 55-gallon kinetic field cell experiments were constructed using random samples of the same waste rock material

that was placed in the experimental pile (Aranda, 2009). Due to a smaller size fraction of waste rock employed in the field cells (i.e., < 10 cm), these cells typically have a higher surface area and a higher general reactivity compared to the test pile. Nearly two years of data is available from these field cells, the chemistry of which was briefly introduced in Chapter 4.

The average, maximum and minimum SO₄, Ca and Zn loading rates [mg/kg/week] calculated for the field cells are compared at each lysimeter and the composite tank (Table 5.5). Results are based on data extending from Jan-2007 to Sept-2008. Lysimeter loading estimates are based on interpolated datasets when flow and chemistry data are absent (Section 5.2.1).

All solute mass loading rates (lysimeter and field cells) vary by nearly 2 - 3 orders of magnitude, demonstrating the large variability in loading rates throughout the study period. Average field cell loading rates are larger than the lysimeters by between a factor of 2 to two orders of magnitude. For example, while average SO₄ loadings rates are nearly 3 - 4 times higher for the field cells than for the total pile, the maximum rate is 4 times higher and the minimum rate is 2 orders of magnitude higher. Similar trends are found in Ca, and Zn reactivity in the field cells is nearly 2 - 3 orders of magnitude higher (Table 5.5).

5.3 ELEMENT DEPLETION ESTIMATES

The time of element depletion is crudely calculated based on mass loading rates. This simplified calculation is only included to provide a rough estimate of the possible leaching potential of the pile into the future.

Based on pile design and assuming vertical flow, infiltrating water will always come into contact with material originating from two or more material placement phases (i.e., protective layer and Tipping Phases I, II & III; Chapter 3). Water reporting to sub-lysimeter B will likely pass through Tipping Phases I and II and the protective layer, whereas water reporting to sub-lysimeter A will likely come into contact with material from Tipping Phases II and III, and the protective layer. Water reporting to sub-lysimeter C will come into contact with Tipping Phase III and the protective layer. The basal lysimeter will contain water in contact with all four

materials. It is for this reason that whole-pile depletions will only be estimated, and will not distinguish between various lysimeters or tipping phases.

Using average pile S, Zn and Ca concentrations and pile mass (Table 2.4), and the total mass of those three elements already released from the pile during the first 2 years (Table 5.1), the depletion estimates are calculated. Nearly 0.4 % of total S has been depleted from the pile, while 0.01 % of Ca and Zn have so far been depleted. To note, Golder (2007b) reported that less than 1 % of available metals in field cell kinetic tests have been depleted from a majority of Class B materials. Based on the assumption that the current rates stay constant in time, then it will take S nearly 500 years to be depleted from test pile 1, Zn nearly 23,000 years and Ca nearly 18,000 years.

5.3.1 Mineral Depletion Uncertainties

The purpose of the above calculation is to illustrate that the pile has the potential to release poor-quality drainage water many years into the future. These metal depletion calculations have several inherent limitations. One major weakness is the assumption that the time-averaged solute mass loading rate remains constant. Calculations do not address the possibility of future decreases to solute release rates in response to a loss of reactivity, mineral coatings, etc. To improve the accuracy of the depletion estimation, longer term observations are required. With a more profound understanding of the geochemical and flow dynamics, higher-order mechanistic models can be used to better predict future loadings and depletion estimates.

To increase the accuracy of these calculations and minimize the limitations, several physical and chemical constraints should be addressed in the future. Some considerations are, but are not limited to, the following:

1. sulphide mineral availability (and surface area for reaction sites),
2. particle size heterogeneity (relative amount of more reactive fine-grained material),
3. composition heterogeneity (i.e., proportion of sulphide minerals),
4. rate and development of mineral coatings (e.g., secondary mineralization),
5. flow pathways and mechanisms (matrix vs. macropore flow),
6. rate of oxidation (availability/replenishment of oxygen, water, sulphide, etc.),

7. precipitation/dissolution tendencies (saturation indices), and
8. acid neutralization capability (and carbonate mineral availability).

5.4 SUMMARY

A total 1343 kg of SO₄, 613 kg of Ca, and 1.4 kg of Zn are estimated to have been removed from test pile 1 during the 2-year long study period. Weekly loadings vary by 2 – 3 orders of magnitude between the wet and dry season, with the highest rates of 4 – 6 mg/kg/week SO₄, 2 – 3 mg/kg/week Ca, and 0.003 – 0.005 mg/kg/week Zn calculated for basal lysimeter D and sub-lysimeters A and C.

Flow rates at test pile 1 have a larger influence on the mass loading rate compared to solute concentration. In general, an increase in flow and mass loading rates at test pile 1 will typically cause a decrease in solute concentration and specific conductance. The high-resolution mass loading calculations indicate that mass loading rates can change by over 50 % over the course of a few days. First-pass elemental depletion estimates indicate that the pile has the potential to release solutes many years into the future. Field cell loading rate estimates are 2 – 200 times larger than those for test pile 1.

TABLES

Table 5.1. Cumulative and average wet and dry season loading rates.

Time		Discharge		Loadings					
		Cumulative [m ³]	Average [m ³ /week]	Cumulative [kg]			Average [mg/kg/week]		
				SO ₄	Zn	Ca	SO ₄	Zn	Ca
Wet	2006-07	447	30.4	513	0.42	242	1.59	1.1E-03	0.79
Dry	2007	96	4.4	115	0.11	55	0.29	2.3E-04	0.14
Wet	2007-08	623	20.5	633	0.76	282	1.31	1.1E-03	0.59
Dry	2008	65	3.0	82	0.10	33	0.18	1.7E-04	0.08
Average Wet		535	25	573	0.59	262	1.45	1.1E-03	0.69
Average Dry		81	4	98	0.10	44	0.23	2.0E-04	0.11
Total / Average		1231	14	1343	1.4	613	0.76	7.9E-04	0.35

Table 5.2. Specific conductance-solute lysimeters and composite tank regression correlations.

Station	[SO ₄]=	r ²	[Zn]=	r ²	[Ca]=	r ²
A	0.0246(SC)+1354.5	0.01	0.00007(SC)+0.822	0.20	0.180(SC)+74.6	0.86
B	0.375(SC)+275.2	0.33	-0.0003(SC)+2.67	0.05	0.223(SC)-18.7	0.65
C	0.465(SC)-0.98	0.63	0.0004(SC)-0.010	0.48	0.222(SC)-12.37	0.75
D	0.532(SC)-37.3	0.56	0.0004(SC)+0.49	0.19	0.250(SC)-56.81	0.82
E	0.393(SC)+226.7	0.58	0.0002(SC)+0.794	0.10	0.225(SC)-11.45	0.80

Table 5.3. High- and low-resolution basal lysimeter loading comparison; 2007.

2007	Unit	Low Resolution ¹	High Resolution ²
March 7-15			
Cumulative Volume	m ³	40.6	40.6
Specific Conductance	μS/cm	1988	1963
SO ₄ Concentration	mg/L	760	1013
Cumulative Mass Loading	kg SO ₄	30.9	39.8
April 19-24			
Cumulative Volume	m ³	15.7	15.7
Specific Conductance	μS/cm	2440	2375
SO ₄ Concentration	mg/L	1055	1233
Cumulative Mass Loading	kg SO ₄	16.6	19.3
May 8-15			
Cumulative Volume	m ³	12.9	12.9
Specific Conductance	μS/cm	2460	2368
SO ₄ Concentration	mg/L	862	1229
Cumulative Mass Loading	kg SO ₄	11.1	15.9

¹ low-resolution specific conductance and SO₄ concentrations are from the end of the sampling period

² high-resolution specific conductance, and SO₄ are averaged over each period.

Table 5.4. High- and low-resolution lysimeter loading comparison; 11- to 19-April-2007.

Solute	Parameter	Unit	Resolution	A	B	C	D	Cumulative
	Cumulative Volume	[m ³]	Low	0.166	0.08	0.7	33.09	31.9 m ³
			High	0.166	0.08	0.7	33.09	31.9 m ³
	Specific Conductance	[μS/cm]	Low	4300	3050	1800	2640	-
			High*	4377	3012	1666	2359	-
SO ₄	Concentration	[mg/L]	Low	1488	1355	689	1055	-
			High*	1462	1405	774	1218	-
	Mass Loading	[mg/kg/week]	Low	4.7	2.0	11.5	10.6	33.5 kg
			High*	4.6	2.1	13.7	12.7	39.4 kg
Ca	Concentration	[mg/L]	Low	800	634	351	525	-
			High*	860	652	357	533	-
	Mass Loading	[mg/kg/week]	Low	2.51	0.95	5.85	5.27	16.7 kg
			High*	2.69	0.97	6.31	5.52	17.2 kg
Zn	Concentration	[mg/L]	Low	0.88	1.25	0.54	1	-
			High*	1.13	1.76	0.66	1.44	-
	Mass Loading	[mg/kg/week]	Low	0.0027	0.0019	0.0090	0.0100	0.031 kg
			High*	0.0035	0.0027	0.0116	0.0151	0.047 kg

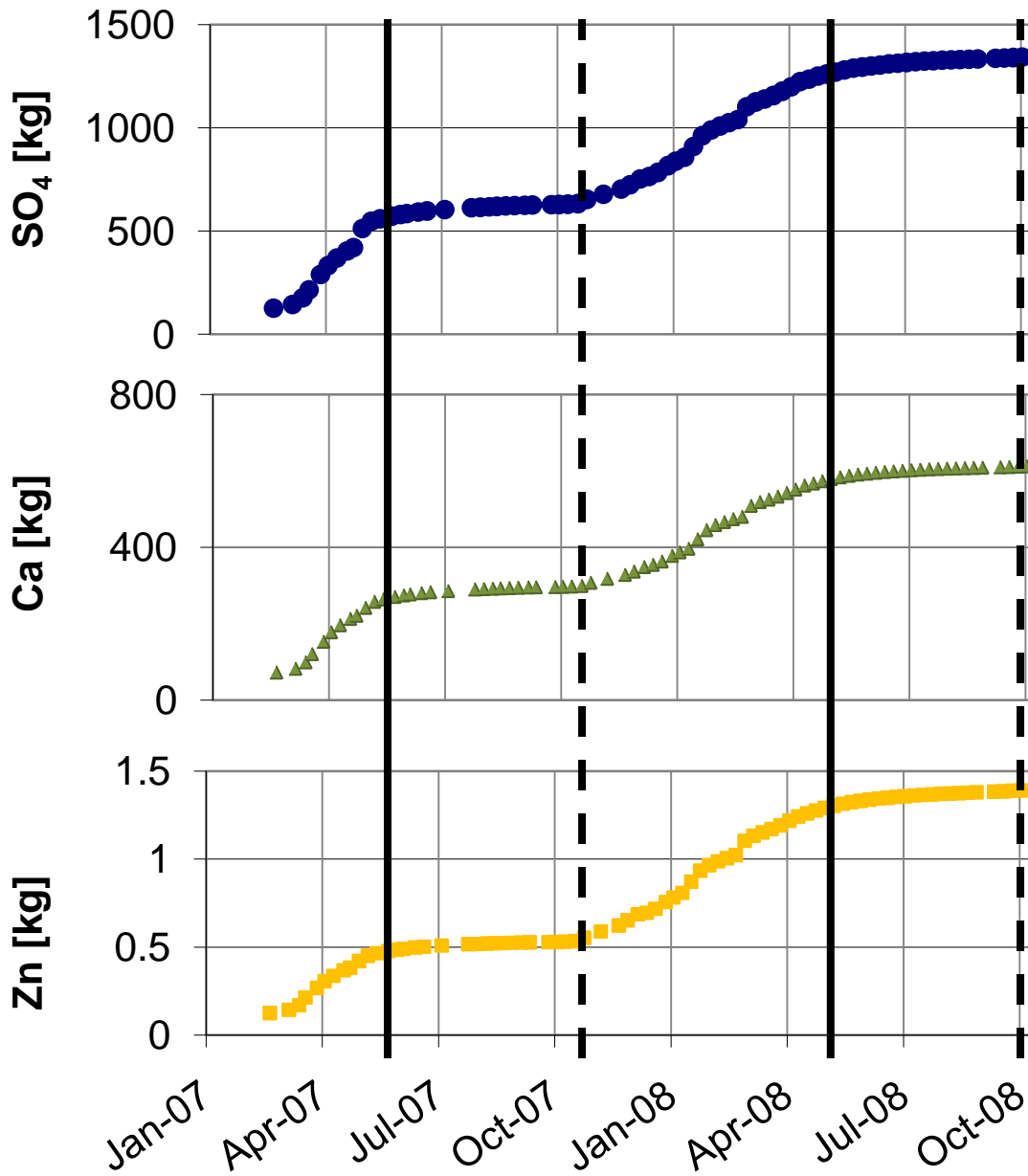
* High-resolution averages over time period for comparison to low-resolution data

Table 5.5. Average field cell and lysimeter loading rates.

	Station	Loadings [mg/kg/week]			Ratio: Field Cell : Station
		Average	Maximum	Minimum	
SO ₄	Pile ¹	0.794	4.734	0.029	4
	D	0.792	4.796	0.03	4
	C	1.164	5.817	0.003	2
	B	0.149	0.807	0.002	19
	A	1.244	4.28	0.003	2
	Field Cell	2.83	16.596	0.894	1
Zn	Pile ¹	8.18E-04	4.12E-03	2.39E-05	44
	D	8.28E-04	4.18E-03	2.49E-05	43
	C	8.44E-04	4.84E-03	4.41E-06	42
	B	1.86E-04	8.99E-04	3.28E-06	192
	A	8.90E-04	3.05E-03	3.73E-06	40
	Field Cell	3.58E-02	3.11E-01	6.94E-03	1
Ca	Pile ¹	0.357	1.546	1.37E-02	4
	D	0.355	1.542	1.43E-02	4
	C	0.54	2.806	7.49E-04	3
	B	0.066	0.367	9.50E-04	22
	A	0.596	2.005	2.14E-03	2
	Field Cell	1.44	6.512	0.375	1

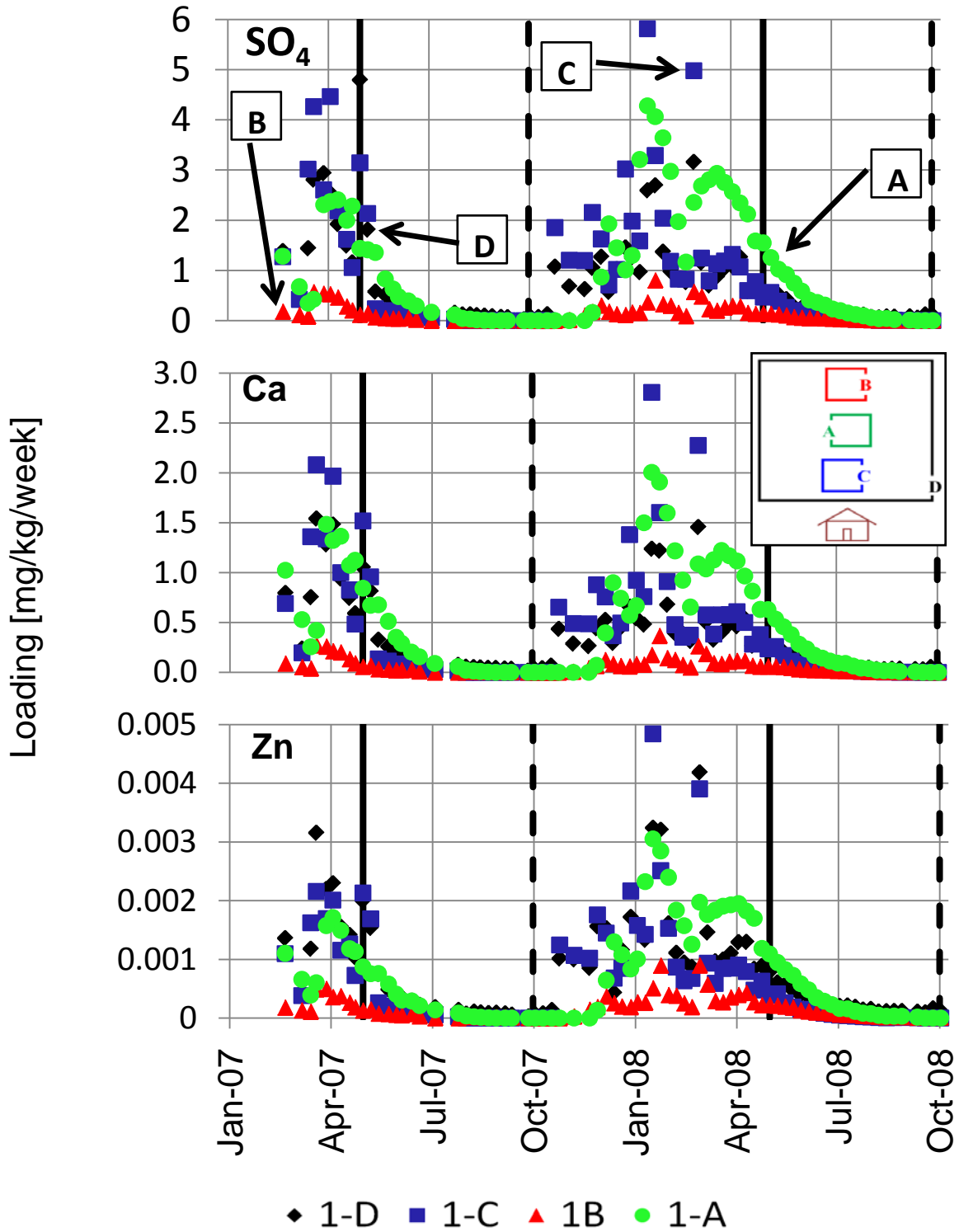
¹Total pile rates are based on weighted average based on estimated mass of material.

FIGURES



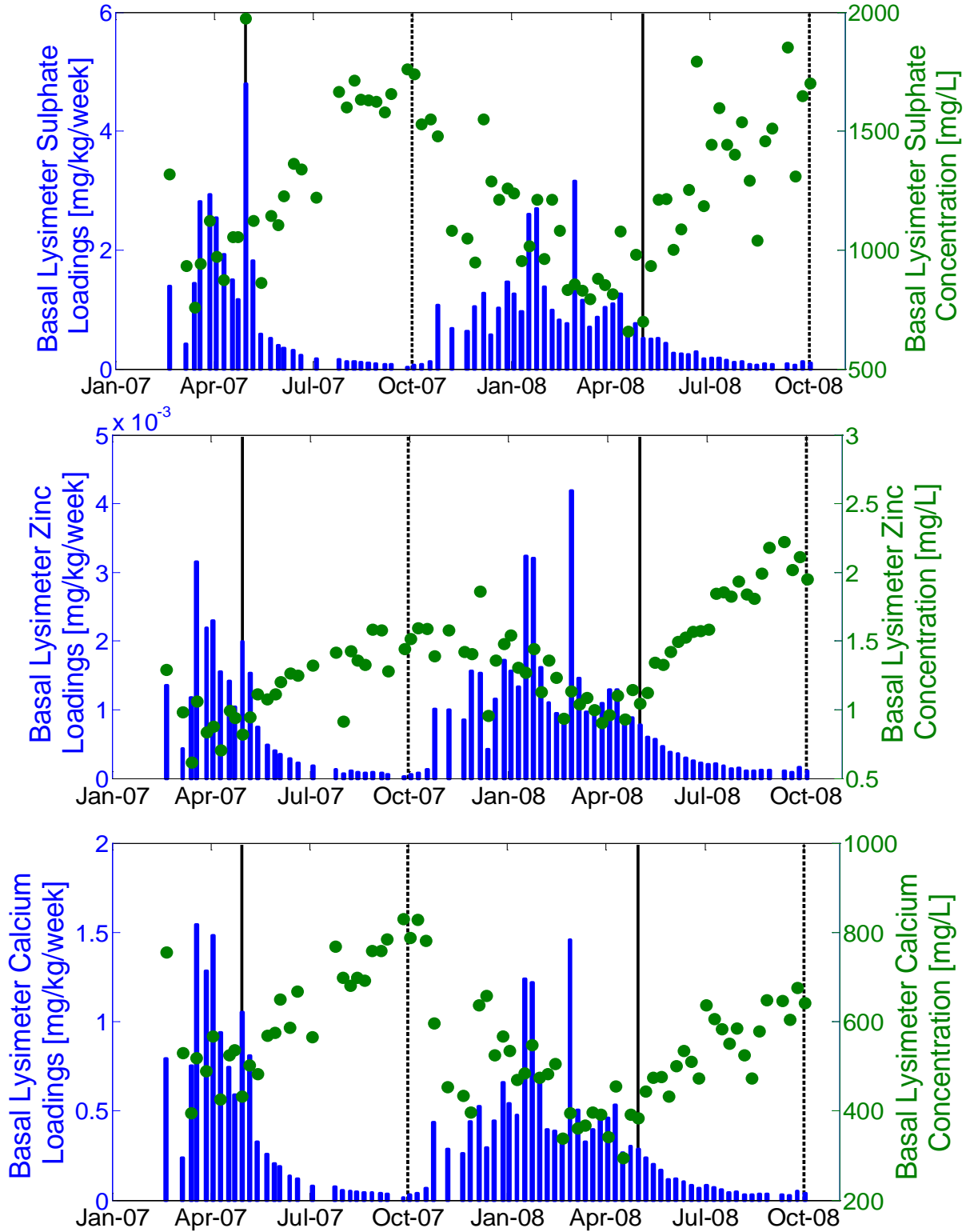
*Solid line = wet-dry season transition; Dotted line = dry-wet season transition

Figure 5.1. Best estimated cumulative pile loadings.



*Solid line = wet-dry season transition; Dotted line = dry-wet season transition

Figure 5.2. Best estimated weekly SO₄, Ca and Zn mass loadings for all four lysimeters.



*Solid line = wet-dry season transition; Dotted line = dry-wet season transition

Figure 5.3. Weekly SO₄, Ca and Zn solute concentration and mass loading.

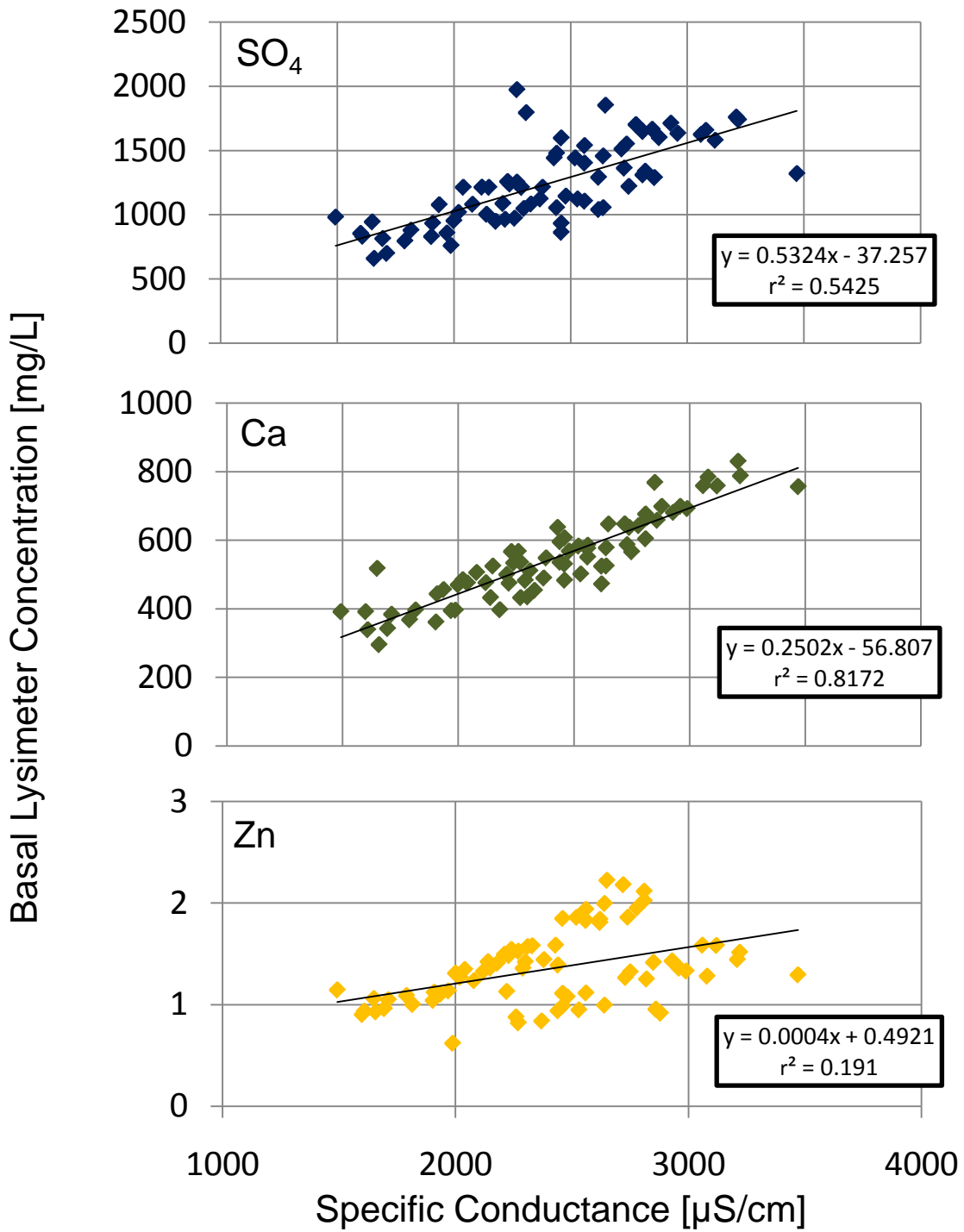
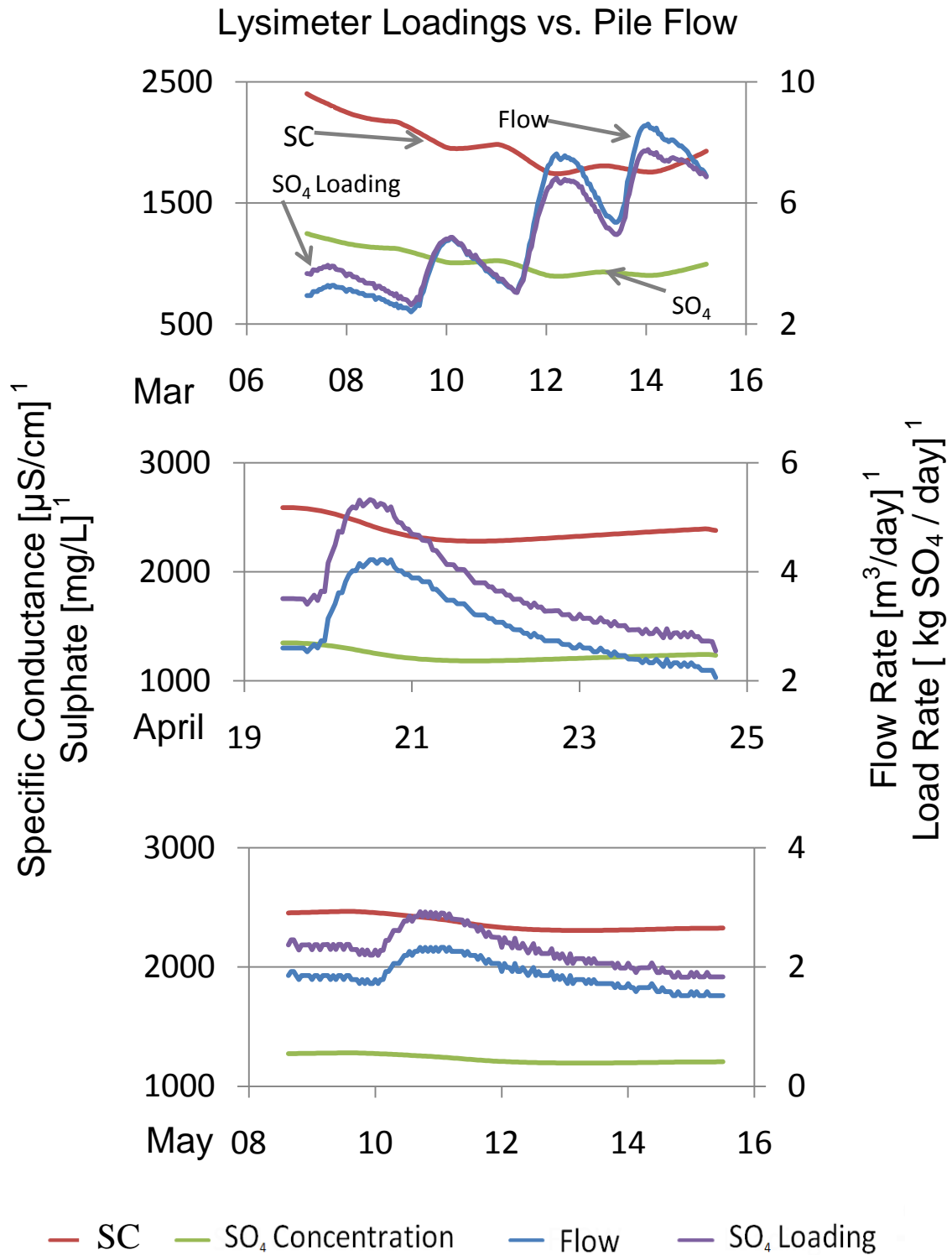


Figure 5.4. Specific conductance correlation to SO_4 , Ca and Zn as measured at D.



¹ based on hourly data

Figure 5.5. Basal lysimeter loading comparison to concentration and flow rate; 2007.

Lysimeter Loadings vs. Pile Flow

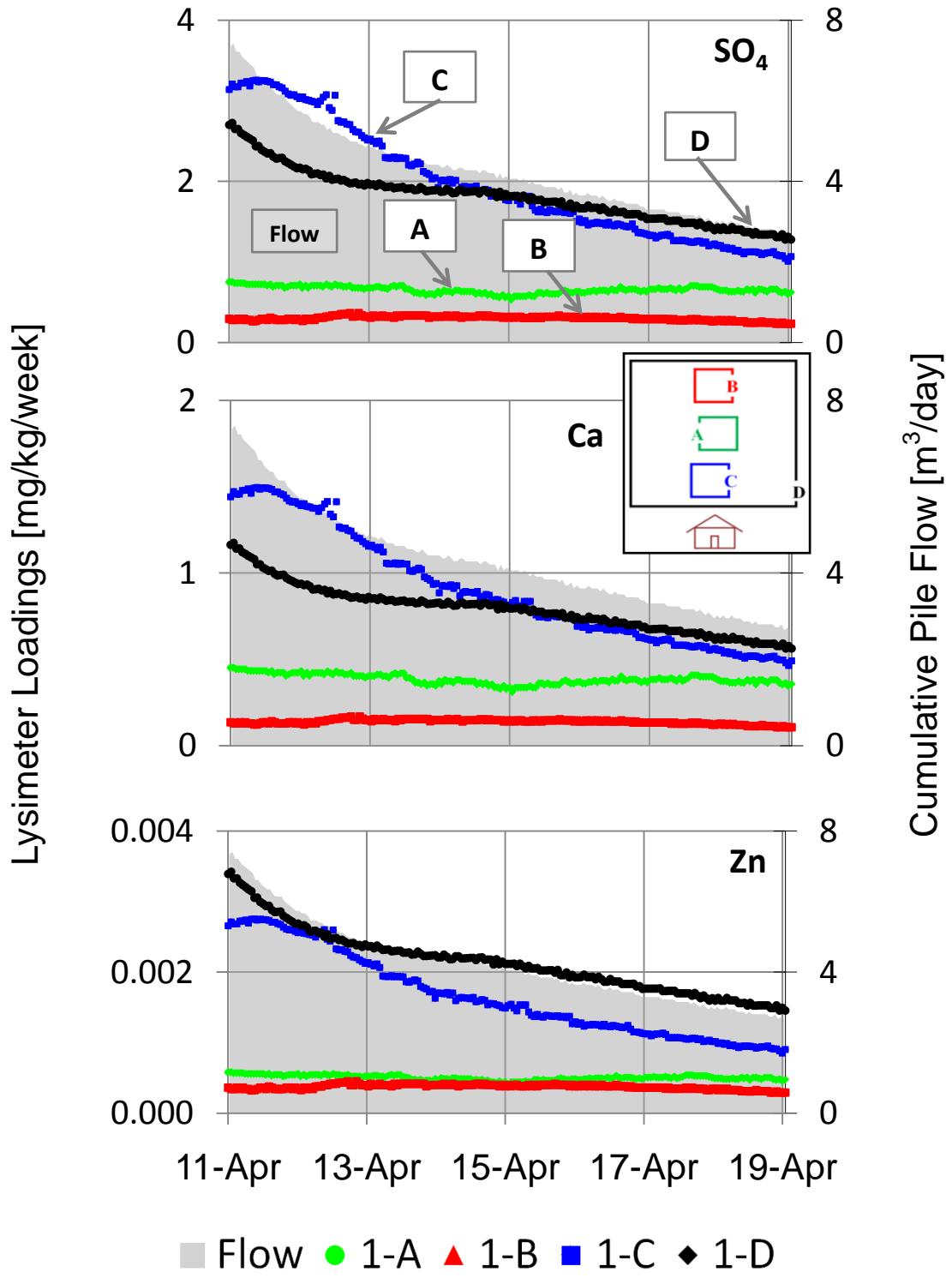


Figure 5.6. Lysimeter loading variation, 11- to 19-Apr-2007.

6 DATA INTEGRATION

This chapter combines selected results previously presented in Chapters 2 to 5. Physical and chemical waste rock properties are integrated with the flow, chemistry and loading results in order to obtain a better understanding of the mechanisms that mobilize metals in test pile 1. Particular emphasis is placed on examining evidence of:

1. different flow mechanisms (matrix vs. macropore flow),
2. pyrite oxidation, and
3. spatial variability of weathering rates in the pile.

6.1 EVIDENCE OF DIFFERENT FLOW MECHANISMS

The 4 x 4 m sub-lysimeters are conceptualized as representing effluent water that spatially averages over matrix and macropore (if activated) flow pathways. The same applies to the 36 x 36 m basal lysimeter flow and chemistry, which averages over various flow and chemistry differences that result from the pile batter and the pile interior. Evidence of matrix flow is identified in Chapter 3, and specific conductivity is used to identify evidence of slow and diffuse matrix flow in Chapter 4. The chemical signature of the matrix flow typically contains a higher dissolved load compared to the relatively fresh slugs associated with macropore flow. In response to higher moisture contents and larger infiltration rates due to large precipitation events, specific conductivity measurements decrease by up 50 % over nearly one week after the precipitation event.

Evidence of preferential macropore flow, pressure-wave responses and non-vertical flow in response to large precipitation events near the middle to end of the wet season was discussed in Chapter 3 and is further confirmed using the effluent chemistry in Chapter 4. Sharp fluctuations correspond with large outflow events characteristic of fresh, low conductivity macropore slugs. Furthermore, higher porewater concentrations during the dry season reflect steadier, gradually changing rates representative of matrix flow, which also confirms flow findings from Chapter 4.

6.2 PYRITE OXIDATION: ESTIMATING SO₄

The total estimated SO₄ generated from pyrite weathering is calculated over the course of the water year (1-Oct-2007 to 30-Sept-2008). Assuming that the temperatures at the top and bottom of the pile reflect the temperatures as measured at the shallowest and deepest porewaters, then $\Delta T = 1.8$ °C (Chapter 4) can be used to describe the average temperature difference between the top and bottom of the pile over the course of the water year. In further assuming that the higher temperatures result from a conservative release of energy from the chemical oxidation of pyrite (and this energy did not leave the system through conduction, convection, etc.), then the total amount of energy released due to pyrite oxidation could be calculated based on the following equation:

$$\Delta Q = mc\Delta T \quad [6-1]$$

where ΔQ is the heat energy associated or taken out of the system [kJ], m is the mass of the substance [kg], c is the specific heat capacity of water (4.185 kJ/(kg K)), and ΔT is the change in temperature [°K]. Using a total of 6.9×10^5 kg of water (690 m³) estimated to have discharged from the base of the pile (Chapter 4), a total energy of $\Delta Q = 5.2 \times 10^6$ kJ of energy was released during pyrite oxidation over the course of the water year. This value corresponds to an estimated 0.2 W of energy that is continuously released by the entire pile, which is a modest amount given the total volume of the pile (approximately 10,000 m³; Chapter 2).

Based on the Gibbs Free Energy released per mol of pyrite mineral oxidation (of $\Delta G_r^\circ = -1440$ kJ/mol; Ritchie, 1994), an estimated 12 kJ of energy is released for every gram of pyrite oxidized. Based on the calculated ΔQ , an estimated 430 kg of pyrite was oxidized in order to release that much heat. Using a 1:2 molar ratio between S in pyrite (FeS₂; 120 g/mol) and sulphate (SO₄; 96 g/mol), an estimated 693 kg of sulphate was associated with the amount of generated heat during the pyrite oxidation described in equation 4-1. Recall that 715 kg of sulphate is reported to have been released from the pile during the same period (Chapter 5).

Even though these two methods produce similar results, they both represent minimum values due to several limitations. The SO₄ estimated based on pyrite oxidation is strongly dependent on a perfect mass balance of S between pyrite oxidation and generated SO₄. This method also assumes that pyrite is the only sulphide mineral oxidizing and there is no loss of energy via

convection, conduction, evaporation, etc. In addition, both methods do not account for the precipitation of gypsum within test pile 1. While it is likely that these limitations may be balanced in both approaches, more quantitative thermal modeling would better constrain these estimates.

6.3 OXYGEN DEPLETION ESTIMATE

To estimate the ability of air to travel through the waste rock pile (and confirm whether it is well-aerated), a first-pass approximation of the total amount of oxygen consumed compared to the total estimated amount of oxygen in all of the void spaces. The number of ‘pore volumes’ of oxygen consumed during pyrite oxidation in test pile 1 throughout the study period (18-Jan-07 through 30-Sept-2008) is calculated.

The volume V of oxygen in 1 mol of pore space in test pile 1 is calculated using the Universal Gas Law:

$$pV = nRT \quad [6-2]$$

where p is the absolute pressure corrected for altitude (57.5 kPa at 4374 m a.s.l.; Appendix D), V is the gas volume (m^3), n is the amount of substance of the gas (1 mol), R is the gas constant ($8.314472 \text{ J K}^{-1} \text{ mol}^{-1}$) and T is the absolute temperature, which is the mean annual temperature of 279.15 K (Chapter 2). The volume of gas V in 1 mol of air is calculated at 0.04 m^3 , and the total volume of oxygen in this volume (at $\text{PO}_2 = 0.21$) becomes $5.2 \text{ mol O}_2/\text{m}^3$ of pore gas in the pile.

Based on an estimated porosity of $n = 0.4$, a pile volume of $10,000 \text{ m}^3$ (Chapter 2), and an average moisture content of $\theta = 0.22$ (Chapter 3), the void volume is calculated to be $V_v = 0.18 \times 10,000 \text{ m}^3 = 1,800 \text{ m}^3$.

The total amount of oxygen in one pore volume of test pile 1 is:

$$1,800 \text{ m}^3 \times 5.2 \text{ mol O}_2/\text{m}^3 = 9,360 \text{ mol O}_2$$

Based on a total mass of 1343 kg of SO_4 released from the pile during the entire study period (Table 5.1), this corresponds to an equivalent molar concentration of O_2 (based on equation 4-1) to be 52,460 mol of O_2 .

Comparing the estimated pore volume of oxygen (9,360 mol O_2) to the total amount of O_2 consumed during the study period (52,460 mol of O_2), then roughly 5.5 pore volumes of O_2 have moved through the pile. This provides further support indicating that the pile is reasonably well-aerated.

6.4 SPATIAL VARIABILITY IN PILE BEHAVIOUR

It has already been established that the loading behaviour of the pile is not spatially uniform (Chapter 5). That is, loading rates have been shown to vary (based on seasonal input) and these rates demonstrate a strong spatial variation throughout the pile.

Based on previous observations that solute loadings are dominated by flow (Chapter 5) and that sub-lysimeter C and basal lysimeter D experience the highest discharge fluxes (Chapter 4), it is no surprise that these two lysimeters experience the highest flow rates. However, it is interesting to note that although sub-lysimeter A experiences lower flow rates that are most similar to sub-lysimeter B, loading rates at A are almost just as high as C and D (Chapter 5). Chapters 3 (hydrology) and 4 (chemistry) assume that the particle size and material composition is similar across the entire pile (i.e., material properties from each placement stage was relatively homogeneous) and that flow and chemistry differences between lysimeters likely result from the structural differences between the pile interior (and thus the upper, less-permeable, traffic-compacted layer) and pile batter (less-consolidated, more-permeable, coarser-sized material). However, these assumptions are not entirely valid because they do not take into account the mineralogical heterogeneity of the waste rock which must also be considered when comparing lysimeter loading rates.

Although the particle size distribution of material from each placement stage is relatively consistent (Figure 2.10), material from each stage originates from different areas of the open pit and will thus have physical and chemical differences (Table 2.3; Table 2.4). To better understand the mechanisms that lead to the spatial loading variability within the pile, an integration of

selected data is required. This involves a comparison between material from Tipping Phases I to III and their respective sub-lysimeters (Figure 4.4). Table 6.1 summarizes the material properties (mass, solid phase concentration, neutralization potential, and relative uniformity), sub-lysimeter attributes (estimated volume of material directly above, total volume of water to have passed through, effluent chemistry, average loading rates) and other data (pile temperature, gas concentrations, etc). Material from the protective layer is discussed first, followed by Tipping Phases I, II and III, and their corresponding sub-lysimeters. In addition, Figure 4.4 is presented again in Figure 6.1 summarizing the ‘big picture’ differences between each material type.

6.4.1 Protective Layer

The protective layer (waste rock) consists of black marble Class B waste rock, which has the lowest average density compared to the rest of the pile (2770 kg/m^3 ; Table 2.6). The weathering behaviour of the protective layer material cannot be deduced because it is mixed with material from the other three tipping phases. Effluent water that drains to any of the four lysimeters will have come into contact with the protective layer as well as one or two other materials. Based on results from the Mineral Liberation Analyzer (MLA; Chapter 2), this material consists of approximately 56 % carbonate, 41 % silicate and 0.5 % sulphide minerals (Table 2.3). This is supported by ICP analyses which indicate that the protective layer material contains the highest reported solid phase Zn concentration (830 ppm) amongst the materials used in the pile (Table 2.4). Compared to the rest of the pile, material from the protective layer contains intermediate masses of Ca, Zn and S (based on solid phase concentration and total mass of the protective layer from Table 2.4), an intermediate net neutralizing potential (NNP; Chapter 2) and the highest neutralization potential ration (NPR) levels (Table 6.1). Figure 6.1 presents an integration of data pertaining to the protective layer.

In general, the particle size distribution of this material is very similar in shape to Tipping Phases I and II and shows that material from all placement stages consists predominantly of coarse particles (Figure 2.10). Approximately 9 % of the material placed in the protective layer has a diameter of 4.75 mm or less and is assumed to represent the proportion of fine material. The median particle size is 250 mm.

6.4.2 Tipping Phase I - Sub-lysimeter B

Tipping Phase I consists of marble diopside (Table 2.3). Approximately 7.5 % of this material has a diameter of 4.75 mm or less and is assumed to represent the proportion of fine material. The median particle size is 200 μ m. Water passing through Tipping Phase I may also pass through Tipping Phase II near the top of the pile before passing through the protective layer and reporting to the back sub-lysimeter B (Figure 6.1). The contribution of material from this tipping phase to the overall pile mass is low because a significant proportion of it was dumped along the back slope until material was finally placed within the pile footprint (Chapter 2; Table 2.6).

Based on MLA results (Table 2.3), this material consists of approximately 48 % carbonate, 50 % silicate and 2.0 % sulphide minerals. This is supported by ICP analyses which indicate an intermediate solid phase Zn concentration (average) compared to the rest of the pile (Table 2.4), yet this material contributes the least amount of zinc to the pile based on the total mass to reside within the pile (Table 6.1). Interestingly, effluent water at B reports the highest Zn concentrations (Figure 4.8) and likely results due to the low velocity of water passing through this region and a higher porewater residence time (Chapter 3).

A 4 x 4 m vertical column of waste rock, amounting to approximately 326 tonnes, lies directly above sub-lysimeter B. A majority of this material originates from Tipping Phase I. The contribution to entire pile flow from this region is proportionally low (~ 0.02 % of total pile), which may be explained by 3 possible reasons:

1. infiltrating water is attracted to the French drain along the back of the pile – slope contact,
2. non-vertical flow focuses water away from the sub-lysimeter, and/or
3. sub-lysimeter B is located under the most compacted region of the pile (i.e., most traffic-compaction).

The most likely explanation includes the latter option, as a less permeable top layer leads to lower fluid infiltration rates which lead to higher porewater residence times and lower pH values as O₂ cannot ingress and CO₂ cannot escape as rapidly.

Accordingly, water chemistry indicates relatively high average SO_4 , Zn and Ca concentrations compared to the rest of the pile, with the highest Zn concentrations reported compared to the rest of the pile. However, due to a low flow rate reported at this lysimeter, this region still exhibits the lowest average solute loading rates (Table 6.1). Based on the distance away from the surface, there is evidence that this region behaves more like a partially-closed system (as evidenced by lowest pH values throughout the pile) and thus explains the chemical differences from this region compared to the rest of the pile, particularly those exposed to the surface.

6.4.3 Tipping Phase II - Sub-lysimeter A

Tipping Phase II consists of the most dense (3140 kg/m^3) marble diopside found within the pile (Table 2.3). Approximately 4 % of this material has a diameter of 4.75 mm or less and is assumed to represent the proportion of fine material. The median particle size is almost 300 μm (Figure 2.10) and the largest uniformity coefficient (Section 2.13.4; Table 6.1). Based on Table 2.3, material from Tipping Phase II consists of approximately 11 % carbonate, 82 % silicates and 4.5 % sulphide minerals (Aranda, 2009). This is supported by ICP analyses which indicate that this material contains the lowest solid phase Ca and Zn concentrations, yet the highest solid phase S concentrations (Table 2.4).

Water passing through Tipping Phase II likely passes through Tipping Phase III near the top of the pile before passing through the protective layer and into sub-lysimeter A in the middle of the pile (Figure 6.1). Average SO_4 and Ca concentrations in sub-lysimeter A effluent are higher than at any other lysimeter, and Zn levels are intermediate (Chapter 4). This material also has the lowest NPR ratio (Section 2.13.3) indicating that it is the ‘dirtiest’ and has the largest potential for acid generation (i.e., lowest acid buffering potential) and metal release. In addition, the average solid phase Fe concentration of this material is more than twice the amount of Fe reported from the rest of the pile (Table 2.4), which confirms MLA results that nearly 4.5 % of this material consists of sulphide minerals. The primary sulphide minerals are pyrite, chalcopyrite, and pyrrhotite.

Based on depleted O_2 concentrations, enriched CO_2 concentrations, pH and an average temperature in lines 2 and 3 that are $1.2 \text{ }^\circ\text{C}$ higher than lines 1 and 4 (Chapter 4), there is

reasonable evidence indicating that this is a relative 'hot spot' in which elevated rates of chemical oxidation are occurring. Furthermore, that the highest dissolved Ca concentrations are reported in sub-lysimeter A despite the lowest solid phase Ca concentration likely indicates that elevated sulphide oxidation is driving the dissolution of calcite to buffer the generated acid, and that this region may be the first to be depleted of its buffering capacity.

A 4 x 4 m vertical column of waste rock, amounting to approximately 330 tonnes, lies directly above sub-lysimeter A. A majority of this material originates from Tipping Phase II. Despite reporting only 0.5 % of the total pile outflow, the average loading rates at A are nearly half of those calculated at C. Average solute loading rates are larger than those at sub-lysimeter B by a factor of 1.5 - 2, and indicate that both water flow and solid phase composition (and susceptibility to weathering) are dominant factors affecting loadings at this site.

That this relatively coarse material contains the highest solute loading rates within test pile 1 is contradictory to previous statements that water flowing through a finer material will have a higher dissolved load (based on the surface area). This is largely because of the material properties and initial sulphide mineral content, which causes the mineral weathering rates to be the highest in test pile 1. This is further corroborated by mineralogical work found in Aranda (2009). When these high weathering rates are combined with the intermediate flow rates, this leads to relatively high loading rates compared to the rest of the pile (i.e., similar to sub-lysimeter C and basal lysimeter D). In addition, since a majority of this material consists of silicate minerals (which are more resistant to weathering than carbonates), this means that the buffering capacity of this material may be depleted much sooner than the buffering capacity in other regions of the pile.

6.4.4 Tipping Phase III - Sub-lysimeter C

Material from Tipping Phase III consists of approximately 68 % marble diopside and 32 % grey hornfels. No particle size distribution test was performed on this material. Water passing through Tipping Phase III passes through the protective layer before reporting to the front sub-lysimeter C which is located under the front batter (Figure 6.1).

Based on Table 2.3, material from Tipping Phase III consists of, on average, approximately 74 % carbonate (highest in pile), 24 % silicate (lowest in pile) and 1.9 % sulphide (intermediate) minerals. This is supported by ICP analyses which demonstrate that this material has the highest initial solid phase Ca concentration, with intermediate Zn and S concentrations (Table 2.4). The NPR is the second highest compared to the rest of the pile (Table 6.1).

A 4 x 4 m vertical column of waste rock, amounting to approximately 240 tonnes, lies directly above sub-lysimeter C. Because C is under the batter, not all of the column is filled with waste rock and thus explains why the amount of material above C is approximately 70 % of the amount above sub-lysimeters A and B. All of this material originates from Tipping Phase III.

The total volume of water reported at sub-lysimeter C over the study period is an order of magnitude higher than that reported at sub-lysimeter B and nearly 4 times higher than sub-lysimeter A. Evidence of non-vertical flow is reported in Chapter 4 and possibly results from inter-bedded fine- and coarse-grained layers that help to channel water to certain locations (likely resulting from the end-dumping method; Chapters 1 and 2). This is the material that makes up the front batter, and is generally coarse and unconsolidated. Water reporting to sub-lysimeter C only has to infiltrate 6 – 9 m (as opposed to the 10 m for the other sub-lysimeters), so C has the fastest response to precipitation events (Chapters 3 and 4).

Solute concentrations in sub-lysimeter C effluent are generally the lowest (Chapter 4) whereas loadings rates are relatively the highest (Chapter 5). The lower concentrations are likely the result of less material, faster infiltration rates and a lower porewater residence time. That carbonate levels are highest in this material despite the lowest dissolved Ca concentrations may be because this material is very well-aerated (as oxygen concentrations are near atmospheric). Since calcite has a higher solubility in open-systems, then calcite dissolution rates may be lower compared to the pile interior. Lower concentrations may be the result of solute dilution based on the high flow rates under the batter. It is possible that the high loading rates result from flow through tipping phase II that reports to sub-lysimeter C, but would imply a net horizontal flow of 5 or more metres, which is largely unlikely.

6.4.5 Entire Pile / Basal Lysimeter D

The average elemental composition of the pile is found in Table 2.4. No NNP or NPR values are available for the entire pile, but based on the (linear) relationship between the proportion of total solid phase Ca and NNP [kg CaCO₃/tonne], the pile has an estimated NNP value of greater than 50, which means that the pile is most likely ‘non-acid generating’ and has a moderate buffering capacity (Chapter 3). The average pile silicates content is 48.4 %, with 47.5 % carbonate minerals, and 2.2 % sulphide minerals (Table 2.3). The remaining 1.9 % consists of phosphates, oxides, sulphates, and others.

Sub-lysimeter D is conceptualized as representative of the entire pile outflow. Average solute concentrations for basal lysimeter D are generally at intermediate levels within the pile compared to the sub-lysimeters, but generally exhibits high loading rates (Table 6.1). Overall, basal lysimeter D is representative of the entire pile response because it incorporates both high-flow/low-concentration and high-concentration/low-flow behaviour of the pile.

6.5 SUMMARY

This chapter examined the different flow mechanisms, pyrite oxidation, O₂ consumption and spatial variability within the pile. The most salient conclusions are that:

1. slow and diffuse matrix flow in test pile 1 has a higher dissolved load than the fresher, more rapid slugs associated with macropore flow,
2. energy calculations indicate that a significant proportion of heat generated from sulphide mineral oxidation is likely from pyrite oxidation, and the mass of SO₄ generated based on the heat released from pyrite oxidation is very similar to the calculated mass of SO₄ removed from test pile 1 based on the cumulative loadings,
3. the pile is relatively well-aerated and has consumed an estimated 5.5 pore volumes of oxygen over the 2-year study period, and
4. there is a strong spatial variability of weathering rates in the pile, with evidence of a ‘hot spot’ of sulphide mineral oxidation present in Tipping Phase II (instrumentation lines 2 and 3) and sub-lysimeter A. Since dissolved Ca concentrations are highest in this sub-lysimeter, despite the lowest proportion of carbonate material in this tipping

phase, this likely indicates that the buffering capacity of this material may be depleted much earlier than material from other parts of the pile.

In addition, it is evident that the quantification and prediction of mineral weathering rates is complicated. A high solid phase mineral or metal content does not necessarily mean that the effluent water will have a correspondingly high concentration of that mineral or metal. Low solute concentrations will not always correspond with low loading rates. Material susceptibility to physical and chemical weathering, in conjunction with certain attenuation tendencies must also be considered. The characterization and prediction of mass loadings is site-specific, and is highly heterogeneous with loading rates that vary by at least an order of magnitude over a distance of just a few meters within the test pile.

TABLES

Table 6.1. Integration of waste rock material and lysimeter effluent properties.

Material Properties								Lysimeters											
Uniformity	Coefficient	mm	Mass			Behaviour		Mass	Flow	Average Concentration			Average Normalized Loadings Rate						
			D ₆₀ /D ₁₀	%	Total	Ca	Zn			S	NNP [kg CaC O3/t]	NNP R	tonnes	m ³	SO ₄	Zn	Ca	SO ₄	Zn
Protective Layer	29	9	5,560	1,757	7,200	13,000	779	192	-	-	-	-	-	-	-	-	-	-	-
Tipping Phase I/B	19	7.5	2,835	758	1,800	2,835	597	75	330	2.8	1374	1,868	628	0.15	1.9E-04	0.07			
Tipping Phase II/A	48	4.1	5,385	1,018	2,400	592	76	6	326	6.4	5084	0,097	387	44	8.9E-04	0.60			
Tipping Phase III/C	N/A	N/A	5,780	1,931	4,800	27,800	837	35-3170	240	23.4	284	658	88	1.16	8.4E-04	0.54			
All / 1- D	33	7.7	19,560	5,463	6,200	108,400	-	-	19,104	1234	1245	1,350	550	0.79	8.3E-04	0.36			

FIGURE

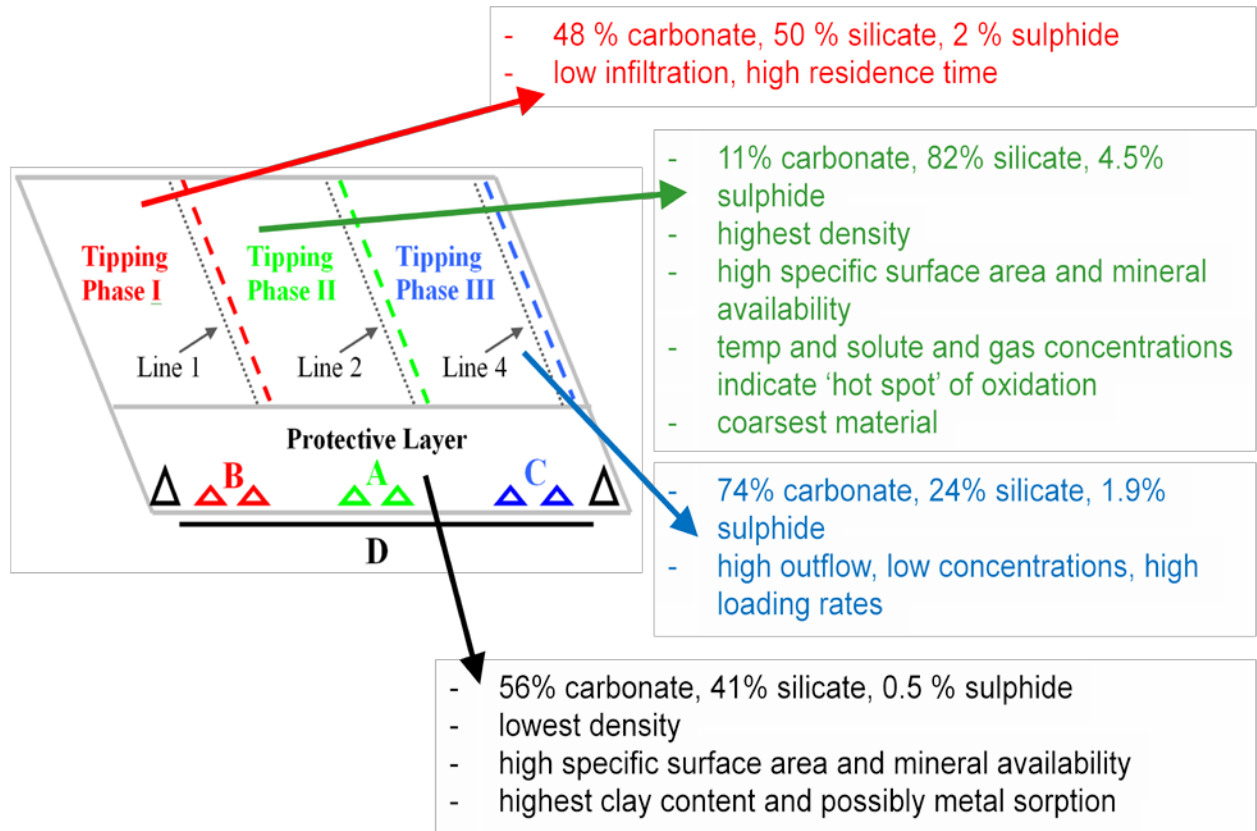


Figure 6.1. Integration of physical properties and observations throughout the pile.

7 CONCLUSIONS

7.1 PROJECT OVERVIEW AND SIGNIFICANCE

There is relatively little information about neutral rock drainage at mine sites (Chapter 1). In 2005, a collaboration among the University of British Columbia, Teck's Applied Research & Technology (ART) group, the Natural Science and Engineering Research Council of Canada (NSERC) and Compañía Minera Antamina S.A. undertook a comprehensive study into the mineralogical, biological, chemical, and hydrological waste rock leaching behaviour at the Antamina mine, Peru (Figure 1.1). Due to the presence of limestone in the region, careful planning of mine waste management must be carried out to avoid far-reaching effects of low-quality drainage conditions.

One component of the Antamina project is the construction, instrumentation and monitoring of a 36 x 36 x 10 m high waste rock test-pile in 2006. The waste rock is classified as non-acid generating (NAG), however mineral weathering leads to the mobilization of several metals and other solutes. No other experiment of this size has ever been constructed to examine neutral waste rock drainage, partly due to the heterogeneous properties of the waste rock material that make it difficult to accurately characterize. In this thesis, the initial two years of data from this experimental waste rock pile were analyzed.

7.2 SUMMARY OF RESULTS

The following summarizes the principal conclusions based on the first two years of data collected from this waste rock test pile:

7.2.1 Material Properties

1. Pile design and instrumentation was sufficient to characterize the hydrogeochemical response of the waste rock test-pile under investigation.
2. Test pile 1 is very heterogeneous in particle composition, size fraction and internal structure, and is not currently generating acidic drainage.
3. Based on the solid phase composition of the waste rock (NPR 6 – 3170), neutral drainage conditions can be expected in the future.

7.2.2 Hydrology

4. Pile hydrology is spatially and temporally variable: pile flow rates reach as high as 15 m³/day (12 mm/day) and as low as 0.1 m³/day (0.09 mm/day), respectively.
5. The maximum wetting front velocity of $v_{wf} = 0.5$ m/day is one order of magnitude higher than the maximum porewater velocity of $v_{pw} = 0.05$ m/day.
6. Some parts of the pile generate drainage throughout the entire year, whereas some parts of the pile stop discharging water during the dry season. The pile batter experiences a disproportionately high flux of outflow water compared to the pile interior.
7. Moisture content rises most rapidly under the batters, and less so near the less permeable, compacted top of the pile.
8. Rapid response to rain events in two of four lysimeters suggests that flow is highly dependent on waste rock heterogeneity, preferential flow paths and the influence of the batter.
9. A reasonable agreement between the water balance components is attained, indicating that the data analysis methodology that was carried out is suitable for the purpose of this investigation.
10. Over the course of the water year, 41 % of precipitation reports as outflow while 59 % evaporates in this humid climate.
11. A majority of outflow originates from matrix flow.
12. The initial wet-up period of test pile 1 took 3 to 4 months.
13. A certain time after a considerable period of rain follows a period of dry conditions, the pile has 're-wetted up' and several flow mechanisms are activated. These mechanisms include: preferential and macropore flow, 'pistoning' or pressure-wave displacement and non-vertical flow.

7.2.3 Chemistry

14. Pile chemistry is spatially and temporally variable: effluent water is pH-neutral (pH = 7 - 8.5), with seasonally varying SO₄ (500 – 2000 mg/L) and Zn (0.5 – 2.5 mg/L) concentrations. Tipping Phase II is generally associated with the highest effluent concentrations and Tipping Phase III generally has the lowest.

15. Pyrite is the principal source mineral of SO_4 , sphalerite is the principal source of Zn, and calcite is the principal source of Ca. The presence of SO_4 and Ca indicates that sulphide mineral oxidation is occurring and that calcite dissolution is buffering the generated acid.
16. Despite a relative increase in CO_2 and a decrease in O_2 concentrations at depth, and with 5.5 pore volumes of O_2 consumed over the study period, this demonstrates that test pile 1 is reasonably well-aerated.
17. The pile interior acts more like a partially-closed system whereas the pile exterior acts more like an open system.
18. Solute concentrations are generally inversely proportional to flow rate, with highest concentrations at the end of the dry season.
19. The range of porewater concentrations generally increases with depth in lines 1 and 2, and remains relatively stable in line 4.
20. Shallow temperature probes in the pile exhibit seasonal responses to atmospheric temperature variations, whereas deeper probes do not fluctuate as much. Instrumentation lines 2 and 3 are on average 1.2 °C higher than lines 1 and 4.
21. Test pile 1 likely underwent an initial pile flushing of weathering products from the most reactive material during the first year of pile operation. Long-term trends cannot be deduced because 2008 values were different from 2007 (i.e., flow, chemistry, temperatures, etc.), but it is clear that effluent water will contain a high dissolved load many years into the future.
22. There is a nearly proportional positive molar relationship between Ca^{2+} and SO_4^{2-} , which is consistent with acid neutralization. These results indicate that CO_2 is degassing and SO_4^{2-} concentrations can be used as a relative (not absolute) indicator for pyrite oxidation within the pile.
23. Geochemical modeling indicates that there are no attenuation mechanisms for Zn, and that calcite and gypsum are both at, or near, saturation.

7.2.4 Solute Loadings

24. Solute loadings are spatially and temporally variable. The maximum calculated SO_4 , Ca and Zn loading rates are 4 – 6, 2 – 3 and 0.003 – 0.005 mg/kg/week, respectively. Loading rates are lowest near the back (interior) of the pile.

25. Solute loadings are generally proportional to flow rate and inversely proportion to solute concentrations because of differences in magnitude of flow and concentration ranges.
26. Under extreme events, flow and loading rates increase by more than 50 % over one day whereas SO₄ and SC experience less proportional, more attenuated responses.
27. Mineral composition and net infiltration rate are more influential in governing solute mass loadings than solute concentration.
28. Nearly 0.4 % of the total initial solid phase S has been depleted, whereas less than 0.01 % of the total initial solid phase Zn and Ca has been depleted.
29. Loading rates from the test pile are smaller than field cell loading rates by a factor of 2 up to 2 orders of magnitude.

7.2.5 Data Integration

30. Each region of the pile is dominated certain key attributes:
 - a. back (Tipping Phase I – sub-lysimeter B): the back of the pile encounters the lowest permeability based on compaction of heavy machinery during pile construction. This results in the lowest infiltration rates reported by the pile, but relatively high concentrations based on a low porewater residence time.
 - b. middle (Tipping Phase II – sub-lysimeter A): although it has a relatively low permeability due to heavy machinery, this region experiences higher flux rates than towards the back. Compared to the rest of this pile, this material also contains a low proportion of carbonate minerals but high sulphide content. Loading rates are almost just as high as under the batter.
 - c. front (Tipping Phase III – sub-lysimeter C): this material is under the batter, which typically consists of the coarsest, unconsolidated material. Infiltration rates are highest along the batter (because evaporation is the lowest). Although the mineralogy of this material is intermediate (compared to the rest of the pile) and the solute concentrations are the lowest because they are diluted, the rate of solute release and transport is the highest in the pile. High loading rates under the batter likely indicate that mineral weathering rates are higher under a faster infiltration flux (despite the shorter porewater residence time).

31. Particle size and/or composition does not always dictate flow behaviour or solute concentrations. Higher solute concentrations are typically due to a higher solid phase composition, but may also be due to a lower infiltration rate and high porewater residence time (e.g., higher susceptibility to weathering).
32. Spatial patterns are likely controlled by rock-type heterogeneity and variability in flow path length and residence time that result from the end-dump construction process.
33. Some regions of the pile (particularly Tipping Phase II, Lines 2 and 3, and sub-lysimeter A) may lose their buffering capacity faster than other parts of the pile.

7.3 RELEVANCE TO THE ANTAMINA MINE

The principal physical, hydrological, chemical, and solute mass loading observations summarized above can be used to better understand the mechanisms that lead to metal and solute leaching from the Antamina waste rock. Results are valuable in helping to determine the most cost-effective ways in which to classify and dispose of the waste rock with minimal environmental impact in short- and long-term timeframes and to limit current and future operational and post-closure costs.

The three principal points that the Antamina mine should take from these observations are that:

1. results indicate that not all Class B material is benign and must be selectively dumped within the Tucush and East Dumps,
2. there is a need for a re-classification of Class B waste rock into sub-classes, and
3. the batters have a strong influence on loadings and have implications for the management of current operational piles.

7.3.1 Tucush Dump

This test-pile represents the closest existing simulation of the Tucush Dump and sheds light on uncertainties surrounding Class B waste rock effluent drainage quality. Results from this test pile cannot be directly extrapolated to the Tucush-scale, but can be used to provide a better idea of the expected leaching behaviour of this material. Since some Class B material is capable of producing poor quality drainage, it cannot be assumed that the wetlands at the base of the Tucush

Dump will be able to remove a sufficient amount of solutes from the discharging water, requiring additional water treatment considerations. A better approach would be to divert the more reactive Class B waste rock away from the Tucush Dump and send it to the East Dump. This requires a re-classification of the Class B waste rock scheme.

7.3.2 Re-Classification of Class B Waste Rock

Some Class B material has the ability to generate very poor-quality drainage that behaves more like Class A material than Class C. Different grades of Class B material should be identified using more variables than just rock description, rock classification, zinc, arsenic, sulphides and visible oxides (Table 3.2). These parameters should be used in combination with additional aspects such as more comprehensive mineralogical descriptions, lithology and friability. Results should also be combined with other investigative components of this neutral drainage waste rock study (e.g., Aranda (2009), Haupt (in progress)).

7.3.3 Possibility to Reduce Solute Concentrations Based on Dump Modifications

Based on the conclusions summarized above, it is clear that there are strong differences between the batter and the pile interior. As material is added to the existent waste rock dumps, the most reactive material could be placed near the back slope of the pile where non-vertical flow and compaction of the upper layer will help to prevent and re-direct water from infiltrating to depth. Although this region will also have the longest porewater pathways and residence times, the resulting effluent will likely be diluted with water from the rest of the pile when it reaches the base. The least-reactive material should then be placed under the batters where the infiltration rate is the highest, but solute concentrations are the lowest. Based on evidence of non-vertical flow due to the end-dumping procedure, it is likely that some of the pockets of high-reactivity material may be by-passed by infiltrating water which may be routed to less reactive parts of the pile.

Results should also be compared with the cover-study that is underway as part of this project and the test plot vegetation study that is currently conducted along waste rock slopes as an internal investigation by Antamina's environmental department.

7.4 RECOMMENDATIONS FOR CURRENT PILE MAINTENANCE AND FUTURE PILE CONSTRUCTION

7.4.1 Instrumentation

- a) always obtain soil-specific calibration (e.g., TDR, ECHO probe) and test all instrumentation before installing,
- b) replace custom-made EC probes with a more robust, improved design or commercial probes,
- c) always use two rain gauges (same manufacturer) in case one fails,
- d) tipping buckets and rain gauge should be connected to their own dedicated datalogger,
- e) quantify and minimize tipping bucket and rain gauge systematic errors,
- f) tipping bucket under the batter (sub-lysimeter C) should have a larger capacity that tips at 10 + seconds at the highest flow rates,

7.4.2 Modeling

- g) examine other methods to estimate missing precipitation and interpolate flow data to determine how results differ and validity of the RANSAC algorithm and performance,
- h) determine reliable scale-up procedures for various physical and chemical properties,
- i) thermal modeling – determine where heat generation is originating from, and whether gas convection is likely occurring within the pile,
- j) further quantification of sulphide mineral oxidation rates,
- k) gas modeling – determine transport mechanisms,
- l) geochemical and reactive-transport modeling (between sub-lysimeters, subsequent piles, etc.),
- m) examine sensitivities of temperature on solubility, solute mobility, etc.,

7.4.3 Data Management

- n) ensure that the water sampling protocol is clear and understood before sampling begins. Maintain consistency (i.e., sampling interval, procedures, priorities, units, QA/QC, etc.) throughout all components of the study: field cells, test piles, cover study, etc.,
- o) better data system management, organization and sharing,

- p) when a new program is sent to the datalogger, the 'date implemented' should be commented at the top,
- q) detailed maintenance notes should be encouraged,

7.4.4 Further Tests

- r) characterize evaporation differences between top of pile and batter,
- s) characterize infiltration of batters,
- t) install tensiometers to provide pressure measurements within the pile to better characterize unsaturated flow behaviour,
- u) isotopic analysis (residence time, etc),
- v) conduct a tracer test (to determine porewater travel time, extend of preferential pathways, etc.),
- w) deconstruct pile. There is no current plan for deconstruction, but this should occur to verify findings and provide a more complete dataset that will help in understanding flow and chemistry mechanisms within this pile,
- x) more lab and field tests to determine: matrix porosity, hydraulic conductivity (bulk and fine-grained), soil water characteristic curve, secondary mineralization, heterogeneity, mineral accessibility, surface area, susceptibility to weathering, texture, etc. of waste rock,
- y) determine physical properties of 'lastre' utilized in the 2B-Protective Layer (e.g., water content) and possible TDR calibration in this material,
- z) determine mechanisms that lead to secondary mineralization (and identify them if possible) and ways in which to promote these surface coatings in waste rock environments as viable strategies for remediation or prevention of poor drainage quality conditions,
- aa) mixing tests for material at this pile – different types of Class B material with itself, with Class A, Class C, etc.,
- bb) better and more reliable measurement of (automated) gas samples,

7.4.5 Personnel

- cc) always have someone on site (UBC or UBC-representative) to deal with instrumentation on site (including datalogger program),
- dd) always have more than one person supervising construction on site, and
- ee) better communication between all parties: UBC, Environmental Department, Contractors, Mining Operations, etc.

7.5 CONCLUDING REMARKS

The fate and transport of water and solutes in unsaturated waste rock environments is difficult to quantify and accurately predict. This investigation has shed light on the various mechanisms that contribute to the neutral drainage waste rock environment at the Antamina mine, Peru. Although long-term trends cannot be determined based on the initial two-years of data collected from this test pile, they are useful in characterizing the initial pile flushing and understanding which flow processes are dominant under certain conditions. The pile experiment is continuing and a suite of data is being collected that will be combined and compared to data from four subsequent test piles and additional mineralogical, microbiological, field cell and cover study experiments to obtain a comprehensive characterization of neutral pH drainage from waste rock. The extensive dataset will continue to improve the characterization of the leaching potential of Class B waste rock and waste rock in general, and will contribute in minimizing the short- and long-term environmental impact of poor quality waste rock drainage at the Antamina mine.

8 REFERENCES

1. Allen, R, Pereira, L., Raes, D., and M. Smith. 1998. Crop evapotranspiration: Guidelines for computer crop water requirements. FAO Irrigation and Drainage Paper No. 56, Food and Agricultural Organization of the United Nations, Rome.
2. Andrina, J., Miller, S. and A. Neale. 2003. The design, construction, instrumentation and performance of a full-scale overburden stockpile for mitigation of acid rock drainage, Grasberg Mine, Papua Province, Indonesia. In: Proceedings of the 6th International Conference on Acid Rock Drainage, Cairns, Queensland, Australia.
3. Andrina, J., Wilson, W., Miller, S. and A. Neale. 2006. Performance of the acid rock drainage mitigation waste rock trial dump at the Grasberg Mine. In: Proceedings of the 7th International Conference on Acid Rock Drainage, St. Louis, MO, USA.
4. Antamina, 2003. "The geology and metal zonation of the Antamina deposit", PowerPoint presentation presented by Lipten, E. and M. Pacheco. Geology Department, Compañía Minera Antamina S.A., Yanacancha, Peru.
5. Aranda, C., Klein, B., Beckie, R. and U. Mayer. 2009. Assessment of waste rock weathering characteristics at the Antamina mine based on field cells experiment. In: proceedings of the 8th International Conference on Acid Rock Drainage, Skellefteå, Sweden.
6. Aranda, C. 2009. Assessment of waste rock weathering characteristics at the Antamina mine based on field cells experiment. M.A.Sc. thesis, University of British Columbia, Vancouver, Canada.
7. AMEC, Resource Modeling – Huaraz, Peru. Project No. 157041. Ch 18.
8. Azam, S., Wilson, W., Herasymuik, G., Nichol, C. and L. Barbour. 2007. Hydrogeological behaviour of an unsaturated waste rock pile: a case study at the Golden Sunlight Mine, Montana, USA. Bulletin of Engineering Geology and the Environment. 66: 259-268
9. Aubertin, M., Mbonimpa, M., Bussière, B. and R. Chapuis. 2003. A model to predict the water retention curve from basic geotechnical properties. Canadian Geotechnical Journal. 40(6): 1104-1122
10. Baver, L., Gardner, W. and W. Gardner. 1972. Soil Physics. 4th Ed. John Wiley & Sons, Inc., Toronto, Canada.
11. Bay, D. Corazao Gallegos, J.C., Peterson, H., Dockrey, J., Singurindy, O., Beckie, R., Mayer, U., Smith, L., Klein, B. and W. Wilson. 2008. Preliminary geochemical and flow responses of neutral drainage from a field-scale experimental waste rock pile at

- the Antamina mine, Peru. In: Proceedings of the Water Air Land Sustainability in Mining Symposium, 47th conference of metallurgists, Winnipeg, Manitoba, Canada.
12. Bay, D., Peterson, H., Singurindy, O., Aranda, C., Dockrey, J., Sifuentes, F., Mayer, U., Smith, L., Klein, B. and R. Beckie. 2009. Assessment of neutral pH drainage from three experimental waste-rock piles at the Antamina mine, Peru. In: Proceedings of the 8th International Conference on Acid Rock Drainage, Skellefteå, Sweden.
 13. Bellehumeur, T. 2001. Mechanisms and spatial variability of rainfall infiltration on the Claude waste rock pile. M.A.Sc. thesis. University of British Columbia, Vancouver, Canada.
 14. Beven, K. and P. Germann. Water flow in soil macropores II. A combined flow model. *Journal of Soil Sciences*. 32: 15-29.
 15. Blowes, D., Jambor, J. and C. Hanton-Fong, C., Lortie, L. and D. Gould. 1998. Geochemical, mineralogical and microbiological characterization of a sulphide-bearing carbonate-rich gold-mine tailings impoundment, Joutel, Quebec. *Applied Geochemistry*. 13(6): 687-705.
 16. Blowes, D. and C. Ptacek. 1994. Acid-neutralization mechanisms in inactive mine tailings. In: Jambor, J., Blowes, D. (Eds), *Environmental Geochemistry of Sulfide Mine-Wastes*, Mineral Association of Canada. Short Course, 22: 271 – 292.
 17. Blowes, D., Ptacek, C., Jambor, J. and C. Weisner. 2003. The geochemistry of acid mine drainage. *Treatise on Geochemistry*. 9: 149-204.
 18. Bouwer, H. 1986. Intake Rate: Cylinder Infiltrometer. In: *Methods of Soil Analysis, Part 1: Physical and Mineralogical Methods – Agronomy Monograph no. 9* (2nd Ed). Madison, WI. American Society of Agronomy – Soil Science Society of America. Chapter 32.
 19. Brett, J. and J. Banfield. 2003. Microbial communities in acid mine drainage. *FEMS Microbiology Ecology*. 44: 139-152
 20. Brierley, J. and C. Brierley. 2000. Present and future commercial applications of biohydrometallurgy. *Hydrometallurgy*. 59(2-3): 223-239.
 21. Bussière, B., Aubertin, M. and R. Chapuis. 2003. The behaviour of inclined covers used as oxygen barriers. *Canadian Geotechnical Journal*. 40(3): 512-535
 22. Buytaert, W., Celleri, R., Willems, P., De Bievre, B. and G. Wyseure. 2006. Spatial and temporal rainfall variability in mountainous areas: A case study from the south Ecuadorian Andes. *Journal of Hydrology*. 329: 413– 421

23. Carey, S., Barbour, S. and M. Hendry. 2005. Evaporation from a waste-rock surface, Key Lake, Saskatchewan. *Canadian Geotechnical Journal*. 42: 1189 – 1199.
24. Carroll, K, Artiola, J. and M. Brusseau. 2006. Transport of Molybdenum in a Biosolid-Amended Alkaline Soil. *Chemosphere*. 65: 778-785.
25. Ciach, G. 2003. Local random errors in tipping-bucket rain gauge measurements. *Journal of Atmospheric and Oceanic Technology*. 20: 752-759.
26. Conlan, M. 2009. Attenuation mechanisms for molybdenum in neutral rock drainage. M.A.Sc. thesis. University of British Columbia, Vancouver, Canada.
27. Corazao Gallegos, J.C., 2007. The design, construction, instrumentation, and initial response of a field-scale waste rock test pile, M.A.Sc. thesis. University of British Columbia, Vancouver, Canada.
28. Corazao Gallegos, J.C., D. Bay, R. Beckie, B. Klein, U. Mayer, L. Smith, W. Wilson, S. Brienne and H. Letient, 2007. Design and Construction of Field-Scale Waste Rock Test Piles at The Antamina Mine, Peru. *Geotechnical News*. 25(1): 49-5.
29. Dawson, R. and N. Morgenstern. 1995. Liquifaction flowslides in Rocky Mountain coal mine waste dumps, Phase 3, Final Report. Natural Resources Canada, Ottawa, Ontario. Contract report 23440-3-9135/01.
30. Diodato, D. and R. Parizek. 1994. Unsaturated hydraulic properties of reclaimed coal strip mines. *Ground Water* 32(1): 108–119.
31. Evans, D., Letient, H. and T. Aley. 2005. Aquifer Vulnerability mapping in karsitic Terrain. In: *The Proceedings of 2005 Society for Mining, Metallurgy, and Exploration (SME) Annual Meeting*, Salt Lake City, Utah.
32. Eriksson, N., Gupta A. and G. Destouni. 1997. Comparative analysis of laboratory and field tracer tests for investigation preferential flow and transport in mining waste rock. *Journal of Hydrology*. 194: 143-163.
33. Fala, O., Aubertin, M., Molson, J., Bussiere, B., Wilson, G. and Chapuis, R. 2003.
34. Numerical modeling of unsaturated flow in uniform and heterogeneous waste rock piles. In: *Proceedings of the 6th International Conference on Acid Rock Drainage*, Cairns, Queensland, Australia. 895-902.
35. Fala, O., Molson, J., Aubertin, M. and B. Bussière. 2005. Numerical modeling of flow and capillary barrier effects in unsaturated waste rock piles. *Mine water and the environment*. 24: 172-185.

36. Feasby, G. and G. Tremblay G. 1995. New technologies to reduce environmental liability from acid generating minewastes. In: Proceedings of Sudbury 1995 Mining and the Environment.643-7.
37. Fines, P., Wilson, W., Williams, D., A. Tran and S. Miller. 2003. Field Characterization of two Full-Scale Waste Rock Piles. In: Proceedings of the 6th International Conference on Acid Rock Drainage, Cairns, Queensland, Australia.
38. Fischler, M. and R. Bolles. 1981. Random Sample Consensus: A paradigm for model fitting with applications to image analysis and automated cartography. *Graphics and Image Processing*, 24: 381-395.
39. Flury, M., Flühler, H., Jury, W. and J. Leuenberger. 1994. Susceptibility of soils to preferential flow of water: A field study. *Water Resources Research*. 30(7): 1945-1954.
40. Frostad, S., Klein, B. and Lawrence, R., 2005. Determining the weathering characteristics of a waste rock dump with field tests. *International Journal of Mining, Reclamation and Environment*. 19(2): 132-143.
41. Gelinas, P., Lefebvre, R., and Choquette, M., 1992. Monitoring of acid mine drainage in a waste rock dump. In: *Environmental issues and Waste Management in Energy and Minerals Production*, 747-756.
42. Gerke, H. and M. van Genuchten. 1993. A Dual-Porosity Model for Simulating the Preferential Movement of Water and Solutes in Structured Porous Media, *Water Resource. Research*. 29(2): 305–319
43. Germann, P. and K. Beven. 1981. Water flow in soil macropores I: An experimental approach. *Journal of Soil Sciences*. 32: 1-13.
44. Golder Associates, 2006. Waste dump and stockpile water quality estimates – Phase 3 – Antamina Mine, Peru. Final Version 4.0. February, 2006. Golder Associates Perú S.A.
45. Golder Associates, 2007a. Estudio de Impacto Ambiental - Proyecto de Expansión del Tajo Abierto y Optimización del Procesamiento [Environmental Impact Assessment: Expansion of the open pit and processing optimization], Compañía Minera Antamina S.A. July, 2007. Golder Associates Perú S.A.
46. Golder Associates, 2007b. Waste Rock and Tailings Geochemistry, Field Cell Monitoring 2002 to 2006, Antamina Mine Peru, Version 4.0, February 2007, Golder Associates Perú S.A.
47. Herasymuik, G., Wilson, G., Barbour, S. and T. Smith, 1995. The characterization of hydrologic properties and moisture migration pathways of a waste rock pile. *Mine reclamation, reclamation in extreme environments*. In: 19th British Columbia Ministry of Energy and Mines, Victoria, BC.

48. Hayashi, M. 2004. Temperature-electrical conductivity relation of water for environmental monitoring and geophysical data inversion. *Environmental Monitoring and Assessment*. 96: 119-128.
49. ICOLD, 1996. A guide to tailings dams and impoundments: Design, construction, use and rehabilitation. International Commission on Large Dams, Bulletin (United Nations Environment Programme). No. 106: 239
50. Jambor, J. and D. Blowes. 1998. Theory and application of mineralogy in environmental studies of sulphide bearing mine wastes. In: *Modern Approaches to Ore and Environmental Mineralogy*. Cabri, L and D. Vaughan. (Eds). Mineralogical Association of Canada, Canada, p. 267-401 (Chapter 12).
51. Kleinmann, R., Edenborn, H. and R. Hedin. 1991. Biological treatment of mine water—an overview. In: *2nd International Conference on Abatement of Acidic Drainage*. MEND Secretariat, Rome. 1: 27–42.
52. Lawrence, W. and Y. Wang. 1996. Determination of neutralization potential for acid rock drainage prediction. MEND project 1.16.3. Vancouver, Canada.
53. Lefebvre, R. 1994. Characterization and numerical modeling of acid mine drainage in waste rock dump. Ph.D dissertation, Université Laval, Quebec, Canada.
54. Lefebvre, R. and P. Gelinias. 1995. Numerical modeling of AMD production in waste rock dumps. In: *Sudbury '95, Conference on Mining and the Environment*, Sudbury, Ontario. 1: 869 - 878.
55. Lefebvre, R., Hockley, D., Smolensky, J. and P. Gélina. 2001. Multiphase transfer process in waste rock piles producing acid mine drainage 1: Conceptual model and system characterization. *Journal of Contaminant Hydrology*. 52: 137-164.
56. Linklater, C., Sincalire, D. and P. Brown. 2005. Coupled chemistry and transport modeling of sulphidic waste rock dumps at the Aitik mine site, Sweden. *Applied Geochemistry*. 20: 275-293
57. Lipten, E. and S. Smith. 2004. The Geology of the Antamina Copper-Zinc Deposit, Peru, South America; in Porter, T.M. (Ed.), *Super Porphyry Copper & Gold Deposits: A Global Perspective*; PGC Publishing, Adelaide.
58. Love, D., Clark, A. and K. Glover. 2004. The lithologic, stratigraphic and structural setting of the giant Antamina copper-zinc skarn deposit, Ancash, Peru. *Economic Geology*. 99: 887-916

59. Machibroda, R. 1994. M.Sc. thesis: Evaluation of evaporative fluxes from mint tailings using the modified Penman formulation. Placer Dome Cover and waste Rock Research program. University of Saskatchewan, Saskatoon, Canada.
60. Malmström, M., Destouni, G, S. Banwart and B. Strömberg. 2000. Resolving the scale-dependence of mineral weathering rates. *Environmental Science and Technology* 34(7): 1375-1378.
61. Marcoline, J. 2008. Investigations of water and tracer movement in covered and uncovered unsaturated waste rock. Ph.D. dissertation. University of British Columbia, Vancouver, Canada.
62. Mayer, K., Benner, S., Blowes, D., and E. Frind, 1999. The reactive transport model MIN3P: Application to acid mine drainage generation and treatment. Nickel Rim Mine Site, Sudbury, Ontario. In: Sudbury '99, Conference on Mining and the Environment, Sudbury, Ontario. 1: 145-154.
63. Mbonimpa, M., Aubertin, M., Aachib, M. and B. Bussière. 2003. Diffusion and consumption of oxygen in unsaturated cover materials. *Canadian Geotechnical Journal*. 40(5): 916-932.
64. Milczarek, M., Hammermeister, D., Buchanan, M., Vorwaller, B. and T. Conner. 2009. In-situ monitoring of a closed waste rock facility. In: Proceedings of the 8th International Conference on Acid Rock Drainage, Skellefteå, Sweden.
65. Moncur, M., Ptacek, C. Blowes, D. and J. Jambor. 2005. Release, transport and attenuation of metals from an old tailings impoundment. *Applied Geochemistry*. 20: 639-659
66. Morin, K., Gerencher, E., Jones, C., and D. Konasewich. 1991. Critical Literature Review of Acid Drainage from Waste Rock. Canadian MEND Report 1.11.1, CANMET, Government of Canada, Ottawa
67. Natural Resources Canada, 2004. Design, construction and performance monitoring of cover systems for waste rock and tailings. Mine Environment Neutral Drainage (MEND) 2.21.4. (ed. O’Kane Consultants Inc.). OKC Report No. 702-01.
68. Nichol, C. 2002. Transient flow and transport in unsaturated heterogeneous media: Field experiments in mine waste rock. Ph.D. dissertation. University of British Columbia, Vancouver, Canada.
69. Nichol, C., Beckie, R. and L. Smith. 2002. Evaluation of uncoated and coated time domain reflectometry probes for high electrical conductivity systems. *Soil Science Society of America Journal*. 66: 1454-1465.

70. Nichol, C., Smith, L and R. Beckie. 2003. Time domain reflectometry measurements of water content in coarse waste rock. *Canadian Geotechnical Journal*. 40: 137-148.
71. Nichol, C., Smith, L and R. Beckie. 2005. Field-scale experiments of unsaturated flow and solute transport in a heterogeneous porous medium. *Water Resources Research*. 41:W05018, doi:10.1029/2004WR003035.
72. Neuner, M. 2009. Water flow through unsaturated mine waste rock in a region of permafrost. M.Sc. thesis, University of British Columbia, Vancouver, Canada.
73. Neuner, M., Gupton, M., Smith, L., Pham, N., Smith, L., Blowes, D. and D. Segó. 2009. Diavik waste rock project: Unsaturated water flow. In: proceedings of the 8th International Conference on Acid Rock Drainage, Skellefteå, Sweden.
74. Newman, L. 1999. Preferential flow in vertically oriented unsaturated soil layers. M.Sc. thesis. University of Saskatchewan, Saskatoon, Canada.
75. Noborio, K. 2001. Measurement of soil water content and electrical conductivity by time domain reflectometry: a review. *Computers and Electronics in Agriculture*. 31: 213-237.
76. Olson, G. and T. Clark. 2008. Bioleaching of molybdenite. *Hydrometallurgy*. 93(1-2): 10-15.
77. Otwinowski, M. 1995. Scaling analysis of acid rock drainage. Canadian MEND report 1.19.7, CANMET, Government of Canada, Ottawa.
78. Parkhurst, D.L., Appelo, C.A.J. and Geological Survey (U.S.), 1999. User's guide to PHREEQC, Version 2: a computer program for speciation, batch-reaction, one-dimensional transport, and inverse geochemical calculations. Water-resources investigations report. U.S. Geological Survey: Earth Science Information Center, Open-File Reports Section, Denver, Colorado, xiv: 312.
79. Pantelis, G. and Ritchie, A. 1992. Rate-limiting factors in dump leaching of pyritic cores. *Applied mathematical modeling*. 16: 553-560.
80. Penman, H. 1948. Natural evapotranspiration from open water, bare soil and grass. In: *Proceedings of the Royal Society of London Series A*. 193:120-145.
81. Petrunic, B., Al, T. and L. Weaver. 2005. A transmission electron microscopy analysis of secondary minerals formed in tungsten-mine tailings with an emphasis on arsenopyrite oxidation. *Applied Geochemistry*. 21: 1259-1273.
82. Price, W.A., 1997. Guidelines and Recommended Methods for the Prediction of Metal Leaching and Acid Rock Drainage at Mine sites in British Columbia - Draft, Smithers, BC, Canada

83. Price, W. 2003. The mitigation of acid rock drainage: Four case studies from British Columbia. Report prepared for CANMET, Natural Resources Canada, Smithers, B.C.
84. Rasmussen, T., Baldwin, Jr., R., Dowd, J. and A. Williams. 2000. Tracer vs. pressure wave velocities through unsaturated saprolite. *Soil Science Society of America Journal*. 64: 75-85.
85. Redwood, D. 1999. The Geology of the Antamina Copper-Zinc Skarn Deposit, Peru. The Gangue, Geological Association of Canada Mineral Deposits Division Newsletter, January. 1999. 60: 1-7.
86. Rhode, T. and D. Williams. 2009. Early hydrological monitoring of Cadia's instrumented trial waste rock dump. In: proceedings of the 8th International Conference on Acid Rock Drainage, Skellefteå, Sweden.
87. Richards, L. 1931. Capillary conduction through porous mediums. *Physics*. 1: 313-318.
88. Ritchie, A. 1994. Sulphide oxidation mechanisms. Controls and rates of oxygen transport. In: *The Environmental Geochemistry of Sulphide Mine-wastes* (eds. J. Jambor and D. Blowes). Mineralogical Association of Canada, Nepean, Ontario. 22: 201-246.
89. Saretzky, G. 1998. M.A.Sc. thesis: Hydrological characterization of a sulphide waste rock dump. Department of Civil Engineering. University of Saskatchewan, Saskatoon, Canada.
90. Sherlock, E., R. Lawrence and R. Poulin, 1995. On the neutralization of acid rock drainage by carbonate and silicate minerals. *Environmental Geology*. 25: 43-54.
91. Sobek, A., Schuller, W., Freeman, J. and R. Smith. 1978. Field and laboratory methods applicable to overburdens and minesoils, EPA-600/2-78-054. West Virginia Geological and economic Survey, West.
92. Soil Cover, 2000. *Soil Cover User's Manual*. Unsaturated Soils Group, Department of Civil Engineering, University of Saskatchewan, Saskatoon, Canada.
93. Sracek, O., Choquette, M., Gélinas, P., Lefebvre, R. and R. Nicholson, 2004. Geochemical characterization of acid mine drainage from a waste rock pile, Mine Doyon, Québec, Canada. *Journal of Contaminant Hydrology*. 69: 45-71.
94. Smith, L. and R. Beckie. 2003. Hydrologic and geochemical transport processes in mine waste rock, *Environmental Aspects of Mine Wastes*, Ed. J. Jambor, D. Blowes, and A.I.M. Ritchie, Short Course Series v. 31, Ed. R. Raeside, Mineralogical Association of Canada.

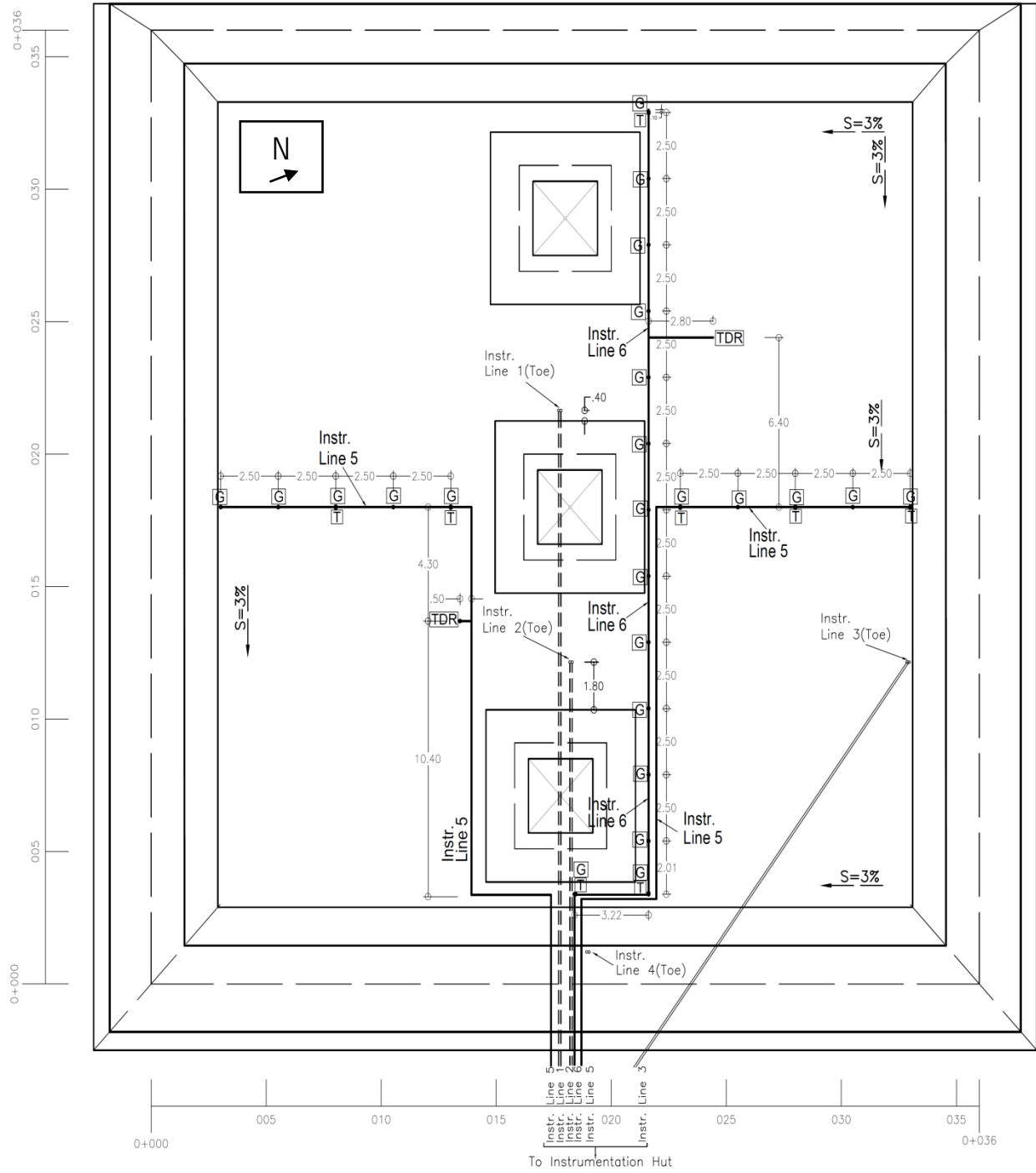
95. Stockwell, J., Smith, L., Jambor, J.L., and R. Beckie. 2006. The relationship between fluid flow and mineral weathering in heterogeneous unsaturated porous media: a physical and geochemical characterization of a waste rock pile, *Applied Geochemistry*. 21: 1347-1361.
96. Stollenwerk, K. 1998. Molybdate transport in a chemically complex aquifer: field measurements compared with solute-transport model predictions. *Water Resources Research* 34: 2727–2740.
97. Strömerg, B. and S. Banwart. 1999. Experimental study of acidity-consuming processes in mining waste rock: some influences of mineralogy and particle size. *Applied Geochemistry*. 14: 1–16.
98. Swanson, D., Barbour, S., Wilson, G. and M. O’Kane. 2003. Soil-atmosphere modeling of an engineered soil cover for acid generating mine waste in a humid, alpine climate. *Canadian Geotechnical Journal*. 40: 276-292.
99. Tuller, M. and D. Or. 2002. Unsaturated hydraulic conductivity of structured porous media: A review of liquid configuration-based models. *Vadose Zone Journal*. 1:14-37.
100. USDA, 1993. Acid drainage from mines on the National Forest: a management challenge. Forest Service Publication. 1505: 1–12.
101. Wagner, K. 2004. Characterization of the geochemistry of discharge waters, pore waters, primary and secondary minerals of an experimental waste rock pile, Cluff Lake mine, Saskatchewan, Canada. M.Sc. thesis. University of British Columbia, Vancouver, Canada.
102. Wagner, K., Smith, L. and R. Beckie. 2006. Hydrogeochemical characterization of effluent from mine waste rock, Cluff Lake, Saskatchewan. In: *Proceedings of the 7th International Conference on Acid Rock Drainage*, St. Louis, MO, USA.
103. Webb, G., Tyler, S., Collord, J., Van Zyl, D., Halihan, T., Turrentine, J. and T. Fenstermaker. 2008. Field-scale analysis of flow mechanisms in highly heterogeneous mining media. *Vadose Zone Journal*. 7: 899-908.
104. Wels, C., Lefebvre, R. and A. Robertson. 2003. An overview of prediction and control of air flow in acid-generating waste rock dumps. In: *Proceeding of the 6th International Conference on Acid Rock Drainage*, Cairns, Queensland, Australia.
105. Wilson, W., Fredlund, D. and S. Barbour. 1994. Coupled soil-atmosphere modeling for soil evaporation. *Canadian Geotechnical Journal*. 31(2): 151-161.
106. Wilson, W., Fredlund, D. and S. Barbour. 1997. The effect of soil suction on evaporative fluxes from soil surfaces. *Canadian Geotechnical Journal*. 34:145-155.

107. Wunderly, M., Blowes, D., Friend, E. and C. Ptacek. 1996. Sulphide mineral oxidation and subsequent reactive transport of oxidation products in mine tailings impoundments: A numerical model. *Water Resources Research*. 32(10): 3173-3187.
108. Yazdani, J. 1995. Soil water characteristic curve for mine waste rock containing coarse material. M.Eng. Thesis, University of Saskatchewan, Saskatoon, Canada.
109. Yazdani, J., Barbour, L, and W. Wilson. 2000. Soil water characteristic curve for mine waste rock containing coarse material, from Proceedings of the 6th Environmental Engineering Specialty Conference of the Canadian Society of Civil Engineers, London, Ontario, Canada.

APPENDIX A: PILE DESIGN AND CONSTRUCTION

Figure A.1. Pile base and instrumentation lines 5 and 6.....	207
Figure A.2. Construction of pile base.....	208
Figure A.3. Tipping Phase I.....	209
Figure A.4. Instrumentation Line 1.....	210
Figure A.5. Tipping Phase II.....	211
Figure A.6. Instrumentation line 2.....	212
Figure A.7. Instrumentation line 3.....	213
Figure A.8. Instrumentation line 4.....	214
Figure A.9. Datalogging system.....	215
Figure A.10. Top of test pile 1.....	216

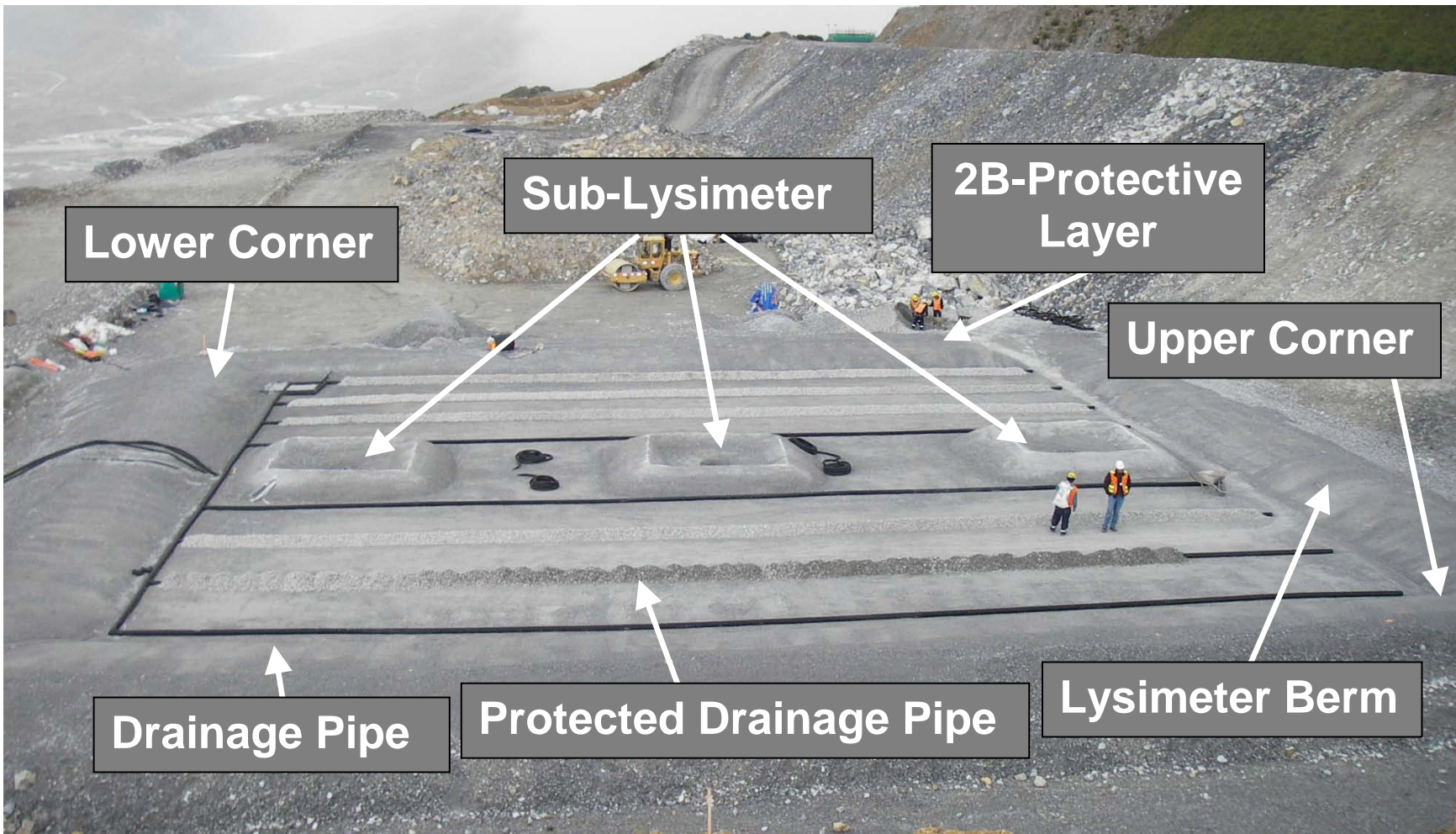
APPENDIX A: PILE DESIGN AND CONSTRUCTION



Plan View of Test Pile 1

SYMBOL	DESCRIPTION
G	Gas Sampling Port
T	Thermistor
TDR	Time Domain Reflectometry Probe

Figure A.1. Pile base and instrumentation lines 5 and 6.



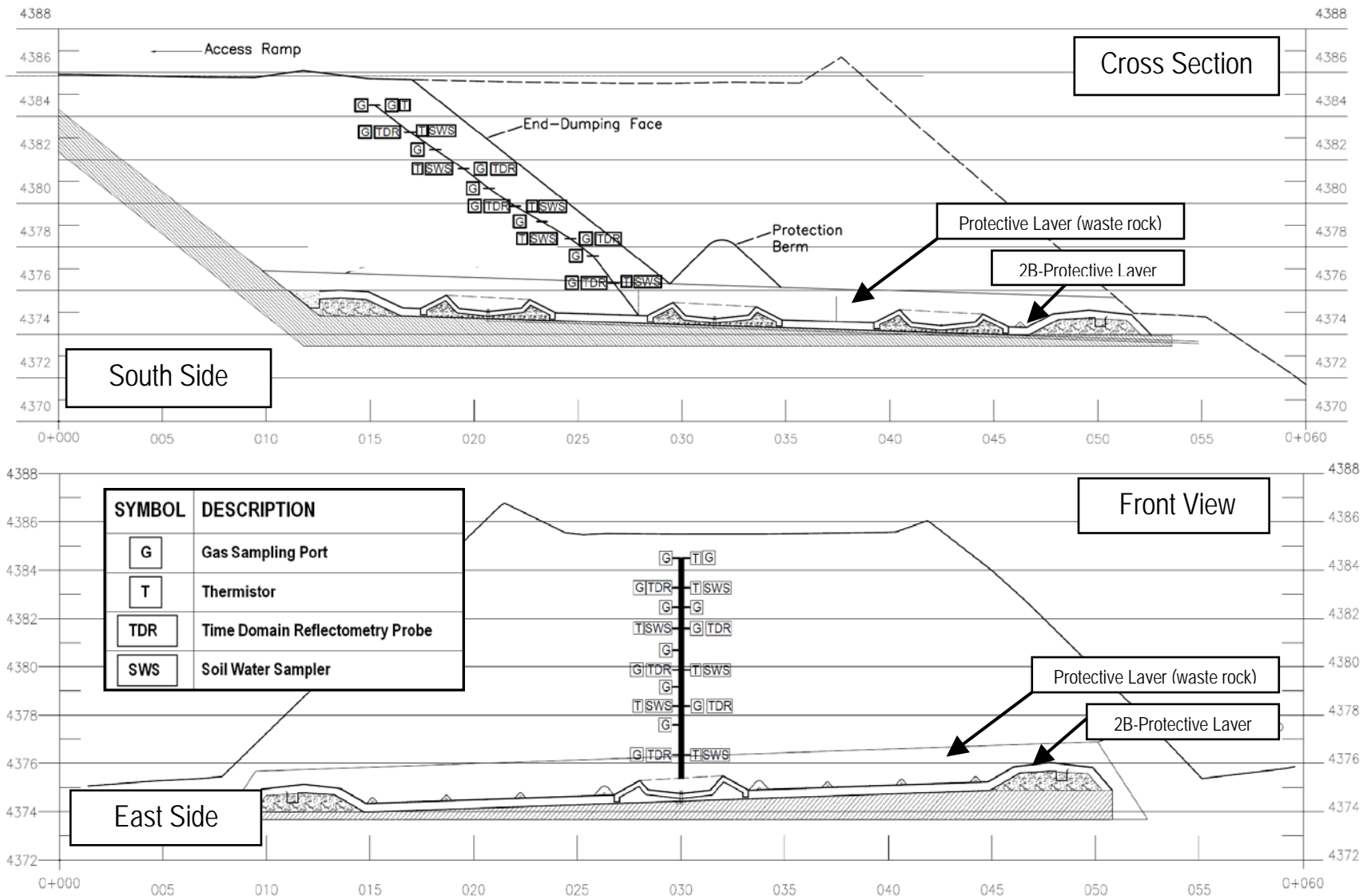
* view from north side

Figure A.2. Construction of pile base.



* view from north side

Figure A.3. Tipping Phase I.

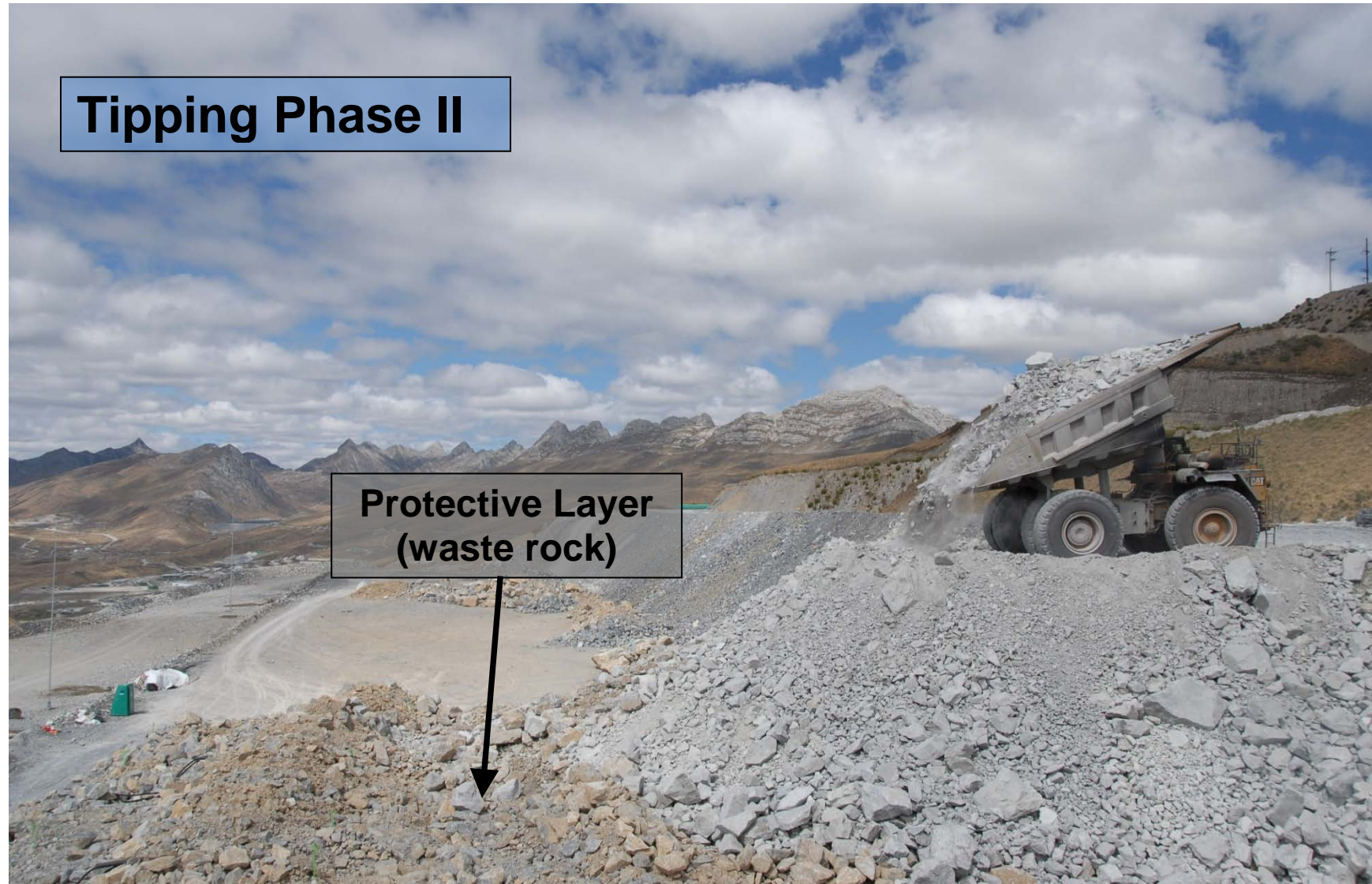


* view from south and east sides, respectively

Figure A.4. Instrumentation Line 1

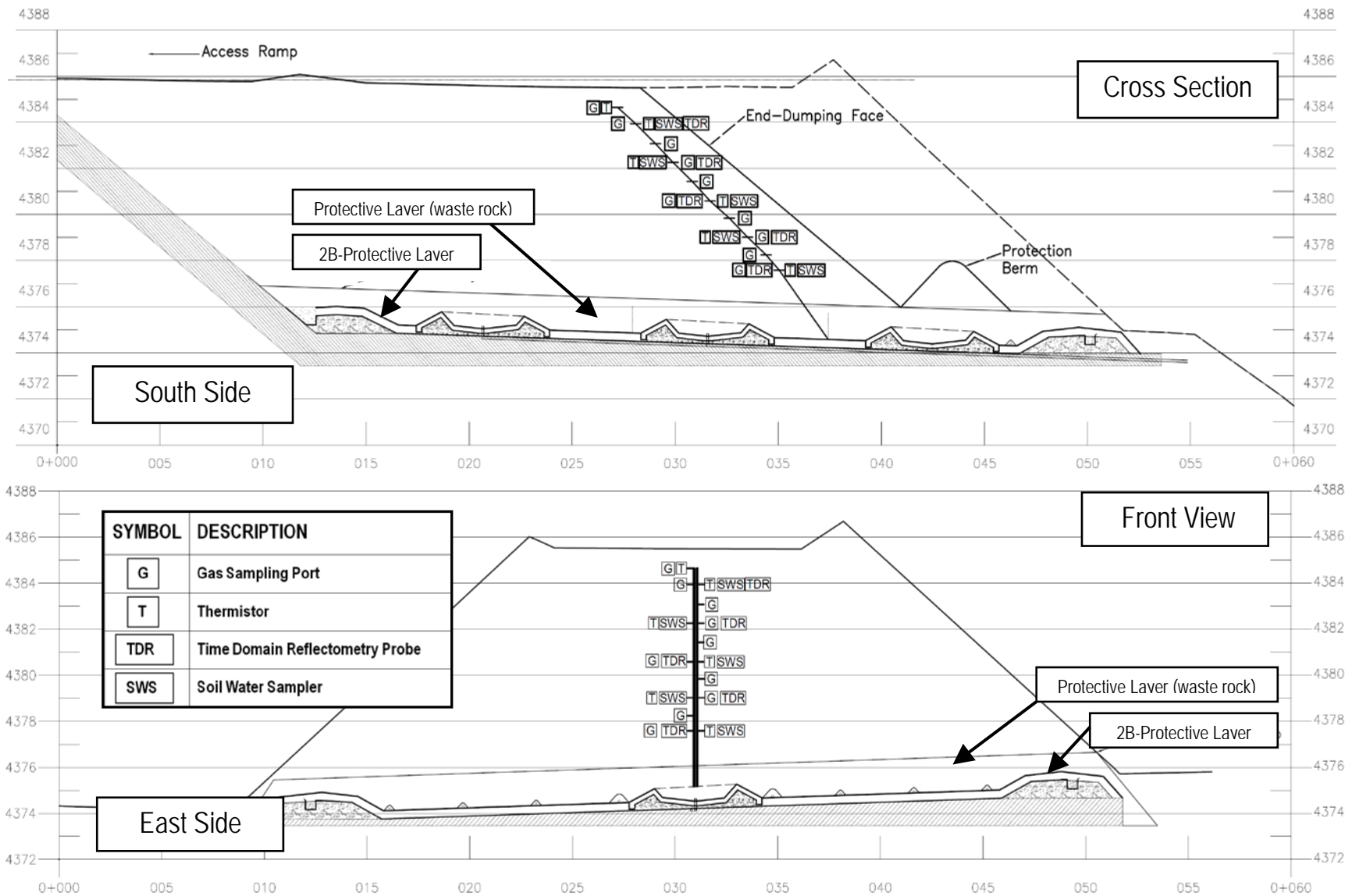
Tipping Phase II

Protective Layer
(waste rock)



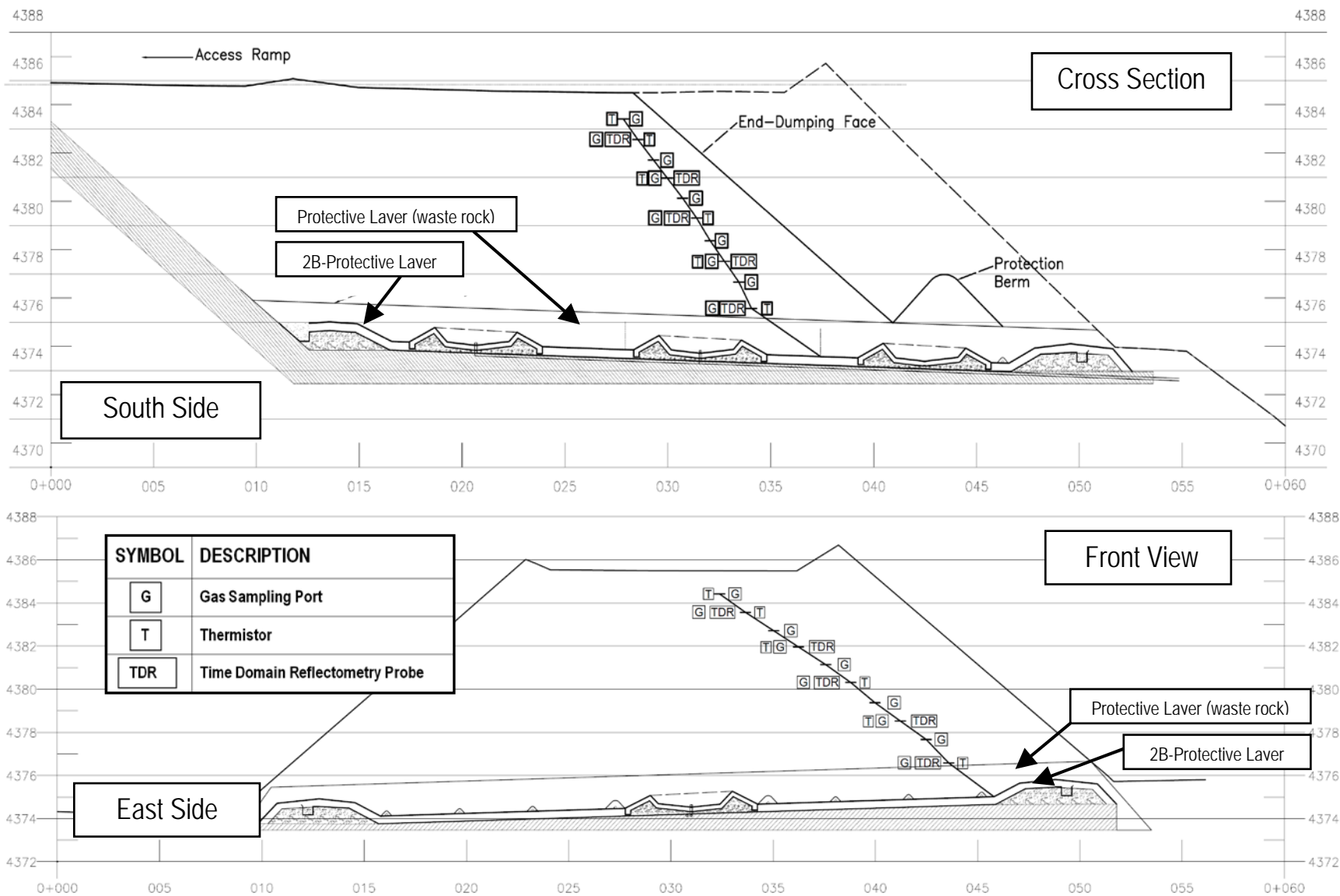
* view from north side

Figure A.5. Tipping Phase II.



* view from south and east sides, respectively

Figure A.6. Instrumentation line 2.



* view from south and east sides, respectively

Figure A.7. Instrumentation line 3.

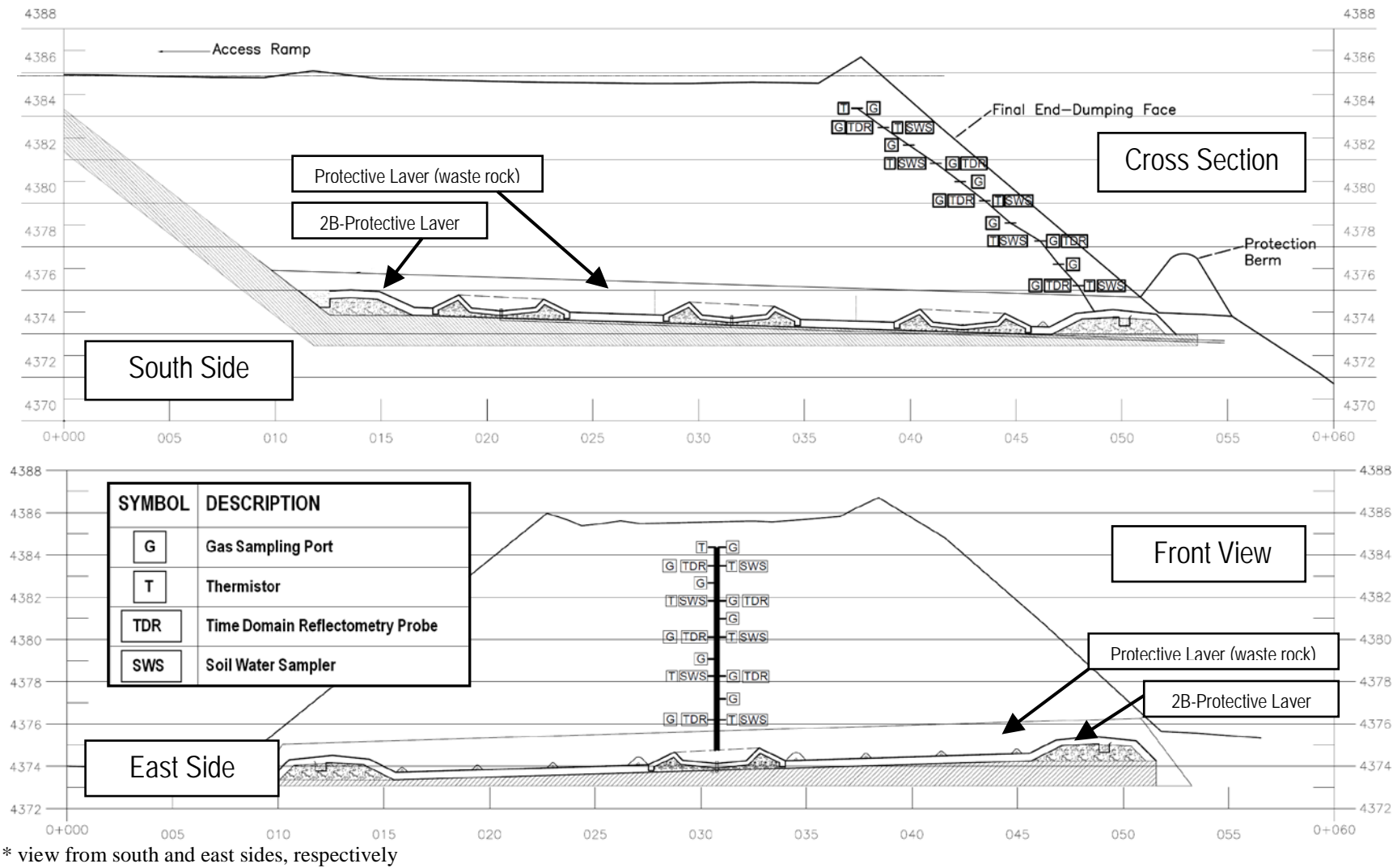


Figure A.8. Instrumentation line 4.

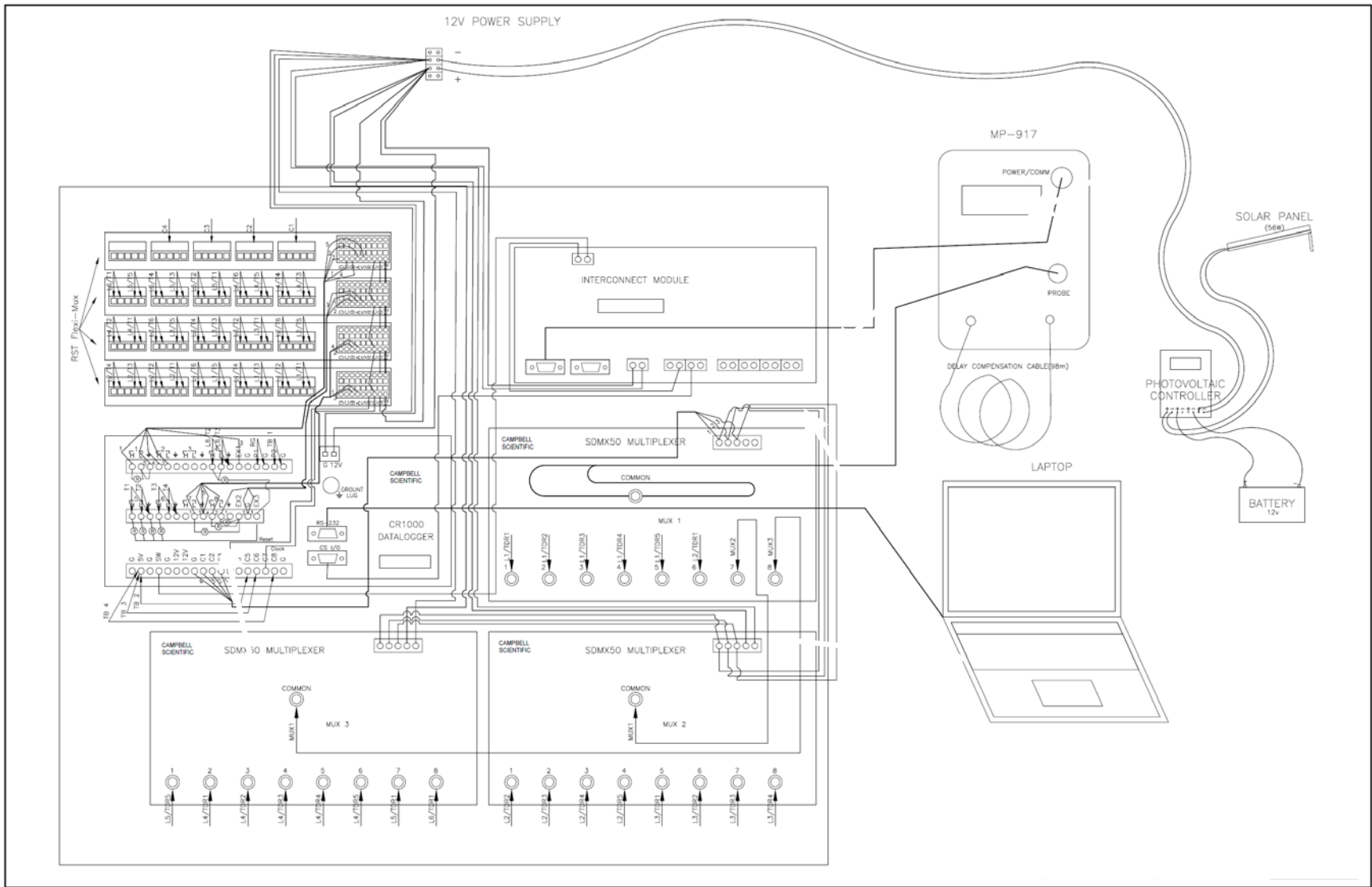


Figure A.9. Datalogging system.



Figure A.10. Top of test pile 1.

APPENDIX B: PILE 2 & 3 CONSTRUCTION MODIFICATIONS FROM PILE 1

B.1	BASE	218
B.2	END-DUMPING AND INSTRUMENTATION	220
B.3	INSTRUMENTATION HUT	222
B.4	REFERENCES.....	225

APPENDIX B: PILE 2 & 3 CONSTRUCTION MODIFICATIONS FROM PILE 1

This appendix summarizes modifications in the original test pile 1 (2006) design (Corazao Gallegos, 2007) that were implemented during the construction of test piles 2 and 3 (2007). Whenever possible, consistency in design was maintained between the piles. This design was also closely followed during the construction of Piles 4 and 5 (2008). Departures from the original pile design are highlighted (**bold**) in this section. Recommendations for test pile 4 and 5 modifications are also presented (*italics*). Test piles 2 and 3 were built almost exactly the same, and will be referred to throughout this section as a single test pile unless otherwise specified.

June 2008 (revisions May 2009)

B.1 BASE

This section describes the construction of the pile foundation and instrumentation. Principal components include the liner and instrumentation lines 5 and 6.

- a) A waste rock foundation pad was compacted with a slope of 3 % towards the south and east. A 0.20 m layer of lastre was placed on top of the foundation pad and subsequently compacted.
- b) The outer berm was placed in 3 separate layers, each separately compacted to a final height of 0.80 m. **Upon verification of the distance between berm apex to apex (N-S and E-W), it was clear that a mistake in the 36 x 36 m capture basin perimeter was not obtained. Modifications resulted in slight departures from the original berm design, but the resulting dimensions of the basal lysimeter remained 36 x 36 m.**
- c) A ditch was dug for the drainage pipes from the sub-lysimeters to the front of the pile. Protective tubes for instrumentation lines 1 and 2 were also placed in this trench. *A possible modification would be to place all protective tubes in their respective places on the slope after the tipping. This will avoid spending time sealing the geomembrane around the protruding pipes and the trench, will require less time protecting the pipes with material before dumping and subsequently excavating the pipe for instrumentation. It would also be easier to pass the instrumentation lines through the protective pipes. Further discussion weighing the advantages and disadvantages is recommended.*

- d) **The drainage pipe for the large lysimeter was placed at the lowest (southeast) corner of the pile, but was modified to leave from the front of the pile (eastward) so as to reduce the distance that water travels to the instrumentation hut and to maintain an appropriate gradient. This pipe was placed within the slope (e.g., between the 4373- and 4371-m platforms; Figure 2.5) until it reached the three other drainage pipes and was then connected to the instrumentation hut. This improved the design in test pile 1, and was more cost-efficient with materials.**
- e) **An NTP4 Bituminous Geomembrane (5.6 mm thick; 216 mil) was used instead of the 60 mil HDPE liner due to stronger, more resilient properties. The initial intent was to lay the geomembrane over the entire base of the pile, construct the three sub-lysimeters and cover them with geomembrane, as was done in test pile 1. On site, it was recommended that we construct the sub-lysimeters upon the lastre and place the geomembrane in one layer over the whole pile base. After, the geomembrane was visibly inspected for possible points of weakness and a patch was positioned upon it. Two different methods, a vacuum chamber and an ultrasonic device was used to detect defects in the geomembrane and at the seams.**
- f) Perforated, 4" HDPE drainage pipes were placed upon the geomembrane and surrounded with 0.10 – 0.20 m of gravel. Between the drainage pipes, a < 4" sorted material was placed using an excavator and Bobcat so that they were flush with the top of the gravel surrounding the drainage pipes.
- g) Two solid 4" HDPE pipes were installed in this layer, one in the front of the pile (east-protruding), and a lateral one on the southern side of the pile. These are the access tubes for which the mineral weathering and microbial samples are placed. **In comparison to test pile 1, the lateral (south-protruding) pipe was placed further back in both test piles 2 and 3 upon discussion with Roger Beckie.** *(Note: based on January 2009 observations of dried mineral samples removed from these tubes, it is likely that they were placed too high (i.e., above the water table, if it is there) and that a large capillary break between the access tube and the protective material around it redirected water away from the tube. These pipes should be placed at the bottom of the protective layer, and no capillary break should be present).*

- h) Instrumentation lines 5 and 6 were then installed on this layer. **All of the instrumentation used in the two piles was the same except for the replacement of the Time Domain Reflectometry (TDR) probes with ECHO-TE probes (Decagon Devices Inc.; www.degacon.com). The TE probes measure moisture content, electrical conductivity and temperature, so no thermistors were required at the same instrumentation port as the TE probes.** The instrumentation and protective tubing was then covered with fine material and a secondary protective layer was placed upon this layer (no sorting required) so that 1.5 m of material was placed upon the geomembrane in order to protect it from the waste rock that would be tipped from above.
- i) Three containment berms were placed near the expected toe of each tipping phase so as to prevent boulders from moving off the pile.

B.2 END-DUMPING AND INSTRUMENTATION

This section pertains to the end-dumping process and the installation of instrumentation lines 1 to 4.

- a) End-dumping was coordinated with geology, mining operations and the contractors (Chacongesa). Once informed by geology that a polygon of the intended type of waste rock would soon be available, we coordinated the transport of waste rock to our site with mining operations. *It is important to insist on sending only a few loads per hour so that the bulldozer or front-end loader can clean the area. If too many trucks are sent in a short amount of time, the trucks will be back-logged.* **Too many trucks were sent to site during Tipping Phase II (Pile 2) and were dumped at the top of the pile because they could not hold up mining operations. More time was required to place this material in the pile, most of it being pushed over the edge of the pile using a front-end loader or bulldozer. As a result, not all of the material was ‘end-dumped’.**
- b) Once sufficient material had been dumped and the first containment berm had been reached, the first tipping phase was finished and instrumentation line 1 could be installed. An excavator was used to create a trench in which to place the instrumentation lines. **The procedure was the same as 2006 except for not using any cable lubricant (we had attempted this for lines 5 and 6, but it was not helpful in pulling the lines through from the bottom).** In addition, two 2” protective tubes (non-perforated) were installed in

each line to reduce the friction of instrumentation lines as they were pulled through the protective tubing. **In test pile 1, instrumentation lines were placed on alternating ports between the two protective tubes. In test piles 2 and 3, the higher instrumentation ports (i.e., highest 5 of 10 total ports) were located on one protective tube, and the bottom half (5 lower ports) was placed on the other. This proved to be easier. The top half was installed first and if any problems were encountered (e.g., stretched gas lines), we were able to re-install the lines in the other protective tube.**

- c) Once instrumentation line 1 was installed and covered/protected, an excavator filled in the trench and the second tipping phase was coordinated. Likewise, instrumentation was installed in line 2 as it was in line 1 (similar to 2006).
- d) Instrumentation line 3 was also installed on this slope. **This line is always problematic due to the bends, curves and long distance that the lines need to travel through in order to reach the instrumentation hut. Typically this creates too much friction and the lines become tangled together making it very difficult to pass through. We had to cut two holes in the exposed protective tubing (at the base of the pile) to help pass the cable, but this was insufficient. In the end, the 1.5 m protective layer was excavated to find the buried protective tubes and gain access to the instrumentation lines. This approach worked, but required time and increased the risk of future damage to the instrumentation lines. This could be avoided by installing Line 3 as Line 4 is installed; after the material is tipped and the excavator has made a trench, the protective tubes can then be placed in its placed (discussed below).**
- e) Instrumentation line 4 was installed similarly to line 1 and 2, 2006, except for the fact that the protective tubes were not placed before the end-dumping began (e.g., under the geomembrane).
- f) Once all of the material was end-dumped and the instrumentation lines were installed and covered, the perimeter of both piles was adjusted to account for material that had been dumped over the designed outer perimeter of the pile. **The lane between Piles 1 and 2 and between 2 and 3 were subsequently cleaned up, and material surrounding the end of all 4 access tubes was removed and the ends were subsequently corked.**

***Note: In September-2007 three instrumentation lines (six 2" protective tubes) were severed by an excavator. Part of the problem stemmed from lack of communication, poor supervision, and an operator unfamiliar with test pile design. *While this has proved to be a useful learning experience, one likely reason of the accident is that the instrumentation lines exited the pile in 2 different locations. Instrumentation lines 1, 2 and 3 exit the pile below the liner, and lines 4, 5 and 6 exit above the liner. It is proposed that this accident could have been avoided had all the lines been exiting the pile on the same plane. Further discussion is required to examine whether the design needs adjusting. One possibility is to not place the 2" tubes of lines 1, 2 and 3 under the geomembrane and to install them after the material has been placed much like line 4.*

B.3 INSTRUMENTATION HUT

The instrumentation hut design was the same as the year before, with minor modifications to the internal design and structure to conform with mine safety standards. The following lists some of the modifications from 2006:

- a) **Two pipes were installed while the concrete instrumentation hut foundation was being laid. One pipe connects the splitter to the composite tank and the other discharges the water flow out from the flow splitter (in 2006, the dry concrete was subsequently removed after it had dried).**
- b) **Pre-fabricated instrumentation huts were acquired. Roof dimensions and internal support were slightly altered to be more load-bearing and to conform with safety regulations of the mine.**
- c) **A fence was installed, using better material than that used for Pile 1.**
- d) **A composite tank was placed above a concrete base in the ground and covered with material. A roof was constructed above the tank to protect it from rain and other elements. The roof consists of lighter materials and opens in the middle in similar fashion to storm-cellar type doors to enable easier access to the composite tank.**
- e) **Inside the instrumentation hut, counters were installed and covered with a different type of wood (with a plastic coating).**

- f) Gas and soil waste sampler panels were constructed of wood (**same as counters**). **They were also placed side-by-side to allow for more efficient use of space within the instrumentation hut.**
- g) Tipping bucket tables were constructed similarly to test pile 1, using a similar type of wood for the table and iron bars for the structure. **PVC valves were connected underneath each of the small-tipping buckets to facilitate easier calibration.**
- h) The plumbing system for the drainage water is similar, with a major exception: **the bypass system, which was moved laterally instead of the vertical orientation in test pile 1. In addition, a modification was made to the parts connecting the electrical conductivity probe to the flow system, which allowed for an easier removal of the probe for calibration and maintenance. The vertical extent of the ‘U’ in the U-system was extended to allow for a larger volume of water to remain in the cell for sampling purposes.**
- i) **Outside, all 4 drainage pipes conveying water from the pile to the tipping buckets, were surrounded with insulating material to minimize diurnal fluctuations in water temperature.**
- j) **The flow splitters were constructed according to the same design, but the material was changed to consist of the same plastic (Lexan) used to construct the tipping buckets. Their support-legs were modified due to available resources.**
- k) **The tipping buckets were made using the same contractor and the same designs with slight modifications. The magnets were replaced with strong, 3/8” rare earth magnets from Lee Valley (www.leevalley.com). The tipping buckets in test pile 1 were also retrofitted.**
- l) **Instrumentation lines from the pile were connected to the instrumentation hut at a lower height so as to enter the hut below the table for aesthetic purposes. Additionally, cable boxes were used to organize the cables and hoses (SWS and gas) also for aesthetic reasons.**
- m) **The datalogging system generally remained the same, but varied slightly since a different multiplexer (AM 16/32) was used for the ECHO probes than were used for the TDRs (SDMX50) and none of the other TDR wires and instrument boxes were used. All of the data is sent to the office computer via telemetry, and thus the**

CFM100 compact flash modules were not required. Wires were arranged in a more orderly manner by the use of plastic cages and connection ports placed along the perimeter of the datalogging board.

B.4 REFERENCES

1. Corazao Gallegos, J.C., 2007. The design, construction, instrumentation, and initial response of a field-scale waste rock test pile, M.A.Sc. thesis. University of British Columbia, Vancouver, Canada.

APPENDIX C: PRECIPITATION

C.1	CLIMATE.....	226
C.1.1	WIND	227
C.1.1.1	WIND AND TOPOGRAPHY	227
C.1.2	TEMPERATURE.....	228
C.1.3	PRECIPITATION	229
C.1.4	RELATIVE HUMIDITY	229
C.1.5	CLIMATE SUMMARY.....	229
C.2	ANTAMINA RAIN GAUGES.....	230
C.2.1	SINGLE VARIABLE REGRESSION ANALYSIS	230
C.2.2	LINEAR LEAST SQUARES REGRESSION ANALYSIS	231
C.3	CUMULATIVE COMPARISON.....	232
C.4	ASSUMPTIONS AND UNCERTAINTY.....	233
C.5	REFERENCES	235

TABLES

Table C.1.	Horizontal and vertical distance of Antamina rain gauges in relation to site.....	237
Table C.2.	Historical monthly temperature at Yanacancha	237
Table C.3.	Historical monthly precipitation at Yanacancha	238
Table C.4.	Historical mean monthly relative humidity.....	238

FIGURES

Figure C.1.	2003 and 2004 quarterly wind rose diagrams at the Yanacancha meteorological station.	239
Figure C.2.	2005 and 2007 quarterly wind rose diagrams at the Yanacancha meteorological station.	240
Figure C.3.	2008 quarterly wind rose diagrams at the Yanacancha meteorological station.	241
Figure C.4.	Representative wind rose diagrams as measured at four Antamina weather stations.	241
Figure C.5.	Predominant wind direction at four Antamina weather stations.....	242
Figure C.6.	Crossplots of weekly precipitation correlations.....	242

APPENDIX C: PRECIPITATION

This appendix describes the steps carried out to estimate the missing site precipitation that was not recorded by the datalogger from 2-Feb-2008 to 23-June-2008. Two linear regression analyses are used to estimate this precipitation based on correlations to other rain gauges less than 5 km away (Chapter 3).

C.1 CLIMATE

Before estimating missing site precipitation, it is important to determine whether no unusual meteorological conditions were reported during the period of missing data. The quarterly aerometric reports compiled by McVehil-Monnett Associates, Inc. from 2000 to 2006 (Mcvehil-Monnett, 2001a-d, 2002a-d, 2003a-d, 2004a-d, 2005a-d, 2006a-b), and additional precipitation, wind (direction and magnitude), temperature and relative humidity data are thus utilized. Six weather stations are located throughout the Antamina mine property, less than 5 km away from the study site (Table C.1; Figure 3.1). The principal meteorological station at Antamina is Yanacancha, which is located near the main offices of the mining camp.

Average air temperature (Table C.2), monthly cumulative precipitation (Table C.3), and average relative humidity (Table C.4) measured at the Yanachancha station are presented from 2000 - 2008. The wet season months of October through April experience higher average temperatures, relative humidity and total precipitation compared to the dry season months of May through September. Wet season months average a temperature of 6.0 °C, 79 % relative humidity, and 140 mm of precipitation. The average wet season precipitation is 86 % of the average annual precipitation. Dry season months average a temperature of 5.2 °C, 70 % relative humidity, and 33 mm of precipitation.

For this analysis, the transition between ‘wet’ and ‘dry’ periods is assumed to occur on one day. The exact transition is difficult to resolve as the transition months of April-May and September-October exhibit both ‘wet’ and ‘dry’ characteristics from year to year. Nevertheless, the delineation between ‘wet’ and ‘dry’ seasons using 1-October and 1-May are used throughout this investigation to characterize the two contrasting climatic periods at Antamina.

C.1.1 Wind

Wind direction and intensity at the Yanacancha meteorological monitoring station are measured using an RM Young Wind monitor that uses a propeller-type anemometer with a fuselage and tail wind vane (Model # 05103; accuracy: wind speed ± 0.03 m/s, wind direction ± 3 degrees; www.youngusa.com). Data obtained from this anemometer is used to compile wind rose diagrams. Wind rose diagrams are useful in presenting the frequency in which and the direction from where winds blow, and can be used to indicate the overall prevailing wind patterns over a given time frame. Each 'spoke' in the diagram represents the direction from which the wind originates, and the magnitude of the spoke indicates the frequency that wind originates from that direction over a given time interval.

The most comprehensive wind data at Antamina exists for the Yanacancha station and dates as far back as the year 2003 (Figure C.1, Figure C.2, Figure C.3). A natural variability in wind direction and intensity is evident. The strongest prevailing wind directions originate from the north and south, with a significant presence of winds from the north-east and south-west. A smaller proportion of wind originates from the east compared to almost no wind emanating from the west. Wind patterns from the same quarter are generally consistent from year to year.

The first and second quarter 2008 wind rose diagrams (period of missing precipitation) are consistent to patterns present in the same quarter in previous years.

C.1.1.1 Wind and Topography

The vertical relief within the Antamina mine property varies by over 700 m, so it is likely that the wind patterns will be different throughout the mine property. In Jan-2007, the Puente Juprog, Dos Cruces, and Ayash monitoring stations began recording wind data. A wind rose comparison between these stations and Yanacancha from Jan-2007 through Aug-2008 demonstrates that each station has a characteristic wind pattern. The Yanacancha data exhibits strong north-northeasterly and south-southwesterly winds throughout the year, while the predominant wind patterns at Puente Juprog originate in the east and west directions. A significant amount of wind at Dos Cruces originates from the northeast (Figure C.4).

Wind patterns are relatively consistent at each station, but exhibit large differences between one another which likely result from differences in the local topography. To illustrate this, the second quarter 2008 wind rose diagrams from Yanacancha, Dos Cruces, Puente Juprog and Ayash are examined (Figure C.5).

The Ayash station is situated within a valley, approximately 400 m below the study site. The steep valley walls around the Ayash station limit the direction in which the wind can move and thus explains why the principal wind directions at this site are from the north east or southwest which is congruent with the valley orientation.

Puente Juprog is located on the southern slope of a mountain ridge, and explains why a small proportion of wind originates from the north at this site. Most of the wind originates from the west or east at Puente Juprog, most likely indicating that wind travelling from the northeast will curve around the side of the mountain, slightly favouring the western side over the eastern side.

Wind at Yanacancha is slightly favoured from the north-northeast over the south-southwest. Yanacancha is situated in a relatively flat, open area particularly close to the tailings pond.

Dos Cruces is the highest monitoring station at Antamina, and is located near a peak at 4528 m a.s.l. Wind at this station originates from the northeast, and is least affected by the surrounding topography and thus most characteristic of the prevailing wind direction of the area. Since the Dos Cruces station is also less than 3 km away from the test site, the prevailing wind direction at Antamina will thus be assumed to be the same as that of Dos Cruces (Figure C.5).

C.1.2 Temperature

Mean annual temperature is calculated based on hourly temperature values recorded at the Yanacancha meteorological station using a Vaisala HMP35C Temperature Probe (± 0.3 °C; www.campbellsci.ca). The maximum and minimum hourly temperatures of 22.7 and -3.6 °C occur on 24-Aug-2000 and 5-Jul-2006 (McVehil-Monnet Associates 2000; 2001a-d; 2002a-d; 2003a-d; 2004a-d; 2005a-d; 2006). Mean daily temperatures are calculated by averaging the maximum and minimum temperature values of each day. A maximum daily temperature of 9.7

°C occurs on 7- and 8-Feb-2007 whereas the minimum daily temperature of 2.1 °C occurs three times on 28-June-2006 and 11-,12-May-2008. Mean monthly temperatures are calculated as the average mean daily temperature for each month (Table C.2). Mean annual temperature (M.A.T.) is calculated as the average of the mean monthly temperature values over 12 months, and ranges between 5.5 and 6.0°C.

Based on the temperatures reported at Yanacancha during the period of missing data, the monthly values are within the normal range based on the previous years' data.

C.1.3 Precipitation

Annual precipitation at the Yanacancha station fluctuates between 1000 to 1320 mm dating back to 2001 (Table C.3). Monthly precipitation is highly variable from year to year, with the dry season exhibiting larger variability than the wet season.

Reported precipitation at Yanacancha during the period of missing data indicates that the monthly values are within the normal range based on the previous years' data.

C.1.4 Relative Humidity

Relative humidity is an indirect indicator of vapour pressure and indicates the tendency of precipitation to form. It is measured at the monitoring station using a Vaisala HMP35C Humidity Probe ($\pm 3\%$) that is coupled to the temperature probe. Table C.4 indicates that relative humidity is variable over time, with distinct wet and dry signatures throughout the year.

Relative humidity reported during the period of missing data indicates that the monthly values are within the normal range based on the previous years' data.

C.1.5 Climate Summary

The comprehensive meteorological dataset reported at the Yanacancha station provides a reasonable proxy for the recent historical meteorological behaviour throughout the Antamina mine property, including the study site. Given that the wind, precipitation, relative humidity and

temperature during the period of missing site precipitation remains consistent with previous years, the precipitation estimate from February to June, 2008 can take place.

C.2 ANTAMINA RAIN GAUGES

Six meteorological monitoring stations are located within 5 km of the study site at various elevations (Table C.1; Figure 3.1). Precipitation from these stations is compared to the study site precipitation in order to determine whether a reasonable correlation exists. Of the six monitoring stations, Yanacancha, Quebrada Antamina and Dam D data are available before 18-Jan, 2007, which is the first day of the study period. The end date for the study period is 30-Sept-2008, which corresponds to a 622 day-long period. Site precipitation is available for 499 of those days, leaving a 123 day-long period of missing site precipitation. Data from three other stations (Dos Cruces, Puente Juprog and Ayash) is available from 1-Sept-2007 and corresponds to a total period of 396 days, of which site precipitation is available for 273 days. The gap of missing data is shortened to only include 119 days (17 complete weeks) of data because rain during the partial week in which the site rain gauge begins reporting data (when it becomes online) is higher than the predicted value and is included because it provides a more accurate representation of precipitation at the site (Chapter 3).

In general, precipitation trends are similar for all gauges from both periods despite the disparity in which some stations report several mm of precipitation while others report less than 1 mm in a given day. These differences can be attributed to several factors including: location, altitude, topography, local environment, gauge type, calibration, frequency of maintenance, etc. Daily data is too variable for this analysis and results in poor correlations between stations. Therefore, weekly precipitation is used in the following regression analyses because it provides a compromise between high frequency resolution (daily) and lower errors (poor correlations).

C.2.1 Single Variable Regression Analysis

A single variable regression analysis demonstrates that the Yanacancha (YANA), Quebrada Antamina (QAN) and Puente Juprog (PJ) stations exhibit the strongest correlations to site precipitation (SITE). Based on 70 complete weeks of precipitation data, correlations of $r^2 = 0.85$ and $r^2 = 0.84$ are calculated for the SITE-YANA and SITE-QAN data respectively (Figure C.6).

Despite a relatively strong SITE-PJ correlation based on available data, there is not enough data to base reliable site precipitation estimates.

Each correlation produces a single variable regression equation that can be applied to the independent variable (Antamina rain gauge data) to estimate the weekly precipitation of a dependent variable (site rain gauge data). Approximately 373 and 396 mm of precipitation are estimated based on the Yanacancha and Quebrada Antamina data, respectively.

C.2.2 Linear Least Squares Regression Analysis

A linear least squares regression analysis provides a more rigorous statistical analysis. Least square problems are typically used to mathematically solve over-determined systems (such as this), which arise when fitting linear models to experimental measurements. This type of model is relatively simple to implement because it is based on a linear relationship between a dependent variable (SITE) and independent variables (YANA and QAN). A statistical matrix analysis produces a single unweighted linear regression model. In this manner, the relationship between the observed SITE, YANA and QAN can be expressed based on the following technique described by Press et al. (1992):

$$f(u_N) = a_1 (M_{x_N}) + a_2 (M_{y_N}) + d \quad [C-1]$$

where N is the number of data points in each basis functions, u_N is the estimated SITE variable at point N , M_x and M_y are the YANA and QAN basis functions during at a given week N ; a_1 and a_2 are the YANA and QAN parameters (i.e., correlation factors to site data); and d is the offset term. Available SITE data is referred to as vector b . By definition, equation C-1 can be re-written in matrix form A . When design matrix A is multiplied by the inverse design matrix, A^T , the matrix is thus referred to as α , and can be rewritten as a square $M \times M$ matrix:

$$\alpha = A^T \cdot A = \begin{bmatrix} [x]_1 & [y]_1 & [z]_1 \\ [x]_2 & [y]_2 & [z]_2 \\ [x]_3 & [y]_3 & [z]_3 \end{bmatrix} \quad [C-2]$$

When matrix α is multiplied by vector b , it creates β as described in the following equation:

$$[\beta] = \alpha \cdot b \quad [\text{C-3}]$$

If there is linear dependence between any of the M_N columns, then β must be constrained. In this case, the basis functions are linearly independent and this is not a problem. In matrix form, the previous two equations can be related by the vector (or coefficient matrix) of parameter a by:

$$[a] = [\alpha]^{-1} \cdot [\beta] \quad [\text{C-4}]$$

and the inverse to the matrix is represented by C , where C is related to the standard uncertainties of the estimated parameters a , which is given as an $M \times 1$ matrix (each M with a value corresponding to each M basis function). Parameters a and b are also commonly referred to as regression coefficients, as described in the following equation:

$$[a] = \begin{bmatrix} a_1 \\ a_2 \\ a_3 \end{bmatrix} \quad [\text{C-5}]$$

The calculated results are then subject to a statistical analysis where, by definition, standard uncertainties are used to provide the variance (σ^2) (and by definition, the standard deviation σ) of the fitted parameters M_N by extracting the diagonal elements of the inverse matrix:

$$C = [\alpha]^{-1} = \begin{bmatrix} [\sigma^2]_1 & [y]_1 & [z]_1 \\ [x]_2 & [\sigma^2]_2 & [z]_2 \\ [x]_3 & [y]_3 & [\sigma^2]_3 \end{bmatrix} \quad [\text{C.6}]$$

The resulting parameters are $a_1 = 0.510 \pm 0.017$ (YANA), $a_2 = 0.354 \pm 0.015$ (QAN), and $d = 2.76 \pm 0.18$. Based on this, the estimated amount of precipitation that had fallen during this gap is 375 ± 15 mm, ranging between 360 and 390 mm.

C.3 CUMULATIVE COMPARISON

Final site precipitation is calculated based on measured site precipitation and results of the linear least square regression analysis, and compared to the cumulative Yanacancha and Quebrada Antamina precipitation (Figure 3.2). That all three curves exhibit similar shapes indicates that

they are correlated to some degree, and are similarly influenced by wet and dry season precipitation differences. The wet and dry period transitions roughly correspond to 1-May (wet to dry) and 1-October (dry to wet). The early decrease in precipitation in Feb-2007 corresponds to the temperature, precipitation and relative humidity data which indicate that this month is an uncharacteristically warmer, drier month in which precipitation is far below average (Table C.2, Table C.3, Table C.4). Site precipitation begins the period registering similar or less rain than YANA and considerably less than QAN, and begins to experience more rain in the 2007-2008 wet season which sees cumulative precipitation nearly approach that of QAN. That the cumulative YANA precipitation differs from QAN by almost 200 mm is not a surprise considering their different locations and the variability of precipitation over the region.

Chapter 3 includes two further comparisons that test the results from this analysis. The first consists of a comparison between the final site precipitation (reported and estimated) and a strictly estimated precipitation in which the model was applied to estimate site precipitation throughout the entire study period (Section 3.1.2). The second comparison involves a 135-day long period in which data is compared to a second rain gauge installed on site. Both analyses indicate that there is a 5 % difference, which indicates that there is a relatively high level of confidence associated with this estimation.

C.4 ASSUMPTIONS AND UNCERTAINTY

In order for this type of analysis to be valid, several assumptions must be discussed. In a linear regression model consisting of a dependent variable, several independent variables and parameters, one can assume that the dependent variable is the outcome of a measurement. One must also assume that the sample size is sufficiently large to be representative, which is why only data from two rain gauges is used. The dependent variable (site precipitation) is a linear combination of the parameters, but not of the independent variables which should themselves be linearly independent. The error is assumed to be a random variable with a mean of zero, and is uncorrelated by definition due to the diagonal distribution in the C matrix described in equation C-7. The error estimates presented are based on the assumption that the residuals are normally distributed even though the rain observations are, by definition, not normally distributed.

In addition, while this analysis acknowledges that the site rain gauge is made by a different manufacturer than the Antamina rain gauges (RainWise Inc. vs. Campbell Scientific), it does not explore whether there are any fundamental differences between them that could result in different readings. The Antamina rain gauges are slightly larger than the site gauge (245 mm in diameter compared to 203 mm) and may have different effects with regards to residual droplets, evaporation, capillarity, etc. that could result in small differences between gauges for each tip, which can be compounded over time. Even the buildup of dirt on the pivot mechanisms can result in a biased result (over time) as it may influence the volume of water required to trigger a tip. A comparison of the field rain gauges proves that the Antamina gauges are well maintained with no visible dirt. The slight build up of dirt on the site rain gauge is assumed to be negligible. These factors are included in the 5 % uncertainty discussed in Chapter 4.

Compared to the same period in which approximately 402 mm was recorded by the site rain gauge in 2007, the 2008 estimate of 375 mm of rain represents a 7 % decrease from 2007. This is well within the natural variability of precipitation observed in the recent historical aerometric data at the mine (Table C.3). An investigation of the relative humidity, temperature, precipitation, predominant wind direction and magnitude were shown to not include any considerable departures from the historical monthly figures dating back to 2000.

While uncertainty is inherent with meteorological variables in general, it is believed that 375 ± 15 mm is a reasonable estimate of precipitation that occurred on site but was not recorded by the datalogger from 2-Feb-2008 to 23-June-2008.

C.5 REFERENCES

Mcvehil-Monnett Associates, Inc., 2001a. Antamina mine aerometric monitoring report: 3rd and 4th quarters 2000 calendar year. Prepared March 2001. Colorado, USA. MMA Project Number 985-99.

Mcvehil-Monnett Associates, Inc., 2001b, Antamina mine aerometric monitoring report: 1st quarter 2001 calendar year. Prepared June 2001, Colorado, USA. MMA Project Number 1216-01-02.

Mcvehil-Monnett Associates, Inc., 2001c, Antamina mine aerometric monitoring report: 2nd quarter 2001 calendar year. Prepared August 2001, Colorado, USA. MMA Project Number 1216-01-02.

Mcvehil-Monnett Associates, Inc., 2001d, Antamina mine aerometric monitoring report: 3rd quarter 2001 calendar year. Prepared October 2001, Colorado, USA. MMA Project Number 1216-01-02.

Mcvehil-Monnett Associates, Inc., 2002a, Antamina mine aerometric monitoring report: 4th quarter 2001 calendar year. Prepared January 2002, Colorado, USA. MMA Project Number 1216-01-02.

Mcvehil-Monnett Associates, Inc., 2002b, Antamina mine aerometric monitoring report: 1st quarter 2002 calendar year. Prepared April 2002, Colorado, USA. MMA Project Number 1412-02.

Mcvehil-Monnett Associates, Inc., 2001c, Antamina mine aerometric monitoring report: 2nd quarter 2002 calendar year. Prepared July 2002, Colorado, USA. MMA Project Number 1412-02.

Mcvehil-Monnett Associates, Inc., 2002d, Antamina mine aerometric monitoring report: 3rd quarter 2002 calendar year. Prepared October 2002, Colorado, USA. MMA Project Number 1412-02.

Mcvehil-Monnett Associates, Inc., 2003a, Antamina mine aerometric monitoring report: 4th quarter 2002 calendar year. Prepared January 2003, Colorado, USA. MMA Project Number 1412-02.

Mcvehil-Monnett Associates, Inc., 2003b, Antamina mine aerometric monitoring report: 1st quarter 2003 calendar year. Prepared April 2003, Colorado, USA. MMA Project Number 1586-03.

Mcvehil-Monnett Associates, Inc., 2003c, Antamina mine aerometric monitoring report: 2nd quarter 2003 calendar year. Prepared July 2003, Colorado, USA. MMA Project Number 1586-03.

Mcvehil-Monnett Associates, Inc., 2003d, Antamina mine aerometric monitoring report: 3rd quarter 2003 calendar year. Prepared October 2003, Colorado, USA. MMA Project Number 1586-03.

Mcvehil-Monnett Associates, Inc., 2004a, Antamina mine aerometric monitoring report: 4th quarter 2003 calendar year. Prepared January 2004, Colorado, USA. MMA Project Number 1586-03.

Mcvehil-Monnett Associates, Inc., 2004b, Antamina mine aerometric monitoring report: 1st quarter 2004 calendar year. Prepared April 2004, Colorado, USA. MMA Project Number 1719-03.

Mcvehil-Monnett Associates, Inc., 2004c, Antamina mine aerometric monitoring report: 2nd quarter 2004 calendar year. Prepared August 2004, Colorado, USA. MMA Project Number 1216-01-02.

Mcvehil-Monnett Associates, Inc., 2004d, Antamina mine aerometric monitoring report: 3rd quarter 2004 calendar year. Prepared October 2004, Colorado, USA. MMA Project Number 1216-01-02.

Mcvehil-Monnett Associates, Inc., 2005a, Antamina mine aerometric monitoring report: 4th quarter 2004 calendar year. Prepared January 2005, Colorado, USA. MMA Project Number 1719-03.

Mcvehil-Monnett Associates, Inc., 2005b, Antamina mine aerometric monitoring report: 1st quarter 2005 calendar year. Prepared June 2005, Colorado, USA. MMA Project Number 1847-04.

Mcvehil-Monnett Associates, Inc., 2005c, Antamina mine aerometric monitoring report: 2nd quarter 2005 calendar year. Prepared August 2005, Colorado, USA. MMA Project Number 1847-04.

Mcvehil-Monnett Associates, Inc., 2005d, Antamina mine aerometric monitoring report: 3rd quarter 2005 calendar year. Prepared October 2005, Colorado, USA. MMA Project Number 1847-04.

Mcvehil-Monnett Associates, Inc., 2006a, Antamina mine aerometric monitoring report: 4th quarter 2005 calendar year. Prepared January 2006, Colorado, USA. MMA Project Number 1847-04.

Mcvehil-Monnett Associates, Inc., 2006b, Antamina mine aerometric monitoring report: 1st quarter 2006 calendar year. Prepared June 2006, Colorado, USA. MMA Project Number 1989-05.

Press, W., Teukolsky, S., Vetterling, W., and B. Flannery. 1992. Numerical Recipes in C: The Art of Scientific Computing, 2nd ed., Cambridge University Press, New York.

TABLES

Table C.1. Horizontal and vertical distance of Antamina rain gauges in relation to site.

Station Name	Abbreviation	Northing (m)	Easting (m)	Altitude (m A.S.L)
Site Rain Gauge*	SITE	0	0	0
Yanacancha	YANA	-3377	1563	-185
Quebrada Antamina	QAN	-2076	-4192	-316
Dos Cruces	DC	-2638	-1340	154
Puente Juprog	PJ	-4137	-2335	-214
DamD	DAMD	4930	1437	-57
Ayash	AY	1342	2989	-569

* Site gauge is origin (see Chapter 2)

Table C.2. Historical monthly temperature at Yanacancha

Year	Temperature [°C]												Average	Std. Dev.
	Jan	Feb	Mar	Apr	May	Jun	Jul	Aug	Sep	Oct	Nov	Dec		
2001	5	5.3	5.2	5.4	5.7	4.5	5	4.5	5.3	6	6.2	6.3	5.4	0.6
2002	6.3	6	5.4	5.6	6	4.7	4.8	4.7	5.5	5.3	5.4	6.4	5.5	0.6
2003	6.5	6.2	5.9	5.8	5.5	5.4	4.3	5.1	5.3	6.4	6.2	5.8	5.7	0.6
2004	6.8	5.8	6	6.1	6.2	4.5	4.4	4.5	4.5	5.6	5.8	5.8	5.5	0.8
2005	6.3	6.5	6	6.2	6.3	6.5	N/A	N/A	N/A	N/A	N/A	N/A	6.3	0.2
2007	7	7.1	5.6	5.9	6.3	5.1	4.9	5.5	5	5.6	6.1	6.2	5.9	0.7
2008	5.7	5.5	5	5.6	5.7	5.5	5.1	5.6	N/A	N/A	N/A	N/A	5.5	0.3
Average	6.2	6.1	5.6	5.8	6	5.2	4.8	5.1	5.1	5.8	6.1	6		
Std. Dev.	0.6	0.6	0.4	0.3	0.3	0.7	0.3	0.5	0.3	0.4	0.5	0.3		
Average Wet	6													
Average Dry	5.3													

* N/A = no data available for that month; 2006 data was not available.

** Based on raw data and McVehil-Monnet Associates (2001a-d, 2002a-d, 2003a-d, 2004a-d, 2005a-d, 2006a-b).

Table C.3. Historical monthly precipitation at Yanacancha

Precipitation [mm]														
Year	Jan	Feb	Mar	Apr	May	Jun	Jul	Aug	Sep	Oct	Nov	Dec	Average	
2001	182	152	220	68	95	19	19	10	44	143	153	206	1312	
2002	87	184	194	139	45	7	49	18	48	142	191	160	1264	
2003	115	130	146	92	70	20	10	31	61	80	117	223	1093	
2004	67	136	110	62	72	24	38	25	68	140	125	182	1048	
2005	183	116	191	78	18	1	8	18	27	139	78	149	1004	
2006	147	121	179	134	18	41	10	17	60	154	146	164	1191	
2007	120	77	236	126	40	9	41	12	41	132	101	118	1052	
2008	191	143	147	91	39	16	7	24	41	N/A	N/A	N/A	611	
Average	137	132	178	99	51	17	25	19	50	133	130	172	1138	
Average Wet								140						
Average Dry								32						

* N/A indicates no data. 2006 data was not available.

** Based on raw data and McVehil-Monnet Associates (2001a-d, 2002a-d, 2003a-d, 2004a-d, 2005a-d, 2006a-b).

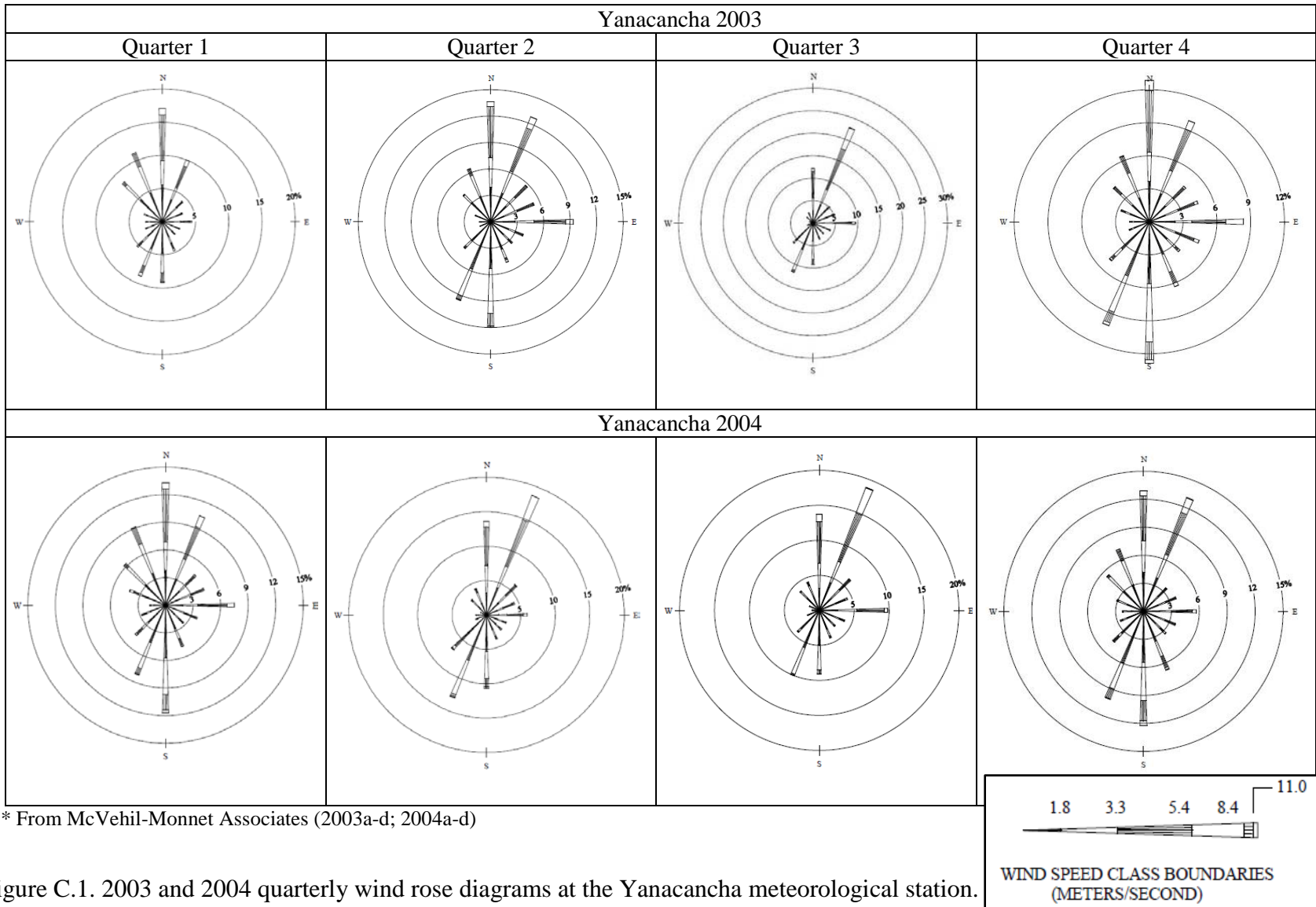
Table C.4. Historical mean monthly relative humidity

Relative Humidity [%]															
Year	Jan	Feb	Mar	Apr	May	Jun	Jul	Aug	Sep	Oct	Nov	Dec	Average.	Stdev	
2001	88	88	90	80	83	N/A	N/A	N/A	N/A	N/A	N/A	N/A	85.8	4.1	
2002	77	84	86	82	77	61	73	68	73	81	84	82	77.3	7.5	
2003	79	79	82	82	80	68	69	66	71	70	74	84	75.3	6.3	
2004	66	82	83	76	75	69	77	70	77	81	79	80	76.3	5.4	
2005	74	82	86	80	60	N/A	N/A	N/A	N/A	N/A	N/A	N/A	76.4	10.1	
2007	82	74	86	81	73	61	70	60	71	74	77	72	73.3	7.7	
2008	83	81.6	80.1	78.3	69	64	62	66.7	N/A	N/A	N/A	N/A	73.1	8.5	
Average	78.4	81.5	84.7	79.9	73.8	64.6	70.1	66.2	73	76.4	78.4	79.4			
St. Dev.	6.6	4.1	3	2	7.1	3.4	5	3.9	2.4	4.3	9.7	4.4			
Average Wet								80							
Average Dry								72							

* N/A indicating no data available for that month. 2006 data was not available.

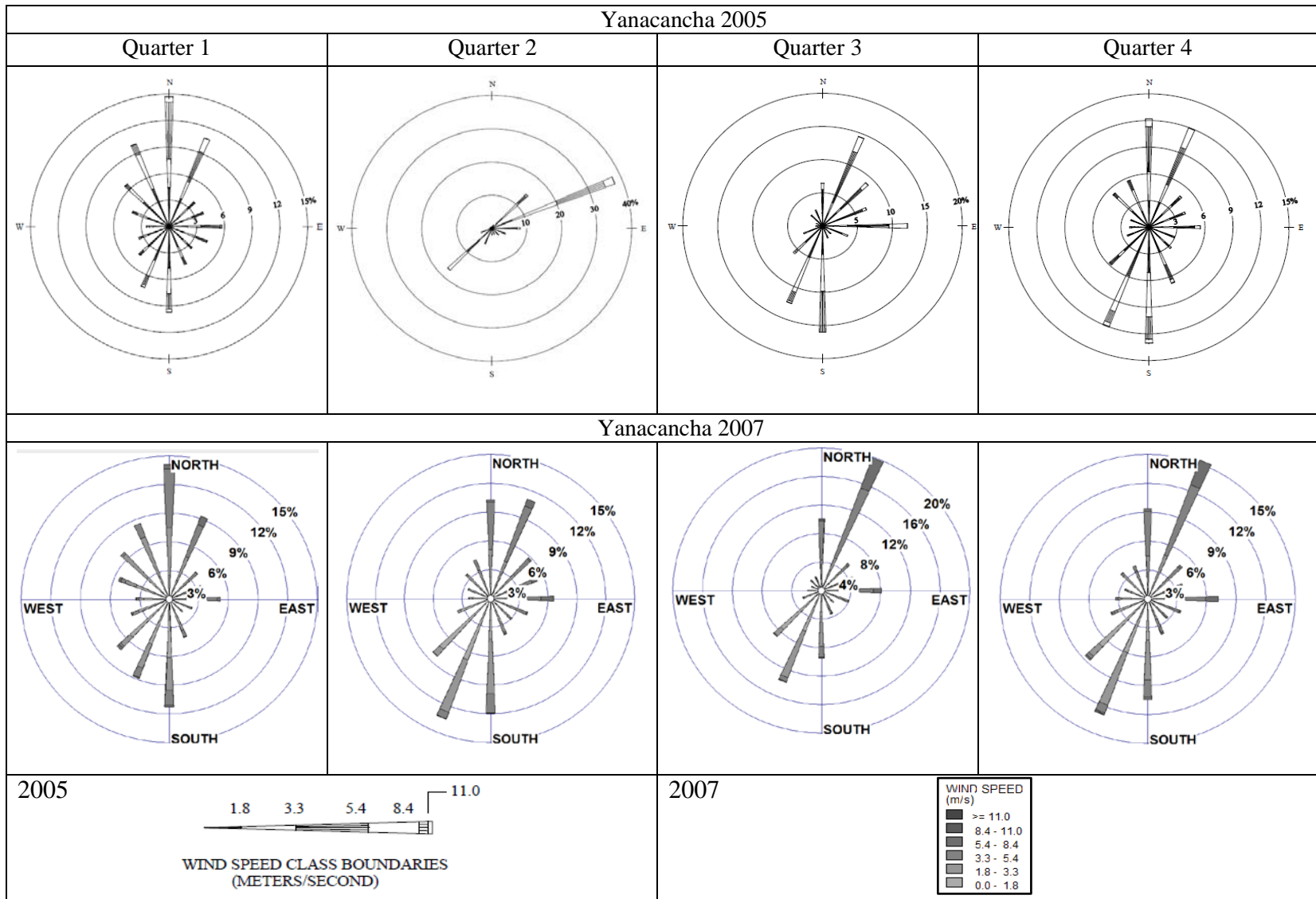
** Based on raw data and McVehil-Monnet Associates (2001a-d, 2002a-d, 2003a-d, 2004a-d, 2005a-d, 2006a-b).

FIGURES



* From McVehil-Monnet Associates (2003a-d; 2004a-d)

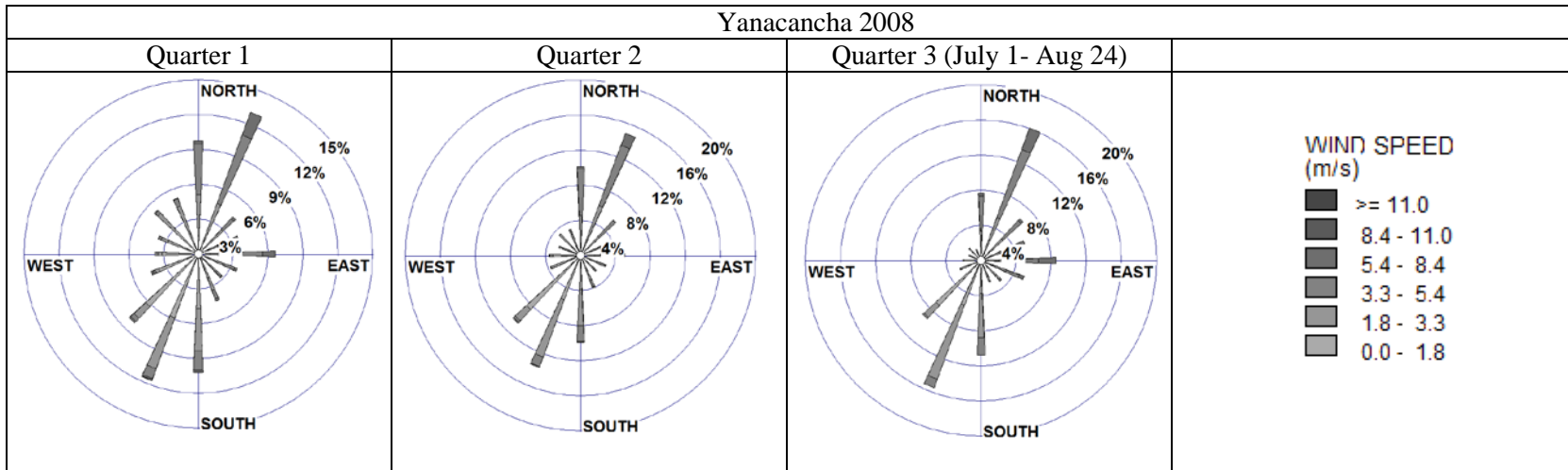
Figure C.1. 2003 and 2004 quarterly wind rose diagrams at the Yanacancha meteorological station.



* 2006 data was not available

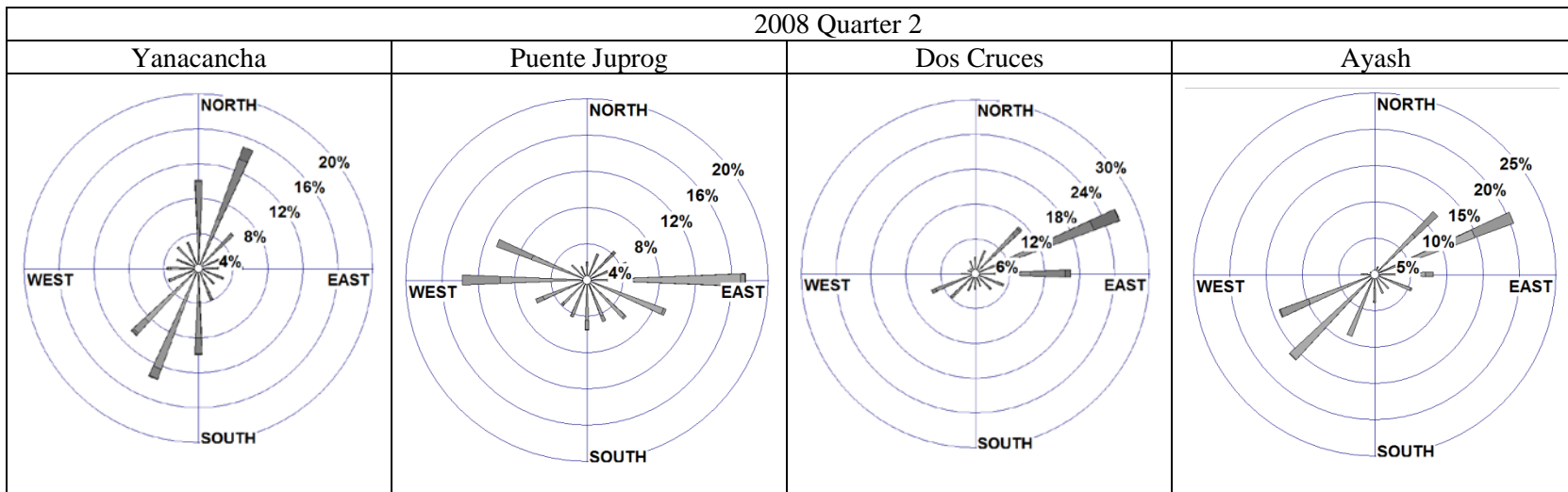
** Based on raw data (2007) and McVehil-Monnet Associates (2005a-d)

Figure C.2. 2005 and 2007 quarterly wind rose diagrams at the Yanacancha meteorological station.



* Compiled from raw data

Figure C.3. 2008 quarterly wind rose diagrams at the Yanacancha meteorological station.



** Compiled from raw data

Figure C.4. Representative wind rose diagrams as measured at four Antamina weather stations.

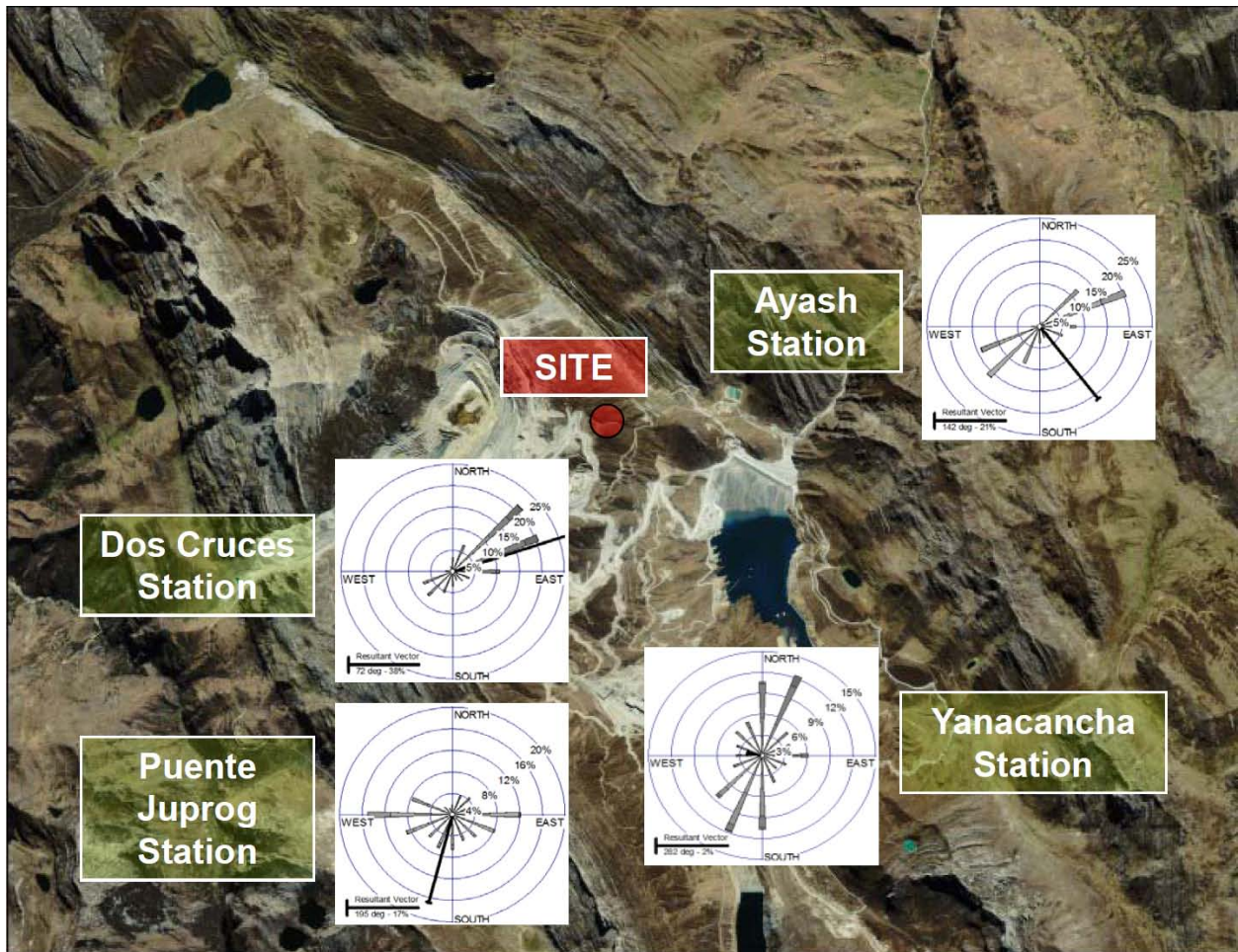


Figure C.5. Predominant wind direction at four Antamina weather stations.

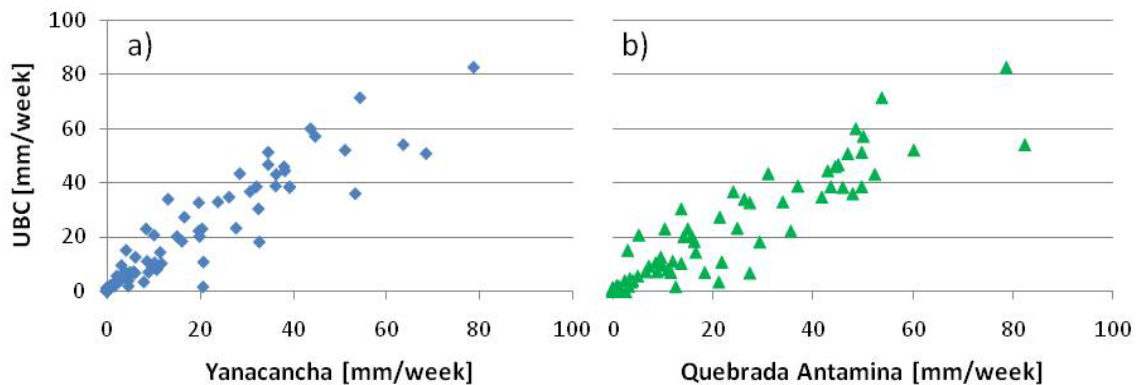


Figure C.6. Crossplots of weekly precipitation [mm] correlations between a) SITE-Yanacancha and b) SITE-Quebrada Antamina.

APPENDIX D: EVAPORATION

D.1 PAN EVAPORATION 245
D.1.1 PAN COEFFICIENT 246
D.1.2 BARE SOIL COEFFICIENT 247
D.2 PENMAN-MONTEITH EQUATION 247
D.3 SOIL COVER 251
D.4 PAN LYSIMETER WATER BALANCE 253
D.5 REFERENCES 254

TABLE

Table D.1. Estimated wind speed at 2 m height above ground surface. 256
Table D.2. SoilCover simulation: Run 1 summary ($K_{sat} = 10^{-3}$ m/s, $n = 0.3$) 257
Table D.3. SoilCover simulation: Run 2 summary ($K_{sat} = 10^{-3}$ m/s, $n = 0.4$) 258
Table D.4. SoilCover simulation: Run 3 summary ($K_{sat} = 8 \times 10^{-6}$ m/s, $n = 0.3$) 259
Table D.5. Soil Cover simulation: Run 3 summary ($K_{sat} = 8 \times 10^{-6}$ m/s, $n = 0.4$) 260

FIGURES

Figure D.1. SoilCover simulation: Run 1 ($K_{sat} = 10^{-3}$ m/s; $n = 0.3$) 261

APPENDIX D: EVAPORATION

Evaporation has the potential to remove a considerable amount of water from a given system. The rate at which evaporation will proceed depends on several climatological parameters such as rainfall intensity and duration, air temperature, relative humidity, wind speed, energy flux, etc., and surface characteristics such as soil properties, permeability, antecedent moisture content, saturated hydraulic conductivity, particle size distribution, orientation and geometry, etc. Differences in these conditions create gradients that drive the exchange of mass and energy that attempt to equilibrate. Water vapour and heat exchange are the primary drivers of evaporation.

Evaporation is often referred to as potential evaporation (*PE*) or actual evaporation (*AE*). *PE* refers to the maximum rate at which water can evaporate from a soil surface, and is only a function of atmospheric conditions. *PE* refers to the maximum evaporation that can occur based on the climatological conditions (independent of soil conditions) and assumes that a continual supply of water is present on the saturated evaporative surface (Machibroda, 1994). *AE* is the evaporation that actually occurs. The rate of *AE* from unsaturated soil surfaces is normally less than *PE*, and is often measured empirically to account for the transient climate and soil conditions of the site. For example, evaporation generally alters the initial moisture content of the soil and adjacent air mass, resulting in a transient evaporation rate in response to the transient air and surface conditions.

There are several approaches to estimate evaporation. Theoretically-derived equations such as Penman (1948), Thornwaite (1948), or Priestley-Taylor (1972) are based on mathematical methods that employ meteorological inputs, whereas field-based pan evaporation measurements provide an empirical way in which to estimate evaporation (Natural Resources Canada, 1994). These methods are typically utilized to calculate the reference evapotranspiration ET_{ref} which is based on a hypothetical grass crop 0.12 m high, a fixed surface resistance of 70 s/m and an albedo of 0.23 (Allen et al., 1998). Values are then reduced to actual evaporation based on some correction factor.

No instrumentation that directly measures potential or actual evaporation is present at the test pile. Four approaches are therefore employed to obtain reasonable evaporation estimates:

1. an empirical (pan evaporation),
2. a theoretical (Penman-Moneith equation),
3. an evaporative flux model (SoilCover), and
4. a large-scale pan lysimetry (water budget).

Each approach has been proven to achieve accurate evaporation estimates (Machibroda, 1994; Natural Resources Canada, 1994; Wilson et al. 1994, 1997; Carey et al., 2005). Site precipitation is used in each approach and meteorological data from the Yanacancha weather station (pan evaporation, wind speed, temperature, relative humidity, net radiation) is supplemented when needed.

D.1 PAN EVAPORATION

Pan evaporation data at Antamina is acquired at the Yanacancha meteorological monitoring station using a ‘Class A’ pan system that consists of a circular, unpainted aluminum ring 120 cm in diameter and 15.2 cm deep (Figure 3.6). Class A pan evaporation designs are commonly used because of the simplicity of the method (Irmak et al., 2002). At Yanacancha, the water level of the pan is re-filled once per week, with daily pan evaporation data (E_{pan}) obtained by measuring the daily difference in water level [mm/day]. In order to use E_{pan} data to determine the AE from the bare soil waste rock conditions, E_{pan} measurements are corrected for using both pan and bare soil correction factors (K_{pan} and K_{BS} , respectively) in order to obtain the bare soil evaporation term, E_{BS} (presented again in Chapter 3).

$$ET_{ref} = E_{pan} \cdot K_{pan} \quad [D-1]$$

$$E_{BS} = ET_{ref} \cdot K_{BS} \quad [D-2]$$

$$E_{BS} = E_{pan} \cdot K_{pan-BS} \quad [D-3]$$

where ET_{ref} is the reference evapotranspiration [mm/day] for an ideal grass surface; K_{pan-BS} represents a combination of the unitless pan and bare soil coefficients, K_{pan} and K_{BS} , respectively; and E_{BS} is the is the estimated bare soil evaporation [mm/day]. The calculation of these coefficients is discussed below.

D.1.1 Pan Coefficient

An understanding of the local environment in which the evaporation pans are located is critical for the proper interpretation of the pan evaporation data. Yeh et al. (2006) explain that K_{pan} values are site-specific, and vary regionally and seasonally. Differences in mean daily wind speed, mean relative humidity, upwind fetch and crop-height of that particular location are all incorporated in the pan coefficient. Since none of these parameters are measured at the study site, values from the Yanacancha meteorological station will be substituted as a proxy. The Yanacancha pan evaporation equipment is placed upon a grass crop that has an estimated height of 0.25 m and a fetch of 100 m. The Case A setup allows for the following calculations to ensue (Allen et al., 1998).

A mean wind speed is calculated using mean quarterly wind speed data measured at the Yanacancha monitoring station from July-2000 to March-2006 (Appendix C). Wind measurements are acquired from a height of 10 m above ground and converted to an equivalent height at 2 m because the temperature and relative humidity instruments are measured at this height (Table D.1). Using methodology provided by Allen et al. (1998), the equivalent mean wind speed of $u_2 = 1.8$ m/s at a height of 2 m was calculated over this period. With a mean relative humidity of $RH_{mean} = 76.8$ % (Appendix C), the K_{pan} can be calculated with a fetch of $FET = 100$ m using the following equation (Allen *et al.*, 1998):

$$K_{pan} = 0.108 - 0.0286 u_2 + 0.0422 \ln(FET) + 0.1434 \ln(RH_{mean}) - 0.000631 [\ln(FET)]^2 \ln(RH_{mean}) \quad [D-4]$$

The resulting K_{pan} is 0.81, but ranges from 0.76 ($FET = 10$ m) to 0.84 ($FET = 1000$ m) when different fetches are applied. For comparison, the Antamina mine uses a K_{pan} value of 0.7 over the entire mine property, a large majority of which is covered by grass and other similar vegetation.

D.1.2 Bare Soil Coefficient

Once the pan coefficient is used to calculate the reference evapotranspiration, a bare soil correction factor is required to correct the ET_{ref} data to an actual evaporation estimate from the bare waste rock soil surface. Allen et al. (1998) introduce a crop coefficient term that divides the various growth stages of different crops into four groups: initial, crop development, mid-season and late. The initial stage ranges from the planting date to approximately 10 % ground cover. During this period, the leaf area is small and the soil evaporative component is dominant compared to the transpirative component. The initial crop coefficient is typically high when the soil is wet from precipitation and low when the soil is dry. This period is most characteristic of the bare soil conditions of the waste rock pile.

Using type curves outlined in Allen et al. (1998), the bare soil coefficient K_{BS} is calculated for the water year. With an average ET_{ref} of 2.3 mm/day over the course of the water year (Section 4.3.1), and assuming a significant rain event refers to any instance in which precipitation was greater than 5 mm/day (i.e., twice the average ET_{ref}), then the average “wetting event” occurred every 4 days. Using this information along with Figure 29 (Allen et al., 1998), an average bare soil coefficient of $K_{BS} = 0.8 (\pm 0.1)$ is used to describe both wet and dry season data over the course of the water year.

Based on estimated K_{pan} and K_{BS} values of 0.81 and 0.8, respectively, the bare soil-corrected pan evaporation coefficient K_{pan-B_S} of 0.65 was calculated to obtain the bare soil evaporation estimate. Upper and lower K_{pan-B_S} values were calculated to be 0.53 ($K_{pan} = 0.76$ at 10 m fetch; $K_{BS} = 0.7$) and 0.76 ($K_{pan} = 0.84$ at 1000 m fetch; $K_{BS} = 0.9$). Therefore, the E_{pan} measurements were converted to E_{BS} estimates using a correction factor of $K_{pan-B_S} = 0.65 \pm 0.11$. Chapter 3 presents the results and discusses limitations of this approach.

D.2 PENMAN-MONTEITH EQUATION

Allen et al. (1998) describe that the FAO Penman-Monteith (P-M) method is recommended as the sole standard for the “definition and computation of the reference evaporation”. This semi-

empirical method calculates the reference evaporation of a grass surface using only meteorological variables using the following equation:

$$ET_{ref} = \frac{0.408(R_n - G) + \gamma \left(\frac{900}{T + 273.15} \right) u_2 (e_s - e_a)}{\Delta + \gamma (1 + 0.34u_2)} \quad [D-5]$$

where ET_{ref} is measured in mm/day; the net radiation R_n and soil heat flux G are both measured in MJ/(m²•day); the mean daily air temperature T is the temperature in °C at a height of 2 m; wind speed u_2 is the mean wind speed in m/s measured at a height of 2 m; the saturation vapour pressure e_s , actual vapour pressure e_a , and the saturation vapour pressure deficit ($e_s - e_a$) are all measured in kPa; the slope of the saturation vapour pressure-temperature relationship Δ is measured in kPa/°C; and the psychrometric constant γ is measured in kPa/°C. These parameters are discussed below. All equations are provided from Allen et al. (1998).

The net radiation R_n [MJ/m²•day] refers to all energy fluxes that need to be considered when deriving an energy balance equation. Put simplistically, R_n is the balance between incoming shortwave (solar) radiation and outgoing longwave (infrared) radiation, and is typically positive during the day and negative at night. Net radiation measurements are obtained at the Yanachanca station at five-minute intervals and converted from W/m² to MJ/(m²*day). The daily net radiation is positive, with an average of 9.02 MJ/(m² * day) and reaches maximum and minimum values of 18.8 and 2.6 MJ/(m² * day), respectively.

Soil heat flux G [MJ/(m²•day)] refers to the energy that is utilized in heating the soil. While positive during the day when the soil is warming and negative at night when the soil is cooling, the overall soil heat flux is small compared to the net radiation and is considered negligible (Allen et al., 1998).

Mean daily air temperature T [°C] is measured at a height of 2 m. By definition this parameter is calculated by averaging the maximum and minimum hourly temperature values for each hour in a day, and then dividing this value by 24 (Appendix C).

Mean daily wind speed u_2 [m/s] represents the equivalent wind speed at a height of 2 m above the ground. This is the average wind speed as calculated based on hourly wind speed measurements.

Saturation vapour pressure deficit ($e_s - e_a$) [kPa] refers to the balance between the saturation vapour pressure and the actual vapour pressure (see below). This is a positive number because the saturation vapour pressure is always greater than the actual vapour pressure. This is an indicator of the actual evaporative capacity of the air.

Saturation vapour pressure e_s [kPa] is the vapour pressure of saturated air at a given temperature. As air temperature increases, so too does the moisture storage capacity and the saturation vapour pressure. The mean daily saturation vapour pressure is calculated using the following equation:

$$e^o(T) = 0.6108e^{\left(\frac{17.27T}{T+237.3}\right)} \quad [\text{D-6}]$$

where $e^{o(T)}$ is the saturation vapour pressure at a mean daily temperature T and e is the natural logarithm (2.7183...). The maximum and minimum saturation vapour pressures are calculated for each day based on the maximum and minimum daily temperatures $e^{o(T_{\max})}$ and $e^{o(T_{\min})}$ by substituting for $e^o(T)$. Based on this:

$$e_s = \frac{e^o(T_{\max}) + e^o(T_{\min})}{2} \quad [\text{D-7}]$$

The actual vapour pressure e_a [kPa] refers to the vapour pressure exerted by the water in the air at a given temperature when the air is not saturated. When not saturated, the actual vapour pressure is less than the saturated vapour pressure. This term is calculated based on relative humidity RH and $e^{o(T)}$ measurements:

$$RH = 100 \frac{e_a}{e^o(T)} \quad [\text{D-8}]$$

where the maximum and minimum daily temperature (T_{max} and T_{min} , respectively) and relative humidities (RH_{max} and RH_{min} , respectively) are available, e_a can be derived using the following equation:

$$e_a = \frac{e^o(T_{min})\frac{RH_{max}}{100} + e^o(T_{max})\frac{RH_{min}}{100}}{2} \quad [D-9]$$

The slope of the saturation vapour pressure-temperature relationship Δ [kPa/°C] is calculated using the following equation:

$$\Delta = \frac{4098 [0.6108 e^{\left(\frac{17.27T}{T+237.3}\right)}]}{(T+237.3)^2} \quad [D-10]$$

The psychrometric constant γ [kPa/°C] accounts for atmospheric parameters that will affect evaporation. The Yanacancha station is located at an elevation of 4189 ± 2 m a.s.l, and the UBC test site is located at 4374 ± 2 m a.s.l. Using the following equation, the pressure at each elevation can be calculated, with a mean annual temperature of 6°C :

$$P = 101.325 \left(\frac{T - 0.0065z}{T} \right)^{5.26} \quad [D-11]$$

where the atmospheric pressure P [kPa], the elevation above sea level z [m], mean annual temperature $T_{M.A.T.}$ [279.15 K] are all employed. The corresponding atmospheric pressure at Yanacancha is 59 kPa (58% atmospheric at sea level) and 58 kPa (57% atmospheric at sea level) at the study site.

In addition, the latent heat of vapourization (λ) is calculated:

$$\lambda = 2.501 - (2.361 \times 10^{-3})T \quad [D-12]$$

The latent heat of vapourization at a mean annual temperature of 6°C is 2.49 MJ/kg, assuming a constant pressure and temperature throughout. This is the amount of energy that is required to change a unit mass of water from liquid to water vapour.

Based on the atmospheric pressure and latent heat of vapourization at the site elevation and mean annual temperature, the psychrometric constant can be computed and applied to the P-M equation.

$$\gamma = \frac{C_p P}{\varepsilon \lambda} \quad [\text{D-13}]$$

where the specific heat of vapourization at constant pressure, C_p , is 1.013×10^3 [MJ/kg °C⁻¹] and the molecular weight of water vapour/dry air ratio, ε , is 0.622. Accounting for the constants, the psychrometric constant at Antamina can be reduced to be only a function of pressure. Based on these calculations, the psychrometric constant at Yanacancha is 0.039 [kPa/°C] and 0.038 [kPa/°C] at the study site.

Using the aforementioned variables and equations, the Penman-Monteith approach is used to estimate the reference evapotranspiration which was subsequently corrected by the K_{BS} to obtain the E_{BS} of the waste rock test pile. Results are presented in Chapter 3 along with a discussion of limitations.

D.3 SOIL COVER

A third approach to estimate evaporation incorporates both pan evaporation data and a modified Penman formulation, along with several other environmental and soil property parameters (Wilson, 1990). SoilCover is a one-dimensional finite element model that is used to describe transient conditions in the unsaturated zone by predicting the coupled exchange of water and energy at the soil-atmosphere interface (Wilson et al., 1994, 1997; Carey et al., 2005). Theory is based on the principles of Darcy's and Fick's Laws which describe the flow of water (liquid and vapour), and Fourier's Law which describes conductive heat flow in the soil profile (Soil Cover, 2000). SoilCover is well-suited for evaporative flux modeling of bare, unsaturated waste rock piles because it integrates environmental and soil property parameters.

Data from one water year (1-Oct-2007 to 30-Sept-2008) was input to the SoilCover model. Temperature [°C], relative humidity [%], wind speed [km/h], radiation [MJ/m² • day], pan evaporation [mm/day] measured at the Yanacancha station are input with site precipitation

[mm/day] to represent the environmental variables. A detailed characterization of soil properties is also required, as bulk porosity, specific gravity, soil moisture content and hydraulic conductivity are some of the soil properties required in the model. Due to the unavailability of several soil property parameters during model simulations, these properties are assumed based on the waste rock from the Golden Sunlight Mine, Montana, USA (Herasymuik, 1996; Fines et al., 2003).

Four model simulations are performed to account for different materials within the pile (Table D.2; Table D.3; Table D.4; Table D.5). A coarse material with a saturated hydraulic conductivity of $K_{sat} = 1 \times 10^{-3}$ m/s is used to represent the pile batters, while a fine material with $K_{sat} = 8 \times 10^{-6}$ m/s is used to represent the top of the pile (recall the average K_{sat} for the compacted, top of the pile is 3×10^{-5} m/s). Porosity estimates of $n = 0.3$ and 0.4 are used to determine the effect of a changing porosity on the two materials. Other model input parameters pertaining to finite element mesh criteria, soil properties, etc. are presented in the model output summaries or below:

- height: 10 m
- site latitude: 15 deg
- no temperature or relative humidity lag
- initial volumetric water content (tip and bottom of pile): 0.18, based on Chapter 4
- boundary condition: mm/day
- oxygen coefficient estimation method: Millington and Shearer (1971)
- soil water characteristic curve: curve fit parameters of A (0.14), N (0.67), M (0.71)
- permeability and soil water characteristic curve method: Fredlund et al, 1994.
- thermal conductivity function method: Johansen, 1975
- volumetric specific heat function: de Vries Method

The flux graph for simulation Run 1 ($K_{sat} = 10^{-3}$ m/s, $n = 0.3$) is presented in Figure D.1. Chapter 3 summarizes results and discusses limitations of this approach.

D.4 PAN LYSIMETER WATER BALANCE

Evaporation calculated using the pan-lysimetry water balance approach provides the most reliable integration of climatic variables and material properties, particularly with regards to the differences between the pile top and batter. This approach is based on the assumption that there is no net change in storage over the course of one complete water year from 1-Oct-2007 to 30-Sept-2008. Chapter 3 summarizes results and discusses limitations

D.5 REFERENCES

- Allen, R., Pereira, L., Raes, D., and M. Smith. 1998. Crop evapotranspiration: Guidelines for computer crop water requirements. FAO Irrigation and Drainage Paper No. 56, Food and Agricultural Organization of the United Nations, Rome.
- Carey, S., Barbour, S. and M. Hendry. 2005. Evaporation from a waste-rock surface, Key Lake, Saskatchewan. *Canadian Geotechnical Journal*. 42: 1189 – 1199.
- Fines, P., Wilson, W., Williams, D., Tran, A. and S. Miller. 2003. Field Characterization of two Full-Scale Waste Rock Piles. In: *Proceedings of the Sixth International Conference on Acid Rock Drainage*, Cairns, Queensland.
- Fredlund, D., Anqing, X. and S. Huang. 1994. Predicting the permeability function for unsaturated soils using the soil-water characteristic curve. *Canadian Geotechnical Journal*. 31(3): 521-532.
- Herasymuik, G., Wilson, G., Barbour, S. and T. Smith, 1995. The characterization of hydrologic properties and moisture migration pathways of a waste rock pile. Mine reclamation, reclamation in extreme environments. In: 19th British Columbia Ministry of Energy and Mines, Victoria, BC.
- Irmak, S., Haman, D. and J. Jones. 2002. Evaluation of Class A pan coefficients for estimating reference evapotranspiration in humid location. *Journal of Irrigation and Drainage Engineering*. 128(3): 153-159
- Johansen, O. 1975. Thermal conductivity of soils. Ph.D. dissertation, University of Trondheim, Norway.
- Machibroda, R. 1994. M.Sc. thesis: Evaluation of evaporative fluxes from mint tailings using the modified Penman formulation. Placer Dome Cover and waste Rock Research program. University of Saskatchewan, Saskatoon, Canada.
- Millington, R., and R. Shearer. 1971. Diffusion in aggregated porous media. *Soil Science*. 111: 372-378.
- Natural Resources Canada. 2004. Design, construction and performance monitoring of cover systems for waste rock and tailing. O’Kane Consultants Inc (Ed). *The Canadian Mine Environment Neutral Drainage initiative (MEND 2.21.4)*. Volume 2. Theory and Background. OKC Report No 702-01.
- Penman, H. 1948. Natural evapotranspiration from open water, bare soil and grass. *Proceedings of the Royal Society of London Series A*. 193:120-145.
- Priestley, C. and R. Taylor. 1972. On the assessment of surface heat flux and evaporation using large-scale parameters. *Monthly Weather Review*. 100: 81-92.
- Soil Cover, 2000. *Soil Cover User’s Manual*. Unsaturated Soils Group, Department of Civil Engineering, University of Saskatchewan, Saskatoon, Canada.

Thornwaite, C. 1948. An approach towards a rational classification of climate. *Geographical Review* 38: 55–94. *doi:10.2307/210739*.

Wilson, W., Fredlund, D. and S. Barbour. 1994. Coupled soil-atmosphere modeling for soil evaporation. *Canadian Geotechnical Journal*. 31(2): 151-161.

Wilson, W., Fredlund, D. and S. Barbour. 1997. The effect of soil suction on evaporative fluxes from soil surfaces. *Canadian Geotechnical Journal*. 34:145-155.

Yeh, H., Chen J., Chen W., Change, K. and C. Lee. 2006. Evaluation of pan coefficients for estimating reference evaporatranspiration in southern Taiwan. American Geophysical Union, Fall meeting, 2006.

TABLES

Table D.1. Estimated wind speed at 2 m height above ground surface.

Estimated Quarterly Mean Wind Speed (m/s) at 2 m Height				
	Quarter			
Year	1	2	3	4
2000			2.1	2.0
2001	1.5	1.6	1.6	1.4
2002	1.4	1.7	2.1	1.6
2003	1.7	1.7	2.0	1.9
2005	1.7	1.9	2.4	1.9
2006	2.0			
Mean			1.8	

Table D.2. SoilCover simulation: Run 1 summary ($K_{sat} = 10^{-3}$ m/s, $n = 0.3$)

SoilCover V. 4.01 Run Summary Page

1. **Project Name:** Run 1
 2. **Project Directory:** c:\scv4\

3. **Run Parameters:**
 a) **Vegetation:** No

d) **Freeze / Thaw:** No

4. **Mesh Information:**
 a) **Convergence Criteria:**

Max. Iterations	Max.Change Suction (%)	Max.Change Temperature (%)	Suction Dampening (%)	Temperature Dampening (%)
50	1	1	0	0

b) **Time Step Control:**

Max.Change Suction (%)	Max.Change Temperature (%)	Minimum Time Step (seconds)	First Time Step (seconds)	Maximum Time Step (seconds)
5	5	1	1	3000

c) **Soil Profile Data:**

Number of Nodes	Number of Layers	Drain Node	Drain Flux (mm/day)
98	3	2	0

5. **Soil Property Summary:**

Soil Name	Porosity	Spec. Grav.	Mv (kPa)	Ksat (cm/s)
GMS Coarse K 1E-1	0.3	2.8	1.00E-03	1.00E-01
Well Graded Grave\Clay	0.32	2.8	1.00E-04	5.00E-04
Tailings	0.32	2.8	1.00E-05	1.00E-05
GSM Fine Mod. AEV K 1E-6	0.32	2.8	1.00E-05	1.00E-06
10706 E-4	0.32	2.8	1.00E-06	8.00E-04
10706 E-5	0.32	2.8	1.00E-06	8.00E-05
GITUFF 1e-4	0.74	2.8	1.00E-05	1.00E-04
clay 1e-7	0.7	2.8	1.00E-05	1.00E-07

6. **Boundary Conditions**

a) First date of run:	1-Oct-07
b) Total run days:	365
c) Top temperature condition:	User
d) Bottom temperature (C):	6
e) Day 1 top moisture condition:	Precip.
f) Day 1 bot. moisture condition:	1
g) Day 1 bottom moisture value:	1

7. **Vegetation Summary:**

a) Moisture limiting point (kPa):
 c) Moisture wilting point (kPa):
 e) Grass quality:

b) First date of growing season:
 d) Last date of growing season:
 f) First day root depth (cm):

8. **Run Output Summary:**

a) Net cumulative precipitation (mm):	1296.922
c) Net cumulative bottom flux (mm):	-5039.609
e) Net cumulative PE (mm):	-892.991
g) Net cumulative PT (mm):	0
i) Net cumulative ET (mm):	-415.804
k) Net cumulative drain node flux (mm):	0

b) Net cumulative infiltration (mm)	880.812
d) Net cumulative runoff (mm):	0.306
f) Net cumulative AE (mm):	-415.804
h) Net cumulative AT (mm):	0
j) Net cum. user monitor flx (mm):	*****
User Node	1
User Elev:	1000.00 cm

Note: Positive fluxes are UPWARDS. Negative fluxes at surface or base are LEAVING the mesh.

Table D.3. SoilCover simulation: Run 2 summary ($K_{sat} = 10^{-3}$ m/s, $n = 0.4$)

SoilCover V. 4.01 Run Summary Page

1. Project Name: RUN 2
2. Project Directory: c:\scv4\

3. Run Parameters:
 a) Vegetation: No

d) Freeze / Thaw: No

4. Mesh Information:

a) Convergence Criteria:

Max. Iterations	Max.Change Suction (%)	Max.Change Temperature (%)	Suction Dampening (%)	Temperature Dampening (%)
50	1	1	0	0

b) Time Step Control:

Max.Change Suction (%)	Max.Change Temperature (%)	Minimum Time Step (secnds)	First Time Step (secnds)	Maximum Time Step (secnds)
5	5	1	1	3000

c) Soil Profile Data:

Number of Nodes	Number of Layers	Drain Node	Drain Flux (mm/day)
98	3	2	0

5. Soil Property Summary:

Soil Name	Porosity	Spec. Grav.	Mv (kPa)	Ksat (cm/s)
GMS Coarse K 1E-1	0.4	2.8	1.00E-03	1.00E-01
Well Graded GravelClay	0.32	2.8	1.00E-04	5.00E-04
Tailings	0.32	2.8	1.00E-05	1.00E-05
GSM Fine Mod. AEV K 1E-6	0.32	2.8	1.00E-05	1.00E-06
10706 E-4	0.32	2.8	1.00E-06	8.00E-04
10706 E-5	0.32	2.8	1.00E-06	8.00E-05
GTTUFF 1e-4	0.74	2.8	1.00E-05	1.00E-04
clay 1e-7	0.7	2.8	1.00E-05	1.00E-07

6. Boundary Conditions

a) First date of run:	1-Oct-07
b) Total run days:	365
c) Top temperature condition:	User
d) Bottom temperature (C):	6
e) Day 1 top moisture condition:	Precip.
f) Day 1 bot. moisture condition:	0
g) Day 1 bottom moisture value:	0

7. Vegetation Summary:

a) Moisture limiting point (kPa):
 c) Moisture wilting point (kPa):
 e) Grass quality:

b) First date of growing season:
 d) Last date of growing season:
 f) First day root depth (cm):

8. Run Output Summary:

a) Net cumulative precipitation (mm):	1296.668
c) Net cumulative bottom flux (mm):	
e) Net cumulative PE (mm):	-892.691
g) Net cumulative PT (mm):	0
i) Net cumulative ET (mm):	-457.742
k) Net cumulative drain node flux (mm):	0

b) Net cumulative infiltration (mm):	838.891
d) Net cumulative runoff (mm):	0.035
f) Net cumulative AE (mm):	-457.742
h) Net cumulative AT (mm):	0
j) Net cum. user monitor flx (mm):	*****

User Node: 1
 User Elev: 1000.00 cm

Note: Positive fluxes are UPWARDS. Negative fluxes at surface or base are LEAVING the mesh.

Table D.4. SoilCover simulation: Run 3 summary ($K_{sat} = 8 \times 10^{-6}$ m/s, $n = 0.3$)

SoilCover V. 4.01 Run Summary Page

1. **Project Name:** Run 3
 2. **Project Directory:** c:\scv4\

3. **Run Parameters:**
 a) **Vegetation:** No

d) **Freeze / Thaw:** No

4. **Mesh Information:**
 a) **Convergence Criteria:**

Max. Iterations	Max.Change Suction (%)	Max.Change Temperature (%)	Suction Dampening (%)	Temperature Dampening (%)
50	1	1	0	0

b) **Time Step Control:**

Max.Change Suction (%)	Max.Change Temperature (%)	Minimum Time Step (seconds)	First Time Step (seconds)	Maximum Time Step (seconds)
5	5	1	1	3000

c) **Soil Profile Data:**

Number of Nodes	Number of Layers	Drain Node	Drain Flux (mm/day)
98	3	2	0

5. **Soil Property Summary:**

Soil Name	Porosity	Spec. Grav.	Mv (kPa)	Ksat (cm/s)
GMS Coarse K 1E-1	0.4	2.8	1.00E-03	1.00E-01
Well Graded Gravel/Clay	0.32	2.8	1.00E-04	5.00E-04
Tailings	0.32	2.8	1.00E-05	1.00E-05
GSM Fine Mod. AEV K 1E-6	0.32	2.8	1.00E-05	1.00E-06
10706 E-4	0.3	2.8	1.00E-06	8.00E-04
10706 E-5	0.32	2.8	1.00E-06	8.00E-05
GTTUFF 1e-4	0.74	2.8	1.00E-05	1.00E-04
clay 1e-7	0.7	2.8	1.00E-05	1.00E-07

6. **Boundary Conditions**

a) First date of run:	1-Oct-07
b) Total run days:	365
c) Top temperature condition:	User
d) Bottom temperature (C):	6
e) Day 1 top moisture condition:	Precip.
f) Day 1 bot. moisture condition:	1
g) Day 1 bottom moisture value:	1

7. **Vegetation Summary:**

a) **Moisture limiting point (kPa):**
 c) **Moisture wilting point (kPa):**
 e) **Grass quality:**

b) **First date of growing season:**
 d) **Last date of growing season:**
 f) **First day root depth (cm):**

8. **Run Output Summary:**

a) Net cumulative precipitation (mm):	1296.922
c) Net cumulative bottom flux (mm):	
e) Net cumulative PE (mm):	-883.735
g) Net cumulative PT (mm):	0
i) Net cumulative ET (mm):	-491.803
k) Net cumulative drain node flux (mm):	0

b) Net cumulative infiltration (mm):	775.655
d) Net cumulative runoff (mm):	29.464
f) Net cumulative AE (mm):	-491.803
h) Net cumulative AT (mm):	0
j) Net cum. user monitor flx (mm):	779.649
User Node	1
User Elev:	1000.00 cm

Note: Positive fluxes are UPWARDS. Negative fluxes at surface or base are LEAVING the mesh.

Table D.5. Soil Cover simulation: Run 3 summary ($K_{sat} = 8 \times 10^{-6}$ m/s, $n = 0.4$)

SoilCover V. 4.01 Run Summary Page

1. **Project Name:** Run 4
 2. **Project Directory:** c:\scv4\

3. **Run Parameters:**
 a) **Vegetation:** No

d) **Freeze / Thaw:** No

4. **Mesh Information:**
 a) **Convergence Criteria:**

Max. Iterations	Max.Change Suction (%)	Max.Change Temperature (%)	Suction Dampening (%)	Temperature Dampening (%)
50	1	1	0	0

b) **Time Step Control:**

Max.Change Suction (%)	Max.Change Temperature (%)	Minimum Time Step (seconds)	First Time Step (seconds)	Maximum Time Step (seconds)
5	5	1	1	3000

c) **Soil Profile Data:**

Number of Nodes	Number of Layers	Drain Node	Drain Flux (mm/day)
98	3	2	0

5. **Soil Property Summary:**

Soil Name	Porosity	Spec. Grav.	Mv (kPa)	Ksat (cm/s)
GMS Coarse K 1E-1	0.4	2.8	1.00E-03	1.00E-01
Well Graded Gravel/Clay	0.32	2.8	1.00E-04	5.00E-04
Tailings	0.32	2.8	1.00E-05	1.00E-05
GSM Fine Mod. AEV K 1E-6	0.32	2.8	1.00E-05	1.00E-06
10706 E-4	0.3	2.8	1.00E-06	8.00E-04
10706 E-5	0.32	2.8	1.00E-06	8.00E-05
GTTUFF 1e-4	0.74	2.8	1.00E-05	1.00E-04
clay 1e-7	0.7	2.8	1.00E-05	1.00E-07

6. **Boundary Conditions**

a) First date of run:	1-Oct-07
b) Total run days:	365
c) Top temperature condition:	User
d) Bottom temperature (C):	6
e) Day 1 top moisture condition:	Precip.
f) Day 1 bot. moisture condition:	1
g) Day 1 bottom moisture value:	1

7. **Vegetation Summary:**

a) Moisture limiting point (kPa):	
c) Moisture wilting point (kPa):	
e) Grass quality:	

b) First date of growing season:	
d) Last date of growing season:	
f) First day root depth (cm):	

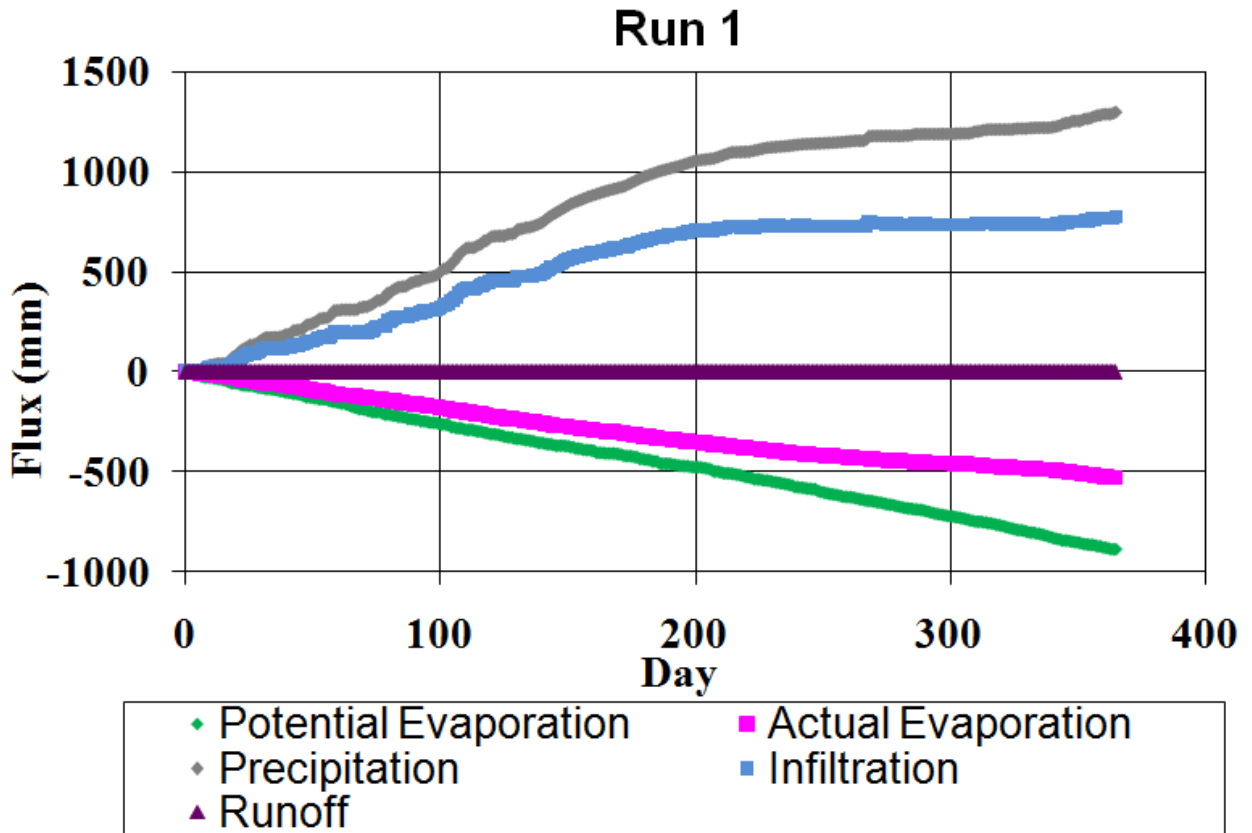
8. **Run Output Summary:**

a) Net cumulative precipitation (mm):	1296.922
c) Net cumulative bottom flux (mm):	
e) Net cumulative PE (mm):	-883.886
g) Net cumulative PT (mm):	0
i) Net cumulative ET (mm):	-528.333
k) Net cumulative drain node flux (mm):	0

b) Net cumulative infiltration (mm):	768.578
d) Net cumulative runoff (mm):	0.011
f) Net cumulative AE (mm):	-528.333
h) Net cumulative AT (mm):	0
j) Net cum. user monitor flx (mm):	774.12
User Node:	1
User Elev:	1000.00 cm

Note: Positive fluxes are UPWARDS. Negative fluxes at surface or base are LEAVING the mesh.

FIGURES



* Positive fluxes at interior nodes are UPWARDS. Negative fluxes at surface or base are LEAVING the mesh.

Figure D.1. SoilCover simulation: Run 1 ($K_{sat} = 10^{-3}$ m/s; $n = 0.3$)

APPENDIX E: OUTFLOW

E.1	TIPPING BUCKET CALIBRATION	263
E.2	DATA: PRE-PROCESSING	265
E.2.1	Maintenance	265
E.2.2	Data Anomalies	265
E.2.3	Missed Tips	266
E.2.3.1	Cause of Missed Tips	267
E.2.3.1.1	Instrumentation.....	268
E.2.3.1.2	Programming	268
E.3	DATA: PROCESSING.....	269
E.3.1	Choosing How To Correct For Missed Tips.....	269
E.3.1.1	Understanding RANSAC	271
E.3.1.2	Ransac Parameters.....	271
E.3.1.2.1	Window Size	273
E.3.1.2.2	Maximum Number of Iterations	274
E.3.1.2.3	Break Size.....	275
E.3.1.3	How RANSAC Works on Tipping Bucket Data.....	276
E.3.2	Overall Performance and Error.....	277
E.3.3	Data Limitations	278
E.3.4	RANSAC Summary.....	279
E.4	POST-PROCESSING: ACCOUNTING FOR TIPPING BUCKET DATA	280
E.5	REFERENCES	283

TABLES

Table E.1.	2007 and 2008 tipping bucket calibrations.....	284
Table E.2.	Summary and extent of missed tips identified by RANSAC for each lysimeter.....	284

FIGURES

Figure E.1.	Large tipping bucket calibration calculated Jan-2007.....	285
Figure E.2.	Missed tip banding for large tipping bucket flow data.....	285
Figure E.3.	Sub-lysimeter C peak flow fluctuations in January, 2008.....	286
Figure E.4.	Regression analysis of sub-lysimeter C and basal lysimeter D daily flow.....	286

APPENDIX E: OUTFLOW

This appendix focuses upon the tipping bucket instrumentation. After a brief explanation of the tipping bucket calibration and maintenance issues, the remainder of this discussion will focus on the reported tipping bucket data. Up to 18 % of the reported tipping bucket data originates from tipping bucket tips that were not recorded by the datalogger and required interpolation. After interpolation, up to 36 % of the resulting (interpolated) dataset originates from missed tips. This interpolation scheme is required so that reasonable hydrological characterization and water balance estimates can occur (Chapter 3).

E.1 TIPPING BUCKET CALIBRATION

Tipping bucket instrumentation has been used in several similar waste rock hydrology investigations (Nichol et al., 2005; Andrina et al., 2006; Neuner, 2009). The principal component of the tipping bucket is a trapezoidal, dual-chambered pivot that rotates around an axle. It is a similar design to a conventional rain gauge tipping bucket and functions analogous to a ‘seesaw’. Water is directed into one of the chambers until a threshold volume is reached, which triggers the pivot mechanism to ‘tip’. During each tip, a magnet mounted to the side of the pivot mechanism passes near a reed switch mounted to the tipping bucket housing unit. When this occurs, a signal is sent to a datalogger which records the time that the pulse is reported. The time between two successive tips is referred to as the ‘tip-time’. As the water-filled chamber drops, it discharges water into the housing unit where it drains and is directed into the flow splitter (Corazao Gallegos, 2007).

An empirical calibration equation converts the tip-time (time between consecutive tips) to a corresponding flow rate [L/min or ml/s] for the large and small tipping buckets, respectively. Multiplying the tip-time by the flow rate produces the equivalent volume of water per each tip. Tips at extremely low flow rates can be triggered by a single drop of water (once the bucket is near the tipping threshold), whereas tips at high flow rates are triggered by a steady stream of water that has a larger momentum. Flow rate and tip-time should not vary significantly over short time periods. The most common way to relate tip-time to flow rate requires the manual calibration of each individual tipping bucket in the field by purposely varying the flow rate over

different runs and measuring the amount of, and time in which, water passes through. The equivalent volume of water during each tip is calculated by multiplying the calibrated flow rate by the reported tip-time. For this investigation, results are totaled on a daily basis and reported as m^3/day .

Each tipping bucket was individually calibrated on 18-Jan-2007 and Aug-2008, the results of which are summarized in Table E.1. The Jan-2008 large tipping bucket (basal lysimeter D) calibration presents the inverse relationship between flow rate and tip-time that all tipping bucket calibration equations share (Figure E.1). A cut-off date of 25-Oct-2007 is used as the midway point between the two calibration dates when the equations are applied to the experimental dataset. The Jan-2007 calibrations are applied to data from 18-Jan to 24-Oct-2007; and the Aug-2008 calibrations are applied to the dataset from 25-Oct-2007 to 30-Oct-2008. This method is believed to most accurately (linearly) describe the evolution of the tipping bucket behaviour after a series of maintenance periods given the available calibration data.

The inverse relationship between tip-time and flow rate illustrates that, in general, a larger tip-time corresponds to a lower flow rate. For example, using the calibration equation provided in Figure E.1, the highest basal lysimeter D flow rates of 13 - 15 L/min (tip-time = 9 s/tip) are calculated and the maximum corresponding volume per tip is near 3 L. Conversely, at the lowest flow rate of near 0.1 L/min (tip-time = 2000 s/tip), the corresponding volume per tip is 2.4 L. Similar patterns are observed in the small tipping buckets, particularly for tipping bucket C, which corresponds to the front sub-lysimeter under the batter. At the highest flow rate (tip-time = 6 s/tip; flow rate = 3.8 ml/s), the volume per tip reaches almost 24 ml, whereas at extremely low flow rates (tip-time = 1 day/tip; flow rate = 10^{-5} ml/s) the volume per tip reaches as low as 15 ml. Therefore, for a given calibration equation applied to the large and small tipping buckets, the volume per tip can vary by up to 25 % and 60 %, respectively.

That high flow rates correspond with fast (i.e., short) tip-times is of particular interest to note, as this is one property that contributes to poor quality tipping bucket data at various times (discussed below).

E.2 DATA: PRE-PROCESSING

E.2.1 Maintenance

Most instrumentation maintenance (tipping bucket, electrical conductivity probe, etc.) was primarily carried out during the dry season (when possible), when flow was minimal if at all. With the exception of a few days in which maintenance was performed on the large tipping bucket, the basal lysimeter reported continuous flow throughout the study period. The sub-lysimeters ceased to flow at various periods in the dry season (Chapter 3). Nevertheless, maintenance generally disrupted the flow, and created various large outliers in the dataset. Poor records exist concerning the extent of when and why the flow-through by-pass systems were initiated, or when the in-let valve was closed (Chapter 3; Corazao Gallegos, 2007). The by-pass tubing was installed vertically and requires a head buildup of nearly 40 cm (estimated to be > 50 - 100 L), which would evidently disrupt the flow response reported in the small tipping buckets and even the large one (this by-pass route was later adjusted in subsequent piles to be horizontal to not require this head buildup).

When the by-pass valve is opened, water typically rushes out and causes the tipping bucket to register higher than expected flow rates. These tips are identified in the data and subsequently excised during pre-processing (i.e., prior to data processing) so that they would not be mistakenly identified as peak flow rates and lead to a higher average flow rate. If these tip-time points are not removed, they may lead to problems in the data processing (described below). Each deleted tip-time point is carefully accounted for, and the equivalent volume of each deleted tip is included in the final water balance analysis. The removal of data is a subjective technique, and is performed very conservatively to only remove extreme outliers that interfere with the data processing. The number of removed tips from the raw data represents nearly 0.2 % of the total estimated volume of water discharging from the base of the pile (Table 3.3).

E.2.2 Data Anomalies

In general, several data anomalies are found in the datalogger data, including the thermistor, TDR probe, electrical conductivity probe and tipping bucket data. Short periods of missing or duplicated data, or data with the wrong year (i.e., 1900) are found in the data and likely result

from small glitches in the datalogger or the data transfer procedure (from datalogger to computer via telemetry). These cases require manual identification and removal where possible.

A program modification implemented on 31-Mar-2008 was intended to improve the scanning resolution of tipping bucket data from 3- to 1-second intervals. The unfortunate effect of this was the result of several random data points. Every reported tip was accompanied by 1 or 2 consecutive 'ghost' tips recorded by the datalogger. That these data points represented actual tips is physically impossible based on their 1-second tip-times, and site observations confirmed that these tips did not result from highly variable flow rates (i.e., pulsing) nor from bouncing of the pivot mechanism, indicating that this was caused by an artifact in the software programming. The cause of these erroneous tips was finally corrected 113 days later on 22-July-2008, requiring the removal of 58,878 data points (i.e., tip-time data points) from the large tipping bucket data (basal lysimeter D), 108,890 from the front tipping bucket corresponding to the front sub-lysimeter (C), 17,023 from the tipping bucket corresponding to the back sub-lysimeter (B) and 33,321 from the tipping bucket corresponding to the middle sub-lysimeter (A). Another program modification on 26-Aug-2008 removed the ghost tips while still allowing a 1-second scanning resolution of the tipping bucket data. The final program is included in Appendix H.

In those cases where flow is not recorded by the datalogger but field observations indicate that the tipping bucket is flowing, this data is estimated so that more accurate water balance calculations can ensue.

E.2.3 Missed Tips

Shortly after the tipping buckets were installed and the datalogger began collecting data, it became evident that some of the tipping bucket tips were not being recorded by the datalogger. Some tip-times varied by a factor of 2 or more from the previous tip-time, and resulted in a highly fluctuating flow rate over a very short time interval and the presence of several distinct, congruent bands became evident in the data over time (Figure E.2). For example, if the average (e.g., base case or field-confirmed) tip-time during a given hour was 30 seconds, then tip-times of 30 ± 10 seconds would be considered to fall within an expected normal variability. Predominant outliers, not included in the base flow rates (i.e., expected or field-observed flow),

were found to exist in distinct bands that were near-multiples of the average base tip-time (e.g., tip-times of 60, 90, or 120 seconds, etc.). An average tip-time over a period in which the larger tip-times were present in the data would thus overestimate the tip-time and by definition underestimate the corresponding flow rate.

This behaviour was beyond the expected noise of these measurements and field observations confirmed that consecutive tip-times did not vary by such large numbers. This led to the conclusion that while the tipping buckets were observed to be functioning properly, the datalogger was failing to account for each tip. This created the discrete banding of flow rates that were congruent with the field-observed flow rate (i.e., varied over time in response to precipitation) as evident in Figure E.2. Due to the inverse relationship between tip-time and flow rate, faster (shorter) tip-times resulted in slower flow rates. One missed tip led to a flow rate that was approximately $\frac{1}{2}$ the field-observed flow rate, and two missed tips led to nearly $\frac{1}{3}$ the observed flow rate, and so on (up to 10+ consecutive missed tips or more). This relationship can be expressed as:

$$tt_2 = \frac{tt_1}{(1+m)} \quad [E-1]$$

where tt_2 is the interpolated (corrected) tip-time (seconds/tip), tt_1 is the observed (uncorrected) tip-time, and m is the integer number that corresponds to the number of missed tips ($m = 0$ for the base case flow i.e., no missed tips; $m = 1$ for 1 missed tip, etc). This correction must be applied to the tip-time and not the flow rate, as the ‘flow rate - tip-time’ relationship is nonlinear.

E.2.3.1 Cause of Missed Tips

The two sources of missed tips was either due to:

1. a physical, hardware problem with the instrumentation, or
2. a software problem with the datalogger program.

Both options are discussed next.

E.2.3.1.1 Instrumentation

The missed tips may have resulted from a poor recognition of the passing magnet by the reed switch. Each tipping bucket was corrected for by:

1. ensuring that the dual-chamber pivot mechanism was directly orthogonal to the axis,
2. replacing the magnet with a stronger rare earth magnet (circular, 3/8" neodymium, 5 lb magnetic strength; www.leevalley.com) in Aug-2007, and
3. re-orienting the reed switch 90° counter-clockwise to allow the switch to recognize the larger region of magnetic influence.

These modifications occurred during the dry season (2007), and several months had passed until the flow was high enough to observe that banding was still present in the data, though slightly improved.

E.2.3.1.2 Programming

In August-2008 it was determined that the cause of missed tips resulted from a conflict in the datalogging program protocol. One major hint that this was a programming issue became evident in the date before and after 4-Jun-2007, when a program modification was introduced to improve data collection efficiency and led to a significant decrease in missed tips (Figure E.2).

As explained by Corazao Gallegos (2007), the CR1000 datalogger is used to record all of the data from several different types of instrumentation (Figure A.9). A program was written directing the CR1000 to record thermistor, Time Domain Reflectometry (TDR) and electrical conductivity data at 30-minute intervals ('slow sequence') while also continuously recording each of the four tipping buckets and the rain gauge ('fast sequence'). Due to a large number (62) of 'slow sequence' instrumentation, several (7) 'multiplexers' were connected to the datalogger. While the multiplexers enable one datalogger to record all of the data from many instruments, this leads to an increased time in which the datalogger is dedicated to storing the 'slow sequence' data. Of particular note is that the collection of data from the (22) TDR probes is much slower relative to the (36) thermistors and (4) EC probes.

Due to the way in which the initial program was structured, it failed to recognize the ‘fast sequence’ data when it was recording the ‘slow sequence’ data. This poor prioritization between the two different types of data created the discrepancy between the number of actual tips by the tipping bucket and those that were recorded by the datalogger. Since no pattern was observed in the missed tips (i.e., did occur at 30-minute intervals), it is evident that this is a very complex issue whose understanding is beyond the scope of this investigation. Recommendations to improve this issue and avoid this problem in the future are described in Chapter 7.

E.3 DATA: PROCESSING

E.3.1 Choosing How To Correct For Missed Tips

It is often the case in experimental datasets that considerable noise and outliers are present. In certain situations, extreme outliers in the data present extensive obstacles in data processing, and require that the data be managed using less conventional smoothing techniques. Several methods exist to iteratively identify certain large errors based on initial model parameters, and delete the erroneous data points until all of the erroneous points are removed or until the dataset includes a maximum deviation that is less than a pre-determined threshold. These techniques are not suitable for the tipping bucket data because each missed tip must be accounted for in order to conduct accurate water balance calculations. An interpolated flow rate is required in order to determine volumetric contributions from each lysimeter at hourly, daily, weekly and monthly resolutions.

To determine the most suitable method to identify and correct for missed tips, three mathematical algorithm routines are compared: the K-means algorithm, a Random Sample Consensus model and a Hough Transformation Technique. These are iterative methods that apply user-specified parameters to a dataset in order to identify certain objects or attributes. The K-means algorithm is a popular heuristic technique employed in clustering objects based on certain attributes, and attempts to find the natural centroid of that particular cluster of data by minimizing the total variance. Given that this method is heuristic, it assumes a normal distribution around the mean and even a small number of outliers can significantly distort results using this application. Both the Random Sample Consensus (RANSAC) model and Hough Transformation Technique (HTT) are considered next.

The RANSAC model and HTT are typically employed in processing applications where imperfections and large errors exist in the datasets, such as in digital image processing. Both employ user-specified parameters to iteratively identify certain objects within a dataset. The HTT can be used to find imperfect instances of objects of certain shapes in a dataset and can perform groupings based on a mathematical equation. The RANSAC model is used to estimate parameters of a mathematical model that contains both ‘inliers’ and ‘outliers’ based on user-specified parameters (Fishler and Bolles, 1981). When applied to an observed dataset, the RANSAC model provides a stochastic approach that is based on the assumption that ‘inliers’ can be described by a mathematical model based on a distribution of observed data and ‘outliers’ result from some extreme value of noise, erroneous measurement or incorrect hypotheses about the data interpretation.

Whereas a classical least squares method will do a poor job characterizing a noisy dataset by fitting a line to all the data points irrespective of whether they are extreme errors, a typical RANSAC model will compute a line by distinguishing between inliers and outliers, and then reevaluating the model using only the inliers. Least squares methods have no internal mechanisms for detecting or rejecting points and they rely on the assumption that the maximum expected deviation from the assumed function is related to the size of the dataset, regardless of the type of data. As a result, any deviations will be balanced out by other outliers and the resulting values will be smooth, averaged out to a representative function that misrepresents the actual behaviour (Fishler and Bolles, 1981).

Comparing the advantages, disadvantages and ease of application to our dataset, the RANSAC model serves as the best option for this dataset despite the fact that it contains a stochastic element. Once outliers are identified, they can be assigned a certain m -integer value ($m = 1, 2, 3$, etc.) associated with the number of missed tips, and can subsequently be corrected for. The RANSAC model is chosen because it is:

1. relatively easy to implement, and
2. capable of interpreting and smoothing data with a significant amount of error.

E.3.1.1 Understanding RANSAC

The Random Sample Consensus (RANSAC) model was selected to correct the raw tipping bucket data in order to produce a reliable estimation of the actual flow rate. This was achieved using MATLAB v. 7.5.0.342 (R2007b) to execute the model on the reported tipping bucket data (Section I.1.3). First applied to image processing by Fishler and Bolles (1981), this model can be used for a variety of scientific applications. RANSAC is typically employed for datasets that contain a heavy presence of noise and outliers, and robustly fits a model to a dataset by using an interpretative algorithm.

The RANSAC model uses as small an initial dataset as possible to determine a hypothetical model and encompasses more tip-time points as long as they are consistent with the model parameters. Based on user-specified criteria (discussed below), data points are assigned inlier and outlier values. Inliers represent data whose distribution can be explained by a set of model parameters, i.e., can be fitted to a line, and represent the ‘base case’ or ‘field-observed’ flow rate. Once identified, inlier points are placed in the inlier ‘bin’ where $m = 0$, according to user-specified parameters. Outliers represent data points that do not fit the model, and are subsequently assigned m -integer values (where $m > 0$) depending on how many missed tips the model estimates that they are associated with, and are then placed in the corresponding ‘bin’ level ($m = 1, 2, 3$, etc). Outliers can consist of both noise and erroneous measurements.

E.3.1.2 Ransac Parameters

The RANSAC model depends on several user-specified parameters. The three main user-specified parameters that are manually adjusted to obtain the “best estimated” interpreted dataset are discussed in this section. The term “best estimated” is used here to address the ability of the interpreted data to incorporate a significant amount of outliers without producing significant spikes in the data. Based on the nature of the data, the model parameters were adjusted to account for both high and low flow rates so that one single model could be used upon the entire dataset. When applied to the tipping bucket data, RANSAC does not perform well under very high flow rates (especially for tipping bucket C) due to certain limitations in equipment and software (described below). Therefore, the model was only applied to the flow data originating

from the wet-season, as this is where a significant proportion of the missed tips occurred. An autonomous RANSAC model with the capability to self-adjust parameters in response to the data at various times of the year is beyond the scope of this thesis and is not explored further.

The three heuristic user-specified parameters in the model that are manually adjusted to achieve the ‘best estimated’ flow rates were:

1. window size,
2. maximum number of iterations, and
3. break size.

Window size refers to the number of points within a given cluster that the algorithm is applied to at one time. The maximum number of iterations describes the maximum trials that the model can tolerate until the maximum deviation is less than a certain threshold and the proposed model fails. Break size refers to the size of the consensus set that is required to belong to the modeled fit compared to the window size i.e., is the number of compatible points used to imply that the correct model has been found and that the model can move to the next window.

Both the maximum number of iterations and break size are probabilistic arguments that dictate the probability and speed in which the model will proceed. Applied to the same dataset, the RANSAC algorithm will likely produce similar but rarely identical results. The probability of correctly choosing only inliers depends on carefully chosen parameters. When holding all parameters constant, the resulting dataset may never have the same size (i.e., same number of data points). This is where the ‘random’ element in the model is introduced.

A parameter sensitivity analysis is carried out in the following sections. It is performed on a subset of the tipping bucket data from each lysimeter (18-Jan-2007 to 30-Apr-2007) because it is the first collected experimental data at this site and includes the largest proportion of missed tips compared to later periods. Results are generally consistent with other applications of the RANSAC algorithm (e.g., Fishler and Bolles, 1981).

E.3.1.2.1 Window Size

Window size w dictates the number of data points of the subset in which the algorithm is performed on at one time. The window must be small enough that the flow rate remains relatively constant in any window, and covers a lower time span at high flow rates and a higher time span at lower flow rates. Various window sizes spanning two orders of magnitude ($w = 10, 50, 150, 175, 250$ and 1000) are applied to the dataset and run ten consecutive times to determine the optimal window size and reproducibility.

Results of each run are rarely identical but are relatively consistent, producing similar-sized datasets at intermediate-window sizes ($50 < w < 200$). At window sizes $w \leq 500$, the average dataset size experiences a very low average standard deviation ($\sigma < 0.5\%$). While very small window sizes (i.e., $w = 10$) have much higher processing times over large window sizes (i.e., $w = 1000$), the resulting dataset size at very large datasets is larger, likely overestimating the flow data (i.e., estimated more missed tips than actually were).

Data becomes excessively noisy when $w \leq 100$ and too smooth (i.e., removes some of the short-term responses to precipitation) when $w = 1000$. The most optimal window size was found to be $w = 175$ because it produces the least amount of erratic spikes, particularly for the front sublysimeter C, and has a modest processing speed. A window difference of $w \pm 25$ has a more noticeable effect on the small tipping buckets than the large tipping bucket. During 10 consecutive runs, a standard deviation of $\sigma < 0.2\%$ when $w \leq 250$ is found for the large tipping bucket data, with an optimal $\sigma = 0.01\%$ at $w = 175$.

Based on statistical and graphical analyses, a window size of $w = 175$ is determined to be an appropriate value and represents a good compromise between data that is too noisy (and eclipses the natural variability in response to precipitation) and too smooth (that it removes natural short-term variability in response to precipitation). This window size value is best suited for the large tipping bucket data, which represents nearly 97 % of the total pile flow (Chapter 3).

E.3.1.2.2 Maximum Number of Iterations

The RANSAC model uses as small an initial dataset as possible to determine a hypothetical model and encompasses more points until a consensus set is attained. It is preferred that for a given number of trials n , the probability of picking a single tip-time point (or more) to be in the ‘inlier’ consensus be as high as possible. The likelihood of this happening depends on the proportion of inliers to the total original (raw) dataset, which is expressed as P . Conversely, the probability of incorrectly choosing an outlier tip-time point p and saying that it fits the model is dependent on P as described below:

$$p = (1 - P)^{E(k)} \quad [\text{E-2}]$$

where $E(k)$ is the number of iterations for k number of trials. A smaller p value means that there is a larger likelihood that a data point will be correctly classified. The P ratio is implicit in the data and will vary over time and among lysimeters. For example, in this sensitivity analysis based on 2.5 months of tipping bucket data, the interpolated datasets are 45 – 63 % larger than the original datasets ($P = 0.37 - 0.55$; average of $P = 0.46$). This means that 46 randomly selected points in the original dataset will likely represent 100 tip-time data points in the interpreted dataset. However, this does not indicate how many of the tip-time data points in the original dataset are assigned outlier values (e.g., 20 tip-time points that represent 1 missed tip or 1 tip-time point that represents 20 missed tips). Therefore, the P value given here represents an overestimation of the actual P , but will serve as the maximum ceiling for P values.

To determine what the ideal maximum number of iterations would be for this dataset, ten consecutive runs are tested with $E(k)$ values ranging between 2 and 250 on basal-lysimeter D and sub-lysimeter C data. In general, a very low maximum iteration ($E(k) = 2$) produces datasets that are approximately 17 % smaller than the average size of datasets at any other number of iterations. Values of $E(k) = 10$ to 250 produce very similar sized datasets, with average deviations of 0.011 % and 0.15 % for basal lysimeter D and sub-lysimeter C, respectively, at the lowest standard deviation at $E(k) = 20$. Based on equation E-2, a larger iteration value corresponds to a smaller probability that the RANSAC model will incorporate an outlier in the inlier bin.

When applied to the dataset, a larger $E(k)$ value smoothes out and ‘cleans up’ the data. There is very little effect on the plotted data at $E(k) = 20, 50$ and 250 . For comparison, a value of $E(k) = 1000$ removes some of the daily variation due to meteorological changes.

Based on statistical and graphical analyses of this dataset, a value of $E(k) = 20$ is determined as the optimal maximum number of iterations because it has a relatively fast processing speed and maintains the short-term variability in response to meteorological changes. This means that at $E(k) = 20$ and $P = 0.46$, equation E-2 dictates that the probability of incorporating an erroneous point in the model will be 1.8×10^{-7} . Conversely, this means that the probability of choosing a correct point in 20 iterations is greater than 99.99 % of the time.

E.3.1.2.3 Break Size

Break size b dictates the proportion of the points in the given subset (dictated by the window size) that must fit the model (i.e., reach the consensus) so that the model can proceed to the next subset of data. The consensus is determined by $b * w$. The break size must be large enough to satisfy that (Fishler and Bolles, 1981):

1. the appropriate model has been chosen, i.e., the ‘inliers’ can be described by an equation, and
2. a sufficient number of points have been found to reach the consensus.

A larger break size means that there is a higher likelihood that a consensus has been reached, and a suitable model has been chosen from the dataset. A sensitivity analysis performed on the data illustrated that $b \leq 70$ % produces slightly larger datasets because the model deviates from the base-case scenario and incorporates a larger proportion of outliers. At $b \geq 75$ %, the resulting dataset size is relatively consistent and indicates that the model is more representative of the base-case scenario. Based on statistical and graphical analyses, a break size value of $b = 90$ % is considered appropriate for this parameter. This means that in a given window size of $w = 175$, approximately 158 of the points must fit the model in order for a consensus to be reached. When this is achieved, the model can proceed to the next subset.

Break size is implicitly dependent on a tolerance factor t , and vice versa. The tolerance factor accounts for the variable noise in the dataset by dictating how far away from the model a point can deviate while still being incorporated as an inlier. Only one of the break size or tolerance factors can be adjusted while the other is held constant. By definition t must be less than 0.5, so a value of $t = 0.3$ is held constant while the break size is adjusted. The tolerance factor allows for a given point to vary from the base case model by up to a factor of 0.3 and still be included in the consensus. This is a function of the size of the width of each m -integer band (or bin) that the model recognizes (Figure E.2).

E.3.1.3 How RANSAC Works on Tipping Bucket Data

Once the user-specified parameters are determined, the RANSAC model randomly selects a subset of tip-time points and assumes that they are all hypothetical inliers. A clustering algorithm then fits a model to the subset based on the user-specific parameters, and then assigns each point ‘inlier’ or ‘outlier’ designations based on this model. Those points that fit the model ($m = 0$) are placed in the inlier bin whereas the rest of the points are placed in outlier bins ($m = 1, 2, 3$, etc). There is only one inlier bin but as many outlier bins as there are missed tips. The model then moves outwards, incorporating more points and classifying them into their respective bins. The model is iteratively calculated when new inliers are included in the model. This continues until a pre-determined consensus has been achieved (i.e., a certain proportion of the points in the window are fitted to the model) and the algorithm moves ahead to the next window. If the model fails to meet a consensus set, a second hypothetical model is offered for which the process continues again. This continues until a consensus is achieved or until the maximum number of iterations has been reached and the model is prematurely terminated. (It is for this reason that certain large outliers resulting from instrumentation maintenance must be omitted before applying the RANSAC algorithm, as they can cause the program to terminate prematurely). If the maximum number of iterations is never reached (and the consensus is achieved), the result is a dataset in which each tip-time has been assigned to either an inlier bin or one of several outlier bins.

Each outlier bin has a specific integer value m , which corresponds to the number of m missed tips. Section E.2.3 explains that the integer value increases with distance away from the base case inlier range ($m = 0$). Those tip-time points that are placed into the $m = 1$ bin represent one missed tip and the tip-time is then divided by $m + 1$. Therefore, a tip-time that results from one missed tip is corrected to two tip-times by dividing the reported tip-time by 2, and linearly interpolating the time stamp value for each point based on the time before and after the reported tip-time data point. Similarly, data points representing two missed tips ($m = 2$) are divided by $m + 1$ and three tip-times are calculated based on linearly-interpolated time stamps. This continues for all missed tips.

E.3.2 Overall Performance and Error

Flow reporting to each lysimeter is highly variable. As a result, the RANSAC algorithm performs differently depending on the lysimeter data that it is applied to as some tipping buckets miss more tips than others. For example, 91 % of the reported basal lysimeter flow is recognized as base case flow (i.e., no missed tips, $m = 0$) by the RANSAC algorithm (Table E.2). The remaining 9 % of reported tip-times represents the data associated with missed tips and is subsequently interpolated. After interpretation, the resulting dataset (which serves as the basis for the analysis throughout Chapter 3) is then adjusted to account for the interpolated data points. Base case flow represents 79.9 % of the new dataset and the proportion of interpolated data points becomes 20.1 %. Of the interpolated 20.1 %, nearly 10.5 % is associated with 1 missed tip ($m = 1$), 5.6 % is associated with 2 missed tips ($m = 2$) and 1.7 % is associated with 3 missed tips ($m = 3$). Less than 0.5 % of the total interpreted data set consists of data originating from 10 or more missed tips ($m \geq 10$). Based on this, an additional error of ± 20 % is attributed to the basal lysimeter flow data.

Similarly, 83.2 % of the reported tipping bucket C data is recognized as base case flow (Table E.2). After interpolation, only 65.8 % of the interpolated dataset consists of base case flow, while the remaining dataset consists of interpolated data points that originate from missed tips. Of the remaining 34.2 % of the interpolated flow, 19.6 % is associated with 1 missed tip, 6.5 % is associated with 2 missed tips, and 2.9 % is associated with 3 missed tips. Nearly 2.2 % of the

total interpreted dataset consists of data originating from 10 or more missed tips. An error range of $\pm 35\%$ is attributed to flow from tipping bucket C.

Approximately 88.7 % of the reported tipping bucket data for sub-lysimeter B is base case flow, but the proportion of base case flow drops to 71.2 % of the interpreted data (Table E.2). Of the remaining 28.8 % of the interpreted data, 11.3 % is associated with 1 missed tip, 5.7 % is associated with 2 missed tips, and 2.9 % is associated with 3 missed tips. Approximately 6.2 % of the interpreted data consists of data originating from 10 or more tips. This number is likely inflated based on the nature of the data from this tipping bucket, which encountered a relatively high flow rate throughout the study period that the RANSAC algorithm is not able to handle as effectively as other tipping bucket data. Nevertheless, an error range of $\pm 29\%$ is attributed to flow originating from tipping bucket B.

Nearly 83.5 % of the reported dataset represents the base case flow, but the proportion of base case flow has changed to 64.6 % of the interpreted data (Table E.2). Of the remaining 35.4 % of the interpreted dataset, 16.6 % of the data is associated with 1 missed tip, 7.9 % is associated with two missed tips, and 3.6 % is associated with 3 missed tips. Nearly 3.0 % of the interpreted dataset originates from 10 or more missed tips. An error of $\pm 35\%$ is attributed to the flow originating from tipping bucket A.

These error bounds are implemented in Chapter 3.

E.3.3 Data Limitations

Several limitations in the data have led to a poor characterization of very high flow rates where tip-times are very short. This is particularly the case for sub-lysimeter C data. For example, a total of 99 mm of precipitation is introduced between 12-Jan and 18-Jan-2008 and has a distinct effect on three of the four lysimeters (B, C and D; sub-lysimeter A was not functioning at that time). On 12-Jan-2008 the average C flow rate is 1 ml/s, and quickly doubles to 2 ml/s by 14-Jan. By midday on 15-Jan the flow rate has reached 3 ml/s, and begins to experience rather erratic flow behaviour as it fluctuates between 4 and 8 ml/s until midday on 17-Jan where the flow rate begins to subside. The erratic behaviour results in flow rates that vary by a factor of 2

over the course of a few minutes. Such high variability in flow rates for a given tipping bucket are not observed in the field and are believed to result from:

1. a 3-second scanning resolution, and
2. the nature of the calibration equation.

The 2007 calibration equation for the front tipping bucket (sub-lysimeter C):

$$q = 23.506(tt)^{-1.019} \quad [E-3]$$

where the flow rate q is expressed in ml/s, and the tip-time tt is the number of seconds between consecutive tips. Based on the nature of the calibration equation, flow rates are nearly asymptotic at very fast (i.e., high) tip-times (e.g., Figure E.1). Since the datalogger scanning resolution was set to search for tipping bucket data at 3 second intervals, this meant that tips were reported in 3-second intervals regardless if they occurred at some time within one of these intervals. When these two factors are combined, they result in a poor reliability of the tipping bucket data at very high tip-times. Based on the capacity of the large tipping bucket and the low flow rate from sub-lysimeters A and B, this is only a problem for sub-lysimeter C which encounters tip-times as fast as 6 seconds. At $tt = 6, 9$ and 12 s, the corresponding q values according to equation E-3 are 3.8, 2.5, and 1.9 ml/s, respectively. The equivalent volume associated with each respective tip would be 22.7, 22.5 and 22.4 ml. To illustrate how much values change at very high flow rates, at $tt = 3$ s, the flow rate is 7.7 ml/s and the equivalent volume of water is 23.0 ml/s, and results in a significant variability in high-flow data (Figure E.3). Overall, this does not have a considerable impact on the entire pile outflow term Q because the fastest tip-time reported by the large tipping bucket is 9 seconds which corresponds to a flow rate of 15 - 20 L/min and an equivalent volume per tip of 2.3 - 3.0 L (depending on the calibration equation).

E.3.4 RANSAC Summary

Implementation of the RANSAC model to the experimental tipping bucket dataset produces suitable results for the purpose of this investigation. Interpolated large tipping bucket data maintains reliability at high flow rates and includes the largest proportion of base case flow in

both the reported and interpolated datasets. This also indicates that the user-defined RANSAC model parameters are also suitable for this application. While the parameters could have been further adjusted to improve the interpretation results for sub-lysimeter C, these parameters were optimally suited to the large tipping bucket (D) because it is most representative of the overall pile flow behaviour. Although sub-lysimeter C data does lose reliability at high flow rates based on the RANSAC parameters, these periods of poor reliability are short-lived (only occur at very fast flow rates i.e., > 3 ml/s) and is accepted as a suitable tradeoff for consistently reliable data for the rest of the tipping bucket data.

It is likely that the RANSAC algorithm does not properly classify every missed tip and that certain limitations in the model led to somewhat flawed results. In graphically comparing the raw and the RANSAC-corrected data, it is evident that a majority of the missed tips are corrected for. The total volume of water estimated to have discharged from the base of the pile throughout the entire study period is up to 35 % higher when based on the interpolated data compared to the reported data. Although results are not entirely reproducible when run consecutively on the same dataset, the differences between each run for the user-specified parameters is < 1 %, an acceptable percentage for the purpose of this investigation. The interpolated dataset is thus used as the basis for the flow characterization and water balance estimates for which this thesis is based on.

E.4 POST-PROCESSING: ACCOUNTING FOR TIPPING BUCKET DATA

For accurate water balance estimates, the following estimates must be considered:

1. the equivalent water of the removed tip-time data points, and
2. the estimated volume of water that the dataloggers failed to record.

The first case involves the addition of equivalent volume of water that was removed from the original dataset (in the form of tip-time data points) during data cleaning/pre-processing. In total, less than 2 % of the total reported tip-times were removed from the dataset, which results in an estimated 2.6 m^3 of water (2.5 m^3 of which was from basal lysimeter D).

The second case involves estimating the volume of water that passes through each tipping bucket but no tipping bucket data is available. Site observations confirm that there were periods in which the tipping buckets were flowing (particularly during the wet season) but the datalogger failed to record this data, likely due to a poor connection between a given tipping bucket and the datalogger. This is particularly the case for sub-lysimeter A which has several large gaps in the data (nearly 50 % of the entire time period) that result from several different maintenance issues (EC probe malfunction, leaks in the flow-through piping, etc). This approach does not produce statistically significant results, but is included to provide a crude estimate of the volume of missing flow data.

In total, 56 m³ of water was estimated to account for the gaps in the tipping bucket data. This value was attained using two different methods:

1. a regression analysis, and
2. a graphical approach.

The regression approach correlates daily flow between each lysimeter in attempt to resolve whether any strong relationships are present so that missing data could be correlated. This approach also provides insight into the flow similarities between the various lysimeters.

Due to the influence of the batters (Chapters 3, 4 and 5), basal lysimeter D and sub-lysimeter C exhibit a strong correlation with $r^2 = 0.86$ (Figure E.4). Sub-lysimeter B exhibits a moderate correlation to C and D, with r^2 values of 0.56 and 0.69, respectively (the correlations could have been higher but C flow was unreliable at high flow rates). Sub-lysimeter A exhibits the lowest correlation to the other lysimeters and cannot be used in this approach ($r^2 = 0.52, 0.36$ and 0.29 for B, D and C, respectively). Correlations are generally better at lower flow rates and become more scattered during the higher flow rates. During the two main gaps in D data (April and Sept-2007; Chapter 3), C data is also missing so no estimations can be carried out using this approach (recall that flow is observed during 97 % of the entire period by D and nearly 74 % of the time for C; Chapter 3). When possible this method is applied to those wet-season periods where D data is available and C gaps could be estimated, such as during March-, October- and December-

2007. While this approach fails to account for each gap in missing data, it does illustrate that there is a similarity in behaviour between basal lysimeter D and sub-lysimeter C, with sub-lysimeters A and B also exhibiting similarities.

The second approach to estimating the missing data involves a more subjective (manual) methodology in which daily flow rates are graphically estimated using the outflow hydrographs. Flow is then interpolated based on prior precipitation events, previous responses to similar precipitation events, and response of the pair lysimeter (i.e., A/B and C/D). In general, results proved to be similar to those obtained by the previous regression analysis.

To summarize, results from these two methods do not present robust or statistically significant approaches to estimating the missing volume of water, but were consistent enough to enable crude volumetric estimations. The regression method does not fully address the lag time differences between the lysimeters, but it does imply that correlations exist between the flow response of each lysimeter, particularly between the D/C and A/B pairs. The final bulk estimated value, an average of the result from the two approaches, was 56 m^3 . This is less than 5 % of the total volume of water interpolated to have drained from the base of the pile (Table 3.3). A significant proportion of this bulk estimate originated during the week of 26-April to 3-May-2007, where nearly 48 m^3 (85 % of the total estimate) of water is estimated to have discharged from basal lysimeter D. This gap corresponds to a trip to site by UBC personnel in which the tipping bucket performance was tested and tipping buckets D, C, and B were poorly connected to the datalogger. The unfortunate mistake led to a gap in data just after a significant rain event. Both basal lysimeter D and sub-lysimeter C data before and after this gap indicate that they would have had a very rapid and large response to that precipitation event.

E.5 REFERENCES

Andrina, J., Wilson, G.W., Miller, S. and A. Neale. 2006. Performance of the acid rock drainage mitigation waste rock trial dump at the Grasberg Mine. In: Proceedings of the 7th International Conference on Acid Rock Drainage, St Louis, U.S.

Corazao Gallegos, J.C., 2007. The design, construction, instrumentation, and initial response of a field-scale waste rock test pile, M.A.Sc. thesis. University of British Columbia, Vancouver, Canada.

Fischler, M. and R. Bolles. 1981. Random Sample Consensus: A paradigm for model fitting with applications to image analysis and automated cartography. *Graphics and Image Processing*. 24: 381-395.

Neuner, M. 2009. Water flow through unsaturated mine waste rock in a region of permafrost. M.Sc. thesis, University of British Columbia, Vancouver, Canada.

Nichol, C., Smith, L. and R. Beckie. 2005. Field-scale experiments of unsaturated flow and solute transport in a heterogeneous porous medium. *Water Resources Research*. 41:W05018,doi:10.1029/2004WR003035.

TABLES

Table E.1. 2007 and 2008 tipping bucket calibrations.

Tipping Bucket	A	B	C	D
18-Jan-2007*	$q = 25.89(tt)^{-1.071}$ ($r^2 = 0.999$)	$q = 25.64(tt)^{-1.053}$ ($r^2 = 0.999$)	$q = 23.51(tt)^{-1.019}$ ($r^2 = 0.999$)	$q = 195.69(tt)^{-1.0316}$ ($r^2 = 1.00$)
Aug-2008	$q = 32.58(tt)^{-1.06}$ ($r^2 = 0.998$)	$q = 28.71(tt)^{-1.014}$ ($r^2 = 0.992$)	$q = 26.05(tt)^{-1.034}$ ($r^2 = 0.997$)	$q = 132.26(tt)^{-0.989}$ ($r^2 = 0.998$)

* Corazao Gallegos, 2007

Table E.2. Summary and extent of missed tips identified by RANSAC for each lysimeter.

Missed Tip Bin <i>m</i>	Basal lysimeter D		Sub-Lysimeter C		Sub-Lysimeter B		Sub-Lysimeter A	
	Raw*	Interpreted	Raw*	Interpreted	Raw*	Interpreted	Raw*	Interpreted
0	91.0%	79.9%	83.2%	65.8%	88.7%	71.2%	83.5%	64.6%
1	5.98%	10.5%	12.4%	19.6%	7.06%	11.3%	10.7%	16.6%
2	2.13%	5.60%	2.74%	6.50%	2.37%	5.69%	3.40%	7.90%
3	0.49%	1.72%	0.91%	2.87%	0.91%	2.93%	1.18%	3.64%
4	0.22%	0.97%	0.31%	1.22%	0.29%	1.15%	0.49%	1.88%
5	0.08%	0.45%	0.16%	0.75%	0.11%	0.53%	0.22%	1.04%
6	0.03%	0.19%	0.09%	0.47%	0.05%	0.30%	0.12%	0.63%
7	0.01%	0.11%	0.04%	0.25%	0.05%	0.30%	0.06%	0.35%
8	0.00%	0.03%	0.03%	0.19%	0.03%	0.23%	0.03%	0.22%
9	0.00%	0.03%	0.02%	0.14%	0.02%	0.18%	0.02%	0.18%
10+	0.01%	0.48%	0.05%	2.22%	0.20%	6.16%	0.10%	2.95%

*raw represents the original dataset

FIGURES

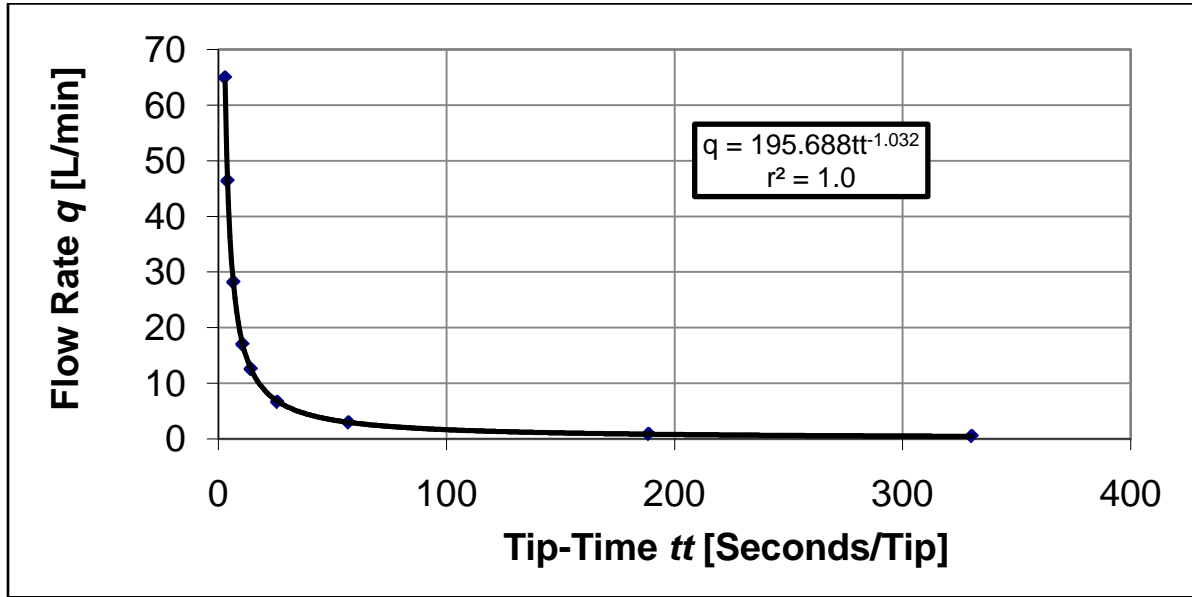


Figure E.1. Large tipping bucket (D) calibration calculated Jan-2007.

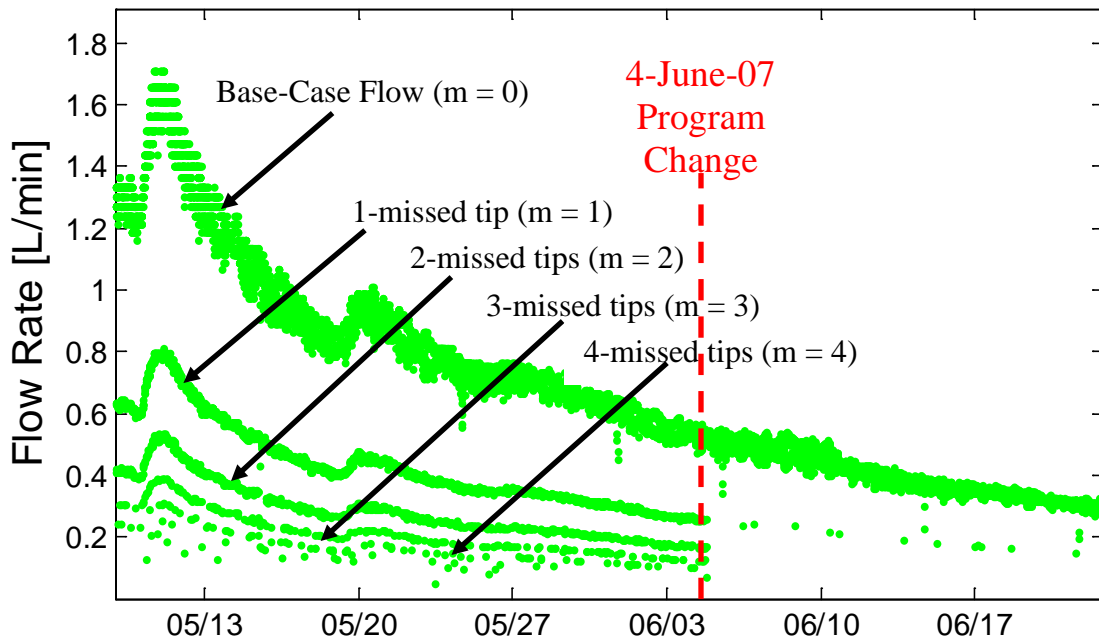


Figure E.2. Missed tip banding for large tipping bucket (D) flow data.

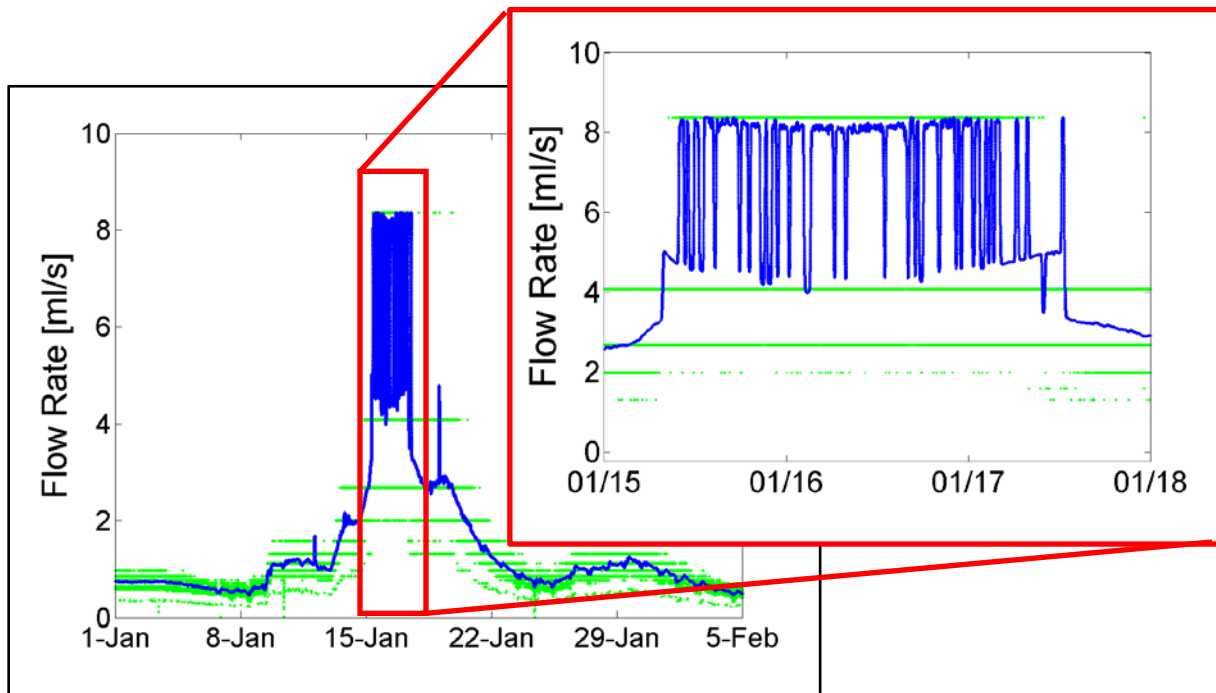


Figure E.3. Sub-lysimeter C peak flow fluctuations in January, 2008.

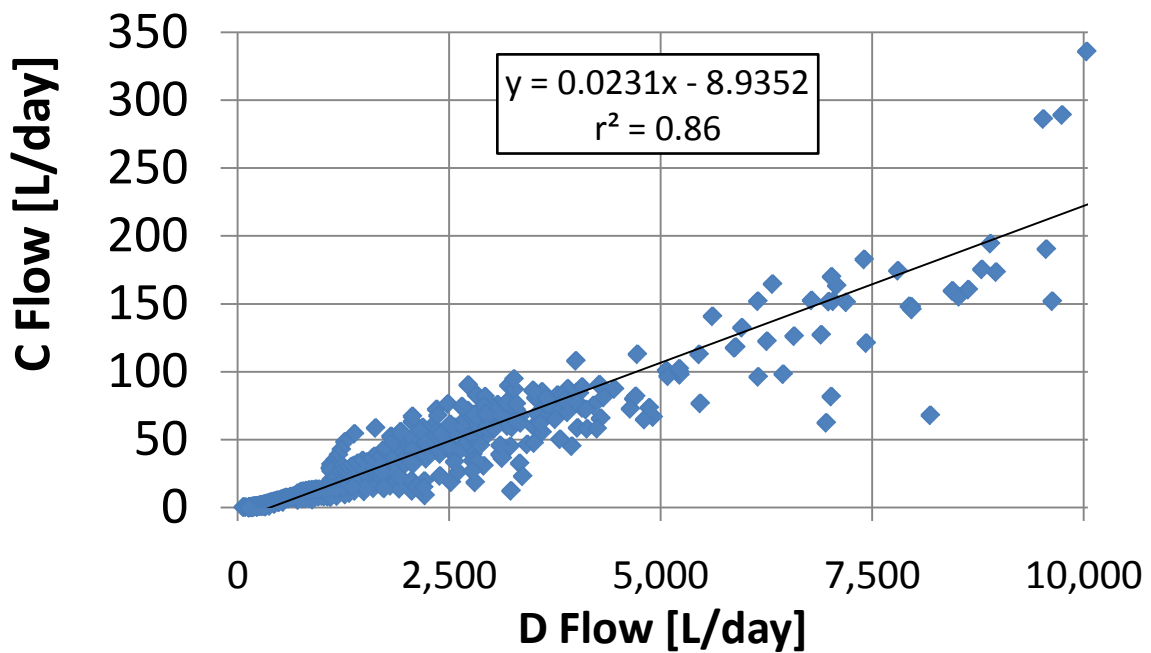


Figure E.4. Regression analysis of sub-lysimeter C and basal lysimeter D daily flow.

APPENDIX F: TIME DOMAIN REFLECTOMETRY PROBES

F.1	HOW THE TDR PROBE WORKS.....	288
F.2	INCORRECT TDR SETTING	289
F.3	TDR CALIBRATION	290
F.4	CLUFF CLAKE CALIBRATION APPLIED TO ANTAMINA WASTE ROCK	292
F.5	UNCERTAINTY	293
F.6	REFERENCES	294

APPENDIX F: TIME DOMAIN REFLECTOMETRY PROBES

Twenty-two custom-built Time Domain Reflectometry (TDR) probes were installed in the test pile to provide continual, automated in-situ volumetric water content readings (Corazao Gallegos, 2007). The TDR probes, capable of accurately measuring moisture content in the saline porewater environment expected in the test pile, were built using the design of Young (1998) that was elaborated by Nichol et al. (2003). These probes are unique because they include a high resistance coating along the centre conductor rod that enables these probes to function better in the saline waste rock porewaters (Nichol et al., 2002; Nichol et al., 2003). A schematic is provided in Figure F.1.

Each probe is connected to a Moisture Point MP-917 TDR instrument (www.esica.com) located within the instrumentation hut (Figure A.9). When instructed, the MP-917 box directs a pulse to a single TDR probe, calculates the travel and outputs the result to the datalogger (details discussed below). The raw TDR output data is typically converted to moisture content using theoretical- or empirically-derived calibration relationships. Standard theoretical relationships such as found in Topp et al. (1980) do not apply to these probes due to the high-resistance probe coating, so an empirical calibration is required.

No soil-specific TDR calibration is yet available for the Antamina waste rock. A soil-specific calibration using similar TDR probes in waste rock at the Cluff Lake mine (Nichol et al., 2005) is used to calibrate the TDR probes at the Antamina test pile (Nichol et al., 2002). In addition, a significant proportion of the TDR data obtained during the study period was not viable for analysis due to an incorrect configuration of the MP-917 TDR instrument (see below). This appendix describes how the TDR instrument was wrongly configured and the effect it had on the raw TDR output. A description of the calibration equation will follow suit.

F.1 HOW THE TDR PROBE WORKS

Moisture content is estimated based on the time it takes an electromagnetic pulse to travel through the exposed portion of a TDR probe. Pulse propagation is dependent on the dielectric properties of the water/rock/air mixture of the waste rock surrounding the probe. The dielectric

permittivity of a porous medium is a measure of the impedance of an electromagnetic pulse travelling through that medium. Each medium has an apparent dielectric permittivity that is a combination of the dielectric constant k of each material in that medium (i.e., rock, water, and air in waste rock), and is calculated by (Topp et al., 1980; Noborio, 2001):

$$k = \left(\frac{ct}{2L}\right)^2 \quad [\text{F-1}]$$

where c is the velocity of an electromagnetic wave in free space [m/s] (i.e., 3×10^8 m/s) and t is the round-trip travel time [ns] in which the pulse travelled the length of the probe L [m]. Based on the difference of dielectric constants k ($k_{\text{water}} \sim 80$, $k_{\text{sand}} \sim 2$ to 5 and $k_{\text{air}} \sim 1$), a higher k value corresponds to a higher water content. In a given soil, as the moisture content increases, the apparent dielectric increases and the travel time of the propagating electromagnetic pulse increases (Nichol et al., 2003).

F.2 INCORRECT TDR SETTING

The Moisture Point MP-917 soil moisture measurement instrument (Environmental Sensors Inc. (ESI); www.esica.com) sends radio-frequency pulses to each TDR probe, analyzes the pulse waveform reflections and calculates a travel time offset that is sent to and stored by a datalogger. Months after the data came online at Antamina, it was determined that the MP-917 was incorrectly configured to the wrong TDR probe type from the first day of the study period (18-Jan-2007) until 8-May-2008 (the beginning of the 2008 dry season), when the wrong setting was corrected. By this time, nearly 16 months had passed and all of the TDR data during this period was not viable in producing viable moisture content data. The following section describes how the instrument was wrongly configured and the effect that this has on the raw data.

TDR probes contain diodes that control the direction in which an electro-magnetic pulse propagates through the probe. When ESI began constructing TDR probes, a negative diode was located at the cable end (“top of probe”) and the positive diode was located at the far end (“probe tail”). This type of probe is referred to as Probe Type 0 (PT0). A TDR Probe Type 1 (PT1) has diodes in reverse order, with a negative diode in the far end and a positive diode at the cable end (Figure F.1). The Antamina probes constructed by Corazao Gallegos (2007) were based on the

same design as those employed by Nichol et al. (2002, 2003) and Marcoline (2008) at the Cluff Lake mine and Neuner (2009) at the Diavik mine, all of which are PT1.

When instructed, the MP-917 TDR instrument directs a signal to activate a specific (far) diode in the TDR probe and searches for the response from the other (close) diode. If the MP-917 is not properly configured for the right probe type, it will direct the signal to the wrong end of the TDR probe and subsequently search for the response in the wrong place. The instrument searches for the raw waveform reflections based on the user-specified Gain, Base, and Offset parameters that direct the window in which the instrument searches for the data. Since the TDR instrument was not searching for the raw waveform signal properly (i.e., at the right time, with the proper Gain, Base and Offset parameters set), it did not capture the main reflection of the TDR signal. Interpreting the partial waveform as the entire waveform, the TDR instrument calculated the travel time offset based on this truncated waveform and output the travel time offset in nanoseconds to the datalogger. Nichol et al. (2002) explains this in further detail.

An examination of the site MP-917 default settings in Apr-/May-2008 determined that it was wrongly configured for PT0. Since the TDR probes are Probe Type 1, the raw waveform reflections truncated the second reflection of the waveform and miscalculated the travel time based on a wrongly interpreted reflection point. The MP-917 does not save the raw waveforms and the datalogger only records the raw travel time offsets. The wave form could not be deduced based on the raw travel time offsets alone. Even if the datalogger had captured the entire raw waveform obtained by the MP-917 instrument, it was found that since the PT0 settings activated the TDR diodes in reverse order, results would not reliably represent any discernable behavior of the material surrounding the probe. This means that the initial 16-months of recorded TDR data is unrecoverable and no moisture content values are available during this time.

F.3 TDR CALIBRATION

TDR probes measure the apparent dielectric permittivity of a medium. Air has a permittivity k of $k \sim 1$, solid soil particles $k \sim 2$ to 5 and water near $k \sim 80$. When a pulse propagates through a TDR probe, the speed at which it travels along the exposed rod is a function of the dielectric properties of the surrounding water/air/rock medium. Since water has a high dielectric

permittivity, a change in the moisture content of the medium surrounding a TDR probe directly affects the time in which it takes the pulse to propagate through the exposed probe.

The travel time of an electromagnetic pulse can be correlated to the moisture content of a material through a mixing model or direct empirical evidence. Due to probe design modifications (e.g., probe coating), empirical calibrations are necessary for site-specific waste rock (Nichol et al., 2002). Lacking a soil-specific TDR calibration using the Antamina waste rock, a theoretical equation provided by Topp et al. (1980), and two empirical calibrations provided by Nichol et al. (2003) and Neuner (2009) are applied to the raw TDR data. The calibration equations are used to relate the travel time (in nanoseconds) to volumetric moisture content (m^3/m^3).

A comparison between the different calibration equations indicates that the ‘washed’ Cluff Lake waste rock calibration (Nichol et al., 2003) provides the most likely range of expected moisture content values in the course Antamina waste rock. The waste rock material selected for this experiment was ‘washed’ to remove any surficial weathering products in order to simulate a low-electrical conductivity environment (much like the test pile 1 pore and effluent water).

From an empirical laboratory calibration using ‘washed’ waste rock from the Cluff Lake mine, Saskatoon, Canada, Nichol et al. (2003) determined a relationship between the raw TDR travel time data and the moisture content using the equation

$$\theta_p = \frac{-b\sqrt{4aTDR-4ac+b^2}}{2a} \quad [\text{F-2}]$$

where θ_p is the volumetric water content of a given probe measurement [m^3/m^3], TDR is the temperature and probe-offset-corrected TDR travel time [ns], and a , b and c are all parameters of a second order polynomial equation, -0.035007, 5.49231 and 1.91, respectively. Where no coincident temperature data is available for the TDR temperature correction, it is linearly interpolated based on adjacent temperature readings. Without a soil-specific calibration, relative changes in moisture content are emphasized over absolute changes.

Before applying the calibration, raw TDR output is corrected in three respects (Nichol et al., 2003; Marcoline, 2008; Neuner, 2009):

1. probe offset correction: this isolates the travel time in which the electromagnetic pulse was exposed to the waste rock,
2. signal normalization by length: the probe offset-corrected data is normalized by the theoretical travel time in air along the length of the exposed probe (this accounts for slightly different probe lengths), and
3. temperature correction: to account for temperatures differences between the field in which the measurements were obtained and the laboratory in which the calibration equation was calculated.

In those areas of the pile where temperature data was not available (e.g., TDR probes along the base or next to malfunctioning thermistors), a linear interpolation based on adjacent thermistors was applied.

F.4 WHY THE CLUFF CLAKE CALIBRATION CAN BE APPLIED TO ANTAMINA WASTE ROCK

It is advantageous to use soil-specific TDR calibrations over theoretical calibrations because they take into account the varying properties of the soil and TDR probe that can impact results. The clay content and electrical conductivity can both affect TDR readings. As Nichol (2002) explains:

the dielectric permittivity of water within a soil environment may not be the same as that of water as a free phase. Water close to mineral surfaces, especially clays, is bound by electrostatic forces, indicating that the dielectric and electrical conductance properties of bound water are different from those of free-phase water.

This can increase the apparent dielectric permittivity of the soil water since most clay particles are negatively charged and can attract the positively charged H-atom in a dipolar water molecule, preventing it from rotating freely and aligning itself when the TDR pulse travels by. For comparison, the dielectric permittivity of ice is similar to that of a dry soil because the water molecules in ice are bound in the crystalline structure and are not available to align themselves as the TDR pulse propagates through the probe. In addition, an increase in dissolved ions decreases

the dielectric permittivity of water directly by reducing the number of highly polarizeable water molecules per unit volume, and indirectly by the interaction of ions with the electrostatic bonding structure of liquid phase water molecules (Nichol et al., 2002; Hasted, 1973). Therefore a higher clay content (and/or electrical conductivity) likely results in an underestimation of the apparent dielectric permittivity and the in-situ volumetric water content. The extent of this, and how clay content affects the soil/air/water/bound water/dissolved ions mixture is not fully understood (Nichol et al., 2002).

In laboratory settings, Nichol et al. (2003) compared ‘washed’ and ‘unwashed’ waste rock calibrations to the Topp equation (Topp et al., 1980), corrected for the dielectric permittivity of the high-resistance probe coating, and found that the Topp equation did not as accurately account for high and low water contents as did the soil-specific calibrations. The TDR travel time is shown to decrease at low water contents in waste rock. This can be explained by the binding of water molecules to clay surfaces, inducing a faster pulse travel time than expected, and creating underestimated water content values. The Cluff Lake waste rock has a significant portion of finer grain sizes than Antamina (~20 % of the < 5 mm fraction is silt and clay compared to < 10 % at Antamina), indicating that TDR probes might perform differently in Antamina’s waste rock. As mentioned above, this could not be corrected for since the effect of clay content is not well understood. Nevertheless, Nichol’s washed calibration was applied to the Antamina TDR probes because it accounts for a lower-conductivity effluent which is more similar to Antamina’s waste rock, and was used over the Topp equation because it is based on waste rock and not the clay- to sandy-loam material that Topp et al. (2008) utilized. Further discussion can be found in Section 3.4.

F.5 UNCERTAINTY

It is clear that uncertainty may be introduced to the system in several forms extending from probe design and installation to the data correction and calibration equation employed. Even with an accurate soil-specific TDR-waste rock calibration, considerable uncertainty may still be present in the data. For the purpose of this investigation and given the resources available at the time of publication, the ‘washed’ calibration determined by Nichol et al. (2003) was used, and analyses emphasize relative moisture content changes over absolute values.

F.6 REFERENCES

- Corazao Gallegos, J.C., 2007. The design, construction, instrumentation, and initial response of a field-scale waste rock test pile, M.A.Sc. thesis. University of British Columbia, Vancouver, Canada.
- Hasted, J. 1973. Aqueous Dielectrics. Chapman and Hall, London.
- Marcoline, J. 2008. Investigations of water and tracer movement in covered and uncovered unsaturated waste rock. Ph.D. dissertation. University of British Columbia, Vancouver, Canada.
- Neuner, M. 2009. Water flow through unsaturated mine waste rock in a region of permafrost. M.Sc. thesis, University of British Columbia, Vancouver, Canada.
- Nichol, C., Beckie, R. and L. Smith. 2002. Evaluation of uncoated and coated time domain reflectometry probes for high electrical conductivity systems. *Soil Science Society of America Journal*. 66: 1454-1465.
- Nichol, C., Smith, L and R. Beckie. 2003. Time domain reflectometry measurements of water content in coarse waste rock. *Canadian Geotechnical Journal*. 40: 137-148.
- Nichol, C., Smith, L and R. Beckie. 2005. Field-scale experiments of unsaturated flow and solute transport in a heterogeneous porous medium. *Water Resources Research*. 41:W05018, doi:10.1029/2004WR003035.
- Noborio, K. 2001. Measurement of soil water content and electrical conductivity by time domain reflectometry: a review. *Computers and Electronics in Agriculture*. 31: 213-237.
- Topp, G., Davis, J. and A. Annan. 1980. Electromagnetic determination of soil water content: Measurement in coaxial transmission lines. *Water Resources Research*. 16(3): 574-582.
- Young, G. D., 1995. Moisture Point MP-917 technical brief 13: single diode probes. Available at http://www.esica.com/support_technical_briefs.php.

FIGURE

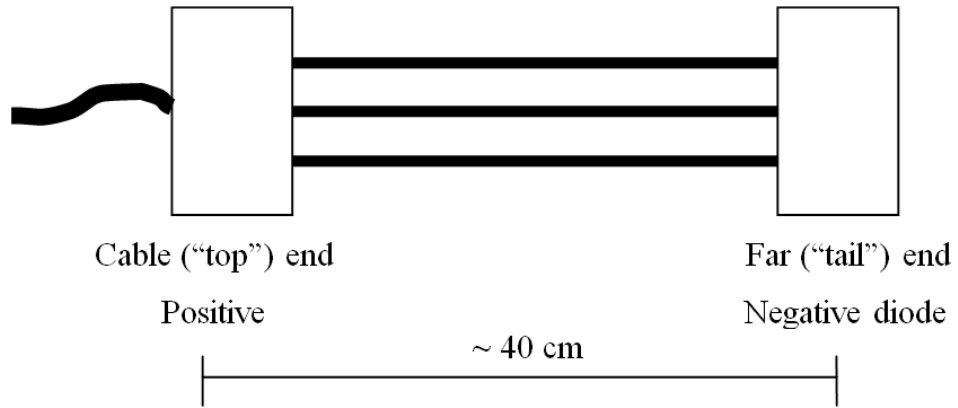


Figure F.1. Schematic of Antamina TDR Probe Type 1.

APPENDIX G: COMPOSITE TANK, FLOW SPLITTER AND SUMP

G.1	COMPOSITE TANK AND FLOW SPLITTER.....	297
G.1.1	HYDROLOGY	297
G.1.2	CHEMISTRY	298
G.1.3	SOLUTE LOADINGS.....	299
G.2	SUMP.....	299
G.2.1	CHEMISTRY	299
G.3	REFERENCE.....	299

APPENDIX G: COMPOSITE TANK, FLOW SPLITTER AND SUMP

G.1 COMPOSITE TANK AND FLOW SPLITTER

A composite tank was installed to enable weekly mass balance (water) and mass loading (solute) calculations for the entire pile, and to provide a secondary check on the integrated pile flow and chemistry from each individual lysimeter.

All of the water draining from the bottom of each of the four tipping buckets converges to a single pipe that directs water to a flow splitter. The flow splitter, 0.8 m long x 0.33 m wide x 0.75 m tall, is designed to separate approximately 6.25 % of the combined effluent water and convey it (under gravity) to a composite tank.

The 2.5 m³ (1.55 m high x 1.60 m wide) composite tank consists of a multi-layered plastic that prevents solar rays from penetrating the tank (so as not to affect the geochemistry of the water) and a high-resistance outer layer that prevents degradation over time. The tank was installed at a 3 % gradient towards the direction of the outlet valve roughly located 2 cm above the base of the tank. It is assumed that there is a negligible amount of water and sediment remaining in the tank after it is drained. For precaution, a roof is located above the tank to prevent any damage from occurring. Corazao Gallegos (2007) contains further details about the design, construction, installation and calibration of the flow splitter.

G.1.1 Hydrology

The volume of water residing in the composite tank is calculated based on the height of the water in the tank and the tank radius. A comparison between the weekly volume of water in the composite tank and the cumulative pile water volume (combination of all four lysimeters) shows that a very poor correlation exists. This is even more prevalent in the wet season, and is likely explained in 3 ways:

1. an inaccurate measurement of height of water in the composite tank,
2. a leak in the composite tank or pipes that transmit water to it, or
3. a poorly functioning flow splitter.

It is most likely that the flow splitter does not function properly. At high flow rates it was noted that performance of the flow splitter began to deteriorate (Corazao Gallegos, 2007). Field observations confirm that there were small leaks in the casing seams that resulted in a loss of water that cannot be accounted for. Evidently, maintenance of the flow splitter was insufficient to stop the leaks, which continue to affect the data during both low- and high-flow rates and explains the poor correlation.

G.1.2 Chemistry

While volume estimates from the composite tank proved to be unreliable, the chemistry is still representative of the large-scale pile behaviour and is discussed in Chapter 4. The composite tank solute chemistry represents an integration of flow from all four lysimeters, whereas the lysimeter chemistry represents an instantaneous snapshot of water chemistry. Theoretically, if the concentrations vary rapidly (i.e., hours), these differences will be exhibited in the discrepancy between the chemistry in the lysimeters and composite tank. On the other hand, if the concentrations are rather similar, this would indicate that concentrations change slowly. This has implications for the solute sampling schedule.

The specific conductance, Zn, Ca, Na, SO₄ and alkalinity in the composite tank are similar to those reported in the basal lysimeter and sump (Table 4.1; Figure 4.9). The difference in pH is likely the result of CO₂ degassing of the effluent water as it comes into contact with atmospheric CO₂ when it passes through the splitter or is retained in the composite, which increases the pH (Section 4.3.4). There are also differences between wet and dry seasons. In general, the average composite tank and basal lysimeter values are more similar during the wet season, with slightly (< 4 %) higher concentrations in the composite tank, with the exception of Mg and alkalinity. In contrast, average composite tank concentrations are 4 – 15 % lower during the dry season with the exception of pH and Na, which are 7 and 9 % higher, respectively (Table 4.1).

Since basal lysimeter and composite tank geochemistry is rather similar, this indicates that D does not register any large spikes in solute concentration that may be missed in the time-averaged composite tank readings. Therefore, although volume estimates based on the composite

tank levels proved to be unreliable, the chemistry data is not. Further discussion is found in Chapters 4 and 5.

G.1.3 Solute Loadings

Based on a low reliability of volume data in the composite tank, no loadings could be calculated.

G.2 SUMP

G.2.1 Chemistry

Three samples were extracted from the sump (12-Apr-2007, 28-Nov-2007, 1-May-2008) and sent for analysis. With the exception of pH and SO₄, most of the solute concentrations in the sump fall within the general parameter range within the pile. For example, specific conductivity, dissolved Cu, K, Mg, Na, and Zn levels in the sump are similar to the basal lysimeter, indicating that the 2B-Protective Layer does not have significantly different chemistry from the rest of the pile. In addition, Figure 4.9 indicates that initial sump concentrations are higher than D and E, particularly with regards to total Fe concentration (3.5 mg/L in April 2007). The high reported Fe levels in the sump, and not in the composite tank or basal lysimeter, suggests anoxic (or slightly-closed system) conditions do exist within the pile, possibly due to the presence of a water table. Further pore gas analyses showing oxygenation and aeration may help to prove this.

Based on the chemistry data in addition to a low hydraulic conductivity of the 2B-Protective Layer, it is likely that this protective layer has a negligible impact on the pile hydrogeochemistry. However, there are not enough data points (n = 3) to significantly document discernable trends from the sump, but it can be concluded that the sump is not significantly affecting the chemistry of the basal lysimeter.

G.3 REFERENCE

Corazao Gallegos, J.C., 2007. The design, construction, instrumentation, and initial response of a field-scale waste rock test pile, M.A.Sc. thesis. University of British Columbia, Vancouver, Canada.

APPENDIX H: DATALOGGER PROGRAM

Cr1000 program: most recent version (implemented 26-aug-2008)

'TODOS_V_08_ANDRE5_PILE1.CR1
'implemented Aug 26, 2008

' CR1000

' A N T A M I N A / UNIVERSITY OF BRITISH COLUMBIA
' Pilas Experimentales de Roca Desmonte

' Pila 1 Typo B

.....
' Written by: David Jones and Matt Neuner 2006
' Revised by: H. Valdivia 2007/8 and A.Wild 2008

.....
' tipping buckets collected on-demand, All others collected every 30 min
' Data collection Rates:
' 30 min: TDR , Temperature, Conductivity

' hardware setup:

' 1)ESI Interconnect Module

' comME part of CS I/O

' SW12 as Power Control of MP-917 from Interconnect Module

' added 78L05 for level shift (12 to 5 v) 2) SDMX50

.....
' 2) SDMX50' SMD protocol

' Port1 = Data

' Port2 = Clock

' Port3 = Enable

' The multiplexer is serially addressed using an 8 bit clocked data stream. Four bits
' are used to specify one of the 16 inputs and the other 4 bits are used to specify the
' address of the multiplexer itself. The multiplexer may be set to one of 16 addresses
' by moving a jumper on the back (bottom of lower of two printed circuit boards)

' ScanRate determined by 22 diodes * 30 sec/diode + Temperature +??

.....
' 3)RST flexi-mux set for 2 wire thermistors and 4 wire conductivity

' Port 4 = Reset for RST Thermistor Muxes

' Port 7 = Clock for RST Thermistor Muxes

' there are 3 muxes in parallel, so 3 thermistors can be measured each mux address cycle

' each mux can control 10 thermistors so 30 thermistors are available

' Half Bridge Resistor = 2255 ohms

.....
' Conductivity resistor = 47.2 ohms

' cond cells are on RST mux configured as as a differential

' It is the last mux and is addressed by clocking thru the first mux

' 10 clocks will get to the cond

.....
Const measCond = 1

Const measMoist = 1

Const measTemp = 1

Const OFF = 0

Const ON = 1

Const MainScanRate = 30

Const fastScan = 200

Const LastDiode = 22

Const DiodePower = 9

```

Const LastTherm = 30
Const TReset = 4
Const TClock = 7
Const RValue = 2255

Const C0 = .0014733
Const C1 = .0002372
Const C3 = 1.074E-07

Const EC_Rf = 47.2
Const k = -1.884

Public TB_1
Public TB_1_total as Long
Public TB_2
Public TB_2_total as Long
Public TB_3
Public TB_3_total as Long
Public Drain
Public Drain_total as Long
Public Rain
Public Rain_total as Long

Public modThing as Long
Public counter as Long

Public ch
Public cch
Public tch
Public ich
Public i

Public Thermistor(4,10)
Public TRatio(4,10)
Public TResist
Public LnR
Public Kelvin

Public Moist(22) As Float
Public DiodeData As String * 50
Public ParseStr(5) As String * 15

Public Full(4)
Public EC_V2_V1(4)
Public EC_Rs(4)
Public EC(4)

Public Batt

Units Rain=tip
Units Drain=tip
Units TB_1=tip
Units TB_2=tip
Units TB_3=tip
Units EC()=mS/cm
Units Thermistor()=deg C
Units MOIST()=ns

DataTable (tblRain,True,-1)
  CardOut(0,-1)
  sample (1,Rain,FP2)
  sample (1,Rain_total,Long)
EndTable

DataTable (tblTB_1,True,-1)
  CardOut(0,-1)
  sample(1,TB_1,FP2)
  sample(1,TB_1_total,Long)
EndTable

```

```

DataTable (tblTB_2,True,-1)
  CardOut(0,-1)
  Sample(1,TB_2,FP2)
  Sample(1,TB_2_total,Long)
EndTable

```

```

DataTable (tblTB_3,True,-1)
  CardOut(0,-1)
  Sample(1,TB_3,FP2)
  Sample(1,TB_3_total,Long)
EndTable

```

```

DataTable (tblTB_4,True,-1)
  CardOut(0,-1)
  Sample (1,Drain,FP2)
  Sample (1,Drain_total,Long)
EndTable

```

```

DataTable(tblTher,True,-1)
  CardOut(0,-1)
  ' DataInterval(0,30,Min,0)
    Sample (1,Batt,FP2)
    Sample(40,Thermistor(),IEEE4)
EndTable

```

```

DataTable(tblEC, True,-1)
  CardOut(0,-1)
  ' DataInterval(0,30,Min,0)
  Sample (4,EC(),IEEE4)
EndTable

```

```

DataTable(tblTDR, True,-1)
  CardOut(0,-1)
  ' DataInterval(0,30,Min,0)
  Sample(22,MOIST(),IEEE4)
EndTable

```

```

Sub SetMux(ch)

```

```

Select Case (ch)
  Case 1
    SDMX50 (1,1)
  Case 2
    SDMX50 (1,2)
  Case 3
    SDMX50 (1,3)
  Case 4
    SDMX50 (1,4)
  Case 5
    SDMX50 (1,5)
  Case 6
    SDMX50 (1,6)
  Case 7
    SDMX50 (1,7)
    SDMX50 (2,1)
  Case 8
    SDMX50 (1,7)
    SDMX50 (2,2)
  Case 9
    SDMX50 (1,7)
    SDMX50 (2,3)
  Case 10
    SDMX50 (1,7)
    SDMX50 (2,4)
  Case 11
    SDMX50 (1,7)
    SDMX50 (2,5)
  Case 12

```

```

                SDMX50 (1,7)
                SDMX50 (2,6)
Case 13
                SDMX50 (1,7)
                SDMX50 (2,7)
Case 14
                SDMX50 (1,7)
                SDMX50 (2,8)
                Case 15
                SDMX50 (1,8)
                SDMX50 (3,1)
Case 16
                SDMX50 (1,8)
                SDMX50 (3,2)
Case 17
                SDMX50 (1,8)
                SDMX50 (3,3)
Case 18
                SDMX50 (1,8)
                SDMX50 (3,4)
Case 19
                SDMX50 (1,8)
                SDMX50 (3,5)
Case 20
                SDMX50 (1,8)
                SDMX50 (3,6)
Case 21
                SDMX50 (1,8)
                SDMX50 (3,7)
Case 22
                SDMX50 (1,8)
                SDMX50 (3,8)
                EndSelect
EndSub

Sub CalcCelsius()
For i= 1 To 4
    For ich = 1 To 10
        TResist = RValue*TRatio(i,ich)/(1-TRatio(i,ich))
        LnR = LOG(TResist)
        Kelvin = 1/(C0+ C1*LnR + (C3*LnR*LnR*LnR))
        Thermistor(i,ich) = Kelvin - 273.15
    next ich
Next i
EndSub

Sub CalcEC()
For cch = 1 To 4
    EC_V2_V1(cch) = Full(cch)*0.001
    EC_Rs(cch) = EC_V2_V1(cch)*EC_Rf
    Select Case cch
        Case 1
            EC(cch) = k/EC_Rs(cch)*10*13.0912
        Case 2
            EC(cch) = k/EC_Rs(cch)*10*13.0378
        Case 3
            EC(cch) = k/EC_Rs(cch)*10*12.6587
        Case 4
            EC(cch) = k/EC_Rs(cch)*10*13.0103
    EndSelect
Next cch
EndSub

Sub getOtherStuff()
    For ch = 1 To LastDiode
        Do
            Call SetMux(ch)

```

```

        Delay(1,1,Sec)
        PortSet (DiodePower,ON)
        Delay(1,1,Sec)

        SerialIn (DiodeData,ComRS232,3000,13,100)
        PortSet (DiodePower,OFF )

        SplitStr (ParseStr(1),DiodeData,CHR(44),5,6)
        moist(ch) = parsestr(3)
        SerialFlush (ComRS232)
        Loop While moist(ch) = NAN
    Next ch

    PortSet(TReset,ON)
    Delay (0,100,mSec)
    For tch = 1 To 10
        PortSet(TClock,ON)
        Delay (0,20,mSec)
        PortSet(TClock,OFF)

        BrHalf (TRatio(1,tch),1,mV2500,14,Vx2,1,2500,True ,0,250,1.0,0)
        BrHalf (TRatio(2,tch),1,mV2500,15,Vx2,1,2500,True ,0,250,1.0,0)
        BrHalf (TRatio(3,tch),1,mV2500,16,Vx2,1,2500,True ,0,250,1.0,0)
        Delay (0,500,mSec)
        next tch
        PortSet(TReset,OFF)

        BrHalf (TRatio(4,1),1,mV2500,7,Vx3,1,2500,True ,0,250,1.0,0)
        BrHalf (TRatio(4,2),1,mV2500,8,Vx3,1,2500,True ,0,250,1.0,0)
        BrHalf (TRatio(4,3),1,mV2500,9,Vx3,1,2500,True ,0,250,1.0,0)
        BrHalf (TRatio(4,4),1,mV2500,10,Vx3,1,2500,True ,0,250,1.0,0)
        BrHalf (TRatio(4,5),1,mV2500,11,Vx3,1,2500,True ,0,250,1.0,0)
        BrHalf (TRatio(4,6),1,mV2500,12,Vx3,1,2500,True ,0,250,1.0,0)

        TRatio(4,7) = .5
        TRatio(4,8) = .5
        TRatio(4,9) = .5
        TRatio(4,10) = .5

        CalcCelsius

        PortSet(TReset,ON)
        Delay (0,100,mSec)

        For cch = 1 To 10
            PortSet(TClock,ON)
            Delay (0,20,mSec)
            PortSet(TClock,OFF)

        Next cch
        PortSet(TClock,ON)
        Delay (0,20,mSec)
        PortSet(TClock,OFF)
        Delay (0,20,mSec)
        PortSet(TClock,ON)
        Delay (0,20,mSec)
        PortSet(TClock,OFF)

        For cch = 1 To 4
            BrFull6W (Full(cch),1,mV2500,mV2500,1,Vx1,1,2500,True ,True ,0,250,1.0,0)
            Delay (0,200,mSec)

            Delay (0,200,mSec)

            PortSet(TClock,ON)
            Delay (0,20,mSec)
            PortSet(TClock,OFF)
            Delay (0,200,mSec)

        Next cch
        CalcEC

```

```

PortSet(TReset,OFF)

Battery (Batt)
EndSub

BeginProg

SerialOpen (ComRS232,9600,0,0,2000)
SerialFlush (ComRS232)

counter = 0
modThing = (MainScanRate*60000)/fastScan

Scan (fastScan,mSec,0,0)

    PulseCount (Rain,1,1,2,0,1.0,0)
    Rain_total=Rain_total+Rain
    If Rain>0 Then
        CallTable tblRain
    EndIf

    PulseCount (TB_1,1,2 ,2,0,1.0,0)
    TB_1_total=TB_1_total+TB_1
    If TB_1>0 Then
        CallTable tblTB_1
    EndIf

    PulseCount (TB_2,1,15,2,0,1.0,0)
    TB_2_total=TB_2_total+TB_2
    If TB_2>0 Then
        CallTable tblTB_2
    EndIf

    PulseCount (TB_3,1,16 ,2,0,1.0,0)
    TB_3_total=TB_3_total+TB_3
    If TB_3>0 Then
        CallTable tblTB_3
    EndIf

    PulseCount (Drain,1,18 ,2,0,1.0,0)
    Drain_total=Drain_total+Drain
    If Drain>0 Then
        CallTable tblTB_4
    EndIf

    if counter >= modThing
        call getOtherStuff()
        CallTable tblTher
        CallTable tblEC
        CallTable tblTDR
    counter = 0
    EndIf
    counter = counter + 1

NextScan

EndProg

```

APPENDIX I: MATLAB M.FILES

I.1	FLOW	307
I.1.1	LOADING TIPPING BUCKET DATA	307
I.1.2	GETTING THE TIP-TIME BETWEEN 2 DATESTAMPS	307
I.1.3	CORRECTION FOR MISSED TIPPING BUCKET TIPS: RANSAC	308
I.1.4	INTEGRATE TIME FLOW	311
I.2	ELECTRICAL CONDUCTIVITY	311
I.3	TDR.....	313
I.3.1	MERGING 2 FILES TOGETHER.....	313
I.3.2	MERGING TDR AND THERMISTOR DATA.....	313
I.3.3	TDR CALIBRATION.....	314
I.4	THERMISTOR DATA: LOADING, PLOTTING AND SMOOTHING	317
I.5	OTHER	317
I.5.1	REMOVING OUTLIERS AND NEGATIVE VALUES	317
I.5.2	REMOVING 'GHOST' TIPS	318
I.5.3	GAUSSIAN FILTER	318

I.1 FLOW

I.1.1 Loading Tipping Bucket Data

% getRawData.m

```
function [tRaw, dtRaw] = getRawData(inName)

% file format constants
dateFormatString = '%f-%f-%f %f:%f:%f',%f,%f\n';
nColumns = 8;
minuteColumn = 5;
hourColumn = 4;
secondsColumn = 6;
daysColumn = 3;
monthsColumn = 2;
yearsColumn = 1;
recordNumberColumn = 7;

% filter for taking derivatives
diffFilter = [1,-1];

% read data from file
Data = fscanf(fopen(inName), dateFormatString);
Data = reshape(Data, nColumns, size(Data,1)/nColumns)';
Data = [Data,(1:size(Data,1))'];

% calculate the time in seconds using matlab's datenum
dateVec = [Data(:,yearsColumn), Data(:,monthsColumn), Data(:,
daysColumn),Data(:, hourColumn),Data(:, minuteColumn),Data(:,
secondsColumn)];
tRaw = datenum(dateVec);

% calculate differences in time
dtRaw = convSame(diffFilter, tRaw);
dtRaw = dtRaw(2:end);

end

function out = convSame(f, data)
    data = [data((max(size(f))/2):-1:1);data;data(end:-1:end -
(max(size(f))/2)+1)];
    out = conv(f, data);
    out = out((max(size(f))):end-(max(size(f))));
end
```

I.1.2 Getting the Tip-Time Between 2 Datestamps

% convSame.m

```
function out = convSame(f, data)
    data = [data((max(size(f))/2):-1:1);data;data(end:-1:end -
(max(size(f))/2)+1)];
    out = conv(f, data);
    out = out((max(size(f))):end-(max(size(f))));
end
```

I.1.3 Correction For Missed Tipping Bucket Tips: RANSAC

% interpdataArray.m

```
% function to calculate missed tips from tipping bucket data
% a modified RANSAC procedure is used to cluster the data into
% integer levels
% andre wild 6.4

function [out, dtRaw, mData] = interpdataArray(tRaw,dtRaw)

%[intd,date,data] = interpdataArray(UBC1D(2:end,1), UBC1D (2:end-1,2))
% file format constants
% call clustering function
display('start clustering')
mData = ransacData(dtRaw);

% call data expansion function on clustered data
display('start expansion')
out = expandData(mData, tRaw);

end

% function to expand data which has a known integer level
function out = expandData(mData, tRaw)

    out = zeros(sum(mData(:,2)),3);
    out(1,:) = [tRaw(1),1,1];
    index2 = 2;

    for index = 1:size(mData,1)
        if mData(index,2) == 1
            out(index2,:) = [tRaw(index+1),index,mData(index,2)];
            index2 = index2 + 1;
        else
            for i = 1:mData(index,2)
                out(index2,:) = [tRaw(index)+(i)*((tRaw(index+1)-
tRaw(index))/(mData(index,2))),index,mData(index,2)];
                index2 = index2 + 1;
            end
        end
    end
end

% function used to cluster the data
function mData = ransacData(data)

    % window size (horizontal) for each set of clusters
    windowSize = 175; %trial and error found this to be good
```

```

% maximum number of iteration of the RANSAC algorithm
maxIterations = 20;

% size of the consensus set needed to break the the loop
breakSize = 0.90*windowSize;

mData = zeros(size(data,1),2);
size(mData)
windows = getWindows(data, windowSize);
i = 1;
sumSet = 0;
for currentWindow = windows
    if mod(i,20) == 0
        display(sprintf('%f of %f windows',[i,size(windows,2)]))
    end
    set = currentWindow{1};
    k = 1;
    bestSet = 0;
    while k < maxIterations
        [inSet, setNum] = getFunctions(set);
        conSetSize = sum(inSet(set(:,1)));
        if conSetSize >= breakSize
            setNumBest = setNum;
            break;
        end

        if conSetSize > bestSet
            setNumBest = setNum;
            bestSet = conSetSize;
        end
        k = k+1;
    end
    setSize = size(set,1);
    sumSet = sumSet + setSize;
    mData(((i-1)*windowSize+1):((i-1)*windowSize)+setSize,:) =
[set,setNumBest(set)];
    i = i + 1;
end
end

% function which returns two functions to determine if it is in a
consensus set and an other to determine which level it is in
function [inSet, setNum] = getFunctions(set)

    f = 0.3;

    point = ceil(rand*size(set,1));
    firstLevel = set(point,1);
    level = firstLevel;
    inSet = '@(x)  ';
    setNum = '@(x)  ';

```

```

i = 1;

while level <= max(set(:,1)) + firstLevel
    if i > 1
        inSet = strcat(inSet, '|');
        setNum = strcat(setNum, '+');
    end

    sSet = sprintf('(x<%f)&(x>%f)', [level + f*firstLevel, level
- f*firstLevel]);
    sNum = sprintf('double((x<=%f)&(x>%f))*%f', [level +
0.5*firstLevel, level - 0.5*firstLevel, i]);

    inSet = strcat(inSet, sSet);
    setNum = strcat(setNum, sNum);

    level = level + firstLevel;
    i = i + 1;
end
inSet = eval(inSet);
setNum = eval(setNum);
end

% returns a cell array containing window of the original data
function out = getWindow(data, windowSize)
    n = floor(size(data,1)/windowSize);

    out = cell(1,n);
    for i = 1:n
        out(i) = {data((i-1)*windowSize+1:i*windowSize,:)};
    end

    if size(data(n*windowSize+1:end,:),1) > 0
        if size(data((n*windowSize+1):end, :),1) > windowSize/2
            out = [out, {data(n*windowSize+1:end,:)}];
        else
            out{end} = [out{end}; data(n*windowSize+1:end,:)];
        end
    end
end

% function to "mirror" the ends of a vector and convolve it with a
filter
% (used to compute rolling averages)
function out = convSame(f, data)
    data = [data((max(size(f))/2):-1:1); data; data(end:-1:end -
(max(size(f))/2)+1)];
    out = conv(f, data);
    out = out((max(size(f))):end-(max(size(f)))));
end

```

I.1.4 Integrate Time Flow

```
%integrateTimeFlow

function out = integrateTimeFlow(a, interval) %input nx2 vector
(date, minute interval) ie. A = integrateTimeFlow(a, 1440);
%Cvol = [UBClAintd(:,1) (UBClAintd(:,2).*UBClAintd(:,3))*(1440)];
%date, %tip-time, flow rate
%v = integrateTimeFlow(Cvol, 1440);
%A Wild, D. Bay - summer 2008

%this function is used to calculate the volume of water (in L for
small and large TBs)
    %interval must be in minutes, and is a variable when calling the
    %function
    %This gives you a nx3 matrix: date, volume, number of rows included
mins = round((a(:,1) - datenum('Jan 01 2007'))*1440); %converts data
to number of minutes since Jan 1, 2007
mins = ceil(mins/interval);
lastmins = mins(1);
x = [0,0];
out = [];
for i= 2:size(a,1)
    if mins(i) ~= lastmins
        out = [out; (mins(i-1)*interval)/1440 + datenum('Jan 01
2007'), x];
        x = [a(i,2), 1]; %CHANGE THE FLOW COLUMN HERE!!!! in killer,
flow is in 3rd column!!!!
        lastmins = mins(i);
    else
        x = x + [a(i,2), 1]; %CHANGE THE FLOW COLUMN HERE!!!!
    end
end
out = [out; (mins(i-1)*interval)/1440 + datenum('Jan 01 2007'), x];
out(:,1) = out(:,1) - interval/(1440*2); %subtracts half of interval
(in minutes) is converted to days (for
```

I.2 ELECTRICAL CONDUCTIVITY

```
% getEC.m

function [temp, temp2, temp3] = getEC(data, TC, x)

% x = time interval
% data = raw EC data and Temp data
% TC = temperature correction = 0.018
f = ones(x,1)/x; % 24 = 12 hrs, 48 = 24 hrs, 72 = 36 hrs

%To correct for temperature variations (assuming nonlinearity effects
are negligible), equation [2.1] was applied (Hayashi, 2004):
%
%           EC25 = SC = ECT[1+a(t-25)]
%Where ECT is the measured EC [ $\mu\text{S}/\text{cm}$ ] at a given temperature t [ $^{\circ}\text{C}$ ],
EC25 is the EC at a standard reference temperature of t = 25  $^{\circ}\text{C}$  and
```

referred to as specific conductance (SC). The temperature compensation factor a [$^{\circ}\text{C}^{-1}$] is an arbitrary value (dependent on the TDS-EC relationship) and accounts for increases to EC with temperature increase. A common used a value is 2 %, which describes a '2 % increase of EC per 1°C of temperature'. Other, more site-specific temperature compensation values

%have been employed previously (e.g., 1 - 3 %; Hayashi, 2004).

```
% -----Apply Temperature Correction-----
ECTC1 = (data(:,6))./((((data(:,2))-25)).*TC)+1); %UBCA
ECTC2 = (data(:,7))./((((data(:,3))-25)).*TC)+1); %UBCB
ECTC3 = (data(:,8))./((((data(:,4))-25)).*TC)+1); %UBCC
ECTC4 = (data(:,9))./((((data(:,5))-25)).*TC)+1); %UBCD
temp = [data ECTC1 ECTC2 ECTC3 ECTC4]; % concatenate all Temp
Correction EC values to this variable

% -----Remove Outliers (NaN)-----%

a = outliersNaNposEC(temp(:,[1 10]));
b = outliersNaNposEC(temp(:,[1 11]));
c = outliersNaNposEC(temp(:,[1 12]));
d = outliersNaNposEC(temp(:,[1 13]));
temp2 = [data(:,1) a(:,2) b(:,2) c(:,2) d(:,2)];

% -----Filter temperature corrected ECall-----%

ECf1 = convSame(f,temp2(:,2));
ECf2 = convSame(f,temp2(:,3));
ECf3 = convSame(f,temp2(:,4));
ECf4 = convSame(f,temp2(:,5));
temp3 = [data(:,1) ECf1 ECf2 ECf3 ECf4]; % concatenate all Temp
filtered data to this variable

% you should probably group this somehow either with grouping.m or an
% integrateEC.m file

%-----plot all raw TEMP-----%
%plot (data(:,1),data(:,2),'b-',data(:,1), data(:,3),'g-', data
(:,1), data(:,4),'c-', data(:,1), data(:,5),'m-' );

%-----plot all raw EC-----%
%plot (data(:,1),data(:,6),'b-',data(:,1), data(:,7),'g-', data
(:,1), data(:,8),'c-', data(:,1), data(:,9),'m-' );
%-----plot Specific Conductance-----%
%plot (temp(:,1),temp(:,10),'b.',temp(:,1), temp(:,11),'g.', temp
(:,1), temp(:,12),'c.', temp(:,1), temp(:,13),'m.' );
%-----plot SC with removed Outliers-----%
%plot (temp2(:,1),temp2(:,2),'b.',temp2(:,1), temp2(:,3),'g.',
temp2(:,1), temp2(:,4),'c.', temp2(:,1), temp2(:,5),'m.' );
%-----plot all filtered (48) , temperature corrected EC-----%
```

```

plot (temp3(:,1),temp3 (:,2)*1000,'b.',temp3 (:,1), temp3
(:,3)*1000,'g.', temp3 (:,1), temp3 (:,4)*1000,'c.', temp3 (:,1),
temp3 (:,5)*1000,'m.' );
datetickzoom('x')
title('Specific Conductance')
xlabel('Date')
ylabel('Specific Conductance (EC @ 25 {}^oC ')
hold on

h = legend('A - SCsmooth', 'B - SCsmooth', 'C - SCsmooth', 'D -
SCsmooth',9);
set(h,'Interpreter','none')

```

```
end
```

I.3 TDR

I.3.1 Merging 2 Files Together

```
% mergedataNaN.m
```

```

function newdat=mergedataNaN(d1,d2)
%newdat = mergedataNaN(UBC1DerrHybrid24,RAIN24);

newdat=[d1,ones*NaN(length(d1(:,1)),length(d2(1,2:end)))]; %initialize new
matrix with zeros
[m,n]=size(newdat); %get dimensions of new matrix
for i=1:length(d2(:,1)) %loop through data to merge
indx=find(newdat(:,1)==d2(i,1)); %find existing dates/labels
if indx
newdat(indx,[n-length(d2(i,2:end))+1:n])=d2(i,2:end); %if label is matched
update the row
else
newdat(m+1,[n-length(d2(i,2:end))+1:n])=d2(i,2:end); %if the label is new,
create new row
newdat(m+1,1)=d2(i,1); %insert new label in first column
end
end

```

I.3.2 Merging TDR and Thermistor Data

```
% consIntMerge.m
```

```

function out = consIntMerge(TDR,Therm,interval)
%hope = consIntMerge(TDRraw2,ThermClean2,60); %2 means after May 8, 2008

%TDR (raw) = n x 23 matrix (date, 22 probes)
%THERM (raw) = n x 33 matrix (date, 32 therms in pile)% calibration uses only
%needed therms

%TDR
A = [];
for i=2:23
tic
temp = integrateTimeAverage(TDR(:,[1 i]),interval);
A = [A temp(:,2)];
display(i)

```

```

toc
end
A = [temp(:,1) A];

%THERM
B = [];
for j=2:33
tic
temp2 = integrateTimeAverage(Therm(:,[1 j]),interval);
B = [B temp2(:,2)];
display(j)
toc
end
B = [temp2(:,1) B];

%z(1,1) = 733060;
%for k = 2:622*(1440/interval);
%z(k,1) = z(k-1,1)+(1/(1440/interval));
%end
%z = z(1:622*1440/interval);
%z = z(1:end)

newdat = mergedataNaN(A,B);

out = newdat;

```

I.3.3 TDR Calibration

% TDRcalibration3.m

```

function [A,B,C,D,E,THERM4TDR] = TDRcalibration3(data,Cor)
% [TDRoff,TDRtc,TDRcali,TDRoutl,TDRsmooth,THERMFINAL] =
TDRcalibration2(hope,Cor);
% data = merged file of [date,22 x tdr probes,32 x therm probes]
% Cor = calibration correction file

%ESTIMATE BROKEN THERMS for TDR Cali (L1:T2,T5 , L3:T3

%to pick thermistors that match with the same port as the TDR
%fix L1,T2 (second from bottom) by averaging L1,T1 and T1,T3
data(:,25) = (data(:,24)+ data(:,26))/2; %column 25
%fix L1,T5 (second from top) by taking dif b/w L2/T4 and L2/T5
data(:,28) = data(:,27)+(data(:,34)-data(:,33));
%fix L3,T3 (3rd from bottom)
%based on may 26,2007 to 9/22,2007
%L3,T4 is on average 0.1942 deg C higher than L3, T3 - so add this
data(:,38) = data(:,37)+0.1942;

%Line 5 TEMP INTERP for TDR
%becuase they one is not always greater than the other...

if (data(:,53)-data(:,52)) > 0
L5interp = data(:,52)-((data(:,53)-data(:,52))*5/17.5);
else
L5interp = data(:,52)+((data(:,53)-data(:,52))*5/17.5);

```

```

end
%Line 6 TEMP INTERP for TDR - straight average of L5,T2 and L6,T3
L6interp = ((data(:,55)+data(:,49))/2);
%Therm files for TDR data
THERM4TDR = [(data(:,[1 24:28 30:34 36:40 42:46])) L5interp L6interp];

%TDR Raw Travel Time Correction
% (TDRraw - Probe offset)/TT air

A = [];
for i=2:23
tic
temp = (data(:,i)-Cor(i-1,6))/Cor(i-1,5); %TDRraw - PoffSet / ttair
%Poffset = TairProbe - TairTheoretical
A = [A temp(:,1)];
display(i)
toc
end
A = [data(:,1) A];

%Get Temperature Correction
%(TDRcorr-(21-THERM)) *((-0.006*TDRcorr)*(0.01587))

B = [];
for j=2:23
tic
temp2 = A(:,j)- (21 - THERM4TDR(:,j)).*((2.645*0.006)-0.006*A(:,j));
%mat2
B = [B temp2(:,1)];
display(j)
toc
end
B = [data(:,1) B];

%APPLY CALIBTATION
% DIAVIK
% CLuff Lake washed and unwashed
C = [];
%washed coefficients
a1 = 10.03576;
b1 = 4.334945;
c1 = 1.845;

%unwashed coefficients --> see 'CPE Soil Calibration Version III.xls'
a2 = -0.35007;
b2 = 5.492317;
c2 = 1.91;

%unwashed coefficients --> modified by dbay
a3 = 0.4305;
b3 = 5.1391;
c3 = 1.9376;

```

```

for k=2:23
tic
%temp3 = (0.093.*(B(:,k).^4))-(0.983.*(B(:,k).^3))+(3.74.*(B(:,k).^2))-
(5.9.*(B(:,k)))+3.29;%Diavik
%temp3 = (-b1+((4.*a1.*B(:,k))-(4.*a1*c1)+(b1*b1)).^0.5)/(2.*a1); %Cluff Lake
unwashed (higher concentration)
temp3 = (-b2+((4.*a2.*B(:,k))-(4.*a2*c2)+(b2*b2)).^0.5)/(2.*a2); %Cluff Lake
washed (low concentration)<<<USE THIS<<<
%temp3 = (-b3+((4.*a3.*B(:,k))-(4.*a3*c3)+(b3*b3)).^0.5)/(2.*a3); %Cluff Lake
Washed (modified by dbay)
%temp3 = (-0.053+(0.0292*(B(:,k)))-
0.00055*(B(:,k).^2))+0.0000043*(B(:,k).^3)); %topp - homogeneous soil
%temp3 = (0.0263-0.1019*B(:,k)+0.0698*B(:,k).^2-0.0055*B(:,k).^3); %topp -
coating correction

C = [C temp3(:,1)];
display(i)
toc
end
C = [data(:,1) C];

%outliers
D = [];
for l = 2:23
tic
temp4 = outliersNaNpos(C(:,[1 l]));
D = [D temp4(:,2)];
display(l)
toc
end
D = [data(:,1) D];

%smoothing
E = [];
f = ones(24,1)/24;
for m = 2:23
tic
temp5 = convSame(f,D(2:end-1,m));
E = [E temp5(:,1)];
display (m)
toc
end
E = [data(2:end-1,1) E];

%figure

%g = bar (RAIN24(289:end,1),RAIN24(289:end,2),'FaceColor',[0.8 0.8 0.8]);
%set(g,'EdgeColor','k')

formats = {'b-','g-','r-','c-','m-','b-','g-','r-','c-','m-','b-','g-','r-','c-','m-','b-','g-','r-','c-','m-','k-','b-','g-','r-','c-','m-'};
hold on
for n=2:23
plot (E(:,1),E(:,n)*100,formats{n-1},'LineWidth',3);

```

```

end
datetickzoom('x')

title('TDR Moisture Data','FontSize',15)
xlabel('Date')
ylabel('% Volumetric Water Content [m^3/m^3]','FontSize',15)
set(gca,'FontSize',15)

h1 =
legend('Precipitation','L1TDR1','L1TDR2','L1TDR3','L1TDR4','L1TDR5','L2TDR1',
'L2TDR2','L2TDR3','L2TDR4','L2TDR5','L3TDR1','L3TDR2','L3TDR3','L3TDR4','L3TD
R5','L4TDR1','L4TDR2','L4TDR3','L4TDR4','L4TDR5','L5TDR1','L6TDR1');

```

I.4 THERMISTOR DATA: LOADING, PLOTTING AND SMOOTHING

% getTemp.m

```

function [A,B] = getTemp(therm) %A = imported Therm text file

%state variables
f = ones(48,1)/48;
A = [];
B = [];

%remove outliers
for i = 3:34
temp = outliersNaNpos(therm(:,[1 i]));
A = [A temp(:,2)];
end
A = [therm(:,1) A];

%smooth using box filter
for j = 2:33
temp2 = convSame(f,A(2:end-1,j));
B = [B temp2];
end
B = [therm(2:end-1,1) B];
end

formats = {'b-','g-','r-','y-','r-','k-','b.','g.','r.','c.','m.-','y.-',
'k.','b:','g:','m.-','y.-','k.','b:','g:','r:','b-','g-','r-','r-','c-
','m-','y-','k-','b.','g.','r.','g.'};
hold on
for i=2:33
plot (A(:,1),A(:,i),formats{i-1});
end
datetickzoom('x')

```

I.5 OTHER

I.5.1 Removing Outliers and Negative Values

outliersNaNpos.m

```

%outliers THERM - POSITIVE NUMBERS
function out = outliersNaN(A)
%temp = outliersNaNpos(therm(:,[1 i]));
out = ones(size(A))*NaN;
threshold = 0.3;

%this section limits the data between 0 and 50 deg C. If it is false, it
%becomes NaN
for j = 1:size(A,1);
    if A(j,2)>0 && A(j,2)< 50, A(j,2) = A(j,2);

    else
        A(j,2) = NaN;
    end
end

%this section removes any values that are large departures from the value
%before and after it...ie. 0.3 degrees in 30 minutes
for i = 2:size(A,1)-1;
    if abs(A(i,2)- A(i-1,2))<threshold && abs(A(i,2)- A(i+1,2))<threshold;
        out(i,:) = A(i,:);
    end
end

end

```

I.5.2 Removing 'Ghost' Tips

% onesectips.m

```

%already used raw data
function [blank,blank1] = onesectips(date,dt)
dtseconds = dt*86400;
blank = ones(size(date))*NaN;
blank1 = ones(size(dt))*NaN;
for i = 1:size(dt,1)
    if dtseconds(i) > 3
        blank(i) = date(i);
        blank1(i) = dt(i);
    end
end
blank = blank(~isnan(blank));
blank1 = blank1(~isnan(blank1));

%blank1 = blank1(1:end-1);

```

I.5.3 Gaussian Filter

% GaussianFilter.m

```

function y = GaussianFilter(sigma) %this Gaussian Filter is better
than a box filter. It is a weighted filter.

x = -3*sigma:0.1:3*sigma;
y = exp(-x.^2/(2*sigma^2));
y = y/sum(y);

```